



ScuDo
Scuola di Dottorato ~ Doctoral School
WHAT YOU ARE, TAKES YOU FAR



Doctoral Dissertation
Doctoral Program in Mechanical Engineering (34th cycle)

Rotary Electromechanical Shock Absorbers for Automotive and Motorcycle Applications

Salvatore Circosta

* * * * *

Supervisors

Prof. N. Amati, Politecnico di Torino

Doctoral Examination Committee:

Prof. M. Gobbi, Referee, Politecnico di Milano

Prof. L. Zuo, Referee, Virginia Polytechnic Institute and State University

Politecnico di Torino
Examination date

This thesis is licensed under a Creative Commons License, Attribution - Noncommercial-NoDerivative Works 4.0 International: see www.creativecommons.org. The text may be reproduced for non-commercial purposes, provided that credit is given to the original author.

I hereby declare that, the contents and organisation of this dissertation constitute my own original work and does not compromise in any way the rights of third parties, including those relating to the security of personal data.

.....
Salvatore Circosta
Turin, Examination date

Summary

The automotive industry is nowadays facing an innovative push towards more efficient and smart vehicles. Emission reduction and driving automation are the major trends that most of the carmakers are chasing. In this scenario, active electromagnetic suspensions attracted many research efforts. These systems integrate an electromagnetic actuator in the suspension to exert active and passive forces.

The significant number of scientific outcomes and patents published in the last decades proves the interest of the industry and the academy in such technology. However, few efforts were dedicated to rotary linkage-based and full-active systems. Furthermore, the scientific literature lacks a design methodology that gives compact linkage-based layouts starting from vehicle performance and packaging requirements. These aspects cover a relevant role when the research goal is the implementation of such technology at an industry level. Lastly, the gap between the academy and the automotive industry is clear: the former mostly proposes regenerative solutions, the latter is mainly interested in the active feature.

In this context, the present work focuses on the investigation and the development of full-active linkage-based rotary electromechanical suspensions for automotive and motorcycle applications. The proposed layout features a rotary permanent magnet electric machine coupled to a planetary gearbox. The latter is connected to the wheel upright through a linkage, which is needed as linear-to-rotary conversion mechanism. The suspension is provided with both active and damping forces, where the last operation enables energy regeneration. Furthermore, the full-active feature allows to completely replace the conventional shock absorber, thus paving the way to novel suspension archetypes. Based on the above-mentioned characteristics, the proposed solution is named *Rotary Electromechanical Shock Absorber* (REmSA), as it operates as a shock absorber with active and regenerative features.

This work proposes a system-level design methodology for REmSAs in the automotive and motorcycle fields, which intends to be a guideline for both academy and industry moving towards the development of such systems. The methodology led to the development of two prototypes: one for the front suspension of a B-class vehicle, the other for the rear swing-arm of a naked motorcycle.

Then, the thesis discusses the control of REmSAs when the electric machine is driven through a three-phase power module. Two control layers—the low and high

level—were identified. The former controls the force that the REmSA applies to the suspension to mitigate the mechanical non-idealities and inertia of such systems. The high level aims at controlling the vehicle dynamics to optimize comfort and handling performance. Conventional high-level control strategies for active suspensions were numerically simulated to investigate the REmSA impact on the handling, comfort, and energetic performance of the vehicle. To this end, a model reproducing the realistic behavior of REmSAs—i.e. dissipative effects of electric machine and gearbox, the backlash, and the mechanical dynamics of the assembly—is proposed and identified through experimental data of the automotive prototype. It was integrated into the vehicle quarter-car model to assess the system performance when an ISO B road unevenness profile is experienced at 70 km/h.

The simulation results highlighted the importance of the low-level control in guaranteeing vehicle dynamics performance. However, the mitigation of the mechanical non-idealities affect the conversion efficiency of the suspension, which reduces its regeneration efficiency up to 36%. The energetic performance of the REmSA changes according to the adopted high-level control logic. Specifically, comfort-oriented strategies usually leads to average power consumption up to 19.5 W in the simulated condition. Conversely, regenerated average power up to 9.8 W results from the simulated handling-oriented strategy. Although the energy balance is little, such result demonstrates how the regenerative feature could mitigate the energy consumption drawback featured by active suspensions.

Finally, the experimentation of the prototype developed for the automotive application is discussed. The campaign aimed at the performance characterization in terms of efficiency, dynamic behavior, and force capability both in active and passive mode. Specifically, static conversion efficiency up to 74% in the four-quadrant operation was obtained. Dynamic testing in passive mode addressed the mechanical impedance of the REmSA when the electric machine was shunted with an external resistance. It resulted in 6 kNs/m in short-circuit condition at low frequency. The active mode dynamic test addressed the mechanical compliance and the force constant of the prototype, i.e. force over current. The latter highlighted a mechanical resonance in the range 60 to 70 Hz. Acoustic characterization was performed in the anechoic chamber by driving the REmSA prototype through the controlled power module with constant speed. The worst scenario gave noise level of 49.63 dBA, which is below the 24-hour exposure limit of 55 dBA established by the United States Environmental Protection Agency. At the end, a Hardware-In-the-Loop architecture is proposed and preliminary tested for demonstration purposes.

*To Serena,
for being always present
with infinite love.*

Acknowledgements

I would like to acknowledge Nicola for advising and supporting my PhD, for trusting my work and providing always constructive feedback. Special thanks to Prof. Renato Galluzzi—who I spent my PhD side-by-side with—for teaching me really a lot. Thanks to Prof. Andrea Tonoli for his supervision.

I would like to acknowledge the innovation team of Marelli Suspension System and the R&D crew of VRM SpA, very experienced and passionate people who supported and actively contributed to the present research.

Thanks to all my colleagues in Laboratorio di Meccatronica for the very enjoyable and constructive vibes. I would like to thank Gennaro and Manfredi, who recently entered the *rigenerativo* team and started contributing to the research.

Then, I would like to acknowledge Officina Meccanica Massola Srl, the workshop that accompanied my entire PhD by manufacturing components and prototypes as well as providing precious advice, and Elettromeccanica di Tarzia Riccardo & C. Sas, who supported and manufactured the windings of the electric machines developed for the prototypes.

I would like to thank all my friends for being always to my side.

Infinite thanks to my whole family and Serena for being present and supporting my passion for engineering and research. Thanks to my dad, who gave me workshop and practical skills that resulted very precious during my PhD. Thanks to my mum, she has always been the strongest, even if she doesn't know. Thanks Cicci for being a reference.

Finally, special thanks to Serena, we reached this achievement together.

Contents

List of Tables	XI
List of Figures	XIII
Acronyms	XIX
1 Introduction	1
1.1 Thesis motivation	5
1.2 Thesis goal	6
1.3 Thesis outline	7
2 State of the art	11
2.1 Controllable suspensions	11
2.2 Electromagnetic active suspensions	14
2.2.1 Working principle	14
2.2.2 Energy recovery	15
2.2.3 Proposed solutions	16
2.3 Final remarks	28
3 Design methodology	31
3.1 Proposed layout	31
3.2 Design methodology	33
3.3 Methodology implementation	37
3.3.1 Vehicle integration	38
3.3.2 Optimization	55
3.3.3 Detailed design	84
3.3.4 Design outcome	94
4 Modeling and control	101
4.1 Modeling	101
4.1.1 REmsA model	102
4.1.2 Vehicle model	107
4.2 Control	108

4.2.1	Low level control	108
4.2.2	High level control	110
4.3	Results	125
4.3.1	REmSA model identification	125
4.3.2	Vehicle dynamics simulations	129
5	Experimental investigation	169
5.1	Experimental equipment	169
5.2	Static characterization	172
5.2.1	First quadrant operation	172
5.2.2	Four-quadrant operation	176
5.3	Dynamic characterization	179
5.3.1	Mechanical impedance	179
5.3.2	Active-mode FRF	182
5.4	Acoustic characterization	183
5.5	Preliminary Hardware-In-the-Loop test	186
5.6	Final remarks	189
6	Conclusions	191
6.1	Future work	193
A	Design of the automotive prototype	195
B	Mechanical impedance and REmSA lumped parameter model	201
	Bibliography	205

List of Tables

2.1	Classification of controllable suspensions [33]	12
2.2	Qualitative comparison between linear and rotary electromagnetic suspension technologies	29
3.1	Outputs of the preliminary packaging design step	41
3.2	Full-vehicle model parameters	44
3.3	Standardized displacement Power Spectral Density (PSD) (G_d) and road-roughness index (G_r) [90].	46
3.4	ISO B road unevenness with 70 km/h cruise speed results for the three actuator control damping cases.	51
3.5	Maximum outputs of the lumped obstacle simulations for the three actuator control damping cases	54
3.6	Results of the motorcycle accelerating at $a_x = 0.9$ g on smooth road for the three actuator control damping cases.	55
3.7	Performance requirements in nominal and overload conditions	55
3.8	Nominal coordinates of linkage hardpoints	57
3.9	Selected linkage configuration	63
3.10	Fixed design parameters of the electric machine	65
3.11	Gear determined parameters	91
3.12	Features of the Rotary Electromechanical Shock Absorber (REmSA) for motorcycle application resulting from the proposed design methodology.	97
4.1	Results of the quarter-car with Linear–Quadratic Regulator (LQR) suspension control when the vehicle experiences the ISO B-class road at 70 km/h.	124
4.2	Nominal parameters and identified design variables of the REmSA mechanical subsystem (Sec. 4.1.1).	127
4.3	Results of the REmSA mechanical subsystem model identification	128
4.4	Parameters of the quarter-car vehicle model	129
4.5	Low level control gains tuned for 60 Hz bandwidth	130
4.6	Energetic and vehicle dynamics performance of the quasi-ideal model with the high level control reproducing the maximum damping characteristic.	135

4.7	Energetic and vehicle dynamics performance of the quasi-ideal model with the high level control reproducing the minimum damping characteristic.	137
4.8	Energetic and vehicle dynamics performance of the quasi-ideal model with the high level control implementing the LQR with comfort-handling trade-off setting.	141
4.9	Energetic and vehicle dynamics performance of the quasi-ideal model with the high level control implementing the LQR with handling-oriented setting.	144
4.10	Energetic and vehicle dynamics performance of the realistic model with the high level control reproducing the maximum damping characteristic.	150
4.11	Energetic and vehicle dynamics performance of the realistic model with the high level control reproducing the minimum damping characteristic.	153
4.12	Energetic and vehicle dynamics performance of the realistic model with the high level control implementing the LQR with comfort-handling trade-off setting.	157
4.13	Energetic and vehicle dynamics performance of the realistic model with the high level control implementing the LQR with handling-oriented setting.	160
4.14	Energetic and vehicle dynamics performance of the realistic model with the high level control reproducing the minimum damping characteristic. Comparison between the enabled and disabled low level control cases.	163
5.1	Results of the static characterization with the electric machine shunted by an external resistance.	175
5.2	Measured sound pressure levels with constant and sinusoidal input velocities.	186
A.1	Comparison between the automotive prototype [83] and the motorcycle one designed in Chap. 3.	198
B.1	Measured and identified coefficients of the REmSA lumped parameter model	204

List of Figures

2.1	Force-velocity plane of electromagnetic active suspensions	15
2.2	General layout of an electromagnetic active suspension	17
2.3	Series (a) and parallel (b) arrangements of the actuator in active suspensions [21]	17
2.4	Linear electromagnetic active suspension developed by Gysen <i>et al.</i> [49]	18
2.5	Electrohydrostatic regenerative shock absorber prototype developed by Li and Tse [59]	21
2.6	Layout of rack-pinion electromagnetic active suspensions [60]	22
2.7	Ball-screw electromechanical shock absorber prototype developed by Tonoli <i>et al.</i> [38]	23
2.8	Linkage-based electromechanical active suspension layout proposed by Jonasson <i>et al.</i> [37]	25
2.9	Linkage-based electromechanical suspension developed by Yu <i>et al.</i> [68]	26
3.1	REmSA scheme	32
3.2	Design methodology flowchart	34
3.3	Retained vehicle: motorcycle Benelli 752s [88]	38
3.4	View of the rear suspension of the retained motorcycle	39
3.5	Orthogonal view of the rear suspension of the retained motorcycle	40
3.6	Full-vehicle model	42
3.7	Reduced damping characteristic of the shock absorbers of the retained motorcycle	43
3.8	Normalized lumped obstacle profile in the spatial domain	47
3.9	ISO B road unevenness with 70 km/h cruise speed: road profile (a), actuator force (b), actuator velocity (c).	50
3.10	Results for the lumped obstacle scenario simulated at diverse cruise speed values and obstacle amplitudes with mixed damping characteristic	52
3.11	Results of the 50 mm pothole at 50 km/h scenario with mixed damping characteristic	53

3.12	Suspension stroke result when the motorcycle accelerates at $a_x = 0.9 g$ on smooth road	54
3.13	Scheme and geometry constraints of the four-bar linkage	56
3.14	Linkage optimization results	62
3.15	Transmission ratio (a) and transmission angles (b) along the wheel travel for the optimized linkage.	63
3.16	Electric machine cross-section geometry	64
3.17	Electromagnetic 2D finite element model of the electric machine	66
3.18	Magnetic characteristic of Silicon Steel NGO 35PN270 [101]	67
3.19	Finite element results as function of the rotor mechanical angle	68
3.20	Finite element results for the electric machine featuring 85 mm outer stator diameter, 12 slots, $w_{bi} = 3.3$ mm and $R_{ro} = 15.7$ mm	69
3.21	Flowchart of the electric machine optimization process	70
3.22	Optimization approach: average magnetic flux density norm over the probe segments of the stator teeth (a) and (b), and torque-to-length ratio (c), as function of the back iron width and rotor outer radius	71
3.23	Optimized electric machine parameters and performance as function of the stator outer radius in the two investigated slot configurations	72
3.24	Scheme of the winding path in the stator top view. The coil wire outputs the slot on the left and enters the one on the right.	77
3.25	Optimization approach at a given electric machine configuration	82
3.26	Transmission ratio (a), active length (b), and cost function (c) at the optimum points of diverse electric machine configurations	83
3.27	Peak phase voltage (a) and peak phase current (b) maps in the force-velocity plane for the optimized electric machine with the winding featuring 7 turns and 22 wires in hand.	86
3.28	Results obtained with the ideal (blue) and saturated (orange) actuator when the motorcycle undergoes a pothole with 50 mm amplitude at 50 km/h	87
3.29	Double-stage planetary gearbox scheme	87
3.30	Load spectra for gearbox input torque (a) and input speed (b)	89
3.31	Isometric cut view of the rotary electromechanical shock absorber prototype designed for the retained motorcycle.	92
3.32	Side cut view of the electric machine assembly	92
3.33	Side cut view of the gearbox assembly	93
3.34	Side cut view detail of the gearbox multiplier	94
3.35	Envelope of the designed prototype.	95
3.36	Designed REmSA mounted on the rear suspension of the retained motorcycle in nominal (a) and compressed (b) configuration.	96
3.37	Plastic mock-up realized in additive 3D printing (a). Check of the packaging on the rear suspension of the retained motorcycle (b).	97

3.38	Components of the manufactured REmSA prototype for the motorcycle application	98
3.39	Manufactured REmSA prototype for the motorcycle application	99
4.1	Complete model scheme	102
4.2	REmSA model scheme	102
4.3	REmSA power flows and adopted convention	103
4.4	Electric machine model scheme	103
4.5	Maximum torque curve (solid black) and electric power loss map in the active quadrant of the electric machine of the REmSA prototype discussed in Appx. A.	104
4.6	Mechanical subsystem model developed in Simulink/Simscape®	106
4.7	Quarter-car vehicle model	107
4.8	Scheme of the REmSA control	108
4.9	Field Oriented Control (FOC) scheme	109
4.10	REmSA force control	111
4.11	Linear description of the quarter-car model used for the investigation of the high-level control.	112
4.12	Quarter-car vehicle model with skyhook control	113
4.13	Carpet plot using the skyhook control logic into the linear quarter-car model	115
4.14	Quarter-car vehicle model with groundhook control	116
4.15	Carpet plot using the groundhook control logic into the linear quarter-car model	117
4.16	Carpet plot using the spring negation control logic into the linear quarter-car model	119
4.17	Carpet plot using the LQR control strategy into the linear quarter-car model	122
4.18	Frequency Response Function (FRF)s of the quarter-car with LQR suspension control when the input is the road displacement	124
4.19	Comparison of the REmSA force in the force-displacement (a and c) and force-time (b and d) planes	128
4.20	Comparison of the REmSA force in the force-displacement (a) and force-time (b) planes	129
4.21	Maximum (blue) and minimum (orange) damping characteristics implemented in the high level damping control strategy	130
4.22	Time history of the ISO B-class road at 70 km/h	131
4.23	Results of the quasi-ideal model with the high level control reproducing the maximum damping characteristic	133
4.24	Results of the quasi-ideal model with the high level control reproducing the maximum damping characteristic	134
4.25	Results of the quasi-ideal model with the high level control reproducing the maximum damping characteristic	135

4.26	Results of the quasi-ideal model with the high level control reproducing the minimum damping characteristic	136
4.27	Results of the quasi-ideal model with the high level control reproducing the minimum damping characteristic	137
4.28	Results of the quasi-ideal model with the high level control implementing the LQR with comfort-oriented setting	138
4.29	Results of the quasi-ideal model with the high level control implementing the LQR with comfort-handling trade-off setting	139
4.30	Results of the quasi-ideal model with the high level control implementing the LQR with comfort-handling trade-off setting	140
4.31	Results of the quasi-ideal model with the high level control implementing the LQR with comfort-handling trade-off setting	140
4.32	Results of the quasi-ideal model with the high level control implementing the LQR with handling-oriented setting	142
4.33	Results of the quasi-ideal model with the high level control implementing the LQR with handling-oriented setting	143
4.34	Results of the quasi-ideal model with the high level control implementing the LQR with handling-oriented setting	143
4.35	Analysis of the realistic model	145
4.36	Analysis of the realistic model	146
4.37	Analysis of the realistic model when the mechanical subsystem friction is amplified by a factor 100	146
4.38	Analysis of the realistic model when the mechanical subsystem friction is amplified by a factor 100	147
4.39	Analysis of the realistic model	148
4.40	Results of the realistic model with the high level control reproducing the maximum damping characteristic	149
4.41	Results of the realistic model with the high level control reproducing the maximum damping characteristic	151
4.42	Results of the realistic model with the high level control reproducing the maximum damping characteristic	152
4.43	Results of the realistic model with the high level control reproducing the minimum damping characteristic	152
4.44	Results of the realistic model with the high level control reproducing the minimum damping characteristic	154
4.45	Results of the realistic model with the high level control reproducing the minimum damping characteristic	155
4.46	Results of the realistic model with the high-level control reproducing the LQR with comfort-handling trade-off setting	156
4.47	Results of the realistic model with the high level control reproducing the LQR with comfort-handling trade-off setting	158

4.48	Results of the realistic model with the high level control implementing the LQR with comfort-handling trade-off setting	158
4.49	Results of the realistic model with the high-level control reproducing the LQR with handling-oriented setting	159
4.50	Results of the realistic model with the high level control reproducing the LQR with handling-oriented setting	161
4.51	Results of the realistic model with the high level control implementing the LQR with handling-oriented setting	161
4.52	Results of the realistic model with disabled low level control	162
4.53	Results of the realistic model with disabled low level control	164
4.54	Comparison between the quasi-ideal (blue) and realistic (orange) models at the diverse high level control strategies	165
4.55	Comparison between the quasi-ideal (blue) and realistic (orange) models at the diverse high level control strategies	167
5.1	Belt-driven test-bed	171
5.2	Hydraulic test-bed	172
5.3	Static characterization of the diverse dissipative contributions of the prototype	174
5.4	Static characterization with the electric machine shunted by an external resistance	175
5.5	Static characterization with the electric machine driven through the three-phase controlled power module	176
5.6	Static characterization with the electric machine driven through the three-phase controlled power module	177
5.7	Static characterization in the four force-speed quadrants	178
5.8	Static characterization in the four force-speed quadrants	179
5.9	Mechanical impedance magnitude obtained by shunting the electric machine through an external resistance	180
5.10	Mechanical impedance magnitude obtained through the controlled electric machine at diverse damping values of the high level control.	182
5.11	Experimental test-bed used for dynamic characterization in active mode	183
5.12	Active-mode dynamic test measurements	184
5.13	Active-mode frequency response function: force-current (a) and compliance (b).	185
5.14	Experimental setup for acoustic characterization	185
5.15	Hardware-In-the-Loop scheme	187
5.16	Hardware-In-the-Loop results with an ISO B-class road at 70 km/h and the high level REmSA control set to reproduce a 1000 Ns/m damping behavior	188

5.17	Hardware-In-the-Loop results with an ISO B-class road at 70 km/h and the high level REmSA control set to reproduce a 1000 Ns/m damping behavior	189
A.1	Previous version of the proposed REmSA design methodology [83] .	195
A.2	Selection of the overall transmission ratio as a function of the maximum regenerative damping capability	196
A.3	Proposed linkage solution (thick solid lines) for the REmSA integration into a double wishbone suspension [83].	197
A.4	Isometric cut view of the REmSA designed for the automotive application [83]	198
A.5	REmSA prototypes designed and manufactured during the present research	199
B.1	REmSA lumped parameter model	202
B.2	Mechanical impedance magnitude (a) and phase (b) of the REmSA lumped parameter model computed at diverse shunt resistances . .	203

List of Acronyms

ADAS	Advanced Driving Assistance Systems
EHA	Electrohydrostatic
PWM	Pulse-Width Modulation
LQR	Linear-Quadratic Regulator
REmSA	Rotary Electromechanical Shock Absorber
GA	Genetic Alghorithm
EMF	Electromotive Force
DOF	Degree-of-Freedom
RMS	Root Mean Square
MTPV	Maximum Torque Per Voltage
MTPA	Maximum Torque Per Ampere
FOC	Field-Oriented Control
PM	Permanent Magnet
PMSM	Permanent Magnet Synchronous Motor
PSD	Power Spectral Density
PID	Proportional Integral Derivative
FRF	Frequency Response Function
HIL	Hardware-In-the-Loop
ASIL	Automotive Safety Integrity Level

Chapter 1

Introduction

The automotive industry is nowadays facing an innovative push towards more efficient and smart vehicles. In this scenario, emission reduction and driving automation are the major trends that most of the carmakers are chasing [1].

The increasing concern about global warming and the energy crisis have made the decarbonization process mandatory. The future economy must rely on sustainable and affordable energy sources [2]. Worldwide governments are adopting strict policies to accelerate such process. For example, the European Union has imposed limits on CO₂ emissions. Specifically, the newly registered cars of a manufacturer must feature CO₂ average emissions below 95 g/km [3]. Penalties of 95€ per sold car, per gram of CO₂ over the limit, are charged to the carmakers breaching the restriction [4]. In this context, the automotive industry is moving towards the electrification of powertrain and chassis. Electric and hybrid vehicles are regarded as a promising solution to significantly reduce emissions and oil dependency of the automotive sector [2, 5]. The transition has already started one decade ago: it is estimated that over 55% of new car sales could be electrified by 2030 [1].

Driving automation has a primary role in the improvement of vehicle safety and comfort. Advanced Driving Assistance Systems (ADAS) are broadly adopted on current vehicles. As most of road accidents are related to human error, such systems led to a significant decrease of the accident occurrence [6]. Furthermore, ADAS could improve driver's comfort by providing assistance in some tasks such as parking or keeping constant speed in straight highway. Five levels of driving automation have been established by SAE to categorize the amount of assistance provided to the driver. The scale ranges up to level 5 that refers to full automation, i.e. the vehicle performs all the maneuvers autonomously without the need of the driver. Higher automation level turns into less tasks asked to the driver. Ideally, full autonomous vehicles allow the driver to accomplish other tasks while driving. Furthermore, errors due to the driver are completely avoided, thus leading to improved safety. Automotive market is predicted to move towards autonomous vehicles in the next decades [1]. One fundamental aspect for autonomous vehicles is the ride comfort. In

addition to the driverless feature that could be a barrier to the human acceptance, passengers would be reluctant to ride uncomfortable vehicles. As stated by Bellem *et al.*, the comfort could strongly affect the acceptance of autonomous vehicles [7].

In the above-reported scenario where emission reduction and improved comfort are of primary importance, advanced vehicle suspensions are a promising technology. Automotive suspension has the role of providing safe and smooth ride. To this end, the suspension system must be able of isolating the car body from external disturbances—i.e. ground irregularities and inertial forces due to vehicle maneuvers—and guaranteeing a firm contact between the wheel and the ground. These tasks are usually referred as comfort and handling requirements. The latter is strictly related to safety, as lateral and longitudinal forces allow the vehicle to hold the road and brake efficiently. Basic suspension systems are passive as they are equipped with passive spring element and shock absorber. The former bears the car body weight and pushes the wheel to the ground. The latter damps the suspension motion by dissipating the vibration energy that comes from external disturbances.

Starting from the first decades of the XX century, passive shock absorbers have been largely used in the automotive industry because of their simplicity, robustness, cheapness, low weight and high reliability. Nevertheless, such technology implements a fixed damping characteristic that cannot be adapted to the operating condition of the vehicle. The suspension must fulfill conflicting requirements, i.e. isolating the car body from external disturbance and guaranteeing a firm contact between wheel and ground. The first task needs soft spring and modest damping so that the forces transmitted to the car body are minimized. This setting causes poor contact between tire and ground as well as large suspension deflection under external disturbances, such as the forces due to vehicle acceleration, braking or turning maneuvers. It is evident that the smooth and safe ride requirements cannot be optimized simultaneously. Race cars are a clear example of this conflict, as the vehicle handling is maximized at the expense of the ride comfort [8].

Moreover, passive shock absorbers damp the suspension motion by dissipating the vibration energy that comes from external disturbances. If harvested, such energy could improve the fuel efficiency of the vehicle. In this context, energy harvesting is a relevant trend in the automotive industry. In fact, significant efficiency improvement could be achieved by reducing energy losses [2]. A well-known example is regenerative braking: in urban driving scenarios, up to to one-half of the driving energy is dissipated during braking [9]. Its recovery produces a substantial impact on fuel consumption, especially for hybrid and full electric vehicles [10]. The vibration energy dissipated by conventional shock absorber depends on the vehicle class and the operating conditions, for instance travelling speed and road profile. Power values ranging from 47 to 7500 W are potentially recoverable at the suspension, thus leading to fuel efficiency improvements up to 10% [10, 11]. Therefore, passive shock absorbers lack the regeneration feature and clashes with the emission

reduction trend of the automotive industry.

In the '70s, semi-active shock absorbers were conceived to overcome the limitations related to the fixed damping characteristic intrinsic to passive dampers [8]. Such technology enables the control of the damping force provided by the shock absorber. Hence, the suspension can adapt to the operating condition by varying its damping characteristic. Both the comfort and handling requirements are significantly improved when compared to passive solutions. Although passive suspensions are not ideal, they are nowadays widely used because of their cost-effectiveness while guaranteeing good enough performance. On the other hand, semi-active dampers has found wide application on mid-range and expensive vehicles, where improved comfort and handling performance justify the cost increase [12]. Although semi-active suspensions solve the fixed-damping trade-off, they provide passive force only. As consequence, the sprung mass motion—occurring at frequency values about 1 Hz and responsible of passenger discomfort and motion sickness—can only be partially attenuated. A further comfort improvement would require active forces at the suspension. Lastly, semi-active dampers rely on energy dissipation and do not allow energy regeneration.

Active suspension systems attracted many research efforts thanks to their advantageous features. Such systems employ an actuator that provides the suspension with passive or active forces, thus overcoming the strong limitation of semi-active systems. Some configurations allow to remove the conventional shock absorber as its function is covered by the actuator. Active suspensions are mainly divided into two groups: hydraulic or pneumatic, and electromagnetic. The former exploits a hydraulic (or pneumatic) actuator composed of a pump (or a compressor) to pressurize the circuit, and some valves to regulate the force generated by the actuator. Electromagnetic active suspension uses an electric machine and a transmission mechanism to provide active and passive forces.

Among these two categories, electromagnetic active suspensions usually feature high bandwidth. Hence, they are classified as full-active as they cover a wide frequency range and enable the control of the wheel dynamics. For this reason, such configuration allows to remove the shock absorber: it can be fully replaced by an actuator that provides the suspension with both active and passive forces.

Electromagnetic active suspensions are the most attractive solution as they work as a shock absorber with active features. This enables the full control of the suspension, paving the way to novel control architectures aimed at the optimization of both passenger comfort and vehicle handling. In the autonomous vehicle context, the suspension control can also interact with the control and trajectory planning algorithms of the vehicle so that comfort and handling performance are maximized [13].

Furthermore, electromagnetic active suspensions rely on electric machines. Their operation is reversible, namely they allow to input energy into the systems but also to extract energy in form of electricity. Conventional shock absorber damps the

suspension by dissipating its mechanical energy into heat. Electromagnetic active suspensions can also provide damping forces to the suspension. In this case, the mechanical energy is not dissipated but converted into electricity. In a few words, the mechanical energy related to the suspension vibration is recovered. This feature is of great potential since it embraces the emission reduction trend of the automotive industry.

Actually, active suspensions encounter electrical energy consumption during active operation. This aspect is one of the main cruxes that limited their implementation with respect to semi-active solutions [14]. Although the latter achieves comfort and handling improvement when compared to passive systems, they are strongly limited by the passivity constraint. In fact, some maneuvers and road conditions—for instance turning or lane change maneuvers and bump or pothole crossing—require active forces to further improve the comfort and handling performance of the vehicle [15]. Therefore, active suspensions are very attractive and their regenerative feature could address the energy consumption issue: the energy harvested from the suspension motion can be invested into the active operation. In this perspective, the suspension control combines the active and regenerative operations to get a trade-off between vehicle performance and energy management [10, 16, 17].

The trend towards 48V systems in the automotive industry [18] makes electromagnetic active suspensions even more appealing. In fact, they can be integrated in the 48V network that is already present on the vehicle without requiring the addition of on-purpose hardware. The harvested energy can be reinvested into the active operation, stored into the vehicle battery, used to supply auxiliary systems, which are nowadays electrified, or the ADAS systems, which requires more and more energy due to more demanding performance.

The industry and the academic research are attracted by the electromagnetic active suspension technology, which is regarded as the future trend of the automotive [19, 20, 21]. When compared to hydraulic or pneumatic active suspensions, the electromagnetic variant features improved dynamic performance and force control, regenerative operation, high bandwidth and simpler layout. By converse, bulkier layouts result from the lower force density with respect to the hydraulic actuation [21]. Differently from the hydraulic or pneumatic variant, electromagnetic active suspensions are still not mature products and few commercial applications are present.

Audi AG proposed an electromagnetic suspension named eRot in 2017 [22]. It enables the energy recovery from bumpy road, although no active features are declared. Few years later, the manufacturer proposed a similar device on the Audi A8, able to regenerate energy and also improve vehicle comfort and safety through active operation [23]. This device is not full-active as its bandwidth is limited to the frequencies of the body dynamics.

Bose proposed a full-active regenerative electromagnetic suspension in 2007 [21].

The innovation demonstrated significant vehicle performance improvement such that some car manufacturer were very attracted. Nevertheless, the project was a technical success but not commercially convenient since the actuator was too heavy and expensive [24].

Note that not all the electromagnetic suspensions feature full-bandwidth or allow active operation. For example, the Audi AG device features limited bandwidth, or several solutions available in the scientific literature allow energy regeneration while active forces cannot be exerted as they use motion rectifiers that make the solution irreversible [25, 26].

Electromagnetic active suspensions are divided in subcategories according to the technology they implement. First of all, there are linear and rotary solutions, which implement linear and rotary electric machines, respectively. The latter features large force density, thus allowing more compact layouts. Nevertheless, a conversion stage is needed to transform the linear motion of the suspension into rotation of the electric machine. To this end, ball-screws, rack-pinions, linkages or electrohydrostatic solutions are used.

Although the conversion mechanism implies additional mechanical complexity, the rotary solution exceeds the linear one thanks to the compact layout and reduced mass [14, 16]. These aspects are fundamental when the electromagnetic suspension must be implemented on the vehicle. Among all the conversion mechanisms, the linkage-based one features good mechanical robustness and efficiency, compact and lightweight layout, low mechanical complexity, and oil-free operation.

1.1 Thesis motivation

The significant number of scientific outcomes and patents published in the last decade proves the interest of industry and academy in electromagnetic active suspensions [11]. Nevertheless, most of the proposed solutions are load-leveling or slow-active due to the mechanical and control complexity of full-active technologies. Extensive work has been done on linear electromagnetic suspensions along with rotary solutions based on ball-screw and rack-pinion conversion mechanism, while few works focuses on the linkage-based technology. Furthermore, most of the solutions proposed by the scientific research are called *regenerative suspensions*, namely electromagnetic suspensions that implement the regenerative feature while active operation is not allowed because of motion rectifiers. Therefore, linkage-based rotary electromagnetic suspension and active solutions have not been properly addressed.

Furthermore, there is a gap between the automotive industry and the scientific research. To the author's experience, the industry is interested more in the active feature than the regenerative one. This point is demonstrated by the marketing articles published by carmakers, where the main focus is the comfort, handling and

safety improvement while few attention is given to the energetic aspect [22, 23, 27, 24]. The regeneration feature is considered as a secondary aspect, which is the mean to limit the energy consumption related to the active operation. Conversely, the academic research focuses on the regenerative aspect and usually disregards the active feature [11]. In fact, most of the research effort addresses regenerative suspensions that are not capable of active operation.

Then, the literature lacks a design methodology that gives a compact rotary electromagnetic suspension starting from vehicle performance and packaging requirements. Although many research efforts focus on the performance optimization of electromagnetic suspensions, the vehicle integration and packaging are usually neglected [16]. These aspects cover a relevant role when the research goal is the technology implementation at the industry level.

Lastly, most of the existing literature about rotary electromechanical regenerative suspensions focuses on the detrimental effect of inertia of such systems. No attention is given to control architectures able to mitigate their mechanical non-idealities and inertia when controlled with dedicated power electronics. In this context, some effort was dedicated to low-level controllers mainly for electro-hydraulic and electro-hydrostatic actuators [28, 29, 30, 31, 32]. However, the inertia features of such systems is not so evident as in rotary electromechanical solutions. Moreover, such references focus on the performance improvement in terms of vehicle dynamics, whereas the impact of the realistic behavior of the actuator on the energy consumption/regeneration was not addressed.

1.2 Thesis goal

In this context, the present doctoral thesis focuses on the investigation and the development of linkage-based rotary electromagnetic suspensions for automotive and motorcycle applications. The proposed solution features a rotary electric machine coupled with a planetary gearbox. A linkage is used as conversion mechanism to transform wheel upright linear motion into rotation of the gearbox shaft. Regenerative operation and full-active features are enabled, so that the developed system can completely replace the conventional shock absorber. The latter can be removed, hence the proposed solution paves the way to novel suspension architectures. The proposed electromagnetic suspensions is not intended as a damping device but a force actuator. Hence, its control strategy is aimed at controlling the force provided to the suspension and not to the damping coefficient, as done in pure regenerative and semi-active technologies. Based on the above-mentioned characteristics, the proposed solution is named *Rotary Electromechanical Shock Absorber* (REmSA), as it operates as a shock absorber with active and regenerative features.

This work proposes a system-level methodology that establishes specific steps to design REmSA prototypes for automotive and motorcycle applications. The present

work intends to be a guideline for both academy and industry that move towards the development of such systems. The methodology starts from the assessment of design constraints and requirements in terms of packaging vehicle performance. The latter differs from the requirements of conventional shock absorbers since the proposed solution must not be seen as a damper but an active device able to actuate and damp the suspension. By means of the proposed methodology, two solutions—one for automotive and one for motorcycle application—have been developed and manufactured.

Then, a model able to reproduce the realistic behavior of REmSA systems is proposed. It accounts for the dissipative effects of both electric machine and gearbox, the backlash, and the mechanical dynamics of the assembly. The developed model is identified through experimental data and then integrated into the quarter-car model of the vehicle.

The control of REmSA devices is discussed. Two different control layers are required: the low and the high level. The former controls the force that the REmSA applies to the suspension, the latter aims at controlling the vehicle dynamics to optimize the comfort and handling performance. The main high level control strategies—i.e. skyhook and groundhook, spring negation, and LQR—are discussed and numerically simulated by means of the identified model.

Finally, extensive experimental work addresses the performance characterization in terms of efficiency, dynamic behavior, and force capability both in active and passive mode. The REmSA impact on the handling, comfort, and energetic performance of the vehicle is addressed.

Overall, the novel contributions of the present work are:

- A system-level methodology that establishes specific steps to design REmSA prototypes for automotive and motorcycle applications. In this perspective, the present work intends to be a guideline for both academy and industry that move towards the development of such systems.
- The performance investigation of electromechanical suspensions by accounting for the non-ideal behavior of such systems. Differently from the existing literature, the focus is given to the energetic performance, which is a delicate aspect when dealing with active suspensions.
- The experimental characterization of the static and dynamic performance of linkage-based rotary electromechanical suspensions in terms of damping, efficiency and noise levels. Furthermore, a Hardware-in-the-Loop architecture is proposed.

1.3 Thesis outline

The remainder of work is organized as follows:

- Chapter 2 discusses the state of the art. At first, a general introduction on controllable suspensions—which is the category the active systems are part of—is given. Then, the focus is moved to the electromagnetic active suspensions: the working principle of energy regeneration and active operation is introduced, the energy recovery capability is discussed, the diverse constructive solutions—namely the linear and rotary type—are described. The main designs available in the literature are explored, while more focus is given to electromagnetic rotary solutions.
- The developed system-level design methodology for REmSA devices is presented in Chap. 3. At first, the layout is described by detailing the diverse parts composing the system. Then, the methodology is explained and applied to a case study that deals with a motorcycle application. The diverse steps are detailed by including considerations, mathematical descriptions, and optimization problem formulations. Finally, the manufactured prototype is presented. The research also led to the development and manufacture of a prototype for automotive applications. Since it was designed with a previous but incomplete version of the proposed methodology, its design is briefly described in Appx. A.
- Chapter 4 presents the modeling and control of the REmSA. At first, a model able to reproduce the realistic behavior of REmSA systems is proposed and integrated into the quarter-car model of the vehicle. Then, the control of the REmSA are discussed and simulated by means of the developed vehicle model. The impact of the REmSA realistic behavior is investigated. To this end, the parameters of the developed model are identified through experimental data. Overall, the investigation addresses the energy balance of the active suspension, as well as the vehicle performance in terms of handling and comfort.
- Chapter 5 presents the experimentation aimed at characterizing the developed REmSA prototype. At first, the equipment is presented. Then, the static characterization is discussed. The prototype was tested with the electric machine shunted by an external resistance, then it was driven through a controlled power module. First-quadrant and four-quadrants operations were addressed. Subsequently, the dynamic characterization is proposed. It was aimed at the assessment of the frequency response of the prototype. Active and passive quadrant operation was characterized. Finally, acoustic tests were carried out in an anechoic room to assess the noise level of the characterized prototype. At the end, a Hardware-In-the-Loop approach is proposed to assess the performance of a vehicle equipped with REmSA devices. Preliminary tests are presented.

- Chapter 6 concludes the work and proposes possible future research in the field of REmSA.

The present thesis is the outcome of the research on electromagnetic suspensions at LIM Mechatronics Lab (Politecnico di Torino), which deals with electrohydrostatic and electromechanical solutions. The latter are the focus of this work: two prototypes—one for automotive and one for motorcycle applications—have been developed and manufactured. Specifically, the motorcycle one was used as case study to explain and demonstrate the proposed design methodology (Chap. 3). However, due to the project timeline, the numerical investigation and the experimentation were based on the automotive prototype. Since it was developed with a previous and incomplete version of the design methodology, its design is briefly reported in Appx. A.

Chapter 2

State of the art

This chapter discusses the state of the art of electromagnetic active suspensions. The first section gives a general introduction on controllable suspensions, which is the category the active systems are part of. Then, the focus is moved to the electromagnetic active suspensions: the working principle of energy regeneration and active operation is introduced, the energy recovery capability is discussed, the diverse constructive solutions—namely the linear and rotary type—are described. The main solutions available in the literature are explored, by focusing on proposed designs and performance assessment. The attention is given to the electromagnetic rotary suspensions as they are the objective of the present dissertation. Therefore, this section gives an insight into the framework of electromagnetic suspensions.

2.1 Controllable suspensions

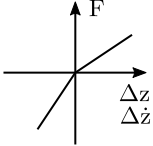
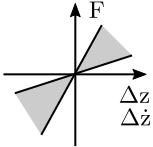
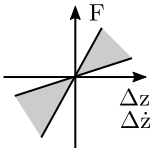
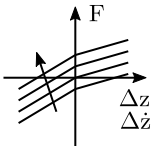
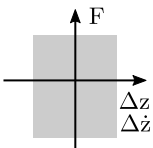
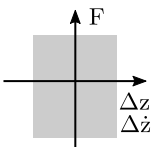
Electromagnetic active suspensions are part of the controllable suspension category. These systems allow to introduce a control action at different levels of the suspension, as a modulation of the elastic or damping forces of the spring and shock absorber, respectively, or directly as a force.

According to the control range, the bandwidth and the control variable, Fischer and Isermann [33] proposed a classification of controllable suspensions. Specifically, the control range refers to the force that the controllable device can provide, the bandwidth indicates how fast the device exerts the control request, the control variable is the physical quantity that the device manipulates by means of its action. This classification is reported in Table 2.1. It also shows the passive suspension family, which is characterized by fixed damping and stiffness characteristics as no control action is allowed.

Five families of controllable suspensions are identified:

- *Adaptive suspensions* allow to modulate the shock absorber characteristic with a bandwidth of a few Hertz.

Table 2.1: Classification of controllable suspensions [33]

System	Control range	Bandwidth	Control variable
Passive			
Adaptive		1 – 5 Hz	damping ratio
Semi-active		30 – 40 Hz	damping ratio
Load-leveling		< 1 Hz	static load
Slow-active		1 – 5 Hz	force
Full-active		> 20 Hz	force

- *Semi-active suspensions* feature a shock absorber that enables a fast modulation of the damping characteristic.

As can be seen in Table 2.1, these two families provide forces in the passive quadrants only, namely quadrants I and III. Such systems are passive as no mechanical energy can be introduced in the system and the suspension cannot be actuated.

- *Load-leveling suspensions* enable a very slow modulation of the static load. In this way, the steady state height of the vehicle can be varied.
- *Slow-active suspensions* allow to fully control the force of the suspension in a frequency range up to a few Hertz.
- *Full-active suspensions* enable the full control of the suspension force in a wide frequency range.

These three categories provide forces in the passive and active quadrants, and allow to introduce mechanical energy into the suspension. For this reason, they are part of the active suspension family. Such systems require the use of an actuator that modulates the spring static force, in the case of load-leveling suspensions, or provides active and passive forces, in the slow-active and full-active variants. In the last case, the actuator superimposes its action to the spring and shock absorber forces or, ideally, it can fully replace these passive components.

Slow-active suspensions operate at frequency values close to the body dynamics—typically about 1 – 2 Hz for passenger vehicle applications— thus enabling the control of the body motions. Consequently, the passenger comfort can be significantly improved. On the other hand, the actuator operates at frequency values below the wheel dynamics, typically in the range 10 – 15 Hz for passenger vehicle applications. Hence, it cannot control the wheel dynamics: the passive shock absorber is still needed in the suspension to damp the wheel vibrations. Conversely, full-active suspensions cover a wide frequency range and enable the control of the wheel dynamics. In such configurations, the shock absorber can be fully replaced by the actuator, which provides the suspension with both active and passive forces.

Active suspensions are mainly divided into two groups: hydraulic or pneumatic, and electromagnetic. The former exploits a hydraulic (or pneumatic) actuator, composed of a pump (or a compressor) to pressurize the circuit, and some valves to regulate the force provided by the actuator. Electromagnetic active suspensions use an electric machine and a transmission mechanism to actuate the system.

Hydraulic and pneumatic active suspensions usually feature limited bandwidth. They are nowadays used in high-end vehicles as load-leveling or slow-active systems. The first mass production in the automotive industry started in the '80s, when Nissan applied a hydraulic active suspension to the Infinity Q 45 [34]. In 1999, Mercedes-Benz AG introduced its Active Body Control system in high-end models such as W220 S-Class. This system combines the conventional shock absorber with adjustable damping valves and a motor-pump unit to control frequency values up to 5 Hz [27]. BMW launched the Dynamic Drive system in 2001 in the 7-series. It is an active stabilizer bar system that relies on a hydraulic valve block, a pump and two active stabilizer bars equipped with rotary hydraulic actuators [35]. Another example is the ACOCAR system proposed by Tenneco [34]. All these solutions still need the presence of the conventional shock absorber. For instance, the BMW

Dynamic Drive system actuator is not able to damp the wheel vibrations occurring at frequency values above the actuator bandwidth. Differently, Mercedes Active Body Control, or Tenneco ACOCAR, embeds the active feature in the conventional shock absorber. The latter is used as hydraulic actuator, while the damping feature is implemented by means of damping valves.

The main drawback of active suspensions is the energy consumption. In this context, Koch *at al.* [36] investigated a system made of a slow-active suspension combined to a continuously variable damper. The the proposed setup was regarded as competitive when cost, energy and implementation aspects are considered. Its performance were numerically compared to passive and high-bandwidth suspensions. Although the latter gave the best results in terms of comfort and handling, the proposed system significantly improved vehicle performance when compared to passive solutions.

2.2 Electromagnetic active suspensions

Electromagnetic active suspensions integrate an electromagnetic actuator into the existing suspension of the vehicle. The actuator exploits an electric machine to exert active and passive forces.

2.2.1 Working principle

A controlled electric machine features 4-quadrants operation. This allows the electromagnetic active suspension to work in both active and passive quadrants [37], as shown in Table 2.1. This does not always hold, as it depends on the transmission mechanism between the electric machine shaft and the wheel upright. If such mechanism is not reversible—for instance a motion rectifier is present—the energy flow is not bidirectional and the suspension can work in the passive quadrants only.

Figure 2.1 shows the force-velocity plane of the electromagnetic active suspension. The present dissertation adopts the passive sign convention, as common practise when dealing with shock absorbers. Specifically, quadrants II and IV refer to active operation, while I and III are the passive ones, where a braking action is exerted on the vehicle suspension and the system works as a damper. In this case, the electric machine is used as a generator. Its rotor is driven by the suspension motion and induces an electromotive force at the stator winding ends. If these are shunted through a resistance, a current flows and a braking action is produced [38]. At the same time, the current through the shunt resistance causes an energy dissipation. This electric energy could be recovered if the resistance is replaced by a proper electronic circuit, for instance a battery connected to a controlled power module or a DC-DC [39, 40].

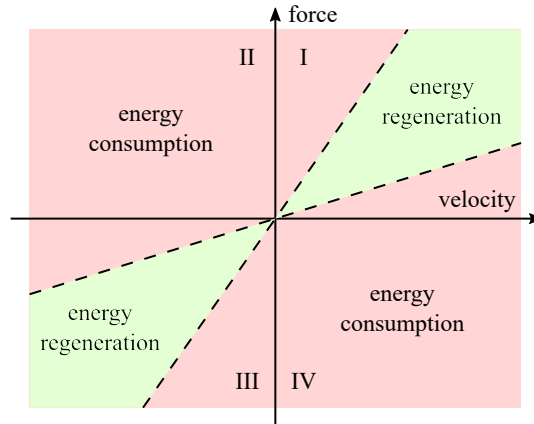


Figure 2.1: Force-velocity plane of electromagnetic active suspensions

As shown in Fig. 2.1, only a restricted region of the passive quadrants allows regeneration. By examining the first quadrant, the lower limit is due to the intrinsic dissipation of the electromagnetic suspension, i.e. mechanical friction. What happens is that the force requested to the suspension is lower than the force caused by the mechanical friction and, consequently, active electrical power must be invested to counteract this effect. In the case of shunted electric machine, this limit is encountered in open circuit operation, namely infinite shunt resistance. The upper bound is due to the intrinsic resistance of the electric machine. At low speed values, the induced back electromotive force is not sufficient to generate enough suspension force because of the intrinsic resistance of the electric machine. Therefore, active electric power must be supplied to achieve larger force at the suspension. When a shunted electric machine is considered, this limit is encountered in short circuit operation, i.e. null shunt resistance. Such behavior is caused by the stator winding resistance.

2.2.2 Energy recovery

Ideally, the amount of energy that can be recovered is equal to the total energy dissipated in the suspension by a conventional shock absorber. The latter is usually included in the rolling resistance, which ranges from 3 to 12 % of the vehicle fuel consumption [11]. In analytical terms, the instant power dissipated by a damper is proportional to its damping coefficient and the square of the suspension velocity. When a random road roughness profile is considered, the average dissipated power gets proportional to the vehicle speed and the tire stiffness along with a coefficient indicating the road quality [41]. Predicted power values go from 10 to 660 W per damper for passenger cars under diverse vehicle speed and road conditions [42]. These values significantly increase when dealing with trucks and military off-road vehicles [43]. Nevertheless, simulation results must be taken with a grain of

salt, as especially passenger cars cannot travel very rough roads with sustained speed. Experimental campaigns were conducted to address the dissipated power in the vehicle shock absorber: values up to 321 W were measured on road tests of passenger cars [11].

Certainly, not all the energy amount available at the damper is harvested. The conversion efficiency of the electromagnetic suspension significantly impacts the recovered energy. In this context, wide effort has been dedicated to assess the conversion efficiency of purely regenerative suspensions. Values ranging from 10 to 70% have been measured on diverse prototypes proposed in the literature [42]. Furthermore, some of these solutions were equipped on vehicles and tested on real roads. This experimentation resulted in recovered energy up to 613 W for a passenger car on rugged township roads [11, 44], and up to 1 kW per shock absorber on a light military truck on standard roads [45].

As shown by Abdelkareem *et al.*, the recovered energy is expected to improve up to 10% the vehicle fuel efficiency [11]. Nevertheless, this result considers a pure regenerative suspension. In case of active suspensions, the recovered energy can be directly reinvested to supply the active operation [46]. Consequently, the fuel efficiency can be improved or worsened according to the suspension control strategy. It makes a trade-off among comfort, handling or fuel efficiency performance [16]. Therefore, the regenerative feature can mitigate the energy consumption issue, which is one of the main arguments against active suspensions when compared with semi-active solutions [25]. In this context, numerical studies demonstrated that active suspensions with regenerative feature allow to improve ride comfort and fuel efficiency simultaneously [10, 17].

2.2.3 Proposed solutions

The general layout of an electromagnetic active suspension is schematized in Fig. 2.2. The electromagnetic actuator—which is mechanically connected to the suspension—is driven by the power electronics module and controlled by the control unit. The latter receives signals from the sensors mounted on the suspension. The power electronics draws or supply energy to the battery when the actuator works in active or regenerative mode, respectively. The double arrow indicates the bidirectional power flow.

The actuator can be placed in series (Fig. 2.3a) or in parallel (Fig. 2.3b) to the passive suspension [21]. The former is typical of load-leveling suspensions, i.e. the height of the vehicle can be changed in a quasi-static way. The latter is used for slow-active and full-active systems. Specifically, slow-active solutions operates at frequency values close to the body dynamics, thus enabling the control of the body motions that results in the improvement of the passenger comfort and safety. They cannot act on the unsprung mass dynamics, therefore the conventional

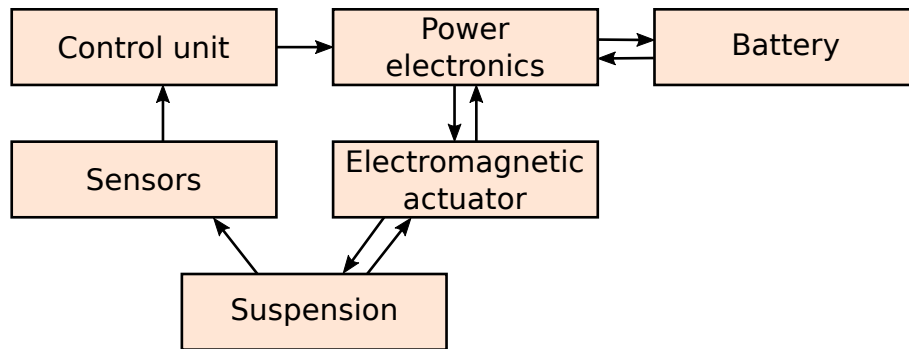


Figure 2.2: General layout of an electromagnetic active suspension

shock absorber is still needed to damp the wheel vibration. Conversely, the full-active solution features large bandwidth and can operate on the unsprung mass vibration. For this reason, the conventional shock absorber can be removed as the electromagnetic suspension is able to damp and control the wheel dynamics. In such case, the actuator can be named *electromagnetic shock absorber* because it works as a shock absorber that provides the suspension with both active and passive forces.

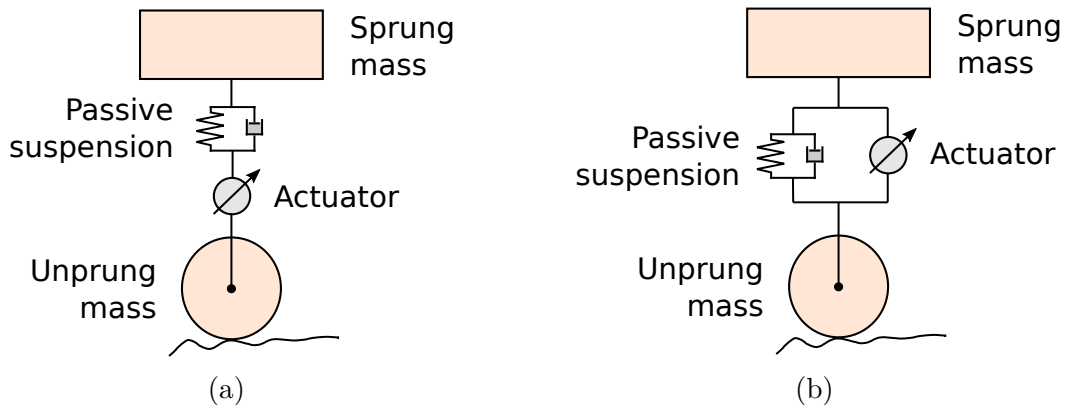


Figure 2.3: Series (a) and parallel (b) arrangements of the actuator in active suspensions [21]

According to the electric machine configuration, electromagnetic active suspensions can be categorized into linear and rotary layouts. Although this classification is usually adopted for regenerative suspensions, it holds also for active solutions.

Linear layout

Linear electromagnetic active suspensions exploit linear electric machines. They are the most immediate solution because of the translation nature of the suspension

motion. Therefore, no transmission mechanism is needed: stator and mover of the electric machine are directly attached to wheel assembly and vehicle body. For this reason, linear electromagnetic suspensions are usually referred as *direct drive systems* [16]. Many solutions arrange the linear electric machine into a tube, thus resulting in layouts very similar to conventional shock absorbers [47].

Gysen *et al.* [48, 49] proposed a direct-drive electromagnetic active suspension for a BMW 530i featuring a permanent-magnet linear electric machine (Fig. 2.4). A Pulse-Width Modulation (PWM) current-controlled three-phase amplifier with 340 V bus voltage is used to work both in active and passive quadrants. Passive damping is included to guarantee fail safe operation. Specifically, if the power electronics fails, a minimum amount of damping is guaranteed. The active suspension is controlled through a LQR tuned for comfort and handling improvement. Measurements were conducted on a quarter-car bench setup that reproduces the road disturbances through an industrial tubular actuator. Two LQR settings were tested: the comfort-oriented tuning resulted in comfort improvement of 36% at the expense of 47 W per wheel, while handling improvement of 54% was achieved through the handling-oriented setting at the expense of 37 W per wheel. The power consumption performance is definitely affected by the passive damping added for fail-safe purposes. Nevertheless, both comfort and handling were improved with low power requirements.

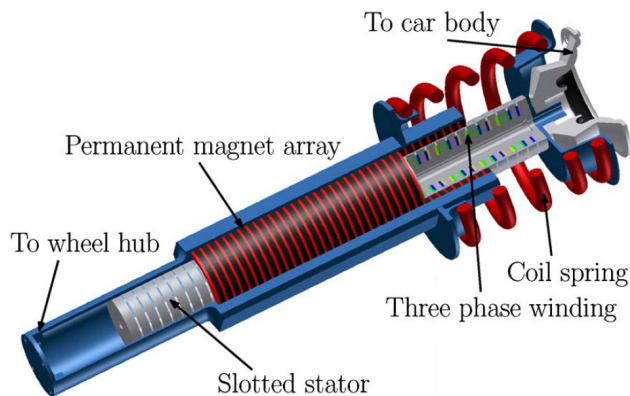


Figure 2.4: Linear electromagnetic active suspension developed by Gysen *et al.* [49]

Another linear solution was developed by Zuo *et al.* [50]. Specifically, they proposed a regenerative shock absorber, so the active operation was not accounted for. The solution mainly consists of magnet and coil assemblies, resulting in a bulky system with total estimated weight of 28 kg. The authors built and tested a 2:1 scale prototype. Experimental campaign was carried out to assess voltage waveforms and regenerated power at different vibration amplitudes and frequencies. The

input profile was imposed through a shaker. As result, the half-scale prototype was able to harvest up to 8 W at 0.5 m/s rms suspension velocity.

Zhang *et al.* proposed a regenerative shock absorber featuring a linear electric machine and a rack-pinion mechanism [51]. The latter is used as motion magnification mechanism to increase the electric machine velocity, thus raising the regeneration capability of the system. This solution was experimentally compared to a regenerative shock absorber without the motion magnification mechanism. A MTS machine was used to impose harmonic displacement profiles at frequencies ranging from 1 to 25 Hz, while the electric machine was shunted through a resistance. Measurements highlighted how the rack-pinion system increase by four times the regenerated electric power.

Gupta *et al.* [52] developed and tested on an all-terrain vehicle two electromagnetic suspensions: linear and rotary. Also in this case, only passive operation was explored to assess the regeneration capability. To this end, the electric machine was shunted with an external resistance to implement the damping operation. The developed prototypes were installed on the reference vehicle in parallel configuration with the passive shock absorber. Tests were performed by running over a wooden beam obstacle. Measurements demonstrated the poor damping capability of the linear solution when compared with its rotary counterpart.

An early work proposed by Karnopp [53] investigated the effect of the electrical dynamics, i.e. the RL pole, on the damping performance of regenerative linear suspensions. The electrical time constant must be well below the vehicle resonant period so that the damper response is negligibly delayed. Overall, the work states that reasonable sized coils features electrical dynamics fast enough to not influence the damping performance.

Although linear electromagnetic suspensions systems could be easily integrated into existing suspension layouts, they suffer poor damping capability and force density. This turns into large systems that are bulky and expensive [14, 38].

Rotary layout

Rotary electromagnetic suspensions exploit rotary electric machines. Motion magnification mechanisms can be used to achieve large force at the wheel with small torque capability at the electric machine. To this end, gearbox stages are used to improve force density as well as damping and regeneration performance [41, 54]. Therefore, very compact and lightweight layouts can be achieved when compared to the linear counterpart [11].

However, motion magnification amplifies the inertia of the rotating components reported at the wheel. This significantly increases the unsprung mass inertia, thus degrading vehicle dynamics performance [54]. Some solutions propose the use of mechanical motion rectifiers, namely they convert the bidirectional suspension vibration into smooth unidirectional rotation of the electric machine [41]. This can

significantly mitigate the negative effect of the amplified rotating inertia [20]. Nevertheless, motion rectification impedes the bidirectional power flow thus excluding the active operation of the electromagnetic suspension [55].

Rotary electromagnetic suspensions require a linear-to-rotary conversion system to transform the wheel translation into rotation of the electric machine. These systems intrinsically implement a transmission ratio between the wheel motion and the electric machine shaft. Consequently, less motion magnification is requested to the gearbox. Hydraulic and mechanical working principles are exploited.

Electrohydrostatic (EHA) The former uses a rotary motor-pump unit and a linear hydraulic actuator. These are interfaced through a hydrostatic circuit [39]. These solutions are commonly labeled EHA suspensions. They feature good mechanical robustness and low noise—its intrinsic lubrication prevents the main tribology concerns—but are affected by poor efficiency. Furthermore, the presence of oil is a disadvantage: oil-free solutions are nowadays sought-after by the industry [11]. Although motor-pump stage and hydraulic lines are used, EHA suspensions differ from hydraulic active suspensions (see Chap. 1). The main difference is in how these systems use the electric machine: hydraulic active suspensions use the electric machine to build pressure in the circuit, then the generated force is modulated through controllable valves. These systems cannot regenerate energy. Conversely, EHA solutions modulate the suspension force by controlling the electric machine and the hydraulic oil is used as transmission mean.

A commercial system was proposed by Clear Motion, Inc., previously known as Levant Power Corporation. The initial solution—known as Genshock—was a regenerative shock absorber developed for heavy trucks and military vehicles. It featured a hydraulic system pushing the fluid through a turbine, which was coupled to a generator [56, 57]. The concept then evolved into a high-bandwidth active suspension technology known as Clear Motion. A gerotor pump stage is coupled to the electric machine, which is controlled by a power stage. The device is then mounted on the conventional shock absorber, which is used as linear hydraulic actuator [58].

Li and Tse [59] developed a EHA regenerative shock absorber by using off-the-shelf components (Fig. 2.5). Experimental campaign was conducted to assess system efficiency and power regeneration performance. The shock absorber was provided with harmonic input and the electric machine was shunted with a resistor. The authors observed how the efficiency deteriorates as the input frequency escalates. This was attributed to the motion inversions of the electric machine. The maximum harvested power was 435 W at 0.8 Hz input excitation with amplitude of 20 mm.

Galluzzi *et al.* proposed a EHA regenerative shock absorber that used a gerotor motor-pump unit directly mounted on a conventional shock absorber [39]. The latter features a twin-tube architecture that rectifies the oil flow, thus providing

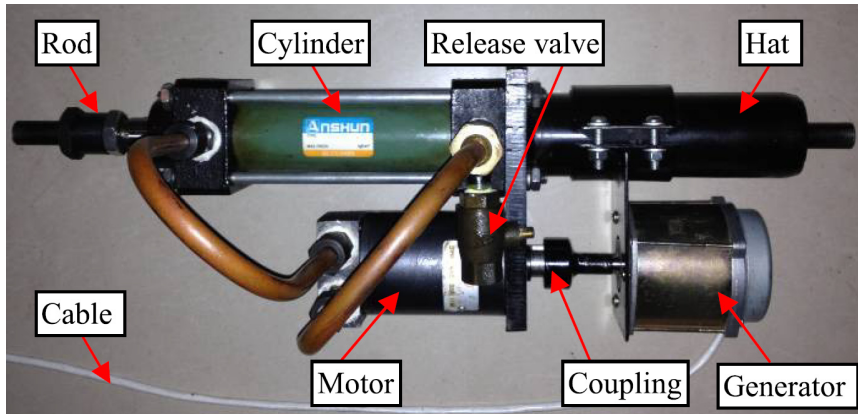


Figure 2.5: Electrohydrostatic regenerative shock absorber prototype developed by Li and Tse [59]

unidirectional motion of the motor-pump unit. For this reason, the proposed solution cannot work in active mode. The developed motor-pump unit was tested on a dedicated test rig to characterize its static regeneration efficiency. To this end, the electric machine was controlled by means of a power module. Constant velocity profiles were given as input. The efficiency map in the force-speed plane was extracted and 41.7% maximum efficiency was found. The hydro-mechanical losses were pointed as the most critical factor affecting the conversion efficiency.

Electromechanical When mechanical-based conversion mechanism is adopted, the active suspension is labeled *electromechanical*. In this category, rack-pinion, ball-screw and linkage-based mechanisms are used.

Rack-pinion These electromagnetic suspensions employ the rack-pinion mechanism as linear-to-rotary conversion system (Fig. 2.6). Main advantages are good conversion efficiency and transmission ratio, thus helping for a less demanding gearbox. On the other hand, electromagnetic suspensions based on rack-pinion mechanism are affected by poor mechanical robustness, backlash, friction and noise issues [38].

Li and Zuo [20] investigated regenerative shock absorbers based on rack-pinion mechanism. Specifically, the focus was given to the effect of the inertia on the overall performance. They experimentally compared comfort and handling of the vehicle when equipped with conventional and rack-pinion regenerative shock absorbers. The analysis showed how the inertia significantly affects the vehicle performance. In this perspective, the importance of the motion rectifier was highlighted. In fact, the prototype with motion rectifier achieved better performance.

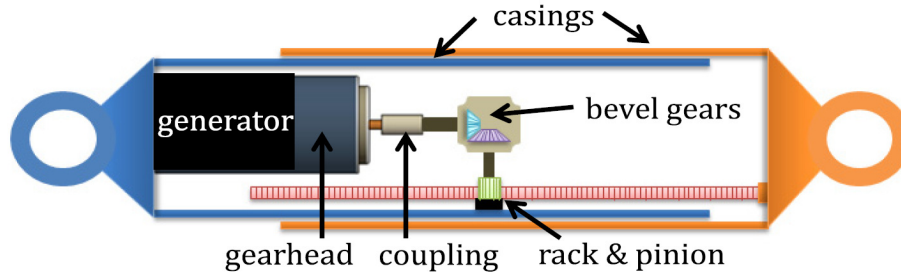


Figure 2.6: Layout of rack-pinion electromagnetic active suspensions [60]

Chen *et al.* proposed a self-powered suspension for the rear fork of a motorcycle [61]. It features a semi-active magnetorheological damper supplied by a rack-pinion regenerative shock absorber. The latter implements a motion rectification system so that a DC voltage is generated. A direct-feedback strategy is used: the semi-active damper electric terminals were directly connected to the regenerative damper generator. Hence, the system self-adjusts without the need of a control logic. Laboratory tests were carried out to characterize the system in terms of force, power generation and self-powered feature. Then, the system was installed on the reference motorcycle that underwent shock excitation. The results showed that the proposed solution leads to better ride comfort when compared to classical magnetorheological suspension architectures with the advantage of no power consumption.

The Center for Electromechanics (University of Texas, Austin) developed a linear electromechanical suspension prototype based on rack-pinion conversion mechanism [62, 63]. The system was designed as a retrofit for military high mobility multi-wheeled vehicles. Specifically, the actuator—capable of producing about 9 kN of force—was mounted in parallel to passive springs and supplied through a 5 kW alternator. Road testing showed significant comfort improvement with an increase in the achievable cross-country speed when compared to conventional passive suspensions. On typical off-road terrain tests, the average power consumption for all four corner was less than 1.5 kW.

Guo *et al.* [64] investigated rotary regenerative suspensions based on rack-pinion conversion mechanism with a focus on the influence of the suspension inertia and the improvement achieved by using a motion rectifier. Specifically, the regenerative suspension was modeled and integrated into a quarter-car vehicle model. Its performance in terms of vehicle dynamics were compared to a quarter-car equipped with a conventional passive shock absorber. The results highlighted that the system with no motion rectifier improves the comfort when the suspension inertia is below a certain value. This constraint was less stringent when the motion rectifier is included. The latter was able to improve simultaneously comfort and handling when compared to a passive shock absorber.

Ball-screw These electromagnetic suspensions employ a ball-screw coupling as linear-to rotary conversion system. Ball-screw mechanisms significantly reduce backlash and noise issues, and feature good efficiency. Conversely, these systems are affected by the relatively high cost when compared to the rack-pinion counterpart [11].

Tonoli *et al.* worked on the modeling and validation of electromechanical shock absorbers [38]. A system featuring a ball-screw coupled to a rotary electric machine was developed for off-road vehicle applications (Fig. 2.7). Experimental campaign was carried out on a dedicated test bench to assess dynamic performance of the prototype when shunted with an external resistance. Specifically, the mechanical impedance was characterized by means of frequency tests up to 60 Hz. The experimental results were used to validate the modeling approach.

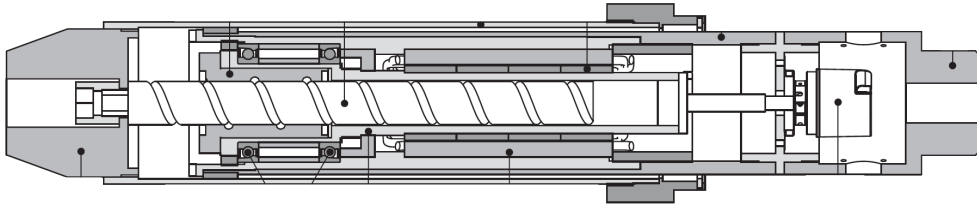


Figure 2.7: Ball-screw electromechanical shock absorber prototype developed by Tonoli *et al.* [38]

Zhang *et al.* proposed a system made up of brushless DC motor coupled to a ball-screw linear-to-rotary conversion mechanism [40]. Although the use of a controlled power module was discussed, the electric machine was shunted with an external resistance during the tests. Extensive laboratory experimentation was conducted. At first, the prototype was mounted on a MTS machine. When harmonic excitation was imposed, the results highlighted how the unsprung mass performance degrades at high frequency input. This was attributed to the influence of the prototype inertia. Then, the reference vehicle was equipped with the proposed suspension and tested on a test bench that provides displacement profiles at the wheels. Frequency sweep and random input showed that the unsprung mass features lower natural frequency due to the inertia of the prototype. Furthermore, the sprung mass performance improves while the unsprung mass dynamics is degraded. The authors highlighted that active forces are needed to compensate for the inertia effect and avoid the performance deterioration.

Montazeri-Gh and Kaviani-pour investigated a regenerative shock absorber featuring a ball-screw conversion mechanism [65]. The influence of shunt external

resistance and ball-screw lead on the vehicle performance was addressed. Specifically, small lead is beneficial for the performance but implies large speed at the electric machine. To cope with such issue, the authors proposed the use of a compliant element in series to the regenerative shock absorber to attenuate very high frequencies implying large speed of the electric machine.

Liu *et al.* proposed an electromechanical shock absorber based on ball-screw mechanism and motion rectifier [66]. The latter features two one-way clutches that make the electric machine rotate at a rather constant velocity. Therefore, good efficiency working point is guaranteed, as well as backlash reduction and mechanical shocks in the transmission mechanism. These were further reduced by using a rubber mount that filters the shocks coming from road disturbances. The electric machine was shunted with an external resistance. Laboratory tests were conducted by providing harmonic inputs at frequency values ranging from 1 to 10 Hz. Maximum efficiency of 70% was found. Similar tests were conducted on a shock absorber featuring a rack-pinion conversion mechanism. It gave very low efficiency performance especially at small input amplitude. This result was attributed to the significant backlash affecting rack-pinion solutions. Finally, the ball-screw prototype was installed on a Ford F250 pickup and tested on a real road at 40 mph with 3 and 10 Ω shunt resistances. Comfort improvement of 11% was achieved with 13.3 W regenerated power.

Li and Zuo [67] proposed an electromechanical regenerative shock absorber featuring ball-screw conversion mechanism and motion rectifier. The electric machine was shunted with external resistance. In simulation, systems with and without motion rectifier were compared. The latter leads to worse vehicle performance because of the strong inertia influence. Then, the prototype with motion rectifier was characterized on a MTS test machine. The effect of the motion rectifier on the force output was addressed and efficiency values up to 60% were found. Finally, the prototype was mounted on a Chevrolet SUV and tested on real road at 15 mph. Up to 100 W regenerated power was achieved [60].

Linkage-based These electromagnetic suspensions feature a linkage system as linear-to-rotary conversion mechanism. Among all the available solutions, the linkage-based one features good mechanical robustness and efficiency, compact and lightweight layout, low mechanical complexity, and oil-free operation.

Jonasson *et al.* [37] developed, in partnership with Volvo, an electromagnetic suspension featuring one leveling and one damper rotary actuator integrated into the upper arm (Fig. 2.8). Therefore, the upper arm itself works as linkage mechanism enabling the linear-to-rotary conversion. The authors proposed an optimization algorithm that integrates the design of the suspension and the control strategy. This was required as more demanding control implies larger actuator. To avoid very large actuator, a conventional shock absorber was used in parallel to the electromagnetic suspension. As control strategy, LQR and Skyhook were used. Numerical

studies showed improvement of the comfort performance, while the handling was slightly influenced. This could be attributed to the low bandwidth of the actuator. Simulations of a passenger vehicle on Belgian pavé highlighted that electric energy can be recovered, although the active operation.

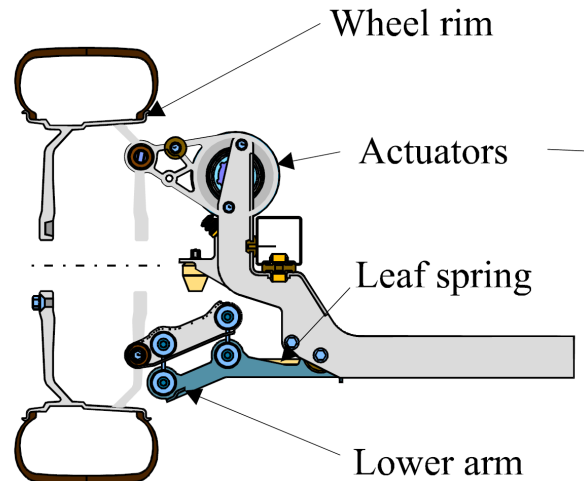


Figure 2.8: Linkage-based electromechanical active suspension layout proposed by Jonasson *et al.* [37]

Yu *et al.* [68, 69, 70] proposed an electromagnetic actuator featuring a rotary electric machine coupled to a gearbox (Fig. 2.9). A rocker-pushrod assembly connects the input shaft to the lower arm of the suspension. Such system works in parallel to the passive suspension of the vehicle by providing active and passive forces. This turns into comfort and handling improvement during maneuvers such as cornering, braking or acceleration, and better aerodynamic performance by adjusting vehicle height. These aspects requires active force, thus making active suspension advantageous when compared to semi-active one. The proposed solution employs off-the-shelf gearbox and electric machine. The linkage was designed to optimize the conversion ratio while accounting for packaging constraints. H-infinity strategy was used to control vehicle dynamics, which cost function accounts for comfort and handling indexes, as well as control effort. The latter is related to the energy consumption of the active suspension. Numerical study demonstrated comfort and handling improvement when the vehicle underwent bump and pot-hole. When ISO road unevenness was considered, performance improvement was achieved at frequencies below 4 Hz. ISO C road profile resulted in 530 W and 210 W peak regenerated and consumed energy, respectively. Experimental tests were conducted on a quarter-car test rig by exciting the wheel through harmonic road, a smoothed bump and hole, and swept frequency road profiles. As result, backlash in

the rocker transmission caused spikes in the variation of the actuator velocity and in the acceleration of the sprung mass. Despite these shortcomings, comfort improvement up to 29% were achieved at the cost of 100 W when a pothole condition was considered.

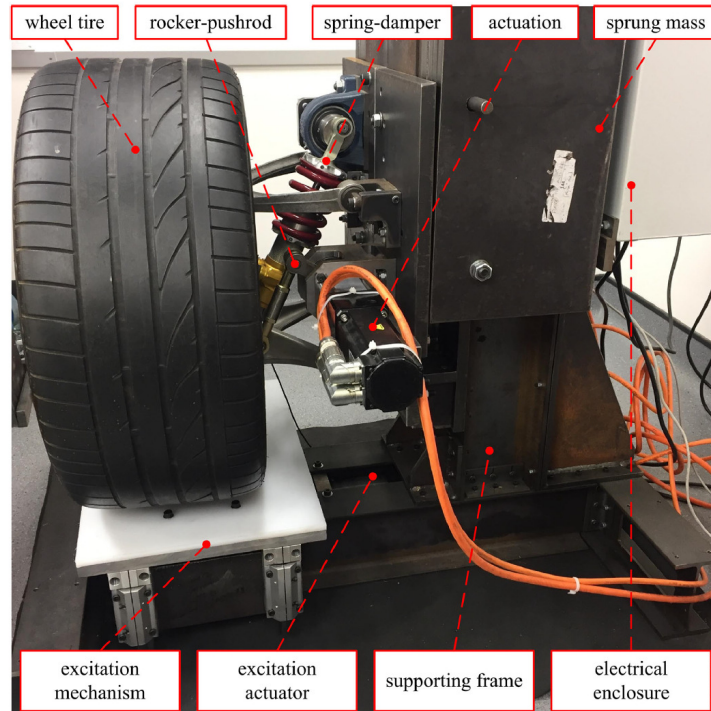


Figure 2.9: Linkage-based electromechanical suspension developed by Yu *et al.* [68]

As mentioned in Sec. 2.2.3, Gupta *et al.* proposed the experimental comparison between linear and rotary electromagnetic suspensions [52]. The latter features rotary DC motor and gearbox coupled to a lever arm. The developed prototypes were installed on the reference vehicle, in parallel configuration with the passive shock absorber. Only passive operation was explored. To this end, the electric machine was shunted with an external resistance to implement the damping behavior. Tests were performed by running over a wooden beam obstacle. The results demonstrated the better damping capability of the rotary linkage-based solution when compared with its linear counterpart.

Todmal and Melzi proposed a rotary electromagnetic shock absorber featuring a brushless DC motor coupled to a parallel-axis gearbox [71]. A crank-lever system is used as linear-to rotary conversion mechanism. Although the linkage design procedure was described, no considerations on the packaging and transmission ratio have been accounted for. Simulations of an off-road vehicle on country road showed regenerated power up to 358 W. Further analyses were conducted to investigate the

effect of the prototype inertia. Specifically, larger inertia implied lower regenerated power, as well as deteriorated comfort and handling performance.

Several patents dealing with electromechanical suspensions based on linkage transmission mechanisms have been filed. In the early '30s, Harrison [72] proposed a shock absorber composed of an electric machine, a multiplier stage and a lever to perform linear-to-rotary conversion. A shunt resistor was used to make the electric machine reproduce a damping action on the suspension. One configuration featured also a motion rectifier to enable unidirectional rotation of the electric machine.

Later, industrial organizations started filing patents on the subject. HQM Sachsenring GMBH [73] holds a patent on an slow-active suspension system for active chassis control. Specifically, it enables the compensation of roll and pitch motions of the sprung body. The system features a hydraulic actuator mounted on the body, whose shaft is connected to the wheel carrier through a linkage.

Audi AG patented an electromechanical shock absorber including an electric generator whose stator is fixed on the vehicle body, and the rotor is driven by the suspension deflection [74, 75, 76]. Specifically, the electric machine is connected to a gearbox. Then, a linkage is used as linear-to-rotary conversion mechanism. Furthermore, if the device is placed into the mounting of the suspension arm, no additional lever are needed [75]. The mechanical energy is harvested and converted into electricity stored for further use. The car manufacturer filed another patent family [77, 78]. It regards a slow-active rotary electromechanical suspension where the motor-gear unit produces active forces at the wheel by acting on the torsion bar. Then, the torsion bar is connected to the wheel upright by means of links. For this reason, the solution can be categorized as linkage-based.

Hyundai Motor Company [79] patented a rotary electromechanical regenerative device able to improve vehicle handling and comfort while harvesting energy from road unevenness. The solution features a bush unit connected to the suspension link through a linkage mechanism. The rotation of the bush unit is given to a one-way transmission mechanism including one-way clutches. Then, the movement is amplified through a planetary gearbox and given to the electric generator. Finally, a rectification stage rectifies the electrical output of the generator. Due to the one-way transmission mechanism, the solution can work only in passive mode.

Other mechanisms Berg *et al.* proposed a rotary electromechanical active suspension featuring a magnetic lead screw as linear-to-rotary conversion mechanism [80]. The prototype was tested on a MTS machine to characterize friction and efficiency when the electric machine was connected to a current controller and shunted with an external resistance. Several durability and thermal tests were conducted as the previous version of the prototype suffered issues in these aspects.

Ali *et al.* [81] proposed a regenerative shock absorber composed of barrel-cam follower mechanism—for linear-to-rotary conversion—and motion rectifier. The electric machine was connected to a diode-bridge rectifier and supercapacitors in

parallel to the load. Laboratory tests on a MTS machine gave power outputs up to 3.85 W. The barrel-cam follower mechanism can be compared to the rack-pinion system as general layout, but featuring more compactness and lower backlash.

Gonzalez *et al.* proposed a regenerative shock absorber for a lightweight electric motorbike. It employs a synchronous belt system for linear-to-rotary conversion [82]. Specifically, the linear movement is transmitted to a piston attached to the synchronous belt through a crimp block. Then, bevel gears are connected to the pulley to correct the motion and finally a gearbox is used to amplify the electric machine rotation. Laboratory experimentation was carried out by providing harmonic inputs at diverse frequency values. The electric machine was shunted with external resistance. Due to the internal resistance of the generator, the regenerated power was lower than expected. The experimental results were used to validate the computational models. These were used to assess the energy recovery potential for different motorbike speed and road profiles.

2.3 Final remarks

Table 2.2 reports a qualitative comparison between linear and rotary electromagnetic suspensions. Linear solutions are very advantageous in terms of mechanical robustness, efficiency and equivalent inertia thanks to the absence of transmission elements. Nevertheless, cost and mass of the system make these solution poorly interesting for future implementation at industry level.

EHA rotary suspensions feature very good mechanical robustness and low noise level thanks to the presence of oil, which lubricates and avoid tribology concerns. However, these solutions showed poor efficiency when compared to other technologies. Furthermore, they are not oil-free, which is nowadays a very appealing feature in the industry environment.

Among the rotary electromechanical suspensions, rack-pinion ones particularly suffer backlash and large equivalent inertia. For these reasons, few solutions can be found in the literature. Ball-screw solutions boast very good efficiency at the cost of large equivalent inertia and bulkiness.

Finally, linkage-based rotary electromechanical suspensions feature very large efficiency, compact and lightweight layout, good mechanical robustness and moderate equivalent inertia. One flaw is the noise level due to the presence of gearbox stages. Nevertheless, among all the electromagnetic suspension layouts, the linkage-based solution is very attractive. In the last decade, it has gained the focus of the academic and industrial research.

The literature survey shows that most of the solutions proposed by the industry are load-leveling or slow-active. On the other hand, the scientific research mostly focused on linear electromagnetic suspensions along with rotary solutions based on ball-screw and rack-pinion conversion mechanisms. Therefore, few efforts were

Table 2.2: Qualitative comparison between linear and rotary electromagnetic suspension technologies

Feature	Technology				
	Linear	Rotary			
		EHA	Electromechanical		
			Rack-pinion	Ball-screw	Linkage
Mechanical robustness	●	●	○	◐	◐
Efficiency	●	○	◐	●	●
Mass	○	◐	◐	◐	●
Equivalent inertia	●	◐	◐	○	◐
Oil-free	●	○	●	●	●
Noise	●	●	○	◐	○
Cost	○	◐	◐	◐	◐

dedicated to linkage-based and full-active systems.

Furthermore, most of the proposed solutions in the scientific literature are called *regenerative suspensions*, namely electromagnetic suspensions that implement the regenerative feature. Active operation is not allowed or it is not investigated at all. This aspect highlights a gap between the automotive industry and the academy: the former is interested more in the active feature than the regenerative one. Energy regeneration is considered as a secondary aspect that could be the mean to limit the energy consumption related to the active operation. Conversely, the academic research focuses on the regenerative aspect and usually disregards the active feature.

Lastly, the literature lacks a design methodology that gives a compact rotary linkage-based electromagnetic suspensions starting from vehicle performance and packaging requirements. Although many research efforts focus on the performance optimization of electromagnetic suspensions, vehicle integration and packaging are usually neglected. These aspects cover a relevant role when the research goal is the implementation of such technology at the industry level.

Chapter 3

Design methodology

This chapter discusses the design methodology of the proposed REmSA. At first, the layout is described by detailing the diverse parts composing the system.

Then, the developed design methodology is explained. It establishes specific steps to design a REmSA. Once design constraints and requirements are assessed, the electric machine and linkage are optimized. Subsequently, the gearbox and electric machine are matched to minimize the inertia features of the prototype, namely its mass and equivalent rotational inertia. The detailed design of the diverse components concludes the methodology. The present work intends to be a guideline for both academy and industry moving towards the development of REmSAs.

For demonstration purposes, the proposed methodology is applied to a case study dealing with a motorcycle application. The diverse steps are detailed by including considerations, mathematical descriptions, and optimization problem formulations. Finally, the manufactured prototype is presented.

The present research also led to the development and manufacture of a prototype for an automotive application. Since it was designed with a previous but incomplete version of the proposed methodology [83], its design is briefly described in Appx. A.

3.1 Proposed layout

The REmSA layout proposed in this dissertation is schematized in Fig. 3.1. It features a suitably controlled electric machine coupled to a gearbox. Since compactness is crucial in this application, Permanent Magnet Synchronous Motor (PMSM) and planetary gearbox are selected.

When dealing with relatively small electric machines, i.e. in the range 1 to 10 kW, PMSMs feature the highest torque-to-mass ratio [84]. The synchronous type offers high efficiency, good and smooth performance both in the high and low speed operation, low rotor inertia, good reliability, and low noise. Furthermore,

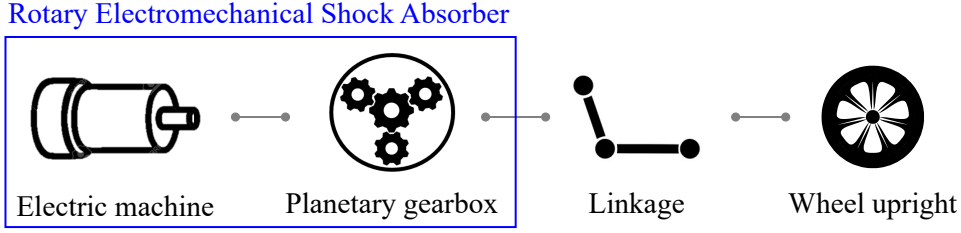


Figure 3.1: REmSA scheme

it outperforms the other electric machine typologies when dynamic force control is requested, which is the present application. These aspects motivate the selection of the PMSM. To increase its compactness, NdFeB magnets are used. They feature higher remanence, coercivity and energy product when compared to other Permanent Magnet (PM)s, at the cost of lower Curie temperature, which is not a concern in the present application. Furthermore, fractional slot winding scheme is adopted. Despite the larger torque ripple, it enables higher efficiency, torque and more compact winding ends when compared to distributed schemes [85].

Since electric machines offer quite small torque and high speed, gearboxes are the obvious solution to raise the torque and drive the load. Garcia *et al.* [86] proposed a comprehensive review of compact gearboxes for robotics applications. Although planetary layouts feature relatively large backlash when compared to more complex schemes, they offer high efficiency, reliability, relatively easy and cheap manufacturing, and compactness. Therefore, the planetary gearbox architecture is selected for the present application, where the input and output of the stage are the carrier (slow shaft) and the sun (fast shaft).

As shown in Fig. 3.1, the rotor of the electric machine transmits a torque T_{em} at angular speed ω_{em} . The gearbox features transmission ratio:

$$\tau_g = \omega_{REmSA} / \omega_{em} = T_{em} / T_{REmSA} \quad (3.1)$$

where ω_{REmSA} and T_{REmSA} are the angular speed and torque of the low-speed high-torque shaft of the gearbox, i.e. the REmSA shaft. The latter is connected to a linkage that converts the linear motion of the suspension into rotation of the REmSA shaft. It features transmission ratio:

$$\tau_l = v_{act} / \omega_{REmSA} \quad (3.2)$$

v_{act} being the linear velocity at the suspension level. A four-bar linkage is used as the simplest closed-chain movable mechanism. The overall transmission ratio τ_t is defined as the ratio between the suspension linear speed and the electric machine angular velocity:

$$\tau_t = v_{act} / \omega_{em} = \tau_l \tau_g \quad (3.3)$$

When considering a static transmission with no power dissipation, the electric machine torque is directly related to the actuator force at the suspension F_{act} :

$$T_{\text{em}} = \tau_{\text{t}} F_{\text{act}} \quad (3.4)$$

Therefore, the overall transmission ratio is a relevant design parameter that directly impacts the size of the electric machine. At a given requested force F_{act} , small transmission ratio implies small electric machine with low torque capability, thus resulting in compact and lightweight layout. By converse, a more performing gearbox with possible additional stages will be . Hence, the ratio τ_{t} impacts also the gearbox size and mass. Furthermore, any inertial (J_{em}) or dissipative contribution (c_{em}) at the level of the electric machine is seen by the suspension as

$$\begin{aligned} m_{\text{eq}} &= J_{\text{em}} / \tau_{\text{t}}^2 \\ c_{\text{eq}} &= c_{\text{em}} / \tau_{\text{t}}^2 \end{aligned} \quad (3.5)$$

Hence, small transmission ratio increases friction loss and equivalent inertia at the level of the suspension. Although friction contributes to the suspension damping, it deteriorates the conversion efficiency of the device and affects the force control of the suspension. Inertia contribution is a key issue in electromechanical active suspensions—as already described in Sec. 2.2.3—as it tends to stiffen and lock the system when high-frequency input occurs.

Therefore, the overall transmission ratio and electric machine size must be matched to optimize the system performance while keeping compact layout.

3.2 Design methodology

The proposed system-level methodology establishes specific steps—which are reported in the flowchart of Fig. 3.2—to design a rotary electromechanical shock absorber. The methodology is based on vehicle integration and packaging aspects that cover a relevant role when the research goal is the technology implementation at the industry level.

The methodology is described below and then detailed in Sec. 3.3, by including considerations, mathematical descriptions, and optimization problem formulations.

1. **Vehicle integration.** Performance requirements and envelope constraints of the REmSA are defined by starting from the retained vehicle architecture and specifications. This step covers a relevant role when the research goal is the implementation of such technology at the industry level. This step includes:
 - (a) *Preliminary packaging.* The REmSA must fit the suspension of the retained vehicle. To this end, a preliminary study about the packaging is

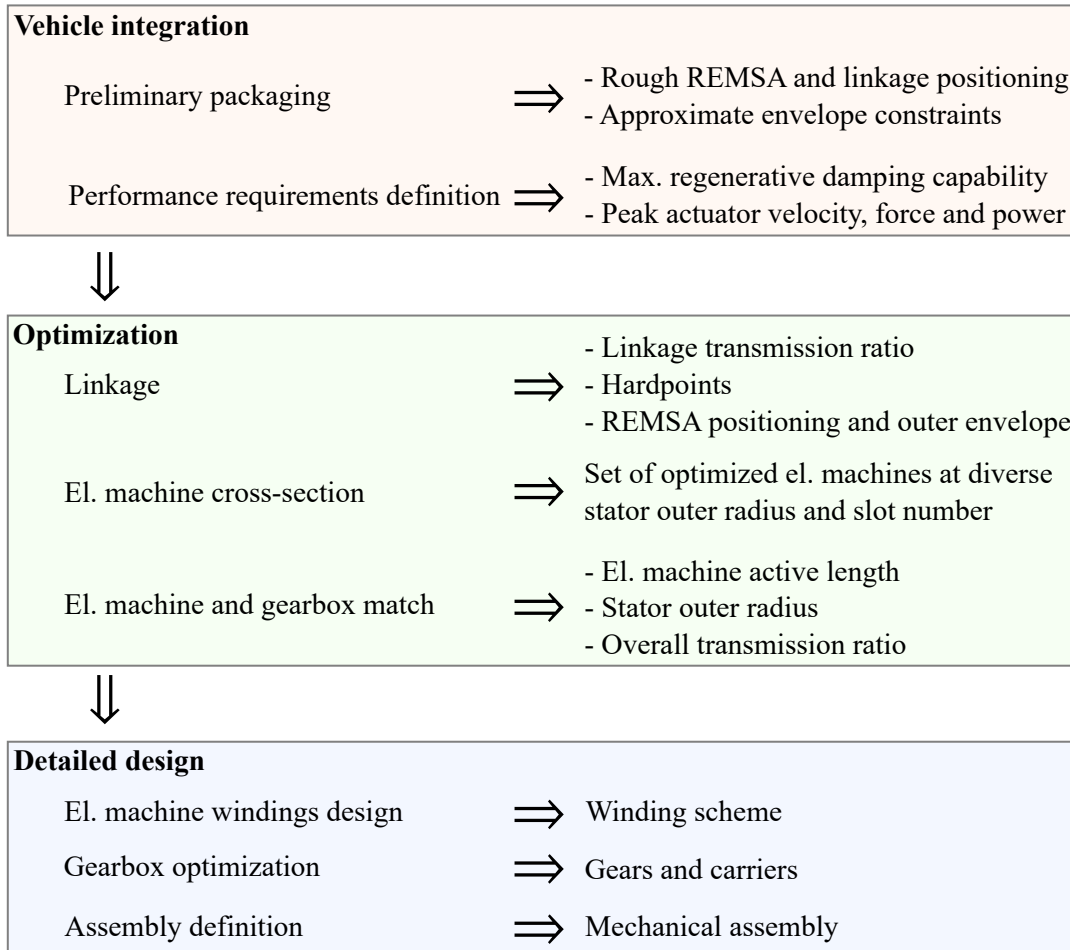


Figure 3.2: Design methodology flowchart

needed. Because of the geometry of rotary electric machine and planetary gearbox, cylindrical envelope of the prototype is considered. When the project deals with an existing suspension, finding vacant space is not a trivial task. To this end, some components that can be moved or removed should be identified. In this context, the conventional shock absorber could be removed to extract some space. This is possible since the REmSA will replace its functions. Nevertheless, when its structure cannot be removed as it fulfills other tasks, the conventional shock absorber cannot be removed. Bump stop or coil spring guidance in coil-over configurations are the most common examples. In such cases, the shock absorber tube can be emptied or the damping valves can be removed to cancel its damping function. Overall, this step outlines rough prototype and linkage positioning along with approximate envelope constraints.

- (b) *Performance requirements definition.* As the conventional shock absorber is completely replaced, its tasks—in terms of vehicle dynamics—must be at least fulfilled by the REmSA. To the author’s experience, carmakers usually require solutions able to cover the whole conventional shock absorber force-velocity characteristic. However, this specification would lead to very large REmSA and expensive power electronics. The physics behind conventional shock absorbers makes them easily achieve very large force at high velocity. Conversely, electric machines withstand power limitations that bound the generated force when the velocity escalates. In this perspective, the designer should question the carmaker requirement. Furthermore, the active and regenerative features go beyond the conventional shock absorber performance. In this context, vehicle dynamics analyses are performed to define the specifications in terms of maximum regenerative damping, suspension velocity, as well as actuator power and force requirements. The retained vehicle is modeled as a quarter-car (or more complex approaches) including the REmSA as an ideal force actuator. The latter is controlled through diverse strategies, according to the carmaker requests. The defined specifications are referred at the wheel level to be independent from the transmission ratio of the elements involved in the REmSA design.
2. **Optimization.** The system sub-components must be optimized to maximize the performance while guaranteeing compact and lightweight layout. These are optimized separately and then matched through a further optimization process. This step includes:
- (a) *Linkage optimization.* The idea is to achieve the best linkage according to the packaging constraints. By considering Eq. 3.3, small linkage transmission ratio τ_1 relieves gearbox requests, thus allowing a more compact solution. To this end, an optimization process minimizes the linkage transmission ratio. However, an acceptable transmission quality must be guaranteed. The latter is indicated by the transmission angle, i.e. the angle between the coupler and the follower when dealing with four-bar mechanisms. It is most favorable when equal to 90° . Therefore, a multi-objective optimization based on Genetic Algorithm (GA) is used to get the best trade-off between transmission ratio and transmission angle. At the same time, no interference must exist between the suspension components, the added levers and the prototype, along the whole suspension stroke. Hence, the constraints defined in step 1(a) are imposed. This step fully defines the linkage transmission ratio and hardpoints, as well as the prototype positioning and envelope constraints.
- (b) *Electric machine cross-section optimization.* An optimization process

maximizes the torque-to-length ratio of the electric machine at diverse stator outer diameter and slot-pole combinations. To this end, the geometry is iteratively refined to maximize the torque while checking magnetic saturation of the stator material. Electromagnetic finite element approach with real material characteristic is needed to account for iron magnetic saturation phenomenon and accurately address the machine performance. Overall, a set of optimized electric machines to be used in the next step is obtained.

- (c) *Gearbox and electric machine match.* Once the linkage has been fully defined, the gearbox contribution τ_g sets the overall transmission ratio τ_t (Eq. 3.3). As discussed in Sec. 3.1, the latter is a relevant design parameter that must be selected to optimize the system performance while keeping compact layout. To this end, the electric machine and gearbox are matched to minimize a cost function that includes the overall mass and equivalent inertia of the REmSA. The electric machine performance is accounted through the set obtained in step 2(b). The gearbox is represented through scaling laws. The same outer diameter is considered for these two components to optimally use the whole prototype envelope. This step selects the electric machine active length and outer radius among the optimized sets—derived in step 2(b)—and defines the gearbox transmission ratio.

3. **Detailed design.** Once the electric machine and linkage have been defined, as well as the gearbox specifications in terms of transmission ratio and outer envelope, the detailed design can be addressed. It includes the following steps:

- (a) *Electric machine windings definition.* Starting from the electric machine geometry obtained in step 2(c), the winding scheme must be defined. This step is heavily guided by manufacturing constraints. In fact, the coil winding technology imposes strict limits to the packing factor. Furthermore, a certain copper volume can be achieved through more turns and thin wire, or conversely few turns and thick wire (or more wires in parallel). The former yields large back Electromotive Force (EMF) thus lowering the electric machine base speed at a given DC bus voltage supply, the latter enhances the base speed at the cost of increased phase current. Large current implies costly and bulky power electronics and cabling. Therefore, the winding design must account for all these aspects.
- (b) *Gearbox optimization.* Starting from the transmission ratio τ_g and outer envelope requirements, an iterative process is required to find the most compact layout. Specifically, the transmission ratio is split into one or more stages. Then, each stage is designed by following static and fatigue

considerations while observing outer envelope constraints. Vehicle dynamics simulations are performed to assess overload conditions and load spectra. The software KISSSoft is used to perform the optimization process that fully defines the planetary gearbox.

- (c) *Assembly definition.* Once all the components have been defined, the mechanical assembly of the REmSA can be completed. Specifically, electric machine and gearbox sub-assemblies are defined and then integrated to achieve a very compact layout. Bearings are selected, casings are designed to provide a stiff and lightweight solution. Also linkages components and the interface with the suspension of the retained vehicle are defined.

The design process is not straight: some steps may not be fulfilled and, consequently, the previous ones must be reviewed to generate different outputs. When concluded the process, design constraints and requirements must be verified by considering the achieved prototype. In particular, the vehicle dynamics analyses should be updated with the prototype features (estimated equivalent inertia, dissipative contribution and transmission compliance) and limitations (electric machine torque and power limits).

Note that the optimization (step 2) is implemented as a multi-step process because the linkage and electric machine cross section can be optimized offline independently on the final configuration of the REmSA. At the same time, the gearbox is accounted for by means of scaling laws that provide the optimal gearbox at a given transmission ratio, outer diameter and transmitted torque. Once these sub-components are optimized, they are matched to obtain the optimal REmSA. This last step allows to define the stator outer diameter, the electric machine active length and the overall transmission ratio.

In the proposed methodology, thermal constraints of the electric machine are accounted by limiting the maximum supply current, as found in the literature [87]. To remove such assumption and push the design to the limit, a thermal model of the system must be used to simulate the behavior of the machine under realistic operation, i.e. road unevenness or lumped obstacle scenarios. However, this would significantly complicate the methodology. For this reason, the thermal behavior of the machine could be verified a posteriori through experimentation.

3.3 Methodology implementation

A case study is exploited to detail and demonstrate the developed design methodology. Considerations, mathematical descriptions, and optimization problem formulations are presented.

The retained vehicle is the motorcycle Benelli 752s (Fig. 3.3), naked motorcycle launched in 2020 by the Italian manufacturer Benelli. The project including the present activity aims at replacing the passive shock absorbers with active ones: a EHA shock absorber at the front fork, a REmSA at the rear suspension.



Figure 3.3: Retained vehicle: motorcycle Benelli 752s [88]

3.3.1 Vehicle integration

This step aims at defining the REmSA requirements and envelope constraints so that it can be integrated in the retained motorcycle. This step required some iterations with the industrial partner to assess feasible modification of the retained suspension along with the desired performance in terms of vehicle dynamics.

Preliminary packaging

The rear suspension of the retained vehicle (Fig. 3.4) is analyzed to identify vacant region able to host the REmSA—which features a cylindrical envelope—and the elements of the four-bar linkage. The positioning must avoid any interference with the suspension links along the whole suspension stroke. To this end, the nominal (Fig. 3.5a) and full compressed (Fig. 3.5b) configurations are explored. In the present application, the coil-over shock absorber can be moved in the transverse motorcycle direction (normal to the view-plane) to extract more space for the linkage. Furthermore, the shock absorber damping function is canceled by removing its damping valves, as the REmSA replaces its functions.

The blue domain indicates the region in which the prototype could be installed. To this end, some considerations about how and where the prototype will be attached to the chassis are needed. In fact, prototype and chassis exchange significant reactions and, consequently, the attaching points must be structural. In the present

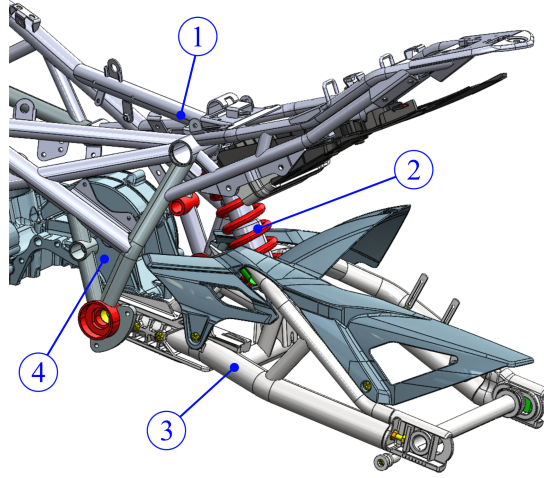


Figure 3.4: View of the rear suspension of the retained motorcycle. Chassis (1), conventional coil-over shock absorber (2), swing arm (3), engine assembly (4).

application, the identified points are the mountings where the engine assembly is connected to the chassis.

A feasible four-bar linkage is identified (solid orange lines in Fig. 3.5). As it lies in a plane, it is treated as a planar mechanism. The rear swing-arm is used as input link of the four-bar mechanism. Hence, hardpoint O coincides with the swing-arm pivot. The achievement of good transmission quality requires angles close to 90 deg between the linkage elements. More performing transmission ratio requires short lever BC as well as hardpoint A as close as possible to the wheel axis. The latter must follow some considerations. In fact, particular relevance is covered by the point where the linkage is jointed to the existing suspension elements because of the significant force exchanged. Consequently, some modifications to these elements could be required. The ideal solution is, when possible, to connect the linkage in the locations that already cover structural functions. This would avoid significant modifications to the structural elements. For this reason, the pivot where the conventional shock absorber was connected to the swing arm has been used in the present application (hardpoint A in Fig. 3.5).

Hardpoint B must be located into the red domain of Fig. 3.5, so that the linkage does not interfere with any component of the motorcycle across the whole suspension stroke. Wide domain is considered to avoid overconstraining of the optimization process.

A sub-domain of the blue region—the green domain in Fig. 3.5—contains the possible location of hardpoint C. It is obtained by decreasing the bounds of the blue domain by half diameter of the considered cylindrical envelope. To this end, $R_{so,max} = 60$ mm outer radius was considered as a first attempt.

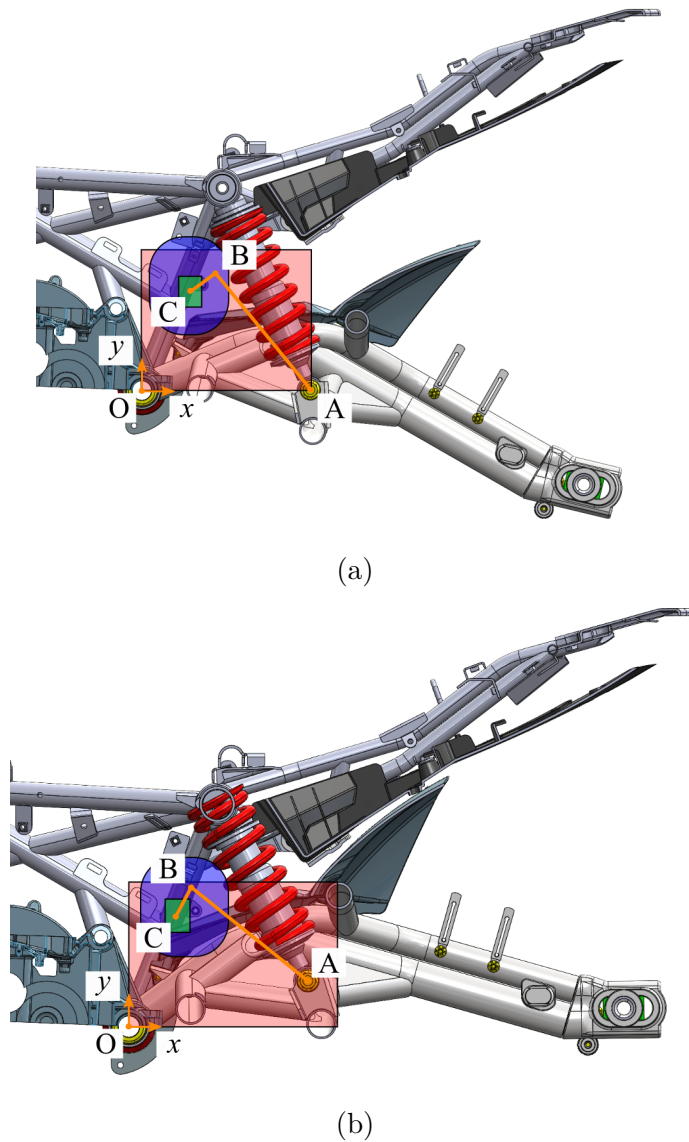


Figure 3.5: Orthogonal view of the rear suspension of the retained motorcycle in the nominal (a) and full compressed (b) configurations. Feasible four-bar linkage (orange solid lines) and its hardpoints. Region in which the prototype could be installed (blue domain), possible locations of hardpoints B (red domain) and C (green domain).

Overall, the outputs of this step are reported in Table 3.1. Specifically, the outer envelope, the coordinates of the defined hardpoints (O and A) and the domain bounds of the remaining ones (B and C) are reported. The reference system centered in hardpoint O is used.

Table 3.1: Outputs of the preliminary packaging design step

Description	Symbol	Value
Max. outer envelope	$R_{so,max}$	60 mm
Hardpoint A	$x_{A,nom}$	218.0 mm
	$y_{A,nom}$	0.9 mm
Hardpoint B	$x_{B,min}$	0 mm
	$x_{B,max}$	220.0 mm
	$y_{B,min}$	0 mm
	$y_{B,max}$	170.0 mm
Hardpoint C	$x_{C,min}$	40.0 mm
	$x_{C,max}$	50.0 mm
	$y_{C,min}$	110.0 mm
	$y_{C,max}$	140.0 mm

Performance requirements definition

Vehicle dynamics analyses are performed to define the specifications in terms of maximum regenerative damping, power and force requirements, which are needed to size the suspension prototype. These are referred at the wheel level to be independent from all the transmission ratios involved in the REmSA design.

Model The in-plane dynamics of the retained vehicle is represented by a full-vehicle model, as schematized in Fig. 3.6. The modeling approach proposed by Cossalter was followed [89].

The system is reduced to an equivalent model represented by two vertical spring-damper units that connect the sprung to the unsprung masses. To this end, the geometry of the motorcycle must be considered. Specifically, equivalent spring stiffness values for the front ($k_{s,f}$) and rear ($k_{s,r}$) are computed:

$$k_{s,f} = \frac{2\bar{k}_{s,f}}{\cos^2 \epsilon_f} \quad (3.6)$$

$$k_{s,r} = \bar{k}_{s,r} \tau_{m,\theta}^2 \quad (3.7)$$

ϵ_f being the inclination angle of the front fork, $\tau_{m,\theta}$ the swing arm velocity ratio (wheel stroke over arm rotation), $\bar{k}_{s,f}$ and $\bar{k}_{s,r}$ the spring stiffness of the front and rear suspensions, respectively. The front stiffness is doubled because of the dual telescopic fork type. The same relationships apply for the shock absorbers, whose reduced characteristics—which are provided by the industrial partner—are reported

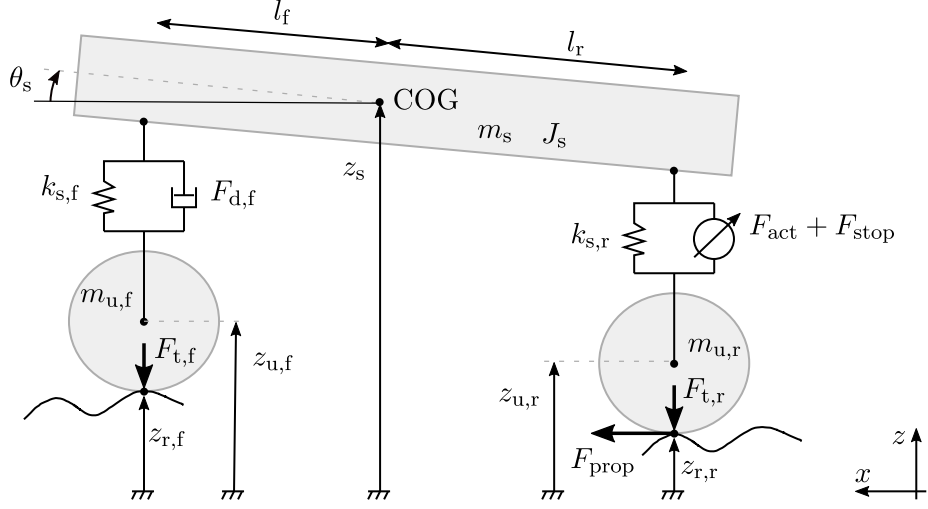


Figure 3.6: Full-vehicle model

in Figs. 3.7. Positive and negative velocity quadrants refer to the extension and compression strokes of the damper, respectively. The maximum damping of the reduced rear shock absorber is $c_{\max,r} = 80 \text{ kN/s/m}$, which occurs in rebound. Note that excessive damping values of conventional shock absorbers are usually unwanted consequences of dry friction and stick slip at very low speed.

The rear shock absorber is replaced by an ideal actuator exerting a force F_{act} . Specifically, it features infinite bandwidth, no force and speed limitations, and any parasitic effect such as dissipation or rotating inertia. Therefore, it behaves as a unitary gain between the control command and the output force. Although this assumption is non realistic, it is imposed by the absence of such details at this stage of the project.

Sprung mass vertical bounce z_s and pitch motion θ_s , front $z_{u,f}$ and rear $z_{u,r}$ unsprung mass vertical motions are taken as Degree-of-Freedom (DOF). The dynamic equilibrium of the reduced system gives the following equations of motion:

$$\begin{aligned}
 J_s \ddot{\theta}_s &= (m_{s,r}g + F_{\text{act}} + F_{e,r} + F_{\text{stop}}) l_r \cos \theta_s + \\
 &\quad + (z_s + h_{\text{COG}}) F_{\text{prop}} - (m_{s,f}g + F_{d,f} + F_{e,f}) l_f \cos \theta_s \\
 m_s \ddot{z}_s &= -m_s g - F_{\text{act}} - F_{d,f} - F_{e,r} - F_{\text{stop}} - F_{e,f} \\
 m_{u,f} \ddot{z}_{u,f} &= -m_{u,f} g - F_{t,f} + F_{d,f} + F_{e,f} \\
 m_{u,r} \ddot{z}_{u,r} &= -m_{u,r} g - F_{t,r} + F_{\text{act}} + F_{e,r} + F_{\text{stop}}
 \end{aligned} \tag{3.8}$$

where g is the gravity acceleration, $m_{s,f} = m_s w\%$ and $m_{s,r} = m_s (1 - w\%)$ the sprung mass share at the front and rear axles, respectively, F_{act} the REMSA actuator force, F_{stop} the reaction of the rear suspension end stop, F_{prop} the propulsion force, $F_{d,f}$ the front damper force, $F_{t,i}$ the tire-ground contact reaction—which is idealized as punctual—and $F_{e,i}$ the elastic force of the suspension springs. The latter is given

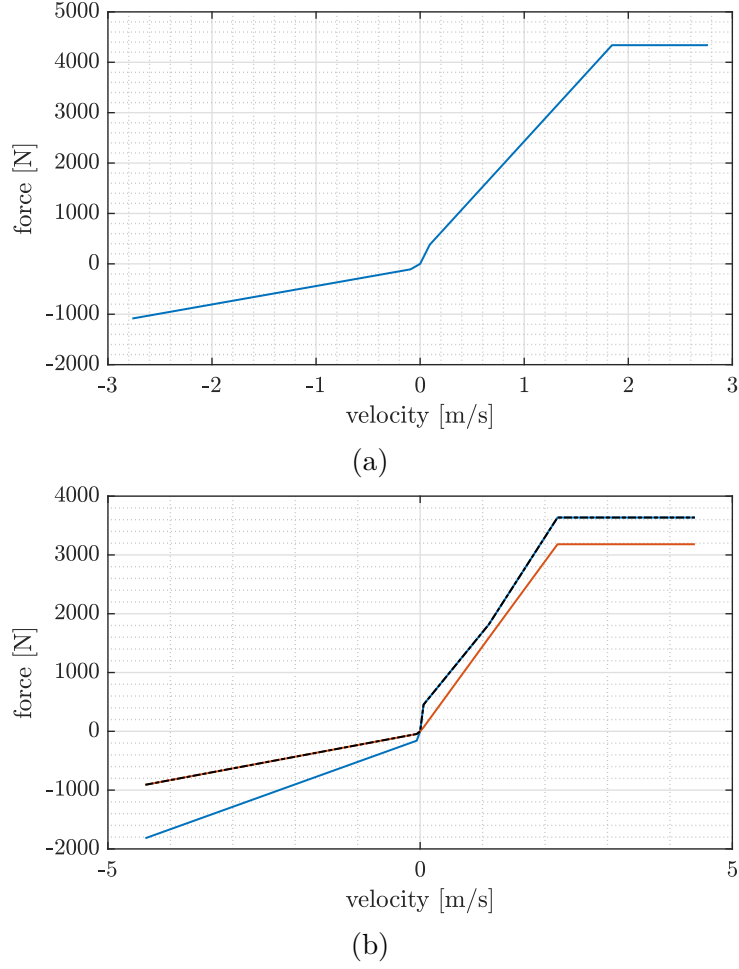


Figure 3.7: Reduced damping characteristic of the front (a) and rear (b) shock absorbers of the retained motorcycle (force and velocity at the wheel level). Maximum (blue), minimum (orange) and mixed (black dash-dotted) characteristics.

by:

$$F_{e,i} = (z_{s,i} - z_{u,i}) k_{s,i} \quad (3.9)$$

where $z_{s,i}$ is the sprung mass vertical motion at the location of front ($i = f$) and rear ($i = r$) suspensions. They are obtained as follows:

$$z_{s,f} = z_s + l_f \sin \theta_s \quad (3.10)$$

$$z_{s,r} = z_s - l_r \sin \theta_s \quad (3.11)$$

being l_f and l_r the COG-to-front wheel and COG-to-rear wheel distance, respectively. All the parameters are reported in Table 3.2. Note that the rear spring features very high stiffness. This is due to the unfavourable motion ratio of the

Table 3.2: Full-vehicle model parameters

Description	Symbol	Value
Sprung mass moment of inertia	J_s	119.3 kg m ²
Sprung mass	m_s	227.0 kg
Sprung weight distribution	$w_\%$	0.506
COG-to-front wheel distance	l_f	721.7 mm
COG-to-rear wheel distance	l_r	728.5 mm
COG height	h_{COG}	505.2 mm
Front unsprung mass	$m_{u,f}$	20 kg
Rear unsprung mass	$m_{u,r}$	28 kg
Front spring stiffness	$\bar{k}_{s,f}$	7 kN/m
Rear spring stiffness	$\bar{k}_{s,r}$	170 kN/m
Fork inclination	ϵ_f	22.8 deg
Swing arm motion ratio	$\tau_{m,\theta}$	0.454 m/rad
Front tire stiffness	$k_{u,f}$	250 kN/m
Rear tire stiffness	$k_{u,r}$	170 kN/m
Bump stroke limit	$\Delta z_{\text{stop,bump}}$	-140 mm
Rebound stroke limit	$\Delta z_{\text{stop,rebound}}$	20 mm
Stop stiffness	k_{stop}	10 ⁷ N/m

swing arm, that significantly decreases the equivalent stiffness seen at the wheel (Eq. 3.7).

The following assumptions are considered: the pitch center coincides with the center of gravity, the suspension is always assumed perfectly vertical with respect to the global reference frame, and the aerodynamic contribution is completely neglected.

The model includes non-linearities. First of all, the tire-ground contact forces ($F_{t,f}$ and $F_{t,r}$) are saturated to give only negative values:

$$F_{t,i} = \begin{cases} k_{u,i} (z_{u,i} - z_{r,i}) & \text{if } z_{u,i} - z_{r,i} \leq 0 \\ 0 & \text{otherwise} \end{cases} \quad (3.12)$$

where $k_{u,i}$ is the tire stiffness and $z_{r,i}$ the road profile at the front ($i = f$) and rear ($i = r$) suspensions. The equation accounts for tire-ground detachment, condition that could occur especially when the vehicle undergoes road irregularities such as bumps or potholes.

Then, trigonometric functions cannot be linearized as the pitch angle is usually non negligible in motorcycle applications.

Furthermore, the front shock absorber includes real damping characteristic (Fig. 3.7) that is a piece-wise function. Hence, the front shock absorber force is given by

$$F_{d,f} = F_{d,f}(v_{d,f}) \quad (3.13)$$

where the reduced front suspension velocity is

$$v_{d,f} = \dot{z}_{s,f} - \dot{z}_{u,f} \quad (3.14)$$

$\dot{z}_{s,f}$ being the first time-derivative of Eq. 3.10

Finally, the end stops are another source of non-linearity. The rear suspension stroke is given by:

$$\Delta z_{\text{susp}} = z_{s,r} - z_{u,r} \quad (3.15)$$

Null suspension stroke refers to the nominal position, which is given by the static equilibrium under the weight action. Then, positive and negative strokes refer to rebound and bump, respectively. Rubber stops limit its value at $\Delta z_{\text{stop,bump}} = -0.140$ m in bump, and $\Delta z_{\text{stop,rebound}} = 0.02$ m in rebound, respectively. The stops are implemented through a lumped stiffness ($k_{\text{stop}} = 10^7$ N/m) providing force only when the stop is hit. Therefore, the stop force is written as:

$$F_{\text{stop}} = \begin{cases} (\Delta z_{\text{susp}} - \Delta z_{\text{stop,bump}}) k_{\text{stop}} & \text{if } \Delta z_{\text{susp}} - \Delta z_{\text{stop,bump}} \leq 0 \\ (\Delta z_{\text{susp}} - \Delta z_{\text{stop,rebound}}) k_{\text{stop}} & \text{if } \Delta z_{\text{susp}} - \Delta z_{\text{stop,rebound}} \geq 0 \\ 0 & \text{otherwise} \end{cases} \quad (3.16)$$

The inputs of the model are the propulsion/braking force F_{prop} , the actuator force F_{act} , and the road profile z_r . The latter is then reported at the front $z_{r,f}$ and rear $z_{r,r}$ wheels as follows

$$z_{r,f} = z_r(t) \quad (3.17)$$

$$z_{r,r} = z_r(t + \Delta t) \quad (3.18)$$

where the rear profile is time delayed by considering the motorcycle wheelbase and traveling speed v :

$$\Delta t = \frac{l_f + l_r}{v} \quad (3.19)$$

Road profile Two road profile scenarios can be considered: road unevenness and lumped obstacle such as bump or pothole.

Table 3.3: Standardized displacement PSD (G_d) and road-roughness index (G_r) [90].

Road class	Description	G_d [m ³ /cycle]	G_r [m · cycle]
A	Very good	$1.6 \cdot 10^{-5}$	$1.6 \cdot 10^{-7}$
B	Good	$6.4 \cdot 10^{-5}$	$6.4 \cdot 10^{-7}$
C	Average	$25.6 \cdot 10^{-5}$	$25.6 \cdot 10^{-7}$
D	Poor	$102.4 \cdot 10^{-5}$	$102.4 \cdot 10^{-7}$
E	Very poor	$409.4 \cdot 10^{-5}$	$409.4 \cdot 10^{-7}$

The former is a random profile usually described as stationary Gaussian stochastic process of a given displacement PSD, which is used to derive the following low-pass filter [83]:

$$H_r(s) = \frac{2\pi\sqrt{G_r}v}{s + \omega_0} \quad (3.20)$$

where s is the Laplace variable, G_r the road roughness index in m · cycle, v the motorcycle speed in m/s, and ω_0 a cutoff frequency needed to limit the displacement at vanishing frequency values. The latter is set to $2\pi v/\lambda_0$ to cut contributions coming from unevenness spatial periods larger than $\lambda_0 = 100$ m.

The road profile z_r is then synthesized by filtering a unit-power white noise. Table 3.3 reports the standardized road-roughness coefficients, where the smoothness increases moving towards grade A. These are extracted from the ISO 8608 standard, which reports the displacement PSD (G_d) for diverse road conditions [90]. Then, the road roughness index is obtained as:

$$G_r = \frac{G_d}{n_0^w} \quad (3.21)$$

where $n_0 = 0.1$ cycle/m is the reference spatial frequency and $w = 2$ the exponent of the fitted PSD [90].

The lumped obstacle is modeled in the spatial domain as shown in Fig. 3.8. The reported profile is normalized, it is then multiplied by the amplitude A_{obstacle} to reproduce diverse bump (positive amplitude) or pothole (negative amplitude) scenarios. Then, the road profile z_r in the time domain is obtained by dividing the spatial coordinate x by the traveling speed v .

Actuator control As the actuator is ideal, its exert a force equal to the control command. The latter is computed according to the used control logic. The industrial partner request was to reproduce the conventional shock absorber operation.

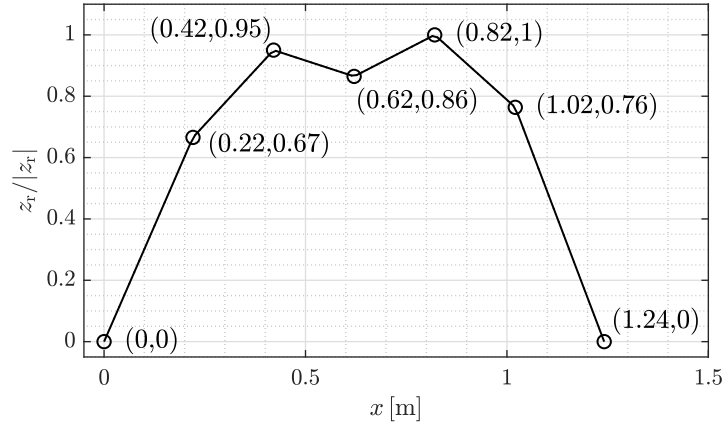


Figure 3.8: Normalized lumped obstacle profile in the spatial domain, which is then multiplied by the amplitude A_{obstacle} to obtain the road scenario.

To this end, simulations were conducted through a control command given by the force that the conventional shock absorber would exert on the suspension:

$$F_{\text{act}} = F_{\text{d,r}}(v_{\text{act}}) \quad (3.22)$$

where $F_{\text{d,r}}$ is the rear damper characteristic (Fig. 3.7b), and the actuator velocity v_{act} is given by the first time-derivative of the suspension stroke (Eq. 3.15). Note that positive and negative values refer to rebound and bump movements of the suspension, respectively.

Outputs of interest The output of this design step are the performance requirements of the REmSA needed for the subsequent design:

- Maximum regenerative damping capability $c_{\text{max,reg}}$. It is the maximum amount of damping that the electric motor can provide in regenerative operation (see Sec. 2.2.1).
- Maximum actuator velocity ($\max(v_{\text{act}})$). It is extracted from the lumped obstacle or the motorcycle acceleration scenario.
- Working points at:
 - Peak actuator force ($\max(F_{\text{act}})$ and $v_{\text{act}}|_{\max(F_{\text{act}})}$) and peak actuator power ($F_{\text{act}}|_{\max(P_{\text{act}})}$ and $v_{\text{act}}|_{\max(P_{\text{act}})}$), where $P_{\text{act}} = F_{\text{act}} \cdot v_{\text{act}}$. These working points represent an overload condition. They are extracted from the lumped obstacle or the motorcycle acceleration scenario.
 - Nominal working point ($\text{rms}(F_{\text{act}})$ and $\text{rms}(v_{\text{act}})$). It is extracted from the road unevenness scenario. It represents a nominal working condition.

If these requirements give an unfeasible design, some limitations must be imposed. Specifically, the regenerative damping could be decreased, or the actuator maximum force and power could be saturated. The latter case would impact vehicle dynamics performance. To this end, some performance indexes must be checked to verify the acceptability of the imposed limitations.

Performance indexes Vehicle performance in terms of ride comfort, road holding and suspension stroke are considered [91].

The acceleration perceived by the driver (or the passenger) is the main source of discomfort. In the present model, the driver's and sprung mass vertical accelerations can be assumed to coincide. Therefore, the latter can be monitored to assess the ride comfort. However, the human perception depends on the acceleration level, frequency and direction. The ISO 2631 [92] indicates the guideline to evaluate the effect of exposure to vibrations on humans. Specifically, the sprung mass acceleration is weighted to account for human perception at diverse vibration frequency. To this end, Zuo and Nayfeh [93] proposed a filter to weights the acceleration time history:

$$H_{2631}(s) = \frac{80.03s^2 + 989s + 0.02108}{s^3 + 78.92s^2 + 2412s + 5614} \quad (3.23)$$

Therefore, the Root Mean Square (RMS) of the filtered sprung mass acceleration ($\ddot{z}_{s,2631}$) is obtained. It can be compared to the six levels of comfort for passenger vehicles proposed by the ISO 2631. Under lumped obstacle scenario, the RMS value is not a representative indicator as the road profile is not a stationary signal. Therefore, the result would depend on the considered time frame. In this scenario, the maximum value can be used as discriminant, although it cannot be compared to the comfort levels of the standard. A rule of thumb is that lower maximum value gives less perception to the driver, although instantaneous acceleration peaks are not indicative of discomfort. In this case, the road holding becomes more important than comfort: vehicle handling must be maintained to avoid dangerous situations.

As the sprung mass acceleration is strongly influenced by the front suspension, a half-vehicle model of the rear of the motorcycle would be more indicated to assess the effectiveness of the active suspension.

Road holding refers to the capability of the vehicle to be controlled during steering, acceleration or braking maneuvers. This turns into good vehicle performance and safety. To this end, sufficient contact force between tire and ground must be guaranteed during dynamic operation. It is given by the superimposition of a static value—given by the static weight supported by the axle—and a dynamic one. The latter could cause a reduction of the contact force and, in some cases, the tire-ground detachment. Hence, the performance is indicated by the road holding index η_{rh} , which is the ratio between dynamic and static force components. In the present

case, it refers to the rear suspension:

$$\eta_{rh,r} = \frac{F_{t,r} + (m_{s,r} + m_{u,r}) g}{(m_{s,r} + m_{u,r}) g} \quad (3.24)$$

The tire-ground contact force includes, in the present model, the static weight. The latter must be deducted to obtain the dynamic component (the tire-ground contact force is negative).

The lowest the index, the better the performance since former contact is guaranteed in all the dynamics conditions. Also in this case, the RMS value can be extracted. Under lumped obstacle scenario, the maximum value can be considered. Unitary road holding index should be avoided as it represents the tire-ground detachment condition.

The suspension stroke is considered as a performance index since excessive value could lead to hit the bump stops with consequently deterioration of ride comfort and possible structural damage [94, 19]. The suspension stroke is given by Eq. 3.15.

Results For the analysis, the maximum regenerative damping capability was set to $c_{\max,reg} = 40$ kNs/m. It is implemented by saturating the maximum slope of the damping characteristic in Eq. 3.22. In this way, the investigation focuses on the vehicle performance when the maximum damping is fully provided in regenerative mode. Note that values of 80 kNs/m results from the maximum damping characteristic of the conventional damper. In case, the REmsA can attain such damping levels by providing active power.

The actuator control (Eq. 3.22) considers three damping characteristics: maximum damping, minimum damping and mixed characteristic. The latter features maximum damping in rebound and minimum damping in bump.

Three scenarios are simulated:

- ISO B road unevenness with 70 km/h cruise speed. Simulation time of 30 s is considered to account for dynamics well below the lowest natural frequency of the system (the undamped pitch mode occurs at 1.8 Hz). For demonstration purposes, the time history of the road profile z_r —which is the disturbance input of the system—is shown in Fig. 3.9a. Figs. 3.9b and 3.9c show the actuator force (F_{act}) and velocity (v_{act}), respectively, when the actuator control reproduces the mixed damping characteristic.

Table 3.4 reports the output of the simulation for the three actuator control damping cases. Larger suspension damping makes the cruise less comfortable but limits the suspension stroke. The latter keeps below the stop bounds in all the three damping cases. Actuator force increases with large damping, while lower velocity values are achieved. The RMS actuator power is comparable in the three cases.

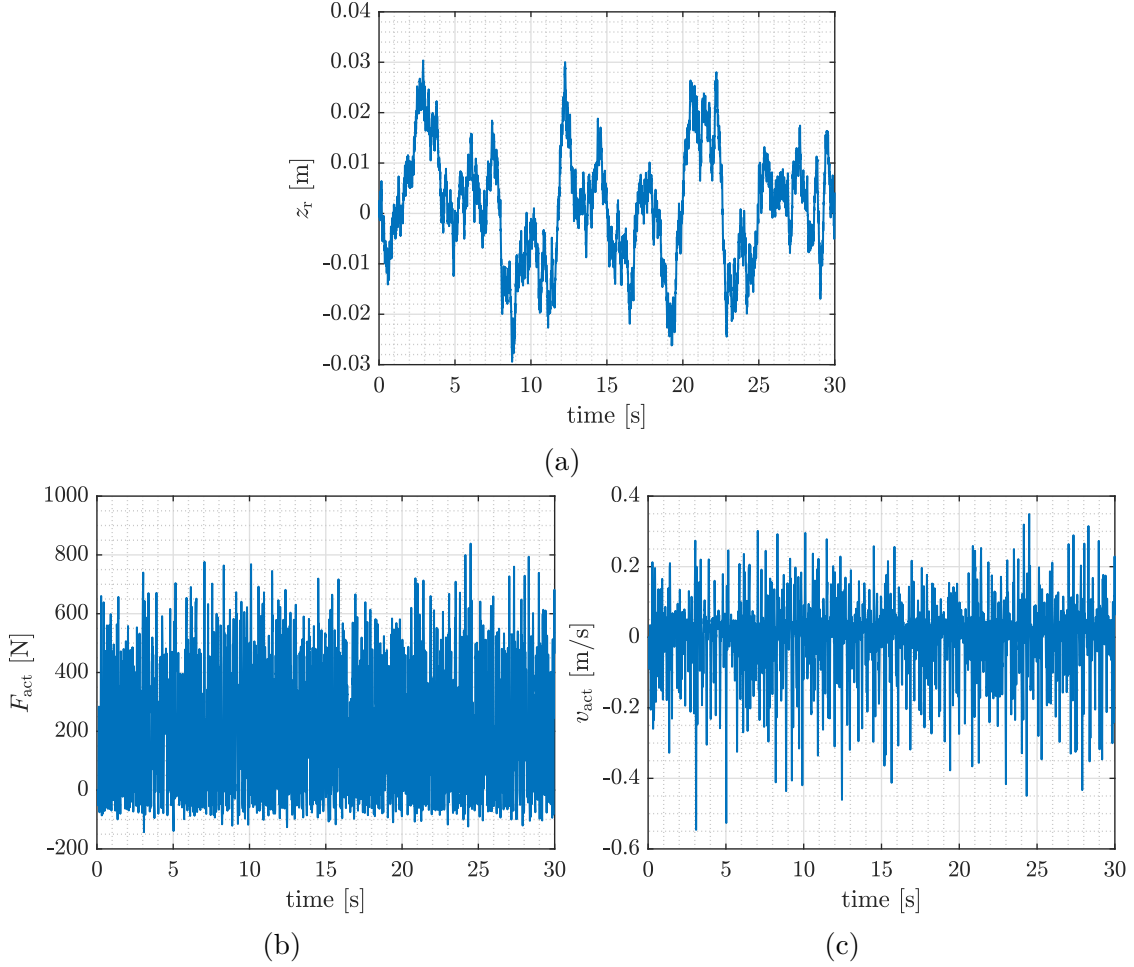


Figure 3.9: ISO B road unevenness with 70 km/h cruise speed: road profile (a), actuator force (b), actuator velocity (c).

- Lumped obstacle at diverse cruise speed values and obstacle amplitudes. Simulation time of 2 s is considered to finish the transient response of the system. Simulations are run at diverse obstacle amplitude $A_{obstacle}$ and motorcycle speed values v . Specifically, the normalized lumped obstacle (Fig. 3.8) is multiplied by the amplitude to obtain the road profile in the spatial domain. Then, the motorcycle speed is used to convert the profile to the time domain. From the obtained time responses, the time instants corresponding to the peak actuator force and power (in absolute value) are found. Then, the actuator force and velocity at those time instants are extracted and plotted versus the motorcycle speed at the diverse obstacle amplitudes. This procedure is repeated for the three actuator control conditions. The mixed damping results are reported in Figs. 3.10, where the dot markers refer to the output of the diverse simulations, and the dashed lines interpolate such points. In this

Table 3.4: ISO B road unevenness with 70 km/h cruise speed results for the three actuator control damping cases.

Description	Symbol	Value		
		Control damping case		
		max	min	mix
Road holding index	$\text{rms}(\eta_{\text{rh,r}})$	0.26	0.26	0.25
Comfort index	$\text{rms}(\ddot{z}_{\text{s},2631})$	0.14 g	0.11 g	0.13 g
Suspension stroke (peak)	$\max(\Delta z_{\text{susp}})$	−15 mm	−21 mm	−19 mm
Actuator force (RMS)	$\text{rms}(F_{\text{act}})$	290.8 N	149.3 N	300.5 N
Actuator velocity (RMS)	$\text{rms}(v_{\text{act}})$	0.09 m/s	0.16 m/s	0.1 m/s
Actuator power (RMS)	$\text{rms}(P_{\text{act}})$	35.7 W	34.6 W	37.4 W

case, the maximum force working points coincide with the maximum power ones. Note that the actuator force and velocity in pothole condition (negative amplitude) decrease above a certain motorcycle speed. In fact, the obstacle is passed quickly and the suspension does not have enough time to reach large extension velocities and, consequently, actuator force values.

Furthermore, it can be observed that the peak force occurs in extension both in the pothole and bump scenarios for most of the motorcycle speed. This result is counter-intuitive, as the bump implies quick compression of the suspension, hence one would expect peak force during the compression stroke. Nevertheless, two aspects must be considered. Figs. 3.11 support the explanation, where the time histories of road profile (a), tire-ground contact force (b), actuator force (c) and velocity (d) are shown. The results refer to the 50 mm pothole at 50 km/h with mixed damping characteristic. First of all, the characteristic used for the actuator control features larger rebound damping and force than the compression ones. Secondly, after the bump climb, the wheel experiences wheel-ground detachment (null contact force). This implies a quick extension of the suspension under the effect of the compressed spring.

Overall, the analysis outputs are reported in Table 3.5 for the three actuator control damping cases. The peak actuator force, power, and velocity occur at 50 km/h motorcycle speed and pothole with 50 mm amplitude. This condition makes the suspension hit the rebound stop. Large damping results in larger actuator force and lower velocities, as can be seen by comparing the maximum and minimum damping results. The peak velocity occurs during the bump of the suspension (negative velocity value), while the peak force working points

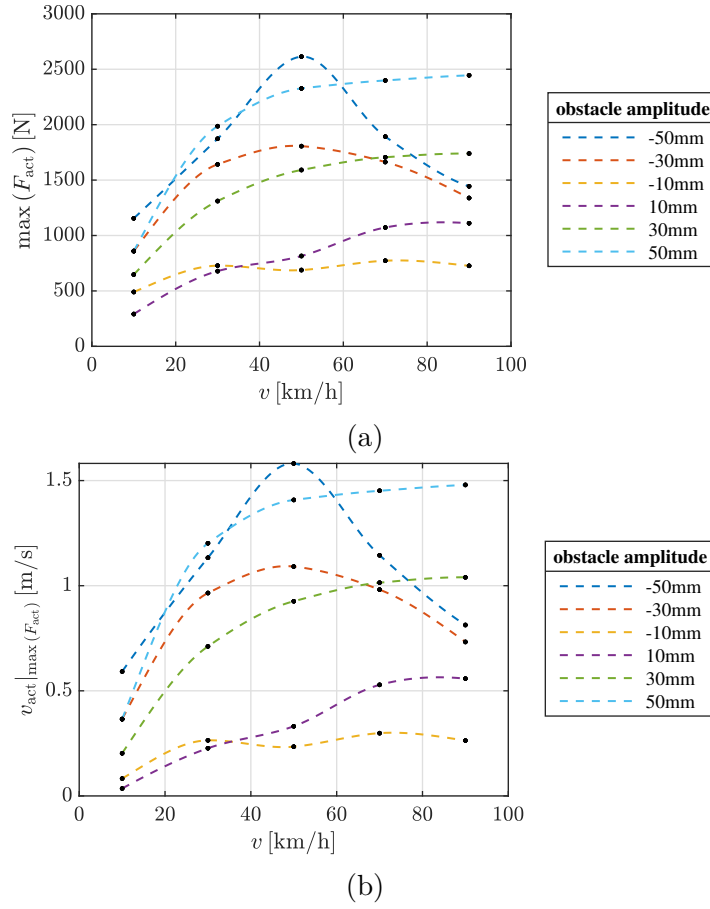


Figure 3.10: Results for the lumped obstacle scenario simulated at diverse cruise speed values and obstacle amplitudes with mixed damping characteristic: maximum actuator force (a) and corresponding velocity (b). Dot markers are the simulated points, dashed lines interpolate such points.

occur during the rebound (positive force value).

- Smooth road with the motorcycle accelerating at $a_x = 0.9 g$. This corresponds to a propulsion force given by

$$F_{\text{prop}} = (m_s + m_{u,f} + m_{u,r}) a_x \quad (3.25)$$

Fig. 3.12 reports the suspension stroke when the the actuator control implements the mixed damping characteristic. After an initial transient, the system reaches steady conditions.

Simulations are repeated for the three damping cases, whose results are reported in Table 3.6. Peak velocity occurs during the compression of the suspension, which is forced by the motorcycle acceleration. Maximum damping characteristic features high damping in compression, which reduces the

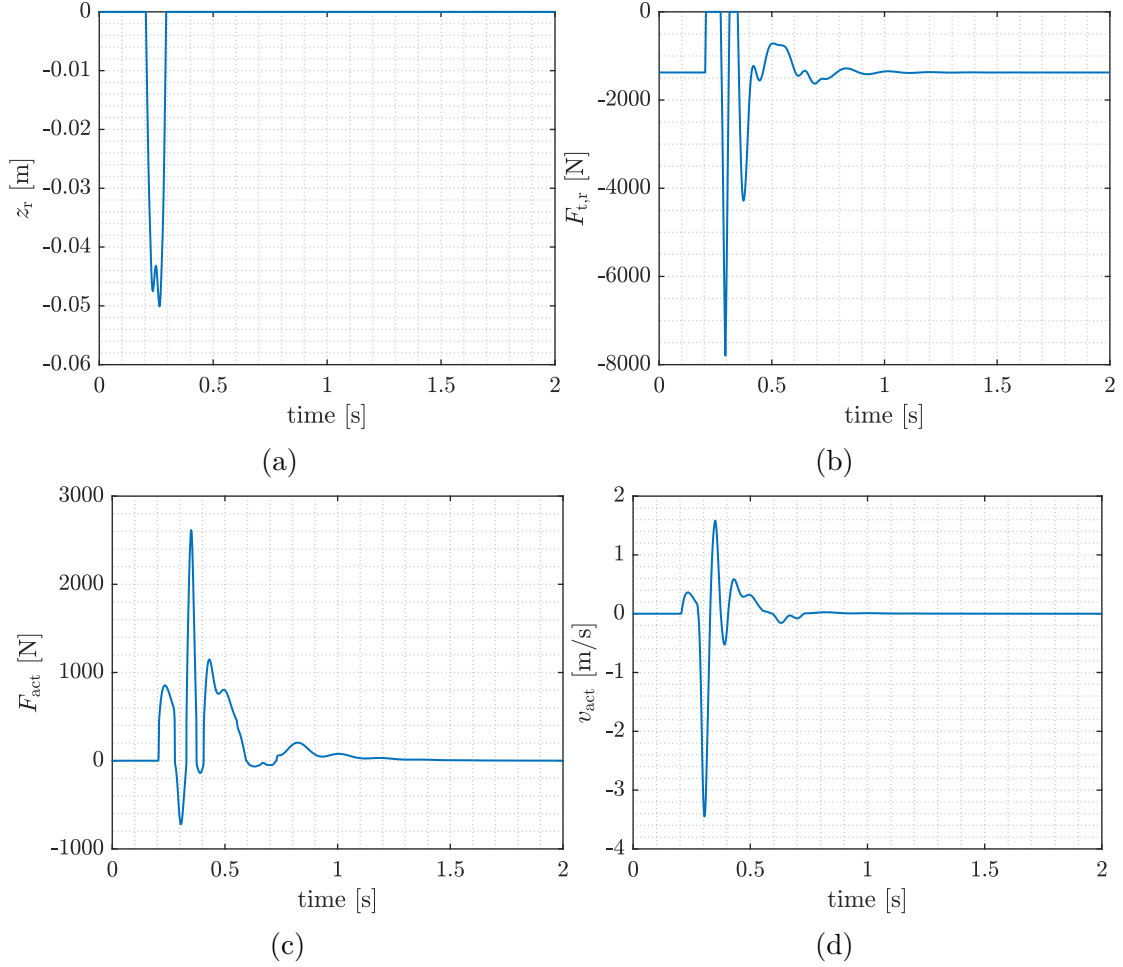


Figure 3.11: Results of the 50 mm pothole at 50 km/h scenario with mixed damping characteristic. Road profile (a), tire-ground contact force (b), actuator force (c) and velocity (d).

suspension stroke. The minimum and mixed characteristics feature minimum damping in compression, hence they achieve the same suspension stroke. The peak force occurs during the suspension extension. This is due to the characteristics, which feature large damping in rebound.

The present step considered a control logic aimed at reproducing the conventional damping characteristic. However, other control strategies could be adopted (Sec. 4).

Among all the results, the most demanding performance requirements are extracted, which are needed for the subsequent design. These are resumed in Table 3.7. Note that the acceleration scenario is far less demanding than the lumped obstacle one. For this reason, the latter is considered as overload condition. If

Table 3.5: Maximum outputs of the lumped obstacle simulations—occurring at 50 km/h motorcycle speed and pothole with 50 mm amplitude—for the three actuator control damping cases.

Description	Symbol	Control damping case		
		max	min	mix
Actuator velocity (peak)	$\max(v_{\text{act}})$	−3.2 m/s	−3.3 m/s	−3.4 m/s
Actuator force (peak)	$\max(F_{\text{act}})$	2277 N	2335 N	2614 N
Actuator velocity	$v_{\text{act}} _{\max(F_{\text{act}})}$	1.4 m/s	1.6 m/s	1.6 m/s
Actuator power (peak)	$\max(P_{\text{act}})$	4253 W	3770 W	4133 W
Actuator force	$F_{\text{act}} _{\max(P_{\text{act}})}$	−1343 N	2335 N	2614 N
Actuator velocity	$v_{\text{act}} _{\max(P_{\text{act}})}$	−3.2 m/s	1.6 m/s	1.6 m/s

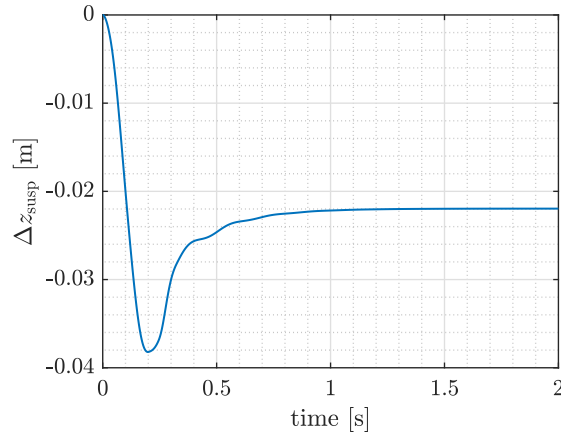


Figure 3.12: Suspension stroke result when the motorcycle accelerates at $a_x = 0.9g$ on smooth road. The mixed damping characteristic is used.

the obtained requirements are too demanding and produce unfeasible design, this step must be repeated by limiting the ideal actuator performance. Then, the performance indexes must be checked to assess if the introduced limitations lead to acceptable performance.

Table 3.6: Results of the motorcycle accelerating at $a_x = 0.9$ g on smooth road for the three actuator control damping cases.

Description	Symbol	Value		
		Control damping case		
		max	min	mix
Actuator velocity (peak)	$\max(v_{\text{act}})$	-0.3 m/s	-0.3 m/s	-0.3 m/s
Actuator force (peak)	$\max(F_{\text{act}})$	482 N	279 N	586 N
Actuator velocity	$v_{\text{act}} _{\max(F_{\text{act}})}$	0.1 m/s	0.2 m/s	0.2 m/s
Actuator power (peak)	$\max(P_{\text{act}})$	66 W	56 W	91 W
Actuator force	$F_{\text{act}} _{\max(P_{\text{act}})}$	-242 N	279 N	586 N
Actuator velocity	$v_{\text{act}} _{\max(P_{\text{act}})}$	-0.3 m/s	0.2 m/s	0.2 m/s

Table 3.7: Performance requirements in nominal and overload conditions

Description	Symbol	Value
Maximum regenerative damping	$c_{\text{max,reg}}$	40 kNs/m
Actuator force (RMS)	$\text{rms}(F_{\text{act}})$	300 N
Actuator velocity (RMS)	$\text{rms}(v_{\text{act}})$	0.1 m/s
Actuator power (RMS)	$\text{rms}(P_{\text{act}})$	37.4 W
Actuator velocity (peak)	$\max(v_{\text{act}})$	-3.4 m/s
Actuator force (peak)	$\max F_{\text{act}}$	2614 N
Actuator velocity	$v_{\text{act}} _{\max(F_{\text{act}})}$	1.6 m/s
Actuator power (peak)	$\max(P_{\text{act}})$	4253 W
Actuator force	$F_{\text{act}} _{\max(P_{\text{act}})}$	-1343 N
Actuator velocity	$v_{\text{act}} _{\max(P_{\text{act}})}$	-3.2 m/s

3.3.2 Optimization

This step aims at optimizing the REmsA sub-components starting from the constraints and performance requirements defined in the first step of the methodology.

Linkage optimization

The best linkage in terms of transmission ratio and transmission quality is searched for. In fact, small linkage transmission ratio τ_l relieves gearbox requests (Eq. 3.3), thus allowing a more compact solution. To this end, an optimization process finds the linkage hardpoints to minimize the linkage transmission ratio while maintaining good transmission quality. The process must fulfill the geometry constraints resulting from the preliminary packaging step (Sec. 3.3.1), which are reported in Table 3.1.

As the estimated four-bar linkage lies in a plane, it is treated as a planar mechanism. Its scheme and geometry constraints are shown in Fig. 3.13. Specifically, the red and green areas are the acceptable domains of hardpoints B and C.

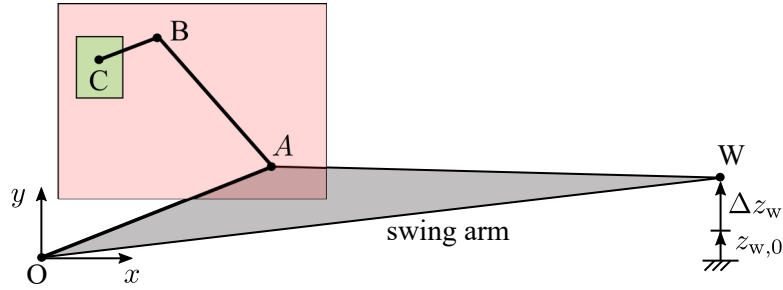


Figure 3.13: Scheme and geometry constraints of the four-bar linkage

The optimization defines the coordinates of hardpoints B and C in the nominal suspension configuration $((x_B, y_B)_{\text{nom}}$ and $(x_C, y_C)_{\text{nom}}$). Coordinates of hardpoints A $(x_A, y_A)_{\text{nom}}$ and W $(x_W, y_W)_{\text{nom}}$ are known from the geometry of the retained motorcycle swing arm (Table 3.8).

In the following, the kinematic equations, constraints and objective functions used in the linkage optimization process are presented.

Kinematics Complex notation is adopted to derive the mathematical description of the linkage kinematics. The reference frame centered in hardpoint O is used.

The planar four-bar linkage features one DOF: the chosen input—which is sufficient to fully define the mechanism—is the wheel travel Δz_w , which coincides with the suspension stroke of the reduced model Δz_{susp} (see Para. 3.3.1). The linkage configuration moves across the wheel travel. Nominal and moved configurations are considered. At first, the nominal configuration must be solved, which is indicated through the subscript *nom* and refers to $\Delta z_w = 0$.

Hardpoint O is connected to the chassis, hence its position does not depend on the wheel travel. The same for hardpoint C, which is located through the vector \vec{OC} . The following relationship can be written:

$$\vec{OC} \equiv \vec{OC}_{\text{nom}} \quad (3.26)$$

Table 3.8: Nominal coordinates of linkage hardpoints

Hardpoint	Coordinate	Nominal value
A	x	218.0 mm
	y	0.9 mm
B	x	design variable [†]
	y	design variable [†]
C	x	design variable [†]
	y	design variable [†]
W	x	572.2 mm
	y	121.7 mm

[†] Set by the optimization every iteration

where $\overrightarrow{OC}_{\text{nom}} = x_C + j y_C$. Conversely, the locations of hardpoints A and W moves with the wheel travel. These are known in the nominal configuration ($\overrightarrow{OA}_{\text{nom}} = x_A + j y_A$ and $\overrightarrow{OW}_{\text{nom}} = x_W + j y_W$), whose nominal coordinates are reported in Table 3.8. From these, the lengths of input link (OA) and swing arm (OW) are computed:

$$l_{OA} = \|\overrightarrow{OA}_{\text{nom}}\| \quad (3.27)$$

$$l_{OW} = \|\overrightarrow{OW}_{\text{nom}}\| \quad (3.28)$$

Also the location of hardpoint B moves with the wheel travel. Its nominal position is expressed by the vector $\overrightarrow{OB}_{\text{nom}} = x_B + j y_B$.

The vectors representing the floating (AB) and output (BC) links in the nominal configuration are obtained as follows:

$$\overrightarrow{AB}_{\text{nom}} = \overrightarrow{OB}_{\text{nom}} - \overrightarrow{OA}_{\text{nom}} \quad (3.29)$$

$$\overrightarrow{BC}_{\text{nom}} = \overrightarrow{OC}_{\text{nom}} - \overrightarrow{OB}_{\text{nom}} \quad (3.30)$$

The link lengths are computed as

$$l_{AB} = \|\overrightarrow{AB}_{\text{nom}}\| \quad (3.31)$$

$$l_{BC} = \|\overrightarrow{BC}_{\text{nom}}\| \quad (3.32)$$

Once the nominal configuration is solved, the moved one can be addressed. Vector \overrightarrow{OA} in the moved configuration is:

$$\overrightarrow{OA} = l_{OA} e^{j\theta_{OA}} \quad (3.33)$$

Angle θ_{OA} is written in function of the input variable Δz_w :

$$\theta_{OA} = \angle \overrightarrow{OA} = \sin^{-1} \left(\frac{\Delta z_w + z_{w,0}}{l_{OW}} + \theta_{OA_{nom}} \right) \quad (3.34)$$

where $\theta_{OA_{nom}} = \angle \overrightarrow{OA}_{nom}$, and $z_{w,0} = \Im(\overrightarrow{OW}_{nom})$ is the wheel vertical position in nominal configuration.

The vectors representing the floating and output links in the moved configuration are obtained as:

$$\overrightarrow{AB} = l_{AB} e^{j\theta_{AB}} \quad (3.35)$$

$$\overrightarrow{BC} = l_{BC} e^{j\theta_{BC}} \quad (3.36)$$

where the link lengths are known from Eqs. 3.31 and 3.32, while angles θ_{AB} and θ_{BC} are obtained by numerically solving the loop closure equation of the mechanism:

$$\overrightarrow{OA} + \overrightarrow{AB} + \overrightarrow{BC} = \overrightarrow{OC} \quad (3.37)$$

It is a vector relationship that gives two equations after being decomposed on the real and imaginary axes. The obtained equations are numerically solved in the unknowns θ_{AB} and θ_{BC} . Note that the loop closure equation depends on the input variable, i.e. the wheel travel.

After the linkage geometry is solved, the angles between input-floating links (λ), and floating-output links (γ) can be computed:

$$\lambda = \theta_{OA} + \pi - \theta_{AB} \quad (3.38)$$

$$\gamma = \theta_{AB} + \pi - \theta_{BC} \quad (3.39)$$

The linkage geometry depends on the wheel travel Δz_w . Hence, it is solved at discrete wheel travel values to explore all the moved suspension configurations. As consequence, angles λ and γ are function of the input variable:

$$\lambda = \lambda(\Delta z_w) \quad (3.40)$$

$$\gamma = \gamma(\Delta z_w) \quad (3.41)$$

Furthermore, the linkage transmission ratio—which is also function of the wheel travel—can be computed as the first derivative of the angle θ_{BC} with respect to the suspension travel:

$$\frac{1}{\tau_1(\Delta z_w)} = \frac{d}{d\Delta z_w} \theta_{BC}(\Delta z_w) \quad (3.42)$$

Note that at the beginning of the process, the nominal configuration must be solved to define all the required parameters. Then, it is solved at the diverse wheel travel positions Δz_w .

Objective functions The objective functions aims at minimizing the transmission ratio τ_1 along the whole suspension stroke by maintaining a good transmission quality. The first goal is represented by the objective function $F_{obj,1}$:

$$F_{obj,1} = w_{\tau_1} \frac{\tau_{1,nom}}{\tau_{1,lim}} + (1 - w_{\tau_1}) \frac{\sigma_{\tau_1}}{\sigma_{\tau_{1,lim}}} \quad (3.43)$$

where $\tau_{1,nom} = \tau_1(\Delta z_w = 0)$ is the nominal transmission ratio and σ_{τ_1} its standard deviation. They are normalized by means of the maximum allowed values $\tau_{1,lim}$ and $\sigma_{\tau_{1,lim}}$, which are defined by the user. In the present design, $\tau_{1,lim} = 350$ mm/rad and $\sigma_{\tau_{1,lim}} = 20$ mm/rad are considered. Coefficient w_{τ_1} moves the optimization towards the minimization of the nominal transmission ratio or its variation along the wheel travel. It was set to one as the considered geometry does not involve large transmission ratio variations.

The transmission quality is indicated by transmission angles γ and λ , which are most favorable when equal to 90 deg [95, 96]. Far from this value, self-locking issues and large unwanted reaction at the joints can occur. Specifically, axial reactions on the input and output links could be generated. Such reactions do not contribute to the transmission as they are absorbed by the joints. This could lead to large forces that need proper structural sizing of the linkage components. To this end, the second objective function aims at minimizing the maximum variation of the transmission angles with respect to the optimal value:

$$F_{obj,2} = \left[\left(\max_{\Delta z_w} \gamma(\Delta z_w) - \pi/2 \right)^2 + \left(\min_{\Delta z_w} \gamma(\Delta z_w) - \pi/2 \right)^2 \right] + \left[\left(\max_{\Delta z_w} \lambda(\Delta z_w) - \pi/2 \right)^2 + \left(\min_{\Delta z_w} \lambda(\Delta z_w) - \pi/2 \right)^2 \right] \quad (3.44)$$

Constraints The optimization process finds the location of hardpoints B and C. These are constrained to be in the domains defined during the preliminary packaging to avoid interference with the suspension components (see Sec. 3.3.1). Upper and lower bounds of the x and y coordinates of hardpoints B and C are reported in Table 3.1.

Geometry and performance constraints are implemented in the form of non-linear inequalities. These are indicated as $g_{c,i}$. Transmission angles λ and γ must be close to 90 deg to avoid mechanism self-locking. The literature indicates the range 40 deg to 140 deg as acceptable to avoid such issue. This turns into a ± 50 deg variation with respect to 90 deg. Therefore, the first set of constraints is defined as follows:

$$g_{c,1} = \left| \max_{\Delta z_w} \lambda(\Delta z_w) - \pi/2 \right| - \Delta \lambda_{lim} \leq 0 \quad (3.45)$$

$$g_{c,2} = \left| \max_{\Delta z_w} \gamma(\Delta z_w) - \pi/2 \right| - \Delta \gamma_{lim} \leq 0 \quad (3.46)$$

where $\Delta\lambda_{\text{lim}}$ and $\Delta\gamma_{\text{lim}}$ are 50 deg.

The second set of constraints regards the linkage transmission ratio. The latter is upper bounded to restrict the number of possible solutions:

$$g_{c,3} = \tau_{1,\text{nom}} - \tau_{1,\text{lim}} \leq 0 \quad (3.47)$$

where $\tau_{1,\text{lim}}$ was defined in Eq. 3.43. Furthermore, the transmission ratio is constrained so that it cannot change sign along the wheel travel:

$$g_{c,4} = -\min_{\Delta z_w} \tau_1(\Delta z_w) \leq 0 \quad (3.48)$$

Finally, the last constraint sets a lower bound to the length of the output link (l_{BC}). Large transmission ratio requires short output link. A too small value could lead to unfeasible link or difficulties in mounting the link in the REmSA prototype. Therefore, the following constraint is defined:

$$g_{c,5} = l_{\text{BC}} - l_{\text{BC},\text{min}} \leq 0 \quad (3.49)$$

where $l_{\text{BC},\text{min}}$ is set to 45 mm.

Optimization The optimization problem is multiobjective, as two objective functions are defined (Eqs. 3.43 and 3.44). It is described by

$$\begin{aligned} & \min \{F_{\text{obj},1}(\mathbf{X}), F_{\text{obj},2}(\mathbf{X})\} \\ & \text{s.t. } g_{\text{obj},i}(\mathbf{X}) \leq 0, \quad i = 1, \dots, 5 \\ & \quad \mathbf{X}_L \leq \mathbf{X} \leq \mathbf{X}_U \end{aligned} \quad (3.50)$$

where $F_{\text{obj},i}$ are the objective functions (Para. 3.3.2), and $g_{\text{obj},i}$ the non-linear constraints (Para. 3.3.2). $\mathbf{X} = [x_B, y_B, x_C, y_C]^T$ is the vector of the design variables, which contains the coordinates $(x_B, y_B)_{\text{nom}}$ and $(x_C, y_C)_{\text{nom}}$. These refer to the nominal suspension configuration ($\Delta z_w = 0$). \mathbf{X}_L and \mathbf{X}_U are the lower and upper bounds of \mathbf{X} defined in Para. 3.3.2).

Afshari *et al.* proposed a review of constrained multi-objective optimization problems [97]. In general, three strategies are commonly adopted. The first uses a linear combination of the objective functions by defining weighting coefficients. The optimal set that minimizes the defined linear combination is unique and the Pareto front is drawn by varying the weighting coefficients. However, no criterion to define the weights introduces further uncertainty in the results. The second strategy is to consider all but one objective functions as constraints. Consequently, the problem is mono-objective and the Pareto front is drawn by repeating the procedure for different combinations of objective functions. The last strategy considers all the objective functions together. As result, multiple optimal sets are obtained, where each set gives a point on the Pareto front.

The last case is mainly used within heuristics and evolutionary strategies, which exploit some form of trial-and-error to find a good solution to an optimization problem. Among these, GA seems to be the most successful approach [98].

Within the proposed framework, part of the first strategy is adopted to limit the number of objective functions. Specifically, functions $F_{\text{obj},1}$ and $F_{\text{obj},2}$ are given by linear combinations of performance indexes with user-defined weights (Eqs. 3.43 and 3.44). Then, the multiobjective optimization is solved through the third strategy, which finds the Pareto front related to the two defined objective functions. To this end, evolutionary GA is used. The process is implemented in Matlab environment, which provides the function *gamultiobj* implementing the multi-objective genetic algorithm.

Results Once the optimization process is tuned, more runs should be carried out. Since the optimization relies on heuristics approach, each run gives different outputs.

The results of the above-described optimization process are reported in Figs. 3.14. Specifically, Fig 3.14a shows the Pareto front in the plane of the objective functions. Among all the optimal solutions, the selection of the best set is demanded to the user. To support this process, Figs. 3.14b and 3.14c are drawn. They plot the nominal transmission angle γ and standard deviation of the transmission ratio versus the nominal transmission ratio. The solution highlighted through the black arrow gives the best trade-off between nominal transmission ratio and transmission angle γ , while featuring small variation of the transmission ratio along the wheel travel, as indicated by the low standard deviation. Therefore, this solution is selected.

To verify and validate the linkage performance, the transmission ratio (Fig. 3.15a) and transmission angles (Fig. 3.15b) are plotted along the whole wheel travel. The transmission angle γ keeps close to 90 deg (70 to 114 deg), while angle λ features values close to the lower bound (50 to 56 deg). This could be improved by unlocking the hardpoint A location. Nevertheless, this constraint cannot be removed as discussed in Sec. 3.3.1.

The nominal transmission ratio and the geometry of the selected linkage configuration are reported in Table 3.9.

Electric machine cross-section optimization

This step optimizes the three-phase PMSM, whose active length is still not defined. For this reason, the optimization focuses on the cross-section: the objective performance is the torque-to-length ratio r_{Tl} :

$$r_{\text{Tl}} = \frac{T_{\text{em}}}{l_{\text{em}}} \quad (3.51)$$

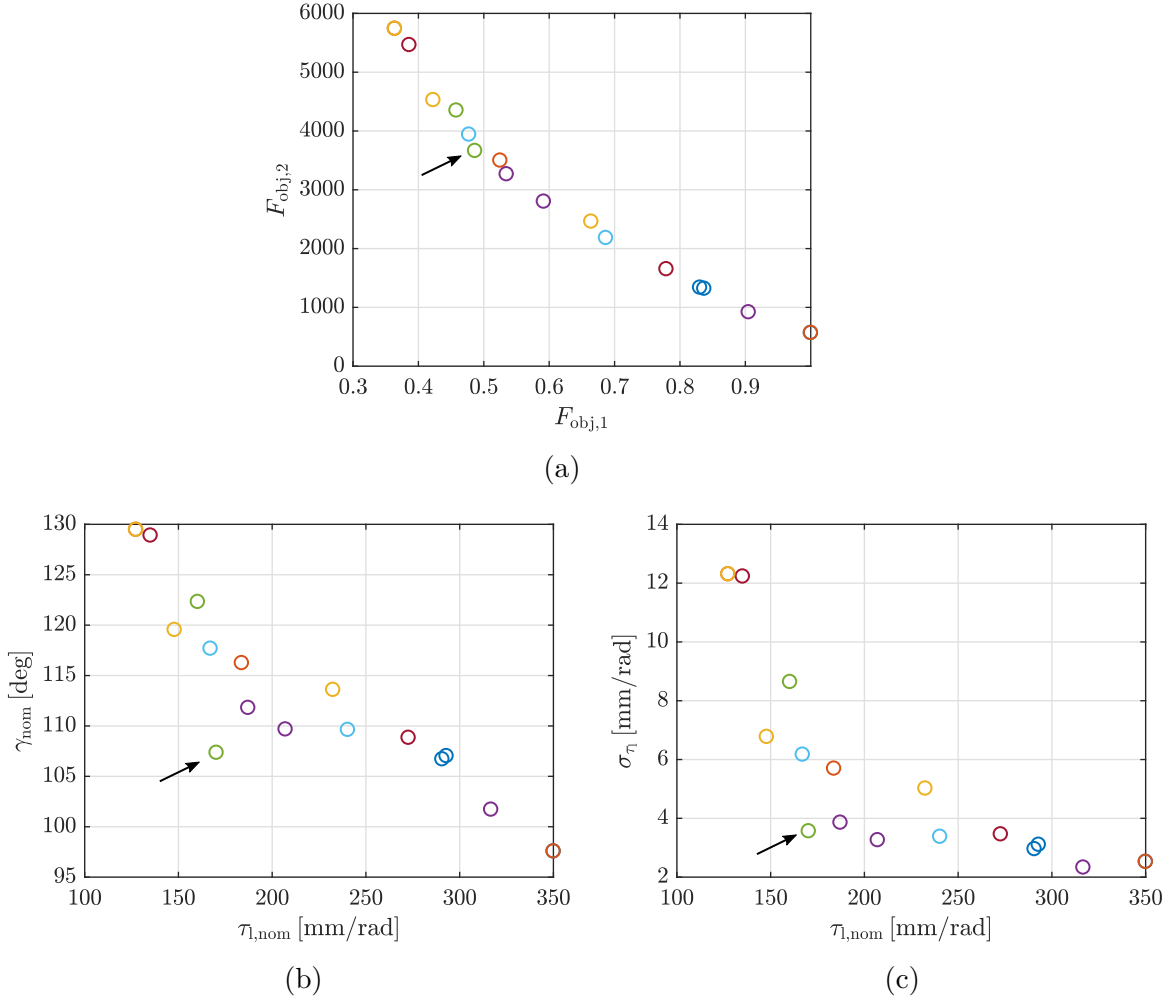


Figure 3.14: Linkage optimization results: Pareto front (a), nominal transmission angle γ vs nominal transmission ratio (b), transmission ratio standard deviation vs nominal value (c). The diverse colors refer to the different solutions, the black arrow indicates the chosen one.

where T_{em} and l_{em} are the electric machine torque and active length, respectively.

Also the electric machine outer diameter is still not defined, as Sec. 3.3.1 returned an approximate outer envelope of the REmSA. The number of slots N_s is varied across the process, while the number of magnets N_m is set to 10: preliminary analyses showed that 10 magnet layouts usually achieve the best torque-to-volume performance for the machine size of interest. Overall, the optimization is run at diverse stator outer radius and number of slots combination to obtain a set of optimized electric machines.

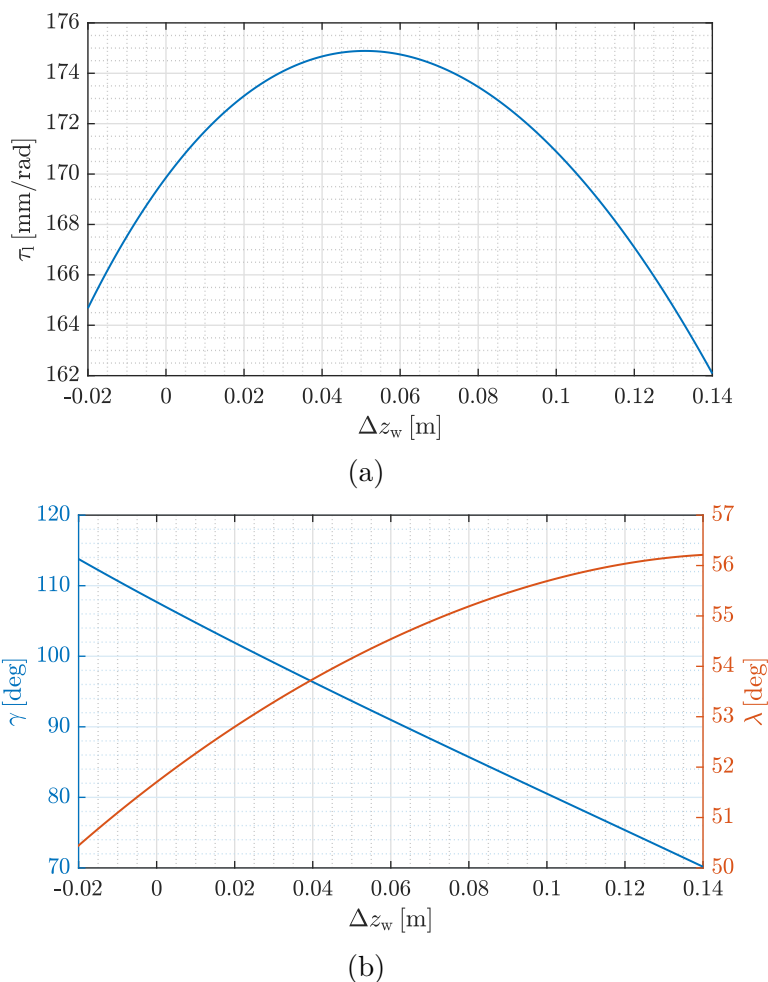


Figure 3.15: Transmission ratio (a) and transmission angles (b) along the wheel travel for the optimized linkage.

Table 3.9: Selected linkage configuration

Description	Symbol	Value
Nominal transmission ratio	$\tau_{1,\text{nom}}$	170 mm/rad
Hardpoint C x-coordinate	x_C	46.6 mm
Hardpoint C y-coordinate	y_C	134.7 mm
Link AB length	l_{AB}	195.3 mm
Link BC length	l_{BC}	53.3 mm

Geometry Fig. 3.16 shows the electric machine cross section, whose geometry is taken by Hanselman’s handbook [99].

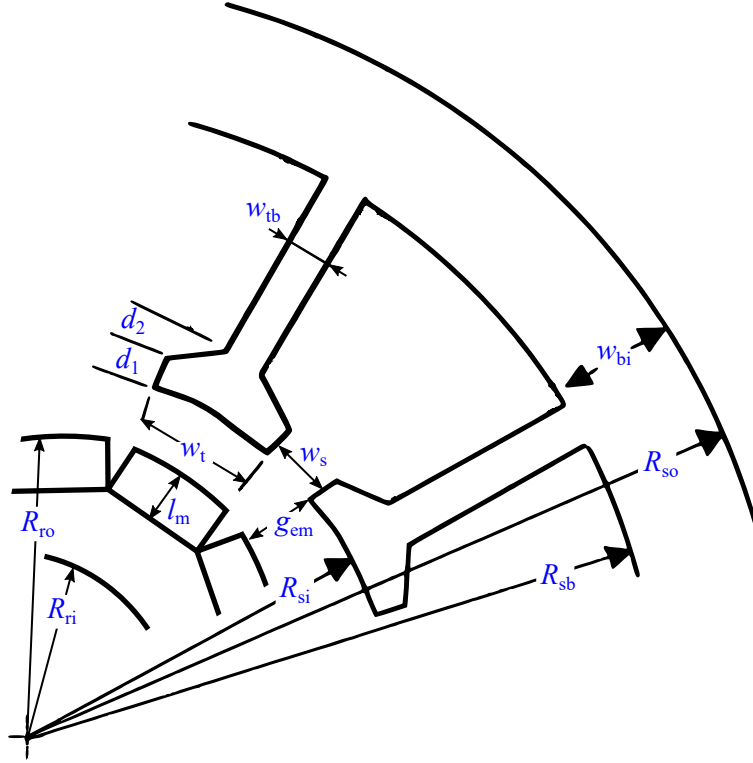


Figure 3.16: Electric machine cross-section geometry

The fixed design parameters are reported in Table 3.10. Specifically, the air gap g_{em} is selected large enough to avoid rotor-stator contact due to possible eccentricity and tolerances. Air gap increase causes performance deterioration. Small slot opening w_s minimizes cogging torque and improves machine performance. Nevertheless, too small value causes flux leakages. The packing factor k_{cp} indicates the portion of slot area occupied by copper. It is upper bounded by the winding manufacturing process. Hand-made windings usually achieve values in the order of $k_{cp} = 0.3$, according to the workshop partnering the present activity. The magnet length l_m yields from considerations on the permeance of the magnet. The latter is written as

$$P_c \approx \frac{l_m}{g_{em}} \quad (3.52)$$

It determines the operating point of the magnet within the electric machine magnetic circuit. The performance optimization requires the magnet to work in the point where its volumetric energy is maximized. If magnets with relative permeability close to one are used, this condition implies unitary permeance. However, such operating condition could cause permanent demagnetization, especially when the magnet temperature increases due to electric machine heating. For this reason, permeance values ranging from 4 to 6 are usually adopted [100]. Permeance

Table 3.10: Fixed design parameters of the electric machine

Description	Symbol	Value
PM remanence	B_r	1.3 T
Magnet length	l_m	2.5 mm
Air gap	g_{em}	0.5 mm
Phase number	N_{ph}	3
Magnet number	N_m	10
Slot opening	w_s	2.0 mm
Slot depth fraction	α_{sd}	0.52
Slot aspect ratio	α_d	1

equal to 5 was chosen in the present application. Hence, 2.5 mm magnet length is obtained from Eq. 3.52.

The parameters tuned through the optimization are the back-iron width (w_{bi}) and the rotor outer radius (R_{ro}). The remaining dimensions can be computed as follows. The tooth width w_{tb} is

$$w_{tb} = 2 \frac{w_{bi}}{N_{sm}} \quad (3.53)$$

where the number of slots per pole $N_{sm} = N_s/2p$ depends on the pole pairs $p = 5$ (because of the 10 magnet configuration).

The shoe width is

$$w_t = \max(\tau_s - w_s, w_{tb}) \quad (3.54)$$

where the slot pitch air gap is

$$\tau_s = \frac{2\pi}{N_s} R_{si} \quad (3.55)$$

and $R_{si} = R_{ro} + g_{em}$ is the stator inner radius. The stator back-iron radius is given by

$$R_{sb} = R_{so} - w_{bi} \quad (3.56)$$

Finally, the shoe dimensions d_1 and d_2 are obtained

$$d_1 = \alpha_{sd} \frac{w_{tb}}{1 + \alpha_d} \quad (3.57)$$

$$d_2 = \frac{d_1}{\alpha_d} \quad (3.58)$$

Model Electromagnetic 2D finite element modeling approach is needed to account for iron magnetic saturation phenomenon and accurately address the machine performance. To this end, the *Rotating Machinery* module of the commercial software COMSOL Multiphysics® is used [101]. The model is reported in Fig. 3.17.

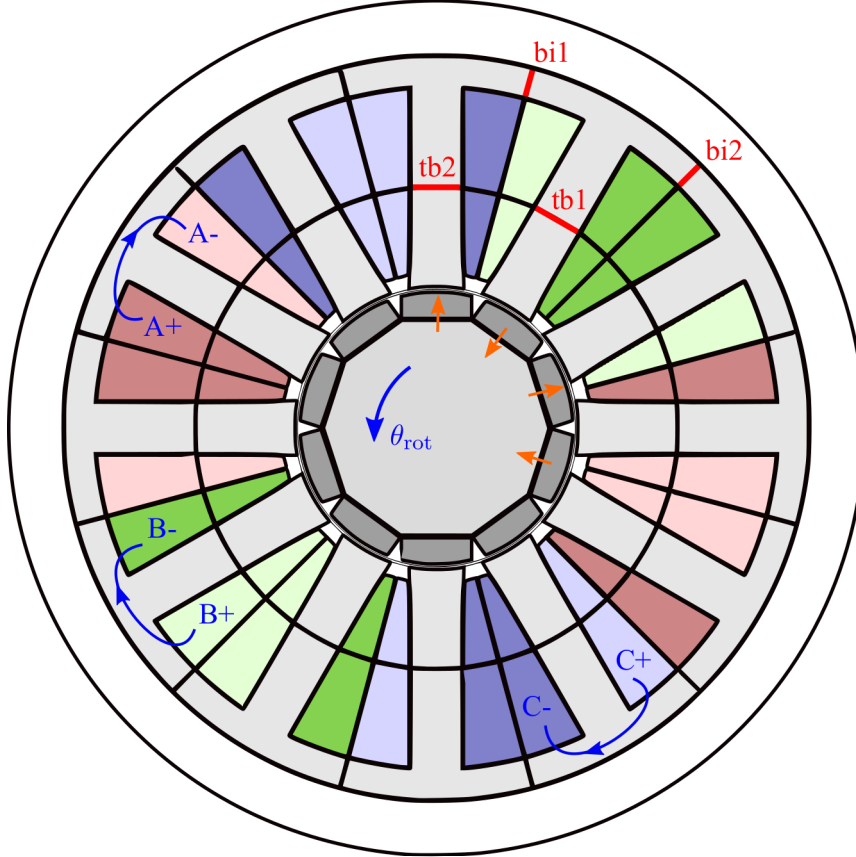


Figure 3.17: Electromagnetic 2D finite element model of the electric machine. The orange arrows show the magnetization direction of the PMs. Red segments are used to probe the flux density in the stator.

The geometry described in Para. 3.3.2 is implemented. Air, copper and PM domains feature the magnetic permeability of vacuum. Additionally, PMs domains have a remanence $B_r = 1.3 \text{ T}$ —characteristic of NdFeB magnets—directed as indicated in Fig. 3.17. The stator and rotor core domains are made of Silicon Steel NGO 35PN270, which features the BH curve reported in Fig. 3.18. Electrical conductivity of such domains is not relevant in the present analysis since static conditions do not involve eddy current phenomena.

The windings current is implemented through external current densities in direction orthogonal to the cross-section to reproduce the three-phase supply. These are schematized in Fig. 3.17, where positive and negative current densities are

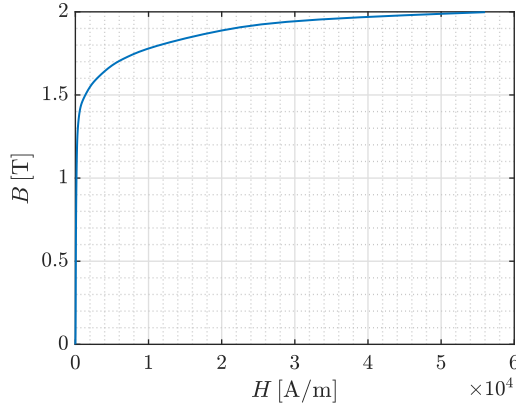


Figure 3.18: Magnetic characteristic of Silicon Steel NGO 35PN270 [101]

represented by means of light and dark colors, respectively: red for phase A, green for phase B, and blue for phase C. The phase current densities are given by:

$$J_A = J_{\text{rms}} \cos(p\theta_{\text{rot}}) \quad (3.59)$$

$$J_B = J_{\text{rms}} \cos\left(p\theta_{\text{rot}} + \frac{2}{3}\pi\right) \quad (3.60)$$

$$J_C = J_{\text{rms}} \cos\left(p\theta_{\text{rot}} + \frac{4}{3}\pi\right) \quad (3.61)$$

where θ_{rot} is the rotor mechanical angle and $p\theta_{\text{rot}}$ the electrical angle. The term J_{rms} is the RMS value of the wire current density. It is set to 6 A/mm^2 , value commonly adopted for nominal operation of totally enclosed electric machines under natural convection conditions [87]. This assumption could be removed by modeling the thermal behavior of the electric machine. However, most of the details are not defined at this stage of the design. Therefore, the thermal model could be done at the end of the design to verify the thermal aspects a posteriori.

Objective function The optimization aims at maximizing the torque-to-length ratio (Eq. 3.51). However, electric machine optimization problems usually focus on the motor constant, which indicates how efficiently the torque is produced [100]. It is directly proportional to the output torque and inversely proportional to the square root of the Joule loss. Therefore, optimizations based on the motor constant result in a trade off between torque output and power loss. Nevertheless, the present activity puts first the compactness of the REmSA. Therefore, the torque output is maximized instead of the motor constant. A direct consequence is that the optimization favours electric machines with large slots to increase the amount of copper. This increases the magnetic flux density in the air gap and, consequently, the generated torque. On the other hand, this causes an increase of Joule loss.

The torque-to-length ratio is computed by integrating the Maxwell's stress tensor over a bound placed at mid air gap (Fig. 3.17).

Fig. 3.19 shows the torque-to-length ratio (a) and the magnetic flux density norm in four diverse stator locations (b), as function of the rotor mechanical angle. One electrical angle revolution is considered. The results refers to the electric machine featuring 85 mm outer stator diameter, 12 slots, $w_{bi} = 3.3$ mm and $R_{ro} = 15.7$ mm. As can be noted, the torque-to-length ratio features a harmonic behavior. This is mainly due to cogging and localized magnetic saturation of the stator iron. The best practice would be to compute the average value across one electrical angle revolution. Nevertheless, this would significantly increase the computational cost of the optimization. In fact, large number of simulations is already required to span the diverse combinations of stator outer radius and number of slots, as well as the optimization variables, i.e. back-iron width (w_{bi}) and rotor outer radius (R_{ro}). For this reason, a single simulation is run at null electrical angle. Within a fixed combination of stator outer radius and number of slots, the maximization of the torque-to-length ratio at the given electrical angle will maximize also its mean value across one electrical angle revolution. This statement holds when no strong saturation conditions occurs.

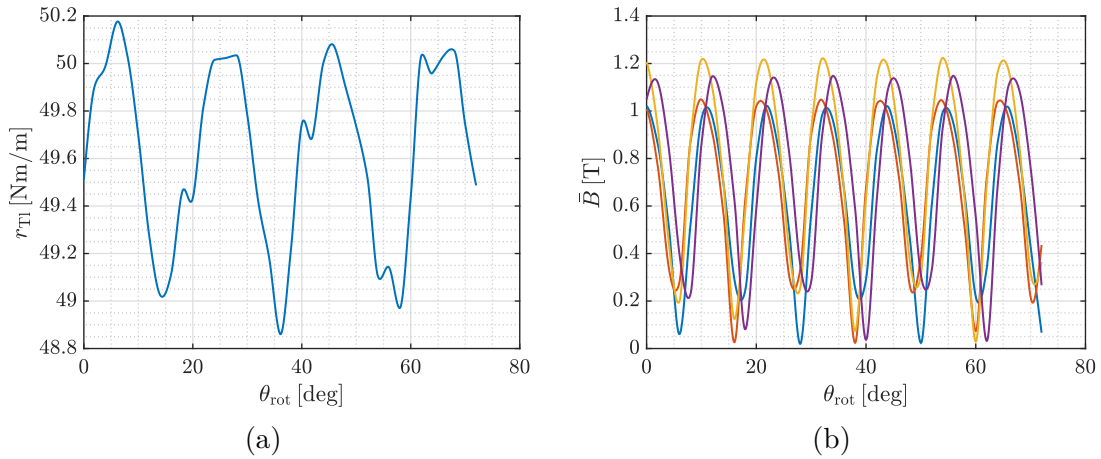


Figure 3.19: Finite element results as function of the rotor mechanical angle for the electric machine featuring 85 mm outer stator diameter, 12 slots, $w_{bi} = 3.3$ mm and $R_{ro} = 15.7$ mm. Torque-to-length ratio (a) and integral averages of the magnetic flux density norm over the probe segments of Fig. 3.17: $\bar{B}_{tb,1}$ (yellow) and $\bar{B}_{tb,2}$ (purple), $\bar{B}_{bi,1}$ (blue) and $\bar{B}_{bi,2}$ (orange).

For demonstration purposes, Fig. 3.20 shows the distribution of the magnetic flux density norm of the electric machine featuring 85 mm outer stator diameter, 12 slots, $w_{bi} = 3.3$ mm and $R_{ro} = 15.7$ mm at null rotor mechanical angle. The electric machine is supplied by considering $J_{rms} = 6$ A. The region close to the probe segments highlighted in Fig. 3.17 exhibits the highest flux density. Nevertheless, norm values smaller than 1.2 T are encountered.

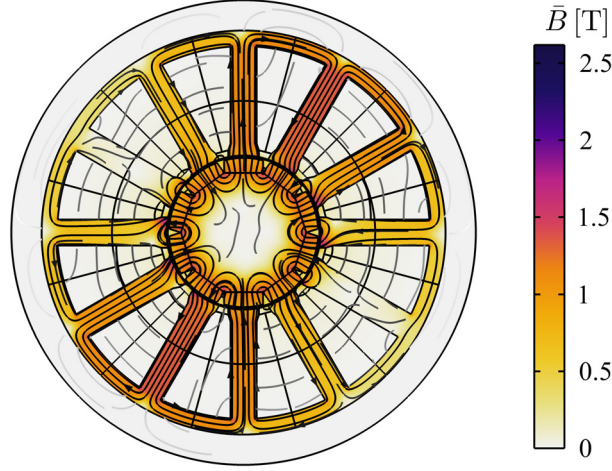


Figure 3.20: Finite element results for the electric machine featuring 85 mm outer stator diameter, 12 slots, $w_{bi} = 3.3$ mm and $R_{ro} = 15.7$ mm. Magnetic flux density norm (colormap) and magnetic vector potential (contour and streamlines).

Constraint The torque maximization tends to increase the slot area and, consequently, decreases the iron domain of the stator. By reducing the cross-sections which the flux flows through, the magnetic flux density increases. Therefore, the limit of the torque maximization is the magnetic saturation of the stator material.

To this end, the maximum flux density in the stator is limited at $B_{max} = 1.2$ T. The norm of the magnetic flux density is computed in some regions that are interested by large field. After some investigations, the segments highlighted in Fig. 3.17 are identified to probe the flux density. Specifically, the integral averages over the probe segments—tooth ($\bar{B}_{tb,1}$ and $\bar{B}_{tb,2}$) and back iron ($\bar{B}_{bi,1}$ and $\bar{B}_{bi,2}$)—are computed and compared to the limit value.

Two aspects must be highlighted. Firstly, the magnetic flux on the stator is mainly caused by the PM remanence. In fact, some design approaches size the stator magnetic circuit with null phase current [100]. The present optimization checks the stator saturation when the windings are supplied, thus resulting in a more precautionary design.

Secondly, the magnetic flux density norm over the probe segments changes in a sinusoidal way with the electrical angle (Fig. 3.19b). The peaks on the tooth and back iron probe segments are reached at different rotor angle. However, tooth and magnet are aligned when the rotor angle is null, which is the configuration reported in Fig. 3.17. This position maximizes the magnetic flux density in the tooth. Then, the flux density in the back iron is always lower because its width was chosen according to Eq. 3.53 [99]. This statement holds if no strong magnetic saturation occurs. Therefore, stator saturation condition is checked at null rotor

angle only, thus avoiding iterative simulations at diverse angular positions.

Optimization approach The optimization process is schematized in Fig. 3.21. Then, the results obtained for the 42.5 mm stator outer radius and 12 slots are reported for demonstration purposes.

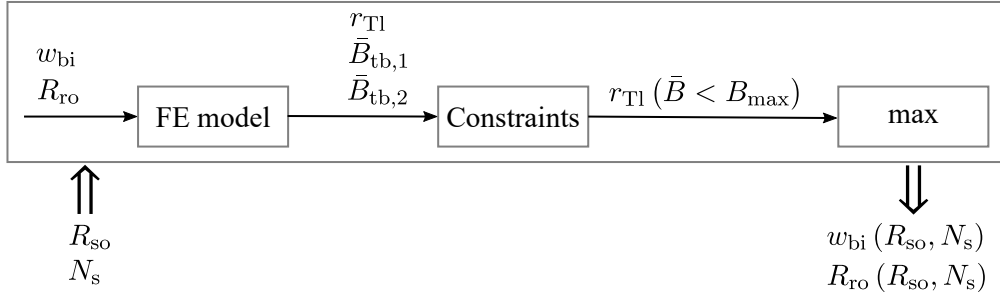


Figure 3.21: Flowchart of the electric machine optimization process

Once the stator outer radius (R_{so}) and slot number (N_s) are set, back iron width (w_{bi}) and rotor outer radius (R_{ro}) are iteratively varied. The obtained geometry is simulated at null rotor angle to obtain the torque-to-length ratio and the average magnetic flux density norm over the probe segments of the stator teeth. The latter are shown in Figs. 3.22a and 3.22b as function of the back iron width and rotor outer radius, for the configuration featuring 42.5 mm stator outer radius and 12 slots. Then, the constraints are applied to restrict the feasible domain. Specifically, back iron width and rotor outer radius combinations that results in magnetic flux density exceeding the limit value B_{lim} are eliminated. The torque-to-length ratio in the remaining domain is extracted (Fig. 3.22c) and its maximum value locates the optimum back iron width and rotor outer radius. The latter are function of the selected stator outer radius and slot number.

Optimization output The optimization process is run at diverse stator outer radius and number of slot combinations to obtain a set of optimized electric machines. Specifically, the stator radius is varied in the range 70 to 115 mm because of the outer envelope of 120 mm defined in the preliminary packaging step (Sec. 3.3.1). The number of slot must be a multiple of the phase number. Therefore, 9 and 12 slot configurations are investigated. More that 12 slots could imply small slot area, thus resulting in difficult winding process.

Fig. 3.23 shows the optimized electric machine parameters and performance as function of the stator outer radius in the two investigated slot configurations. In addition to the rotor outer radius and back iron width, also the half-slot area is computed since it is needed in the subsequent design of the REmSA. Specifically, it is half of the area enclosed in two teeth since it is the space occupied by one coil.

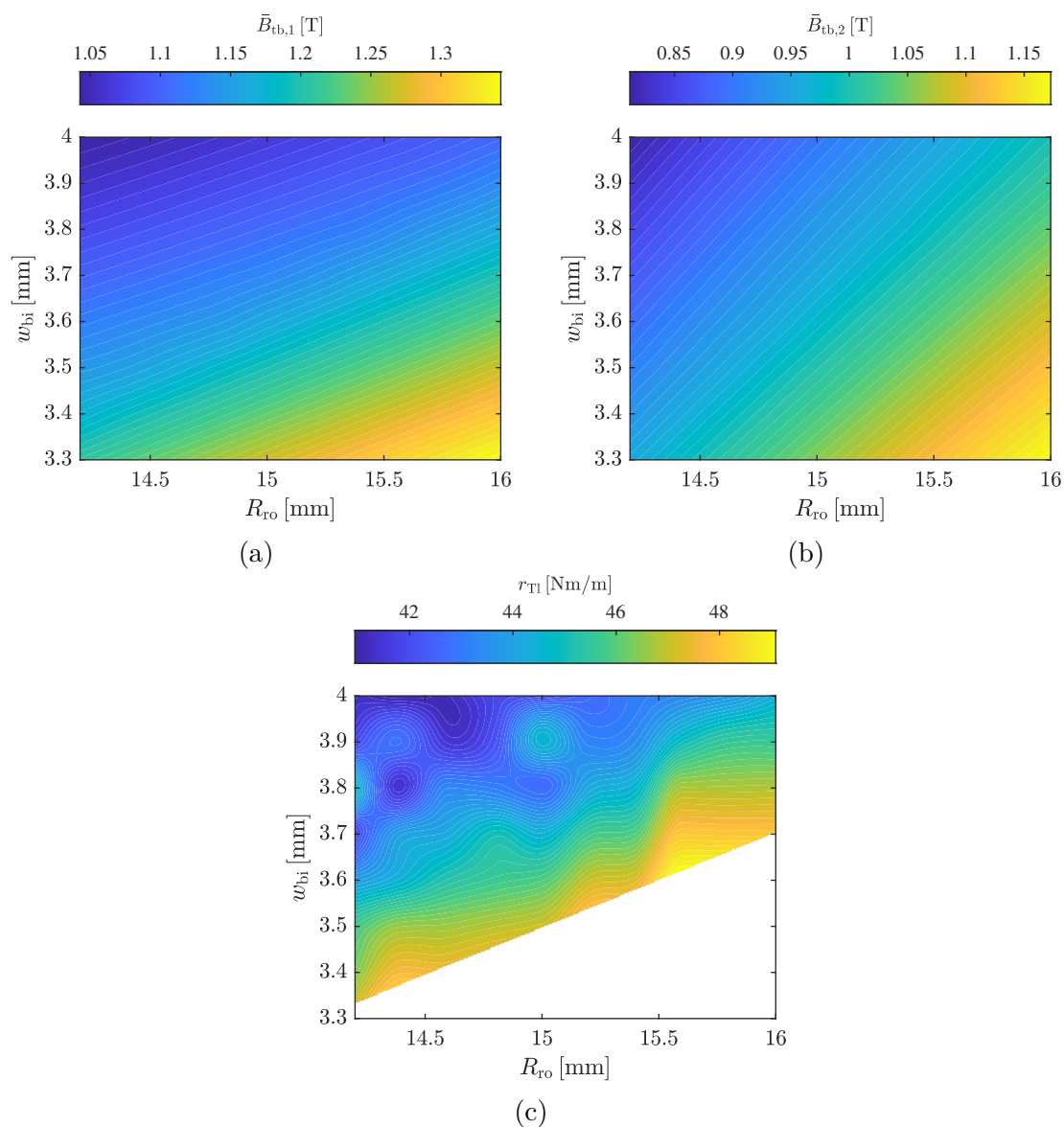


Figure 3.22: Optimization approach: average magnetic flux density norm over the probe segments of the stator teeth (a) and (b), and torque-to-length ratio (c), as function of the back iron width and rotor outer radius. Results for the configuration featuring 42.5 mm stator outer radius and 12 slots. The torque-to-length ratio is evaluated in the domain restricted by the constraints.

These curves feature a quadratic trend. Hence, they can be interpolated through a second-order polynomial in the form $p_2 R_{so}^2 + p_1 R_{so} + p_0$.

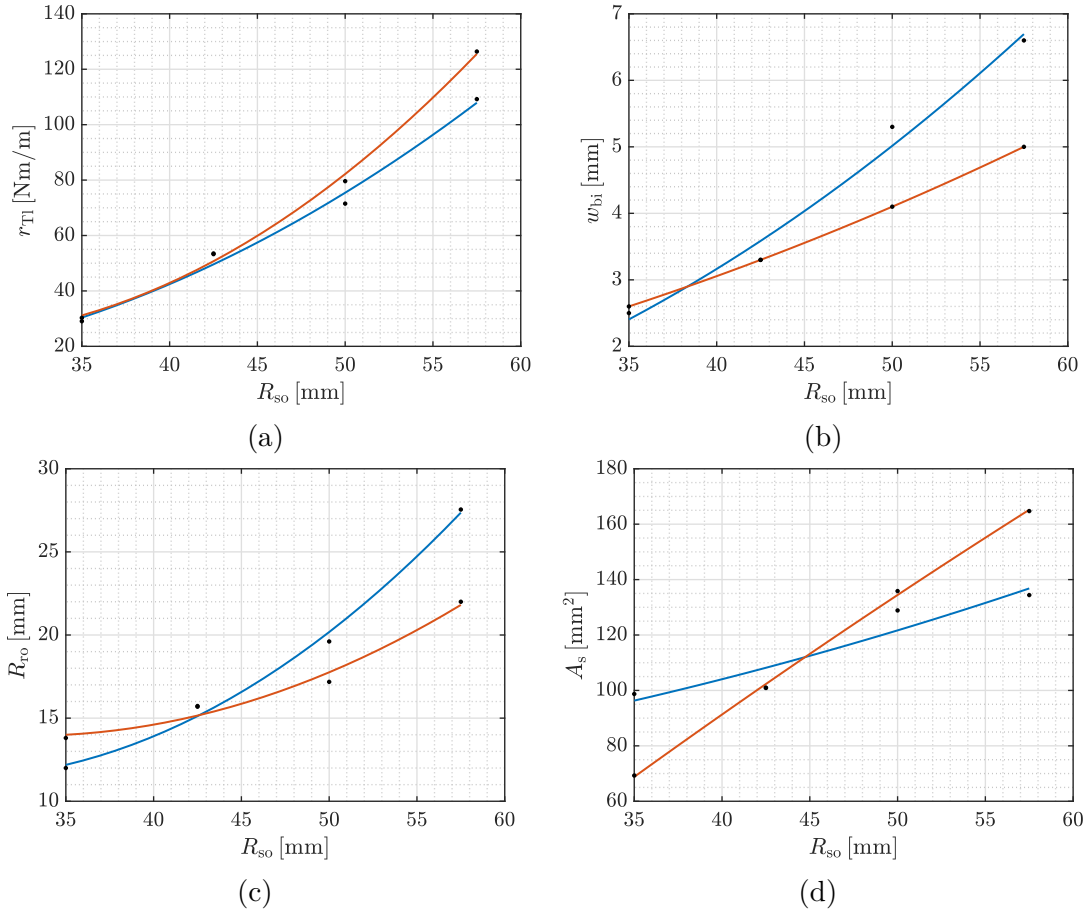


Figure 3.23: Optimized electric machine parameters and performance as function of the stator outer radius in the two investigated slot configurations: $N_s = 9$ (blue) and $N_s = 12$ (orange). Torque-to-length ratio (a), back iron width (b), rotor outer radius (c), and half-slot area (d).

Gearbox and electric machine match

The electric machine and gearbox are matched to minimize a cost function that includes the overall mass and equivalent inertia of the REmSA. Specifically, the electric machine and gearbox outer radius, electric machine active length and gearbox transmission ratio are optimized.

Constraints The first constraint limits the electric machine active length:

$$l_{em} \leq l_{em,max} \quad (3.62)$$

The limit is set to 70 mm by considering packaging constraints. Furthermore, too slender rotor of the electric machine must be avoided because of rotordynamics considerations.

The second constraint bounds the electric machine angular velocity to avoid bearing damage and limit the centrifugal stress of the rotor. The latter could cause the detachment of the surface-mounted PMs. Large angular velocity would require rotor containment sleeves, thus implying additional mechanical complexity. The constraint is formulated as:

$$\omega_{em,max} = \frac{\max(v_{act})}{\tau_t} \quad (3.63)$$

where $\omega_{em,max}$ is the maximum allowed angular velocity of the rotor, set to 2618 rad/s, and $\max(v_{act})$ is the maximum actuator velocity extracted from vehicle dynamics simulation (Table 3.7). Therefore, this constraint sets a lower-bound for the REmSA transmission ratio:

$$\tau_t \geq \frac{\max(v_{act})}{\omega_{em,max}} \quad (3.64)$$

The REmSA must also fulfill the performance specifications reported in Table 3.7. The electric machine output torque can be expressed in function of the electric machine length:

$$T_{em} = r_{Tl} l_{em} \quad (3.65)$$

By combining Eq. 3.4—which relates the actuator force at the wheel level and the electric machine output torque—and Eq. 3.65, the electric machine active length is related to the force request at the wheel level and the overall transmission ratio:

$$l_{em} \geq \frac{F_{act}}{r_{Tl}} \tau_t \quad (3.66)$$

where the inequality is introduced since the electric machine must be large enough to provide at least the requested force.

The torque-to-length ratio r_{Tl} was obtained for an optimized set of electric machines as function of the stator outer radius (Fig. 3.23) with RMS current density amplitude $J_{rms} = J_{nom} = 6 \text{ A/mm}^2$ (Eq. 3.61). The latter is commonly adopted for nominal operation of totally enclosed electric machines under natural convection [87]. Therefore, Eq. 3.66 can be rewritten for the force request in nominal condition:

$$l_{em} \geq \frac{F_{act,nom}}{r_{Tl}|_{J_{nom}}} \tau_t \quad (3.67)$$

Differently, the RMS current density $J_{rms} = J_{oload} = 20 \text{ A/mm}^2$ represents an overload condition that can be withstood for transient periods up to 10s. By assuming electric machine linearity with respect to the supplied current, the torque-to-length ratio in overloading can be computed as:

$$r_{Tl}|_{J_{oload}} = r_{Tl}|_{J_{nom}} \frac{J_{oload}}{J_{nom}} \quad (3.68)$$

This relationship holds since the magnetic flux on the stator is mainly caused by the PM remanence, as mentioned in Para. 3.3.2. Hence, no saturation in nominal condition ensures almost linear behavior also in overloading. Eq. 3.66 can be rewritten for the force request in overload condition:

$$l_{em} \geq \frac{F_{act,oload}}{r_{T1} |J_{nom} \frac{J_{oload}}{J_{nom}}|} \tau_t \quad (3.69)$$

A further constraint is dictated by the maximum regenerative damping. In fact, the electric machine should be able to yield the largest damping coefficient without providing any active power to the system. A shunted brushless PM machine features a well-known electromagnetic torque versus angular speed characteristic [102], which is described by:

$$T_{em} = \frac{K_t K_e \omega_{em}}{(R_{ph} + R_{shunt}) [1 + (p\omega_{em}/\omega_p)^2]} \quad (3.70)$$

where ω_{em} is the rotor angular velocity, K_t and K_e the machine torque and back EMF constants, respectively, R_{ph} its phase resistance and R_{shunt} the load shunting the windings. The electromagnetic pole ω_p is defined by:

$$\omega_p = \frac{R_{ph} + R_{shunt}}{L_{ph}} \quad (3.71)$$

L_{ph} being the machine inductance in d and q axes. At low rotor frequency ($\omega_{em} \ll \omega_p/p$), Eq. 3.70 gives:

$$T_{em} = \frac{K_t K_e}{R_{ph} + R_s} \omega_{em} \quad (3.72)$$

which represents a viscous damping behavior with electromagnetic viscous damping

$$c_{em} = \frac{K_t K_e}{R_{ph} + R_{shunt}} \quad (3.73)$$

The maximum regenerative damping capability coincides with the short circuit case, i.e. null shunt resistance. Furthermore, the torque and back EMF constant of brushless PM machines can be expressed as [103]:

$$K_e = \frac{2}{3} K_t \quad (3.74)$$

Hence, the maximum regenerative damping of the REmSA can be written as

$$c_{em,max} = \frac{2K_t^2}{3R_{ph}} \frac{1}{\tau_t^2} \quad (3.75)$$

where the overall transmission ratio carries the damping from the rotary to the linear domain, according to Eq. 3.5.

This performance request must be satisfied in nominal condition. Consequently, the torque constant figuring in Eq. 3.75 refers to nominal operation and can be written as:

$$K_{t,\text{nom}} = \frac{T_{\text{em}}|_{J_{\text{nom}}}}{I_{\text{ph},\text{nom}}} \quad (3.76)$$

where the nominal phase current amplitude is

$$I_{\text{ph},\text{nom}} = \sqrt{2}J_{\text{nom}}A_{\text{w}}N_{\text{h}} \quad (3.77)$$

A_{w} being the wire cross-section and N_{h} the number of wires-in-hand of the coil. The coefficient $\sqrt{2}$ converts the RMS of the current density into an amplitude value. The wire cross section is:

$$A_{\text{w}} = \frac{k_{\text{cp}}A_{\text{s}}}{N_{\text{t}}N_{\text{h}}} \quad (3.78)$$

where N_{t} is the number of turns per coil, k_{cp} the slot packing factor, and A_{s} the half-slot area. According to Eq. 3.65, the output torque of the electric machine under nominal operation is:

$$T_{\text{em}}|_{J_{\text{nom}}} = l_{\text{em}}r_{\text{Tl}}|_{J_{\text{nom}}} \quad (3.79)$$

which is introduced into Eq. 3.76 to obtain the torque constant in nominal operation:

$$K_{t,\text{nom}} = \frac{l_{\text{em}}r_{\text{Tl}}|_{J_{\text{nom}}}N_{\text{t}}}{\sqrt{2}J_{\text{nom}}k_{\text{cp}}A_{\text{s}}} \quad (3.80)$$

By substituting into Eq. 3.75, the maximum regenerative damping capability is written as:

$$c_{\text{em},\text{max}} = \frac{2 \left(\frac{l_{\text{em}}r_{\text{Tl}}|_{J_{\text{nom}}}N_{\text{t}}}{\sqrt{2}J_{\text{nom}}k_{\text{cp}}A_{\text{s}}} \right)^2}{3R_{\text{ph}}} \frac{1}{\tau_{\text{t}}^2} \quad (3.81)$$

The phase resistance is function of the electric machine active length l_{em} :

$$R_{\text{ph}} = 2(l_{\text{em}} + l_{\text{et}}) \frac{\rho_{\text{cu}}N_{\text{c}}N_{\text{t}}}{N_{\text{h}}A_{\text{w}}} = 2(l_{\text{em}} + l_{\text{et}}) \frac{2\rho_{\text{cu}}N_{\text{c}}N_{\text{t}}^2}{k_{\text{cp}}A_{\text{s}}} \quad (3.82)$$

where $\rho_{\text{cu}} = 1.68 \cdot 10^{-8} \Omega\text{m}$ is the electrical resistivity of copper at 20°C, N_{c} the number of coils in series per phase—slots to phase number ratio ($N_{\text{s}}/N_{\text{ph}}$)—and l_{et} the length of the end-turn path. By substituting into Eq. 3.81 and manipulating the relationship, the maximum regenerative damping capability becomes:

$$c_{\text{em},\text{max}} = \frac{r_{\text{Tl}}|_{J_{\text{nom}}}^2}{6N_{\text{c}}\rho_{\text{cu}}k_{\text{cp}}A_{\text{s}}J_{\text{nom}}^2} \frac{l_{\text{em}}^2}{l_{\text{em}} + l_{\text{et}}} \frac{1}{\tau_{\text{t}}^2} \quad (3.83)$$

The length of the end-turn path l_{et} can be written as function of the slot geometry. In fractional slot configurations, the coil is wound around one single stator tooth. Fig. 3.24 schematizes the winding path in the stator top view. The coil wire exits from the slot, make a 180 deg bend, and then enters the other slot. The end-turn path—which refers to the mid-point of the slot area—is given by:

$$l_{et} = \frac{\pi D_{et}}{2} \quad (3.84)$$

D_{et} being the distance between the center points of the slots surrounding the stator tooth. It is written as:

$$D_{et} = \frac{R_1 + R_2}{2} \theta_w \quad (3.85)$$

where

$$\begin{aligned} R_1 &= R_{ro} + g_{em} + d_1 + d_2 \\ R_2 &= R_{so} - w_{bi} \end{aligned} \quad (3.86)$$

d_1 and d_2 being dimensions related to the shoe, as shown in Fig. 3.16. The geometry of the stator was defined in Sec. 3.3.2. Angle θ_w can be written as:

$$\theta_w = \theta_t + \frac{\theta_c}{2} \quad (3.87)$$

where

$$\begin{aligned} \theta_t &= 2 \sin^{-1} \left(\frac{w_{tb}}{R_1 + R_2} \right) \\ \theta_c &= \theta_s - \theta_t \\ \theta_s &= \frac{2\pi}{N_s} \end{aligned} \quad (3.88)$$

By combining these relationships, angle θ_w is written as:

$$\theta_w = \frac{\theta_t + \theta_s}{2} = \frac{\pi}{N_s} + \sin^{-1} \left(\frac{w_{tb}}{R_1 + R_2} \right) \quad (3.89)$$

Finally, the end-turn path relationship is obtained by combining Eqs. 3.85, 3.86, and 3.89:

$$l_{et} = \frac{R_{ro} + g_{em} + R_{so} - w_{bi}}{4} \left[\frac{\pi^2}{N_s} + \pi \sin^{-1} \left(\frac{w_{tb}}{R_{ro} + g_{em} + R_{so} - w_{bi}} \right) \right] \quad (3.90)$$

The terms of Eq. 3.83 that are constant with respect to the active length l_{em} and transmission ratio τ_t can be grouped in the coefficient α_{em} :

$$\alpha_{em} = \frac{r_{T1} |J_{nom}|^2}{6 N_c \rho_{cu} k_{cp} A_s J_{nom}^2} \quad (3.91)$$

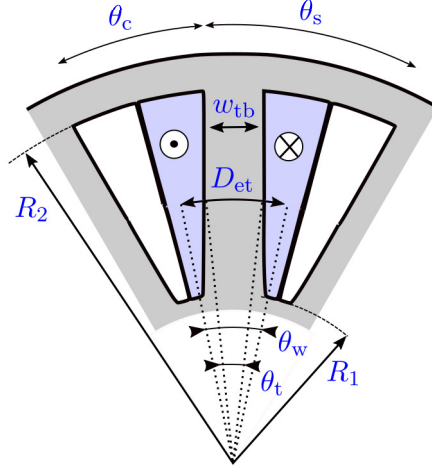


Figure 3.24: Scheme of the winding path in the stator top view. The coil wire outputs the slot on the left and enters the one on the right.

Therefore, Eq. 3.83 can be written as:

$$c_{em,max} = \alpha_{em} \frac{l_{em}^2}{l_{em} + l_{et}} \frac{1}{\tau_t^2} \quad (3.92)$$

It is a quadratic equation in the variable l_{em} :

$$\frac{\alpha_{em}}{c_{em,max} \tau_t^2} l_{em}^2 - l_{em} - l_{et} = 0 \quad (3.93)$$

which features two roots, one positive and one negative. The latter is not physical, hence the unique solution is:

$$l_{em} = \frac{1 + \sqrt{1 + 4l_{et} \frac{\alpha_{em}}{c_{em,max,reg} \tau_t^2}}}{2 \frac{\alpha_{em}}{c_{em,max} \tau_t^2}} \quad (3.94)$$

The damping constraint imposes that the electric machine must be able to provide at least the maximum regenerative damping request (Table 3.7) without the need of active power ($c_{em,max} \geq c_{em,max}$). Therefore, Eq. 3.94 is written as inequality. It constitutes, together with Eqs. 3.67 and 3.69, the set of constraints that the REmSA must observe:

$$l_{em} \geq \frac{F_{act,nom}}{r_{T1} |J_{nom}} \tau_t \quad (3.95)$$

$$l_{em} \geq \frac{F_{act,oload}}{r_{T1} |J_{nom} \frac{J_{oload}}{J_{nom}}} \tau_t \quad (3.96)$$

$$l_{em} \geq \frac{1 + \sqrt{1 + 4l_{et} \frac{\alpha_{em}}{c_{em,max,reg} \tau_t^2}}}{2 \frac{\alpha_{em}}{c_{em,max} \tau_t^2}} \quad (3.97)$$

These constraints relate the electric machine active length and the REmSA transmission ratio with the performance requirements. Furthermore, the torque-to-length ratio r_{Tl} and coefficient α_{em} depend on the electric machine, whose optimized parameters are introduced as second-order polynomial (Fig. 3.23). Note that the latter depends on the stator outer radius and number of slots of the electric machine.

Objective function The electric machine and gearbox are matched to minimize a cost function that includes the REmSA mass (m_{tot}) and equivalent inertia at the wheel (m_{eq}):

$$F_{cost} = w_{R_{so}} \frac{R_{so}}{R_{so,lim}} + w_m \frac{m_{eq}}{m_{eq,max}} + (1 - w_m) \frac{m_{tot}}{m_{tot,max}} \quad (3.98)$$

where the mass and equivalent inertia are normalized with respect to their maximum target value. These are set to 4 kg and 15 kg, respectively. The weighting coefficient w_m moves the optimization towards the minimization of the mass or the equivalent inertia. It is set to 0.5 to give the same weight to the two inertia features. A term that penalizes large outer envelope is introduced because of packaging considerations. The stator outer radius is normalized with respect to the limit value, which is set to 50 mm (radius) to be compliant with the 120 mm envelope constraint (diameter) defined in Sec. 3.3.1. The weight $w_{R_{so}}$ is set to 0.2.

The REmSA mass and equivalent inertia are composed of the electric machine and gearbox contributions:

$$m_{tot} = m_{em} + m_{gb} \quad (3.99)$$

$$m_{eq} = m_{eq,em} + m_{eq,gb} \quad (3.100)$$

As a first approximation, the electric machine is considered as a cylindrical volume with radius R_{so} (stator envelope) made of steel. Hence, its mass is computed as:

$$m_{em} = \rho_{steel} \pi R_{so}^2 l_{em} \quad (3.101)$$

where $\rho_{steel} = 7800 \text{ kg/m}^3$ is the mass density of steel. The equivalent inertia is given by the rotating components—i.e. the rotor, which is considered as a cylinder—reported at the wheel level:

$$m_{eq,em} = \frac{1}{2} \rho_{steel} \pi R_{ro}^2 \frac{l_{em}}{\tau_t^2} \quad (3.102)$$

The gearbox contributions are computed by considering the scaling laws proposed by Saerens *et al.* [104], which considers the static sizing of the gears. The procedure refers to a planetary gearbox with N stages.

The same outer diameter is accounted for the gearbox and the electric machine to optimize the prototype envelope. Then, the ring primitive diameter is set to

be smaller than gearbox outer envelope, as the ring is an inner gear whose outer diameter coincides with the gearbox envelope. Hence, the ring primitive diameter is set as:

$$d_{\text{ring}} = 0.85 \cdot 2R_{\text{so}} \quad (3.103)$$

According to Eq. 3.3, the gearbox transmission ratio can be computed from the overall ratio:

$$\tau_g = \frac{\tau_t}{\tau_l} \quad (3.104)$$

By considering an equal distribution among the gearbox stages, the transmission ratio of each stage is:

$$i_{\text{stage}} = \frac{1}{\sqrt[N]{\tau_g}} \quad (3.105)$$

Note that another strategy commonly used in multistage gearbox transmissions is to move the transmission ratio towards the fastest stages, as they transmit lower torque. Nevertheless, this would imply larger face width of the fastest stage thus turning in larger equivalent inertia.

Once the transmission ratio of the stage and the ring primitive diameter are known, the primitive diameter of sun and planets, and carrier center distance can be derived by following well-known kinematic relationships:

$$d_{\text{sun}} = d_{\text{ring}} \frac{1}{i_{\text{stage}} - 1} \quad (3.106)$$

$$d_{\text{planet}} = d_{\text{ring}} \frac{i_{\text{stage}} - 2}{2(i_{\text{stage}} - 1)} \quad (3.107)$$

$$d_{\text{carrier}} = d_{\text{ring}} \frac{i_{\text{stage}}}{2(i_{\text{stage}} - 1)} \quad (3.108)$$

The j th stage mass is computed by summing the contributions of the wheels (one stage, one ring and three planets) and the carrier:

$$m_{\text{stage},j} = \frac{\pi}{4} \rho_{\text{steel}} b_{\text{stage},j} \left[d_{\text{sun}}^2 + 3d_{\text{planet}}^2 + d_{\text{carrier}}^2 + \left((2R_{\text{so}})^2 - d_{\text{ring}}^2 \right) \right] \quad (3.109)$$

where $b_{\text{stage},j}$ is the face width of the j th stage. The overall gearbox mass is obtained as:

$$m_{\text{gb}} = \sum_{j=1}^N m_{\text{gb},j} \quad (3.110)$$

The equivalent inertia of the j th stage reported at the wheel level is obtained as [104]:

$$m_{\text{eq},j} = \frac{\pi}{128} \frac{\rho_{\text{steel}} b_{\text{stage},j} d_{\text{ring}}^4 i_{\text{stage}}^2}{(i_{\text{stage}} - 1)^4} \left(i_{\text{stage}}^2 - 3i_{\text{stage}} + 7 \right) \frac{i_{\text{stage}}^{2(j-1)}}{\tau_l^2} \quad (3.111)$$

where $j = 1$ is the first stage on the linkage side. The overall gearbox equivalent inertia is obtained as:

$$m_{\text{eq,gb}} = \sum_{j=1}^N m_{\text{eq},j} \quad (3.112)$$

In the above-reported relationship, the face width of the j th stage is unknown. It must be computed according to mechanical strength considerations involving pitting sizing [104]. To this end, the nominal working point is considered since the pitting refers to fatigue operation ($\text{rms}(F_{\text{act}})$ and $\text{rms}(v_{\text{act}})$ reported in Table 3.7). Force and velocity at the wheel level are translated into torque and angular velocity of the carrier of the j th stage as follows:

$$\omega_{\text{stage},j} = \frac{\text{rms}(v_{\text{act}})}{\tau_1} i_{\text{stage}}^j \quad (3.113)$$

$$T_{\text{stage},j} = \frac{\text{rms}(F_{\text{act}}) \tau_1}{i_{\text{stage}}^j} \quad (3.114)$$

The facewidth is computed by considering the pitting of the sun-planet meshing, which is more limiting than the planet-ring contact [104]. The allowable contact stress of nitride steel ($\sigma_{\text{H}} = 1500\text{MPa}$ [105]) is used:

$$b_{\text{stage},j} = \frac{T_{\text{stage},j}/3}{\left(\frac{\sigma_{\text{H}}}{Z_j}\right) \frac{i_{\text{stage}}^{-2}}{[2(i_{\text{stage}}-1)]^2} d_{\text{ring}}^2} \quad (3.115)$$

where the coefficient $1/3$ is due to the torque split on the three sun-planets mesh points, and factor $Z_j = Z_E Z_H Z_\epsilon \sqrt{K_A K_{v,j}}$ is computed according to Shigley's handbook [105]. The elastic factor Z_E depends on the elastic properties of the meshing gears material (steel):

$$Z_E = \sqrt{\frac{E_{\text{steel}}}{2\pi(1-\nu_{\text{steel}}^2)}} \quad (3.116)$$

where $E_{\text{steel}} = 210\text{GPa}$ and $\nu_{\text{steel}} = 0.3$. Contact ratio factor Z_ϵ was set to the unity, which is a worst case assumption. Factor Z_H depends on the pressure angle $\alpha = 20\text{deg}$:

$$Z_H = \sqrt{\frac{2}{\cos \alpha \sin \alpha}} \quad (3.117)$$

The overload factor K_A is set to 1.5, and the dynamic factor K_v is computed according to:

$$K_{v,j} = \frac{5.6 + \sqrt{v_{\text{sun},j}}}{5.6} \quad (3.118)$$

$v_{\text{sun},j} = i_{\text{stage}} \omega_{\text{stage},j} d_{\text{sun}}/2$ being the peripheral speed of the sun.

Optimization approach The constraints depend on the electric machine optimized geometry, which is function of the stator outer radius and number of slot. Therefore, the gearbox and electric machine match consists in an iterative optimization that minimizes the objective function (Eq. 3.98) for all the combinations of stator outer radius and number of slot.

For demonstration purposes, the results related to the electric machine with 12 slots and 85 mm outer stator diameter are reported in Fig. 3.25. The plots features the transmission ratio τ_t on the x-axis. At first, the constraints are applied to find the feasible transmission ratio and active length combination, as shown in Fig. 3.25a. Specifically, the performance constraints result in lines for the force requirements, and a parabola for the damping one. At a given transmission ratio, the system of inequalities (Eqs. 3.95 to 3.97) gives as solution the point lying on the curve with largest active length. Then, the feasible domain is limited by the transmission ratio lower bound and the active length upper bound. Therefore, the solution must lie on the highlighted thick solid curve: each point is well sized to satisfy the constraint it lies on, but it is oversized for the other ones because also a smaller active length would be sufficient. Nevertheless, a reduction of the active length makes the more stringent constraint unobserved.

The objective function can be now computed on the constrained domain (Fig. 3.25b). It is a convex function as larger transmission ratio reduces the moment of inertia reported at the wheel, while requiring an actuator with larger force capability. This turns in larger prototype with increased mass. Therefore, the minimum defines the optimum transmission ratio, which locates an univocal point on the highlighted thick curve in Fig. 3.25b. Note that the minimum of the objective function could fall outside the feasible domain. In such case, the solution lies on the minimum transmission ratio or the maximum active length bounds.

Optimization output The above-reported procedure is repeated for the selected number of slots (9 and 12) by varying the stator outer radius. At each configuration, the procedure returns the transmission ratio, active length, and the value of the objective function at the optimum point. These results are plotted versus the stator outer radius, as shown in Figs. 3.26. Specifically, results for the 9 and 12 slots are reported. Overall, larger outer envelope reduces the electric machine active length, while the transmission ratio encounters an absolute minimum for the 12 slot machine. The objective function is minimized at approximately 85 mm stator outer diameter ($R_{so} = 42.5$ mm) for the 12 slot configuration, which results in active length of 36 mm and transmission ratio of 2.3 mm/rad. The 9 slot configuration gives a minimum outside the investigated stator radius range.

The 85 mm stator outer diameter with 12 slot electric machine was selected. Lower diameter values lead to a small reduction of the cost function for the 9 slot configuration, while yielding to a lower transmission ratio that would require a more demanding gearbox.

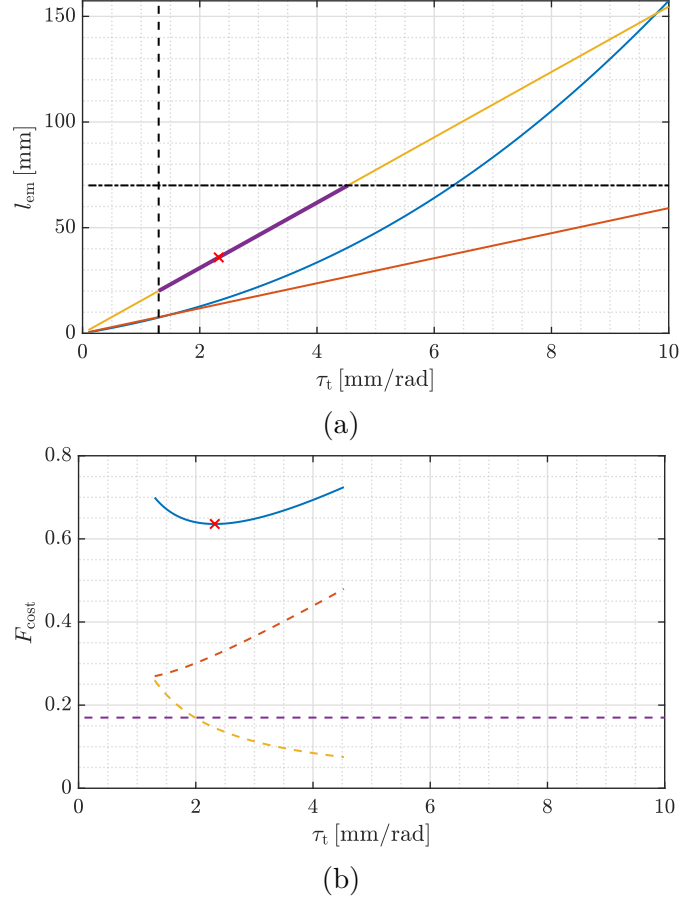
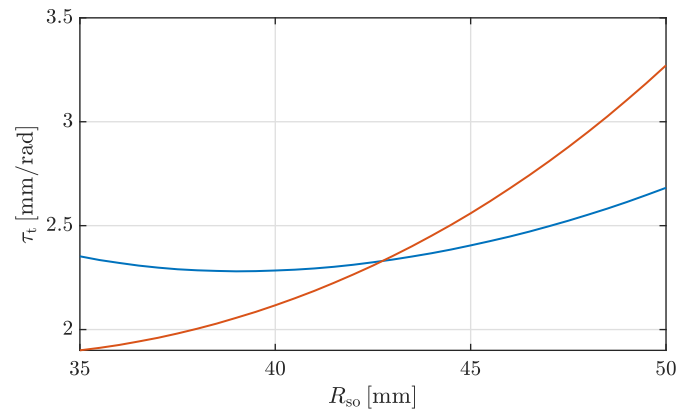
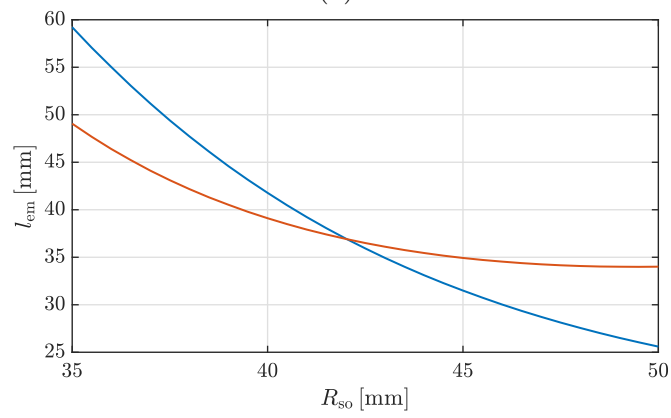


Figure 3.25: Optimization approach at a given electric machine configuration. Active electric machine length (a) and cost function (b) vs the overall transmission ratio. The red cross identifies the optimum point. Figure (a): maximum regenerative damping (blue), maximum (yellow) and RMS (orange) force constraints. Solid purple curve indicates the possible solutions, dashed and dash-dotted lines are the angular velocity and active length constraints. Figure (b): cost function (solid blue) and its contributions (dashed curves): mass (orange), equivalent inertia (yellow), stator outer radius (purple) terms.

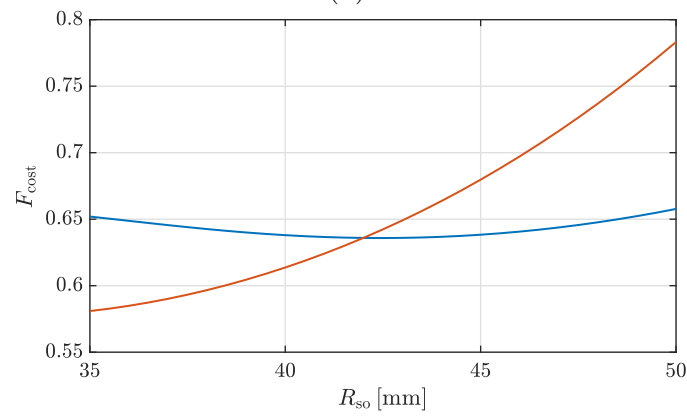
The transmission ratio of the gearbox can be computed according to Eq. 3.3, by considering the linkage transmission. The latter varies along the wheel travel. The worst-case for the gearbox is represented by the maximum value of the linkage transmission ratio (175 mm/rad), which results in $\tau_g = 1/76$.



(a)



(b)



(c)

Figure 3.26: Transmission ratio (a), active length (b), and cost function (c) at the optimum points of diverse electric machine configurations (stator outer radius and number of slots): 9 (orange) and 12 (blue) slot machines.

3.3.3 Detailed design

This step completes the design of the REmSA. It starts from the performance and packaging requirements, as well as the output of the previous optimization.

Electric machine windings definition

The electric machine optimization step (Sec. 3.3.2) and the gearbox and electric machine match (Sec. 3.3.2) defined the electric machine cross-section geometry and its active length. The full definition of the electric machine requires the design of the winding. To this end, the commercial software FluxMotor[®] by Altair is used, which is dedicated to the global design of electric motors.

The synchronous three-phase inner-rotor PM motor available in the software library is modified to reproduce the geometry of the optimized electric machine. Then, the materials are applied: NdFeB 1370 PMs, pure iron and M300-35A steel for the rotor and stator magnetic circuits, respectively. After some preliminary analyses, the active length of the machine is increased to 41 mm to achieve the requested peak torque. Such increase is mainly due to the differences between the FluxMotor and COMSOL models, both in the geometry and material characteristics. The requested peak torque is 6 Nm, which is obtained from Eq. 3.4 with the optimized transmission ratio $\tau_t = 2.3$ mm/rad and the peak actuator force at the wheel level (Table 3.7).

The winding is composed of copper wire with 0.5 mm diameter with 44 μ m insulator thickness. The three phases are connected in wye configuration. The number of turns per coil (N_t) and number of wires in hand (N_h) must be defined. These parameters can assume only integer values and must observe the following constraint:

$$N_t N_h \frac{A_w}{A_s} \leq k_{cp} \quad (3.119)$$

where A_w is the wire cross-section (copper only), and k_{cp} is the gross packing factor. For performance maximization, the winding must be designed to achieve a packing factor as close as possible to its limit. The latter is set to 0.3, as discussed in Sec. 3.3.2.

The electric machine must guarantee the peak actuator force working point ($\max(F_{act})$ and $v_{act}|_{\max(F_{act})}$) and peak actuator power (P_{max}), defined in Sec. 3.3.1. The former imposes a lower bound on the base speed N_{base} :

$$N_{base} \geq \frac{60 v_{act}|_{\max(F_{act})}}{2\pi} \tau_t \quad (3.120)$$

The *Sine Wave Performance Mapping* test available in FluxMotor is performed, which characterizes the behavior of the machine in the torque-speed plane when

the machine undergoes sinusoidal phase supply. The motor operation only is investigated, no generator simulations are carried out. Maximum Torque Per Ampere (MTPA) and Maximum Torque Per Voltage (MTPV) command modes are used to explore velocity values above the base speed, where field weakening operation allows efficient operation of the machine. The maximum line-line RMS voltage must be set to account for DC bus limitation, which in the present case is $V_{DC} = 48$ V. Therefore, the maximum line-line RMS voltage is $V_{DC}/\sqrt{2}$ when considering sinusoidal phase supply. The torque-speed plane is explored by varying the RMS current density and the machine velocity, which span ranges 0 to 20 A/mm² and 0 to 15 000 rpm, respectively.

The number of turns and wires in hand are tuned by trial-and-error process to respect the constraint of Eq. 3.119, while staying as close as possible to the packing factor limit. Then, the simulation is performed and the resulting base speed and maximum output mechanical power are checked and compared to the performance requirements.

According to Eq. 3.119, wires in hand and number of turns are inversely proportional. However, some considerations must be taken into account. The more the wires in hand, the larger the phase current that must be supplied by the power electronics. This turns into more expensive power electronics and bulkier cabling. On the other hand, larger number of turns increases the back EMF of the machine. Therefore, higher DC bus voltage is required to achieve larger base speed. Since the present application features limited DC bus voltage, the more the number of turns, the lower the base speed.

Therefore, if the simulation shows that the selected configuration of wires in hand and number of turns largely satisfies the base speed and power constraints, the number turns must be increased and the wires in hand decreased according to the packing factor limit. This is done to keep as low as possible the maximum phase current. The opposite must be done if the base speed and power constraints are not satisfied.

After some iterations, the configuration with $N_t = 4$ and $N_h = 39$ is identified, which features a base speed of 7624 rpm (1.8 m/s at the wheel level) and maximum mechanical power of 4.75 kW. However, this configuration gives maximum RMS phase current values in the order of 150 A, which correspond to 210 A peak phase current (the factor $\sqrt{2}$ is applied as sinusoidal supply is considered). Such currents are very demanding for the power electronics. Therefore, the performance constraints were relaxed to decrease the maximum currents at the cost of lower base speed and power rating. The selected configuration features $N_t = 7$ and $N_h = 22$. It gives a base speed of 4311 rpm (1 m/s at the wheel level) and maximum mechanical power of 2.69 kW. The resulting phase-to-phase resistance and inductance values are 27.4 m Ω and 168 μ H, respectively.

The resulting peak phase voltage and current maps are shown in Figs. 3.27. The phase voltage features maximum value of 27.7 V, which is below the limit imposed

by the DC bus $V_{\text{DC}}/\sqrt{3}$. The phase current features maximum RMS value of 86 A, which results in 121 A peak value.

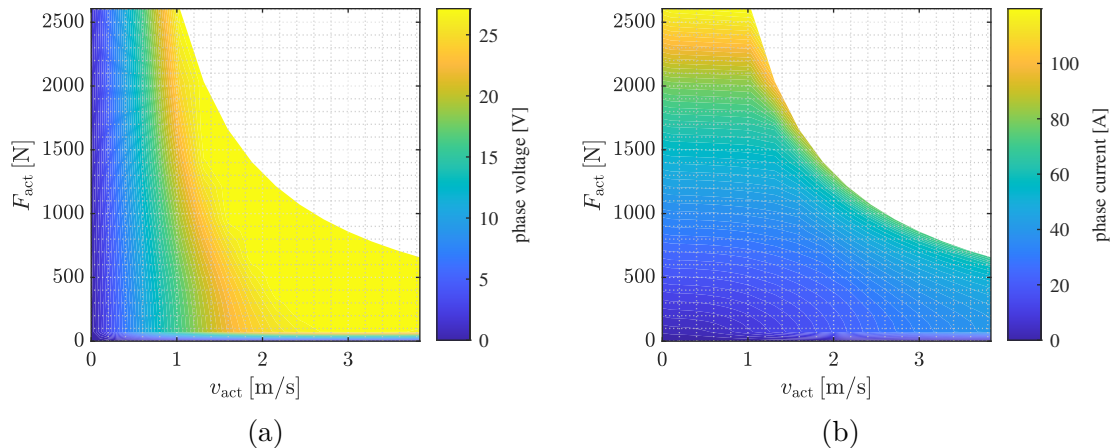


Figure 3.27: Peak phase voltage (a) and peak phase current (b) maps in the force-velocity plane for the optimized electric machine with the winding featuring 7 turns and 22 wires in hand.

Therefore, the electric machine with the designed winding does not allow the REmSA to satisfy the performance requirements derived from the lumped obstacle scenario (Sec. 3.3.1). Specifically, it can operate only in a portion of the force-speed quadrants, which is delimited by the maximum power and torque curves at speed above and below the base speed, respectively. For this reason, the vehicle performance must be checked by accounting for the electric machine limits. To this end, the model presented in Sec. 3.3.1 is used. Specifically, the actuator force F_{act} is saturated through the maximum torque and speed curves delimiting the maps of Figs. 3.27.

The lumped obstacle simulation is performed. The worst-case is considered, namely the pothole with 50 mm amplitude at 50 km/h (see Sec. 3.3.1). The results obtained with the ideal and saturated actuator are compared in Figs. 3.28. Specifically, the actuator working points in the force-velocity plane (a) and the time history of the rear tire-ground contact force (b) are shown. The former highlights how the actuator force saturates. This slightly reflects on the vehicle handling, as can be seen from the tire-ground contact force. Therefore, the selected winding configuration can be considered satisfactory.

Gearbox optimization

The gearbox features a double-stage planetary configuration, as schematized in Fig. 3.29. The two stages features one planet carrier, three planets, one sun and one ring gear. The latter is shared between the two stages. The input is fixed on

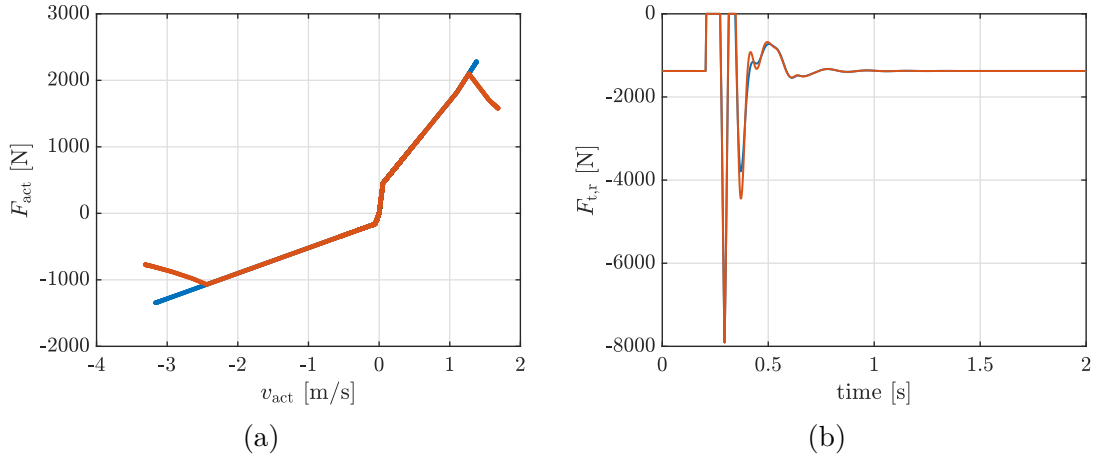


Figure 3.28: Results obtained with the ideal (blue) and saturated (orange) actuator when the motorcycle undergoes a pothole with 50 mm amplitude at 50 km/h. Actuator working points in the force-velocity plane (a), time history of the rear tire-ground contact force (b).

the planet carrier, the output on the sun gear. Therefore, the sun on the first stage is mounted on the carrier of the second stage. The input of the first stage is driven by the linkage, whereas the output of the second stage drives the electric machine rotor.

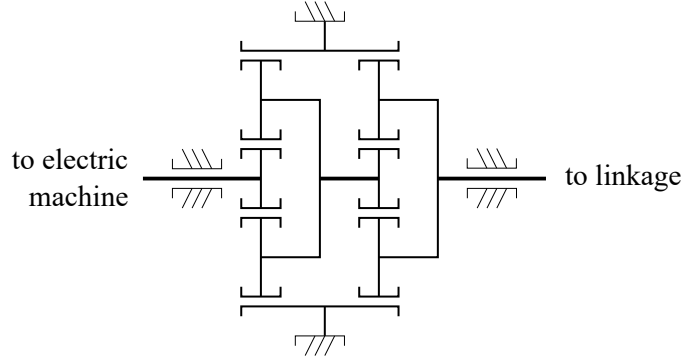


Figure 3.29: Double-stage planetary gearbox scheme

The previous steps defined the outer envelope (85 *mm* diameter) and overall transmission ratio ($\tau_g = 1/76$), which is equally split between the two stages. The gearbox optimization aims at finding a design that minimizes its mass and equivalent inertia at the input shaft.

Gearbox components must be sized to withstand overloads and fatigue. The former corresponds to the working condition at peak actuator force obtained in Sec. 3.3.1 ($\max F_{act}$ and $v_{act}|_{\max(F_{act})}$). The fatigue condition is represented by the force and velocity load spectra. These are extracted from the simulation of the

full-vehicle model running through the ISO B road profile at 70km/h with mixed damping characteristic (Sec. 3.3.1). From the obtained results, the ordinate axis of the actuator force time history (Fig. 3.11c) is discretized into 10 Nm-wide intervals. The duty cycle is calculated as the time fraction in which the device operates inside each load interval with respect to the total simulation time. Then, these load bins are translated to their speed counterpart through the damping characteristic used in the actuator control (Fig. 3.7b). Since the operating conditions are defined at the suspension level, the linkage transmission ratio is used to convert the force and velocity to the gearbox input shaft, as follows:

$$T_{\text{REmSA}} = F_{\text{act}} \tau_1 \quad (3.121)$$

$$\omega_{\text{REmSA}} = \frac{v_{\text{act}}}{\tau_1} \quad (3.122)$$

where the maximum transmission ratio $\tau_1 = 0.175$ mm/rad is used as it gives a worst-case torque value. The resulting spectra are shown in Fig. 3.30.

The considered reference life for fatigue sizing is 750 h, which corresponds to approximately 50 000 km for a vehicle traveling at 70 km/h.

Gear sizing The gears are designed by means of the commercial software KISSsoft[®], which performs sizing calculations of machine elements according to industrial standards [106]. Specifically, the gear sizing observes the ISO 6336 method B [107, 108, 109, 110]. The load conditions at the input shaft is corrected to account for non-ideal operation. Firstly, the dynamic K_V and transverse K_α load factors must be calculated according to the ISO standard [107]. The same reference is followed to compute the face load factor K_β , which accounts for uneven load distribution along the tooth face width. Finally, the application factor is set to $K_A = 1$ both for static and fatigue analysis.

The alternating bending factor Y_m requires some considerations. In case of constant angular motion, it is set to one for both the sun and the ring, and 0.7 for the planets as they experience alternate bending every cycle. However, the considered fatigue condition involves incomplete rotations of the gearbox input shaft. This forward/backward movement leads to alternate bending of sun and ring teeth as well. Consequently, the procedure suggested by the software guide is applied [106]. At first, the factor Y_m is set to 0.7 for sun, ring and planets. Then, the equivalent number of load cycles per revolution of the generic j th gear is computed as follows:

$$N_j = a_{1,j} a_{2,j} \cdot \max\left(1, \frac{360}{\Delta\theta \tau_j}\right) \quad (3.123)$$

τ_j being the transmission ratio between the input of the stage and the j th gear, and $\Delta\theta$ the angular region spanned by the input shaft of the stage. For the first

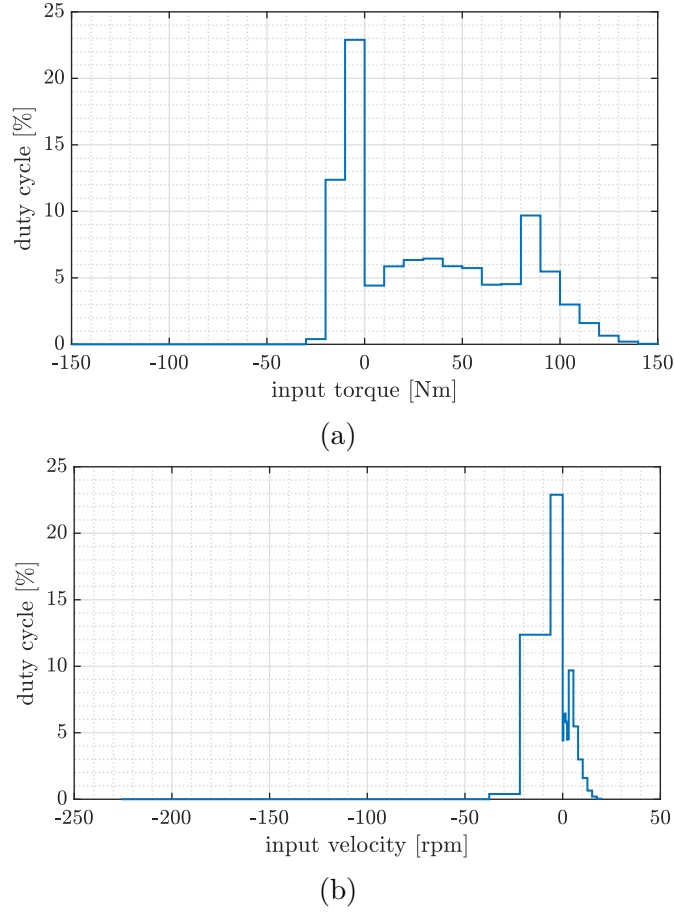


Figure 3.30: Load spectra for gearbox input torque (a) and input speed (b) calculated through the full-vehicle model running through the ISO B road profile at 70km/h with mixed damping characteristic (Sec. 3.3.1).

stage, the latter coincides with the movement of the input shaft. It is extracted from the simulation at the ISO B road unevenness reported in Sec. 3.3.1, where the suspension stroke is converted into gearbox angular motion by means of the linkage transmission ratio. Then, the maximum value is computed, resulting in $\Delta\theta = 7.6$ deg for the first stage.

Coefficient $a_{1,i}$ indicates the number of load cycles of the j th gear in the case of continuous rotation. Specifically, a unitary coefficient is used for the planets, $a_{1,i} = 3$ for the sun and the ring. In fact, the sun and the ring encounter three planets in a complete revolution. Coefficient $a_{2,i}$ considers that sun and ring experience one complete alternate bending cycle in two revolutions (one forward and one backward), not in one as considered by $Y_m = 0.7$. Hence, coefficient $a_{2,i}$ is set to 0.5 for the sun and ring, one for the planets.

The first stage is the most loaded. Therefore, it is designed firstly. The software

performs both static and fatigue design in two routines. Initially, a rough sizing identifies several configurations that satisfy the required transmission ratio and the radial envelope within a certain range. Among these, one configuration is selected for the fine sizing, which fully defines the gears and returns several possible solutions. The optimal one is chosen by comparing different parameters such as efficiency, safety factors, mass and equivalent inertia at the input shaft, and contact ratio. The latter indicates the number of teeth pairs in contact at the same time. Values larger than 1.2 are suggested to guarantee smooth and continuous operation.

After the fine sizing, the strength of the gears can be manipulated to obtain safety factors close to 1.1 by slightly tuning the tooth face width. The latter must observe the following constraints to maintain a certain proportion with the gear diameter

$$\begin{aligned} b_{\text{stage}} &\leq 1.6 d_{\text{sun}} = 1.6 m_n z_{\text{sun}} \\ b_{\text{stage}} &\in [6 m_n ; 20 m_n] \end{aligned} \quad (3.124)$$

where m_n is the normal module. The constraints are applied to smallest gear, i.e. the sun gear.

The selected configuration is reported in Table 3.11, which gives a transmission ratio of the stage $\tau_{\text{stage}} = 1/8.8$. This yields a gearbox transmission ratio $\tau_g = 1/76.9$, which is very close to the initial request (1/76). The chosen configuration features contact ratio of 1.4 and 1.8 for the sun-planet and planet-ring mesh, respectively. Gears are made of steel grade 3 AGMA 2001 C95. The worst case scenario is represented by the static overload, which gives a safety factor of 1.3 for the bending strength at the tooth root. The fatigue is less demanding, which gives a safety factor of 2.0 for the pitting strength of the flank.

The two stages features the same transmission ratio and share the same ring gear. Therefore, they have the same features except for the tooth face width. Obviously, it is shorter for the second stage as it transmits low torque. This enables a significant reduction of the gearbox inertia. The rough and fine sizing are not carried out for the second stage. Starting from the configuration of the first one (Table 3.11), static and fatigue verification are performed. The tooth face width is tuned to obtain safety factors close to 1.1 and observe the constraints of Eq. 3.124. The operating conditions at the gearbox input are converted to the input of the second stage by applying the transmission ratio τ_{stage} . As result, the tooth face width is set to 4.5 mm. It follows from the constraints in Eq. 3.124, whereas the achieved safety factors are well above 2 both in static and fatigue conditions.

As a final remark, the REmSA undergoes alternate motion during its operation. Therefore, the gearbox will be subject to backlash. However, the correction coefficients defined by ISO 6336 account for the presence of backlash. Furthermore, backlash introduces a dead-band effect in the load spectra: assuming zero backlash in the gearbox design remains a conservative choice.

Table 3.11: Gear determined parameters

Description	Symbol	Value
Normal module	m_n	0.75 mm
Pressure angle	α	20°
Center distance	a	22.9 mm
Number of teeth, sun	z_{sun}	14
Number of teeth, planet	z_{planet}	46
Number of teeth, ring	z_{ring}	-109
Profile shift coefficient, sun	χ_{sun}^*	0.483
Profile shift coefficient, planet	χ_{planet}^*	0.076
Profile shift coefficient, ring	χ_{ring}^*	0.768
Tooth face width, first stage	b_1	12.0 mm
Tooth face width, second stage	b_2	4.5 mm

Assembly definition

Once the gearbox and electric machine have been defined, the mechanical assembly of the REmSA is designed with the aim of compact and lightweight layout, while featuring stiffness and mechanical strength. To this end, extensive structural analyses supported by finite element approach were carried out by accounting for the static overload scenario resulting from the lumped obstacle simulation (Sec. 3.3.1). The resulting design is shown in Fig. 3.31

The gearbox and electric machine assemblies are detailed in Figs. 3.32 and 3.33, respectively, whereas the gearbox stages are highlighted in Fig. 3.34.

For compactness purposes, the sun of the second stage is machined directly on the rotor of the electric machine (1). The latter is supported by two single-row ball bearings axially preloaded by a wave spring. The bearing on the gearbox side is supported by a an O-ring to avoid hyperstatic scheme, as the sun-planet mesh acts as an additional support. The stator of the machine (3) is held inside its casing through a preload ring. To estimate the rotor angular position, its end was equipped with a PM (7), whose magnetic field is measured through an absolute position transducer (6). The latter is provided by the microelectronics engineering company Elife International® [111]. Cable glands (8) are mounted on the electric machine cover to pull out the electric machine phases.

For the sake of compactness, the suns of both stages (13,15) are machined on their respective shafts, which are the carrier of the second stage (28) and the electric machine rotor (1). The ring (23) is an external gear whose outer diameter is 85 mm. All planet gears (22,24) house a bearing whose inner ring is supported

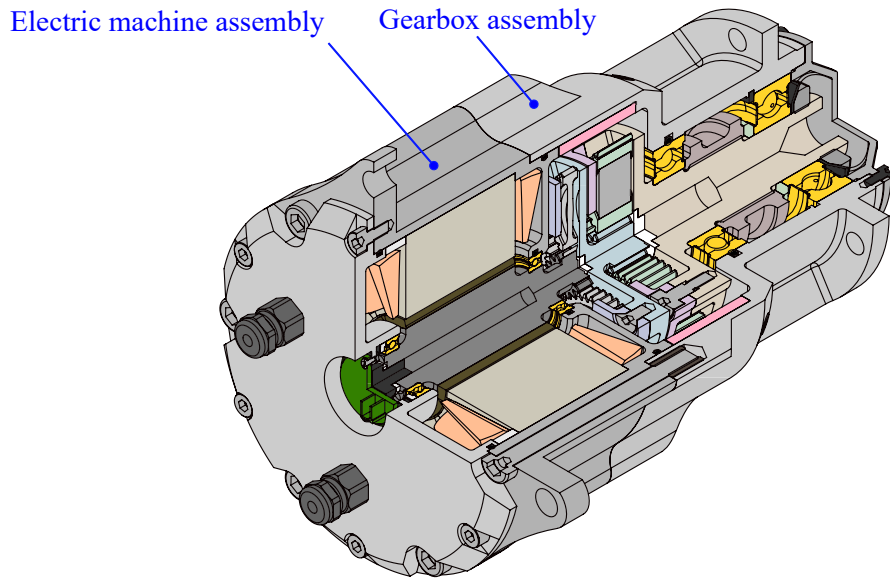


Figure 3.31: Isometric cut view of the rotary electromechanical shock absorber prototype designed for the retained motorcycle.

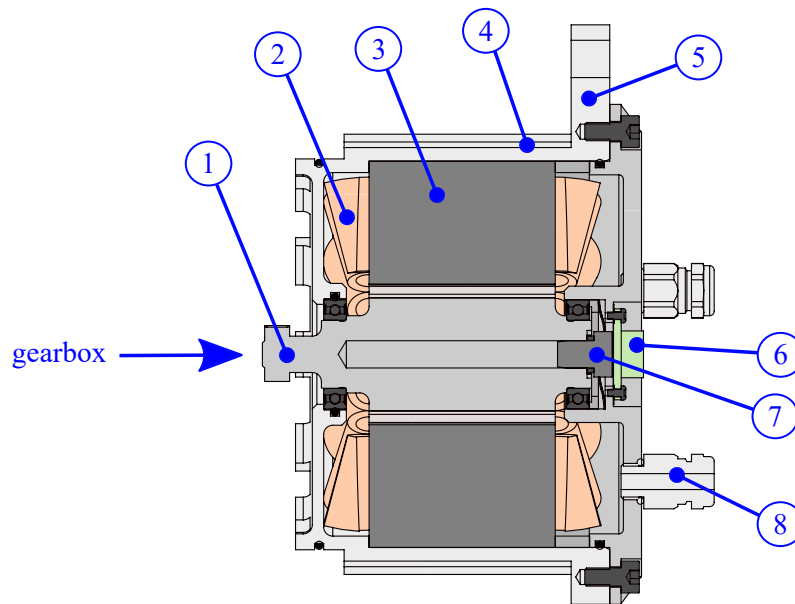


Figure 3.32: Side cut view of the electric machine assembly. Rotor (1), windings (2), stator (3), motor casing (4), interface with the mounting flange (5), angular position sensor (6), sensor magnet (7), cable gland [$\times 3$] (8).

by a pin (20,26). Needle roller bearings (25) and ball bearings (21) are used for the first and second stage, respectively. Pins and carriers are optimized to achieve stiff assembly while reducing the stage inertia. To this end, a case hardening steel

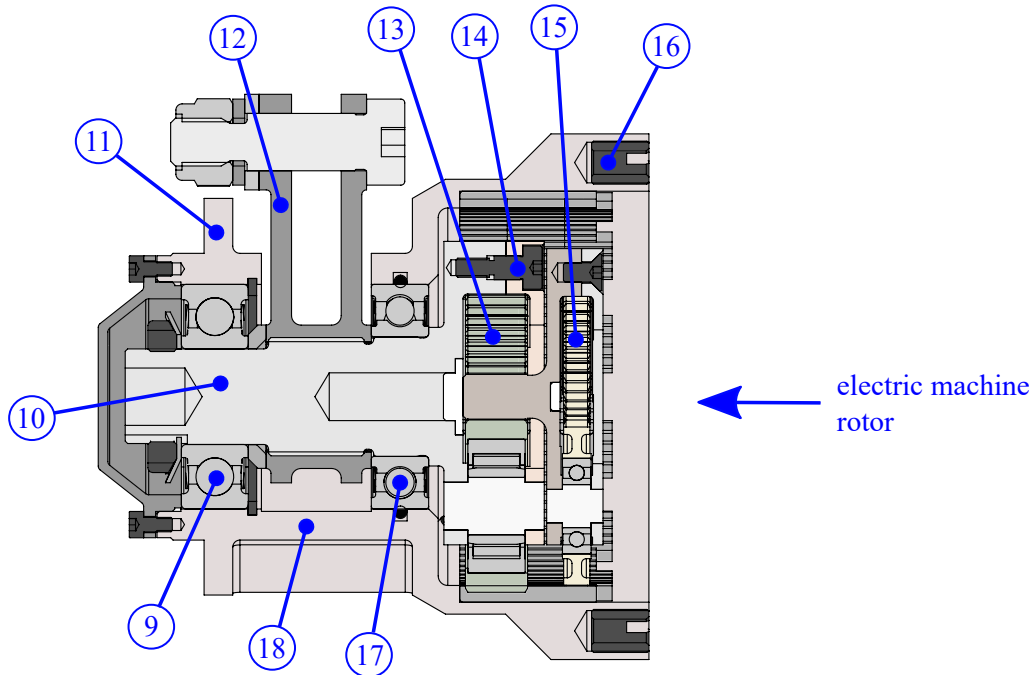


Figure 3.33: Side cut view of the gearbox assembly. Ball bearing (9), input shaft (10), interface with the mounting flange (11), lever (12), first stage (13), calibrated screw [x3] (14), second stage (15), threaded insert [x6] (16), ball bearing (17), casing (18).

(18CrNiMo7-6) is used for these components. The carriers are composed of two flanges: elements (19) and (28) for the second stage, (10) and (29) for the first one. The latter are bolted through calibrated screws to improve the assembly stiffness. Steel grade 3 AGMA 2001 C95 is chosen for the carriers.

The input shaft of the REmSA (10)—which is also the carrier of the first stage—is coupled with the linkage lever (12) by means of a splined profile. It is directly machined on the input shaft, which is supported by two deep groove ball bearings (9,17). This is one of the main differences with respect to the design reported in Appx. A, where a double-row angular contact ball bearing is adopted as the shaft has one support only. The bearings and the lever are axially packed through a lock nut. The external casing is provided with the interfaces between the REmSA prototype and the flanges fixed on the retained motorcycle. As discussed in Sec. 3.3.1, the supports are fixed on the mountings where the engine assembly is connected to the chassis. By following this constraint, two interfaces are designed on the external casing: one (11) is at the level of the gearbox input shaft, the other (5) is on the back of the electric machine. The resulting mounting scheme makes the casing a structural part as it undergoes both bending and torsion actions. For mass reduction purposes, Series 7 aluminum alloy is chosen because of its highest

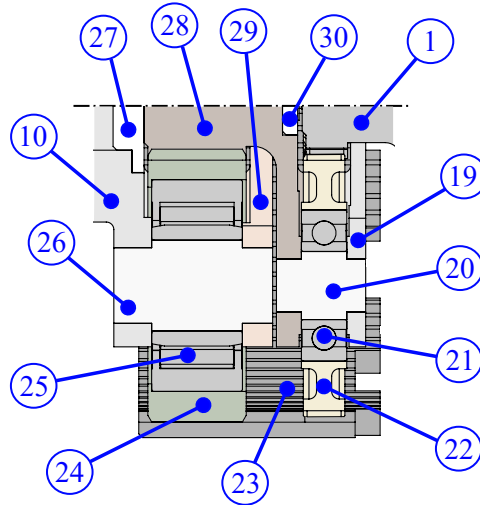


Figure 3.34: Side cut view detail of the gearbox multiplier. First stage: input shaft/carrier (10), planet [$\times 3$] (24), needle bearing [$\times 3$] (25), pin [$\times 3$] (26), plastic end stop (27), carrier flange (29). Second stage: carrier flange (19), pin [$\times 3$] (20), ball bearing [$\times 3$] (21), planet [$\times 3$] (22), plastic end stop (30). Electric machine rotor/second stage sun gear (1), outer ring gear (23), first stage sun gear/second stage carrier (28).

strength among aluminum alloys.

The casing consists of two main parts: the electric machine (4) and the gearbox (18) ones. The latter features an opening to allow the lever angular movement. Specifically, the opening covers an angular portion such that the lever does not interfere with the casing along the whole suspension stroke. However, the opening must be designed as small as possible since it significantly affects the assembly stiffness. Electric machine and gearbox sub-assemblies are connected through six screws that engage threaded inserts.

3.3.4 Design outcome

The inertia features of the designed REmSA are estimated by means of the CAD model. It weighs 4.5 kg, divided into 1.7 kg of the gearbox and 2.8 kg of the electric machine assemblies.

In the present configuration, the actuator is attached to the motorcycle chassis. Therefore, its weight contributes only to the sprung mass. The moment of inertia at the REmSA shaft is $J_{REmSA} = 0.151 \text{ kg m}^2$, which accounts for the rotating inertia of the lever, gears and carriers of the gearbox, as well as the rotor of the electric machine. It is reported at the wheel by means of the linkage transmission ratio (in

nominal configuration):

$$m_{\text{eq}} = \frac{J_{\text{REmSA}}}{\tau_1^2} = 4.9 \text{ kg} \quad (3.125)$$

It contributes to the unsprung mass in dynamic conditions, thus being a well-known drawback of electromagnetic shock absorbers that can be mitigated through active control. The proposed methodology approach minimizes this effect and achieves a good trade-off between equivalent inertia and system mass. This is clear when comparing the resulting features with the ones of the prototype presented in Appx. A. The achieved design envelope is shown in Fig. 3.35. The axial length is 196 mm, whereas the diameter envelope (excluding the lever) is 110 mm.

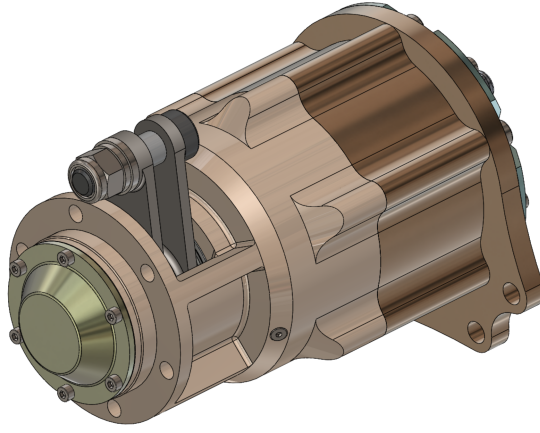
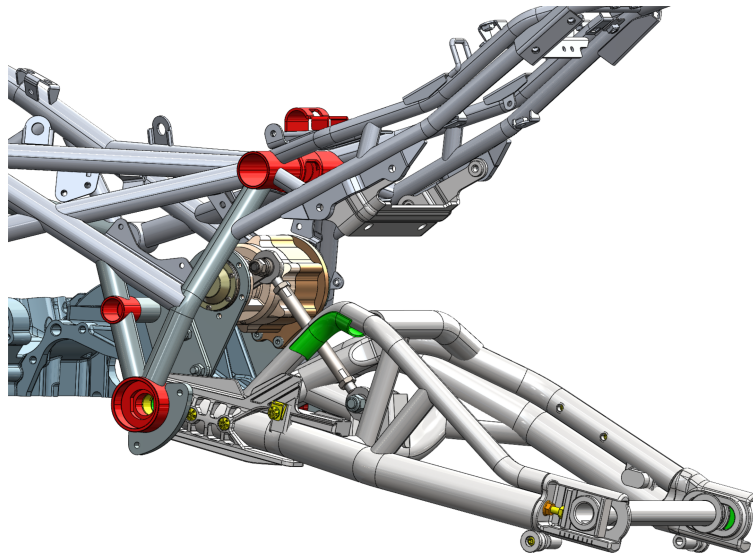


Figure 3.35: Envelope of the designed prototype.

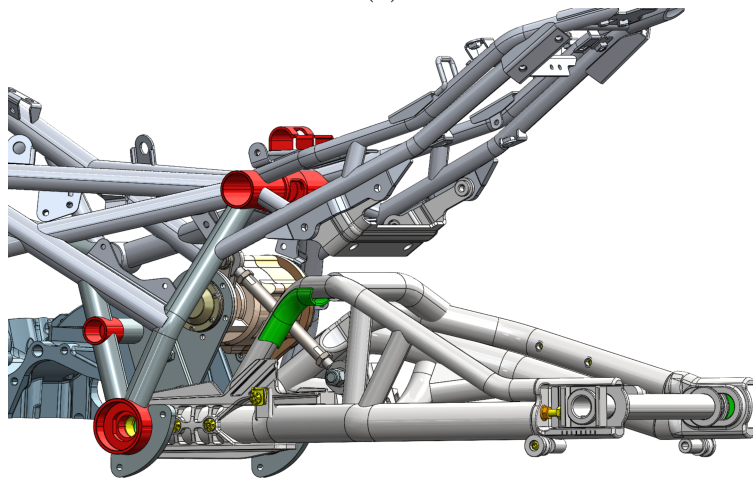
A first check of the packaging on the retained motorcycle is done by means of the CAD tool. To this end, the flanges are introduced and the prototype is located in the suspension. Fig.3.36 shows the suspension in the nominal (a) and compressed (b) configurations. All the linkage elements are introduced to connect the prototype to the rear swing arm. The achieved design well fits the suspension with no interference among the diverse elements.

Overall, the features of the designed prototype are resumed in Table. 3.12. Both the linkage and the overall transmission ratios refers to the wheel nominal position, i.e. null suspension stroke. Note that the overall transmission ratio is slightly different from the initial request (2.3 mm/rad). This is due to the gearbox design, whose output is a device with transmission ratio 1/76.9 instead of 1/76. For the same reason, the peak force at wheel is different from the maximum force shown in Fig. 3.27.

Before the manufacturing process, a further check of the packaging was done by realizing a plastic prototype in additive 3D printing (Fig. 3.37). It was mounted on the rear suspension of the retained motorcycle. No interference with the existing suspension was found.



(a)



(b)

Figure 3.36: Designed REmSA mounted on the rear suspension of the retained motorcycle in nominal (a) and compressed (b) configuration.

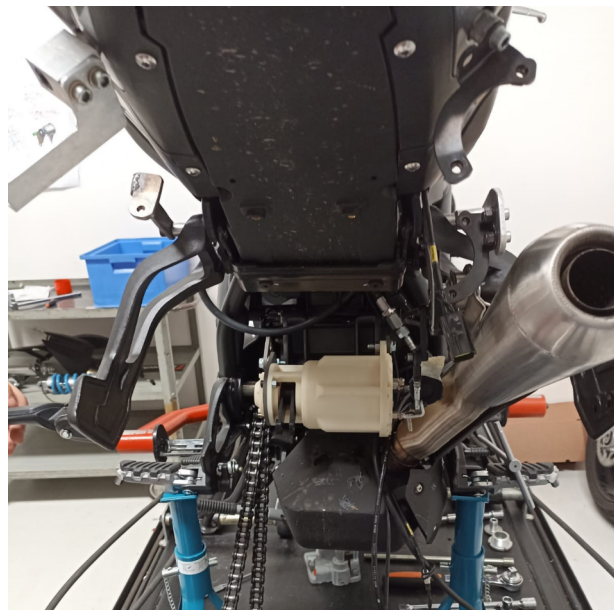
Finally, the prototype has been manufactured. Its components and the assembly are shown in Fig. 3.38 and Fig. 3.39, respectively. Overall, the proposed system-level methodology established specific steps to design a rotary electromechanical shock absorber starting from vehicle integration and packaging aspects. As result, the developed prototype fits in the existing suspension of the retained motorcycle and guarantees actuating performance such that the conventional shock can be removed. It is worth highlighting that vehicle integration aspects cover a relevant role for the transition of the research at the industry level.

Table 3.12: Features of the REmSA for motorcycle application resulting from the proposed design methodology.

Feature	Value
Peak force at wheel	2700 N
Peak torque at REmSA shaft	459.0 Nm
Peak torque at el. machine shaft	6.0 Nm
Equivalent inertia	4.9 kg
Overall transmission ratio	2.21 mm/rad
Gearbox transmission ratio	1/76.9
Linkage transmission ratio	170 mm/rad
Mass	4.5 kg
Diameter envelope	110 mm
Axial envelope	197 mm



(a)

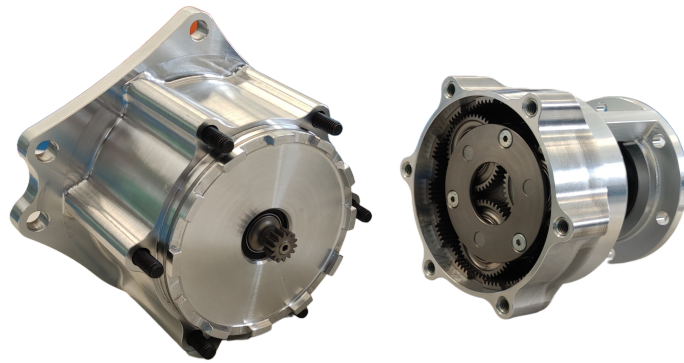


(b)

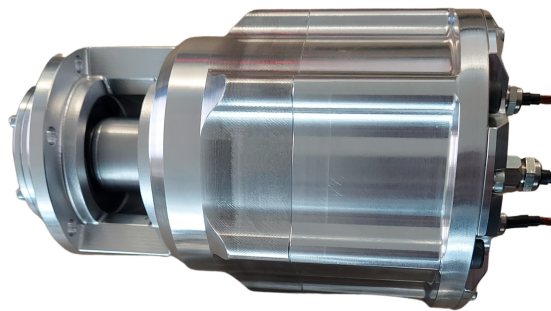
Figure 3.37: Plastic mock-up realized in additive 3D printing (a). Check of the packaging on the rear suspension of the retained motorcycle (b).



Figure 3.38: Components of the manufactured REmSA prototype for the motorcycle application. Gearbox: casing (1), cover (2), first stage planets (3) and carrier (4), second stage carrier (5) and planets (6), lever (7), ring gear (8). Electric machine: stator (9), cover (10), rotor (11), spacer (12), casing (13).



(a)



(b)

Figure 3.39: Manufactured REmSA prototype for the motorcycle application. Electric machine and gearbox sub-assemblies (a), prototype assembly (b).

Chapter 4

Modeling and control

This chapter proposes the modeling and control of the REmSA. At first, a model able to reproduce the real behavior of REmSA systems is presented. It accounts for the dissipative effects of both the electric machine and gearbox, the backlash, and the mechanical dynamics. The developed model is integrated into the quarter-car model of the vehicle.

Then, the control of the REmSA is discussed. Two different control layers are required: the low and the high level. The former controls the force that the REmSA applies to the suspension. It is a cascade of a force control, which compensates for the REmSA dynamics, and a classic current control for PMSMs. The low level control must act up to frequencies able to control the unsprung mass dynamics. The current control is not included into the model as it involves frequency values well above the dynamics of interest. The high level aims at controlling the vehicle dynamics to optimize comfort and handling. The main strategies are discussed, i.e. skyhook and groundhook, spring negation, and LQR. Specifically, it is demonstrated that the LQR gives a combination of skyhook, groundhook and spring negation.

Finally, the developed vehicle model is simulated to assess the performance of the diverse high level control strategies. The impact of the REmSA realistic behavior is investigated, along with the effect of the low level compensator. The parameters of the REmSA model are identified through experimental data. Due to the project timeline, the prototype developed for the automotive application (Appx. A) was used. Overall, the investigation addresses the energy balance of the active suspension, as well as vehicle performance in terms of handling and comfort.

4.1 Modeling

The system is modeled in Matlab/Simulink[®]. Specifically, a lumped parameter modeling approach is adopted. Fig. 4.1 schematizes the complete model, which

integrates the vehicle, the REmSA and its control. These subsystem exchange suspension velocity and REmSA force, the vehicle states and torque request.

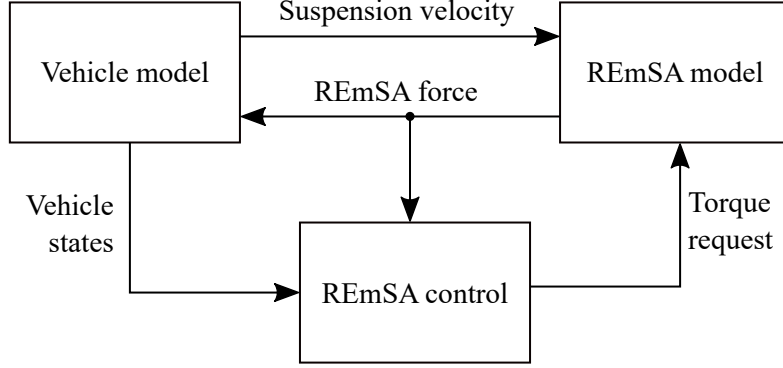


Figure 4.1: Complete model scheme

4.1.1 REmSA model

The REmSA model is schematized in Fig. 4.2. It is composed of two sub-models: the electric machine and the mechanical subsystem. These exchange mechanical power signals, i.e. torque and angular velocity. Specifically, the electric machine receives a control command and generates a torque. The latter is then provided to the mechanical subsystem, which outputs the force at the suspension level. The suspension velocity is provided to the mechanical subsystem, which outputs the electric machine angular velocity.

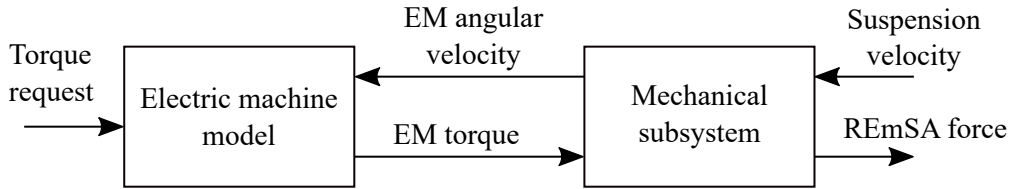


Figure 4.2: REmSA model scheme

The power flows with the adopted convention is schematized in Fig. 4.3. The mechanical power $P_{\text{mech,REmSA}}$ is positive when flowing from the suspension to the REmSA. Then, part of this power is lost in the REmSA mechanical friction ($P_{\text{loss,mech}}$), the remaining amount $P_{\text{mech,EM}}$ goes to the electric machine. After the power lost in the electric machine $P_{\text{loss,EM}}$ is deducted, the remaining part is the electrical power P_{el} sent to the battery. The power balance is written as

$$P_{\text{mech,EM}} = P_{\text{mech,REmSA}} - P_{\text{loss,mech}} \quad (4.1)$$

$$P_{\text{el}} = P_{\text{mech,EM}} - P_{\text{loss,EM}} \quad (4.2)$$

for the mechanical subsystem and the electric machine, respectively. Overall, the mechanical and electric power flows are positive when the system works passively, i.e. the power goes from the suspension to the battery.

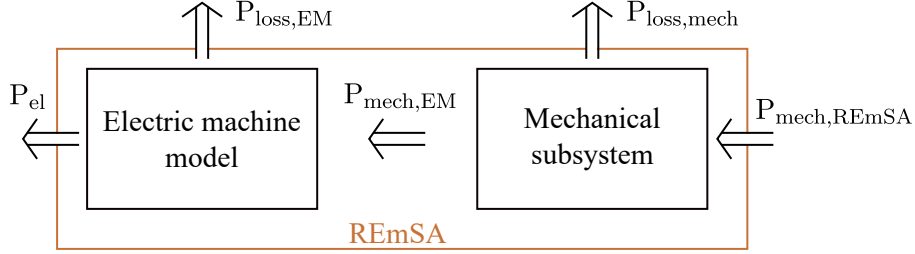


Figure 4.3: REmSA power flows and adopted convention

As will be demonstrated in the remainder of this chapter, electric energy consumption of the electric machine ($P_{el} < 0$) does not always translate into active operation of the suspension ($P_{mech,REmSA} < 0$). This is due to the mechanical dynamics and the power dissipation of the REmSA. Moreover, operation in the passive quadrants of the electric machine features positive mechanical power ($P_{mech,EM} > 0$). If the latter exceeds the electric machine loss, positive electric power is obtained from Eq. 4.2, which indicates electrical energy regeneration. Conversely, electric power is consumed when the mechanical power is lower than the power loss. This reproduces the electric machine operation in the passive quadrants discussed in Fig. 2.1.

Electric machine

The electric machine is modeled as a mapped motor. The model is shown in Fig. 4.4, which includes the Simulink *MappedMotor* block.

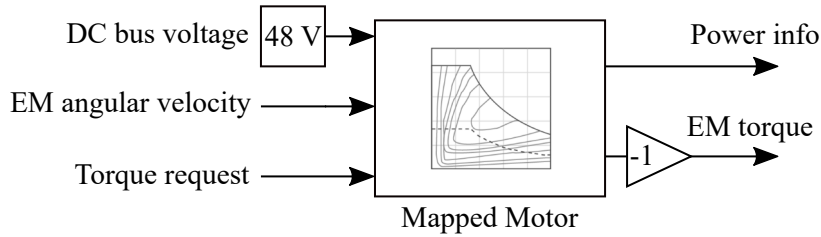


Figure 4.4: Electric machine model scheme

The inputs are the DC bus voltage (48 V), the torque command and the actual velocity of the electric machine shaft. As output, the block gives the power signals (mechanical, electrical and power loss), and the generated torque. The latter is changed in sign to make the model compliant with the present dissertation that

adopts the passive sign convention, whereas the Simulink block implements the active one.

The *MappedMotor* block models the drive electronics and torque control as a response time constant, which determines how the torque tracks the reference demand.

The model reproduces the behavior of a controlled electric machine under torque-control operation in the four quadrants of the torque-velocity plane. It accounts for the torque and power limitations of the electric machine, along with its power loss. To this end, the maximum torque curve and the electric power loss map are needed. These are extracted from the FluxMotor simulation of the electric machine working as a motor (see Sec. 3.3.3). Fig. 4.5 shows the resulting electric power loss map and the maximum torque curve in the active quadrant for the electric machine of the prototype discussed in Appx. A. The map includes both the copper and iron losses. The former increases with the phase current, thus resulting in the large loss in the region close to the maximum torque curve. The iron loss is due to eddy current and magnetic hysteresis effects in the stator core: this loss contribution increases with the angular velocity, thus dominating the high speed region.

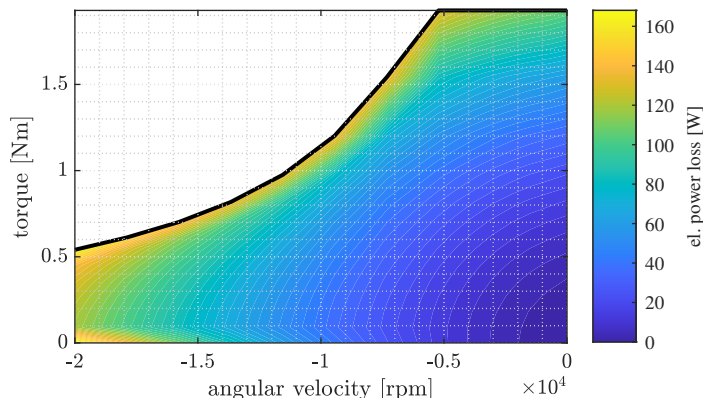


Figure 4.5: Maximum torque curve (solid black) and electric power loss map in the active quadrant of the electric machine of the REmSA prototype discussed in Appx. A.

As already mentioned, the power loss map is extracted in the active quadrants. Passive operation is assumed to be symmetrical, hence the map is mirrored into the remaining quadrants. This assumption holds as the electric machine efficiency is modeled through its electrical power loss. The latter is reasonably identical whether the machine works in active or passive mode: the copper and iron losses depends on the phase current and the angular velocity of the machine, whereas the direction of the mechanical and electric power flows should not influence the loss.

Note that the mapped motor block is characterized by a power convention different from the one used in the present dissertation (Fig. 4.3). Specifically, it

considers positive power when entering the electric machine:

- Mechanical power: positive value means that the electric machine absorbs mechanical energy. Conversely, negative value means that the electric machine is actuating the REmSA.
- Electrical power: positive when absorbed by the electric machine, which translates into electrical energy consumption. Conversely, negative electric power refers to energy regeneration.
- Power loss: always negative because it indicates the amount of power dissipated, which always exits the electric machine.

To adapt to the convention used in Fig. 4.3, the power loss and electrical power given by the block must be changed in sign.

Overall, the modeled electric machine allows to link electrical and mechanical power, which is essential for the assessment of the energy performance of the active suspension. Furthermore, the model accounts for electric machine maximum ratings in terms of torque and power, which is an important physical limitation. No mechanical features of the electric machine—such as inertia or friction—are considered, as they are included into the mechanical subsystem.

Mechanical subsystem

The mechanical subsystem models the effect of the inertia, friction and compliance of the REmSA. It is schematized in Fig. 4.6. The model is developed in Simscape[®], which enables the rapid modeling of physical systems within the Simulink[®] environment. Specifically, the mechanics library is used (green blocks in Fig. 4.6). It works in equivalent terms at the suspension level: translatory motion is considered and the overall transmission ratio τ_t is used to convert rotary quantities at the electric machine into the linear ones at the suspension.

The inputs are the suspension velocity and the electric machine torque, whereas the REmSA force at the suspension level and the electric machine velocity are the outputs. All the rotating inertia of the system is lumped into an equivalent mass. It represents the electric machine rotor, whose inertia contribution dominates the REmSA, and all the rotating components of the gearbox. It is actuated through the electric machine torque converted to the linear domain. The equivalent mass velocity is measured and converted into the rotary domain, which is the electric machine velocity. All the mechanical friction loss are modeled through a viscous damper connecting the equivalent mass to the ground.

A translation hard stop is used to model the mount, i.e. the linkage and the flanges that fix the REmSA to the chassis of the vehicle. The stop is implemented as a spring-damper parallel that hits the slider at the bounds. The hard stop applies the forces smoothly through a defined transition region. The latter accounts for

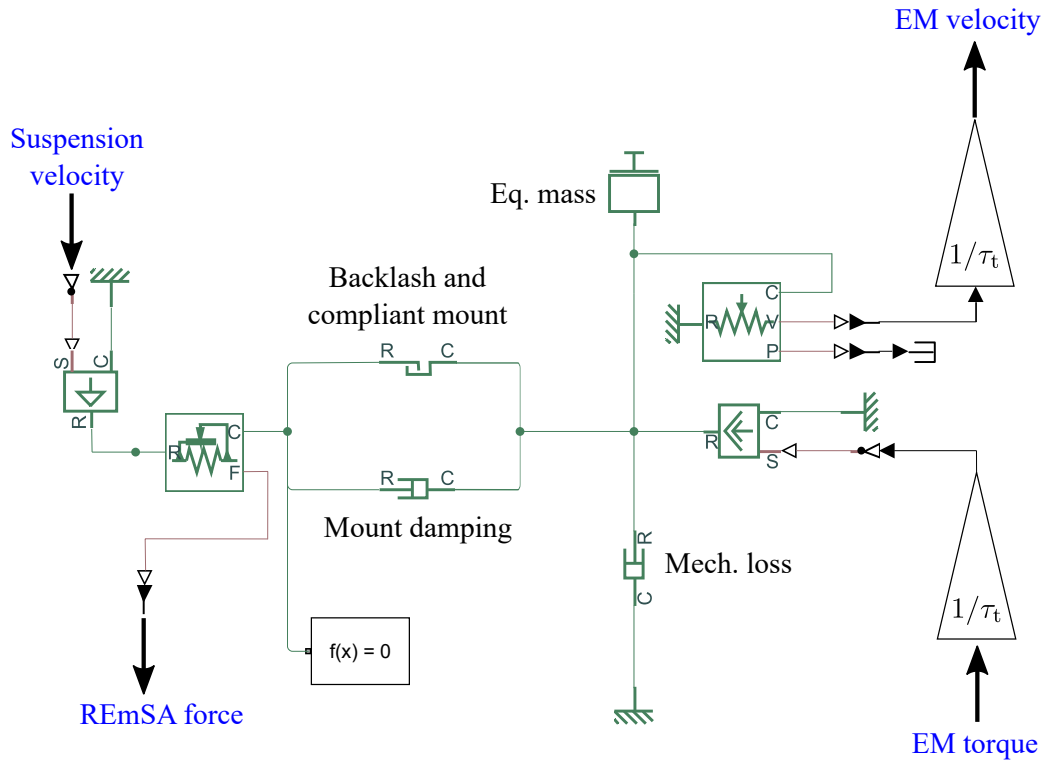


Figure 4.6: Mechanical subsystem model developed in Simulink/Simscape®

the backlash of the gearbox, whereas the damping and stiffness features of the stop represent the compliance of the kinematic chain that goes from the linkage to the rotor of the electric machine combined to the compliance of the mounting flanges. At one side, the translation hard stop is connected to the equivalent mass. At the other, the suspension velocity is imposed, while the REmSA force is measured.

After some attempts, an additional damping term was added to the mount to better fit of experimental data. It can be physically explained as a dissipative contribution of the mount that acts during the backlash phase. Conversely, the damping included into the hard stop block is fully applied only outside of the transition region.

Overall, the mechanical subsystem model decouples the suspension and electric machine DOFs by means of the mount compliance. The latter, combined with the equivalent inertia, filters the electric machine torque, thus limiting the REmSA bandwidth. Moreover, the backlash is a relevant aspect that cause a dead band on the actuation of the suspension. Finally, the mechanical loss impacts the energy performance of the system.

4.1.2 Vehicle model

The quarter-car model schematized in Fig. 4.7 is used to represent the vertical dynamics of the vehicle.

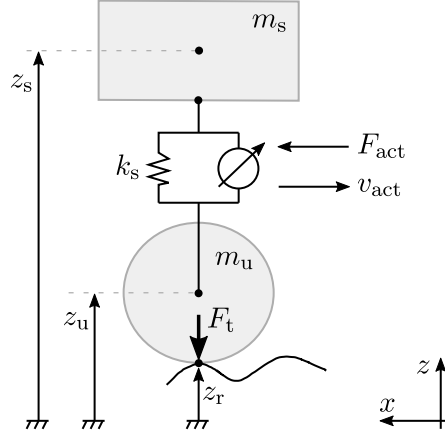


Figure 4.7: Quarter-car vehicle model

The sprung and unsprung masses are connected through the secondary suspension, which includes the spring stiffness k_s and a force actuator that applies the force F_{act} . The latter is the input of the quarter-car, which comes from the REmSA model. The other input is the road displacement z_r , whose derivation is discussed in Sec. 3.3.1. The suspension velocity $v_{\text{act}} = \dot{z}_s - \dot{z}_u$ is the output, which is given to the REmSA model.

The system features the following equations of motion:

$$\begin{aligned} m_s \ddot{z}_s &= -m_s g - F_{\text{act}} - F_e \\ m_u \ddot{z}_u &= -m_u g - F_t + F_{\text{act}} + F_e \end{aligned} \quad (4.3)$$

where g is the gravity acceleration, F_t the tire-ground contact force, and F_e the elastic force of the suspension spring. The latter is given by:

$$F_e = k_s \Delta z_{\text{susp}} \quad (4.4)$$

where $\Delta z_{\text{susp}} = z_s - z_u$ is the suspension deflection. The tire-ground contact forces F_t is saturated to give only negative values:

$$F_t = \begin{cases} k_u (z_u - z_r) & \text{if } z_u - z_r \leq 0 \\ 0 & \text{otherwise} \end{cases} \quad (4.5)$$

where k_u is the tire stiffness and z_r the road displacement. The equation accounts for tire-ground detachment, condition that could occur especially when the vehicle undergoes road irregularities such as bumps or potholes.

4.2 Control

This section discusses the control of the REmSA. It is a cascade of two layers: the high level controls the force that the REmSA applies to the suspension, the low level manages the vehicle dynamics to optimize comfort and handling performance. The overall control scheme is reported in Fig. 4.8.

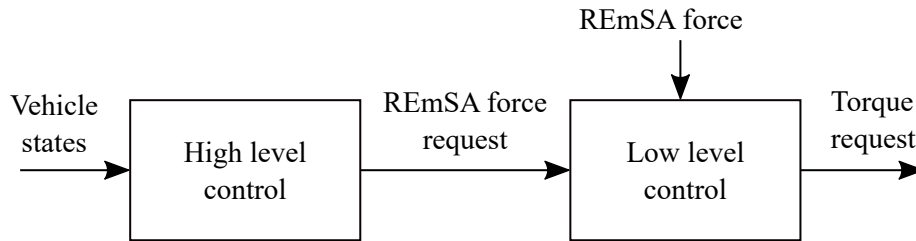


Figure 4.8: Scheme of the REmSA control

4.2.1 Low level control

The low level is a cascade of a force loop and a classic current control for PMSM. The former controls the REmSA dynamics and generates a torque request that is given to the current control. The latter manages the power module that drives the electric machine. Overall, the control bandwidth must be at least in the order of 60 – 70 Hz so that the unsprung mass dynamics can be effectively controlled. The latter stays in the range 10 to 15 Hz for passenger vehicles. The motor current control operates at frequencies 0.5 to 1 kHz that are well above the dynamics of interest. For this reason, it is not included in the present dissertation: the low level block of Fig. 4.8 implements the force control only, which outputs directly the torque request. However, the current control introduces a small dynamic effect, which is modeled as a low pass filter in the electric machine model. It features a time constant in the order of the millisecond.

Electric machine current control As mentioned above, the motor current control is out of the purpose of this work. However, the present research activity involved wide effort on the electric machine current control and its implementation on hardware [112]. For this reason, a brief explanation is provided in this paragraph.

A three-phase power module is needed to drive the electric machine. This device commutes the DC bus voltage into a three-phase voltage field. According to the commutation method, different phase voltage wave-forms can be generated. In this context, two driving techniques are mainly used for three-phase PMSM: the six-step and the Field-Oriented Control (FOC).

The six-step (or two-phase on) control is the simplest strategy. The power module phases are commuted to generate trapezoidal voltage wave-forms that result into pseudo-square phase current signals and, consequently, quasi-constant generated torque.

The FOC represents a more complex technique, which is widely discussed by Krishnan [103]. Its basic scheme is reported in Fig. 4.9.

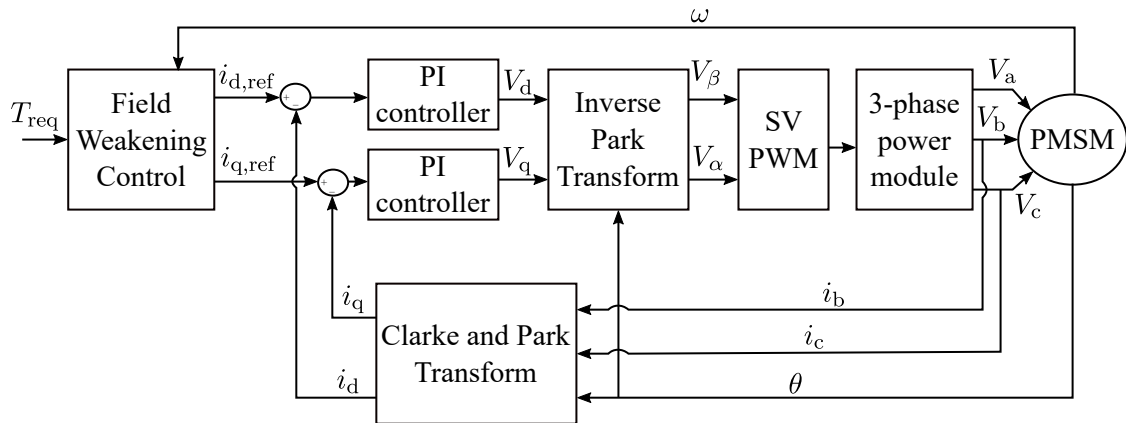


Figure 4.9: Field Oriented Control (FOC) scheme

The three-phases are commuted to generate sinusoidal voltage wave-forms. These are achieved by means of modulation techniques, which enable to regulate the amount of electrical energy transferred from the DC bus of the power module to the electric machine phases. The most common technique is the PWM, where the voltage references of the three phases are modulated individually. When sinusoidal voltage wave-forms are targeted, Space Vector PWM results in better performance. It applies a given voltage vector to a three-phased electric machine. To this end, the six switches of the three-phase power module are commuted to emulate a three-phased sinusoidal waveform. As result, better usage of the DC bus voltage is achieved, with a 15.5% increase of the fundamental output voltage with respect the one produced by other PWM techniques [113]. Low torque ripple and switching losses are additional advantages.

The voltage vector is referred to the stationary $\alpha\beta\gamma$ reference frame. It is computed by transforming the dq voltage requests (inverse Park transform), which are obtained from two current loops implemented to control the currents on the quadrature (q) and direct (d) axes. The former is responsible of the torque generation, the latter produces a magnetic field that increases or counteract the one generated by the machine PMs. For this reason, the direct current reference is null below the motor base speed. Conversely, field-weakening operation is required to go beyond such limit [114, 115]. In this case, the direct current is controlled to counteract the field of the PM field and decrease the back EMF of the machine. The increase of the direct current implies a reduction of the quadrature one to observe the maximum

current and the voltage supply limitation. As consequence, the maximum torque rating cannot be achieved.

The FOC implementation requires the angular position of the rotor and the measurement of two of the three-phase currents. Therefore, one position sensor and two current probes are needed.

Overall, the FOC combined with the field-weakening control guarantees efficient operation of the electric machine and low torque ripple, thus reducing noise and mechanical vibrations [103].

REmSA force control The force control compensates for the REmSA dynamics and non-ideal behavior. Specifically, the mount compliance combined with the rotating inertia limits the actuation bandwidth, thus resulting in poor vehicle performance at frequencies close to the unsprung mass natural frequency. As consequence, the REmSA would be unable to control and damp the unsprung mass, as the force applied to the suspension would be attenuated and phase-delayed with respect to the force request computed by the high level control. This aspect is worsened by the friction and backlash features of the REmSA.

To this end, a Proportional Integral Derivative (PID) compensator is used to improve the REmSA force tracking performance. The control must guarantee an actuation bandwidth well above the unspung mass dynamics, which is in the range 10 to 15 Hz for passenger vehicles. A rule of thumb is to set the actuation bandwidth 5 to 10 times the dynamics of interest. Too large bandwidth would raise the actuator demand and cause issues related to noise amplification. For this reason, the present application tunes the PID compensator to guarantee a REmSA actuation bandwidth in the range 50 to 75 Hz. Overall, the compensator outputs a torque request.

The control scheme is reported in Fig. 4.10. The tracking error is computed from the REmSA force reference and actual force. The latter is a measured signal in the numerical model, whereas it is hard to be measured in real on-vehicle implementation. In this perspective, a force observer could be designed to estimate the REmSA force and close the control loop.

Dynamic saturation with conditional integration anti-windup method is used to prevent the controller output from wandering away. To this end, the saturation bounds are dynamically computed as function of the actual angular velocity of the electric machine. Specifically, the maximum torque curve of the electric machine—Fig. 4.5 for the automotive prototype discussed in Appx. A—is included into the model as a one-dimensional lookup table.

4.2.2 High level control

The high level control focuses on the vehicle dynamics. Specifically, it outputs the force that the REmSA must apply to the suspension to control the comfort and

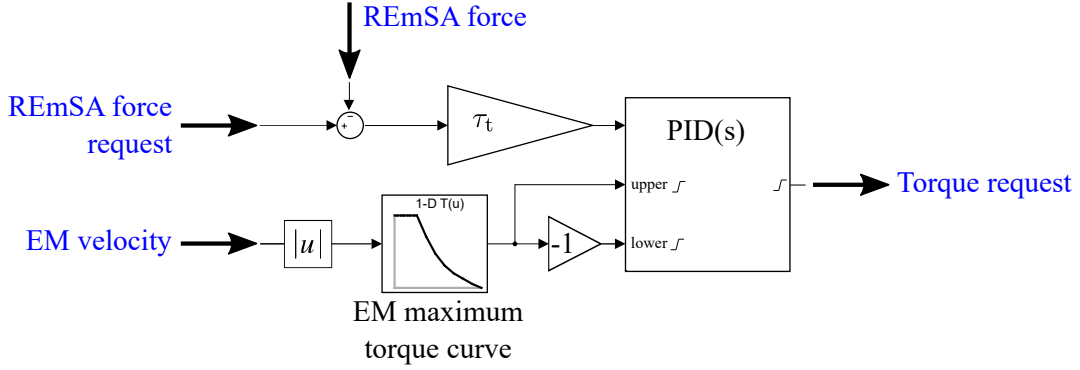


Figure 4.10: REmSA force control

handling performance of the vehicle. To this end, the control strategy elaborates the vehicle states to compute the control action, as shown in the control scheme of Fig. 4.8.

In this context, the literature proposes several strategies aimed at controlling the vehicle dynamics. For instance, active roll control is widely used for active suspensions [116]. In passenger vehicles, roll stiffness is usually small thus causing large roll angle in static cornering. Increasing the anti-roll bar stiffness solves this issue but makes the roll dynamics more underdamped. Active roll control has the advantage of reducing the roll angle on cornering maneuvers, while providing proper damping to the roll dynamics. Furthermore, it enables the control of the load transfer on the axles so that the handling response of the vehicle can be modified.

The basic operation of active suspensions regards the vertical dynamics of the vehicle, which is considered in the present dissertation. In this context, advanced strategies are discussed by Son *et al.*, who mainly focuses on approaches such as constrained H_∞ , terminal sliding mode, adaptive robust control and fault tolerant control [28]. Less complex and commonly adopted control approaches are the skyhook and groundhook logic [116], along with the LQR [94].

The present dissertation focuses on the latter strategies. The vehicle dynamics is addressed through a linear description of the quarter-car model, which is schematized in Fig. 4.11. Specifically, the secondary suspension—which is composed of the spring and REmSA parallel (Fig. 4.7)—is replaced by an actuator that provides the force F_s :

$$F_s = -F_{\text{spring}} - F_{\text{act}} \quad (4.6)$$

F_{act} being the REmSA force and $F_{\text{spring}} = k_s(z_s - z_u)$ the spring force. The system features the following equations of motion:

$$\begin{aligned} m_s \ddot{z}_s - F_s &= 0 \\ m_u \ddot{z}_u + F_s + k_u(z_u - z_r) &= 0 \end{aligned} \quad (4.7)$$

where the weight of the masses is omitted as its contribution is balanced in the

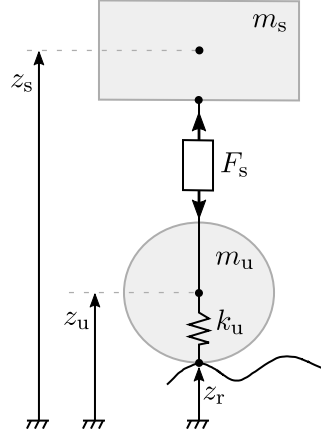


Figure 4.11: Linear description of the quarter-car model used for the investigation of the high-level control.

static equilibrium. The inputs of the model are the secondary suspension force F_s and the road profile z_r . The latter is discussed in Sec. 3.3.1. The equations can be arranged into the state space formulation:

$$\dot{\mathbf{z}} = \mathbf{A}\mathbf{z} + \mathbf{B}\mathbf{u} \quad (4.8)$$

$\mathbf{z} = [z_s \ z_s \ \dot{z}_s \ \dot{z}_u]^\top$ being the state vector, and $\mathbf{u} = [z_r \ F_s]^\top$ the input vector. The dynamic and input matrices are:

$$\mathbf{A} = \begin{bmatrix} 0 & 0 & 1 & 0 \\ 0 & 0 & 0 & 1 \\ 0 & 0 & 0 & 0 \\ 0 & -\frac{k_u}{m_u} & 0 & 0 \end{bmatrix} \quad \mathbf{B} = \begin{bmatrix} 0 & 0 \\ 0 & 0 \\ 0 & \frac{1}{m_s} \\ \frac{k_u}{m_u} & -\frac{1}{m_u} \end{bmatrix} \quad (4.9)$$

The performance indicators have been discussed in Sec. 3.3.1. Specifically, the comfort level is assessed through the sprung mass acceleration filtered by means of the ISO 2631 function [92], whereas the road holding index is given by:

$$\eta_{rh} = \frac{k_u (z_u - z_r)}{g (m_s - m_u)} \quad (4.10)$$

The suspension stroke is a further performance indicator as excessive value could lead to hit the bump stops with consequently deterioration of ride comfort and possible structural damage [19, 94].

The outputs of the state space are the signals needed to assess the performance indexes, and the states of the system. The latter are required as input for the high level controller (Fig. 4.8). Therefore, the output vector is:

$$\mathbf{y} = [z_s \ z_u \ \dot{z}_s \ \dot{z}_u \ \ddot{z}_s \ z_u - z_r \ z_s - z_u]^\top \quad (4.11)$$

which includes the sprung mass acceleration, the tire deflection and the suspension stroke. The output equation of the state space formulation is:

$$\mathbf{y} = \mathbf{Cz} + \mathbf{Du} \quad (4.12)$$

where

$$\mathbf{C} = \begin{bmatrix} 1 & 0 & 0 & 0 \\ 0 & 1 & 0 & 0 \\ 0 & 0 & 1 & 0 \\ 0 & 0 & 0 & 1 \\ 0 & 0 & 0 & 0 \\ 0 & 1 & 0 & 0 \\ 1 & -1 & 0 & 0 \end{bmatrix} \quad \mathbf{D} = \begin{bmatrix} 0 & 0 \\ 0 & 0 \\ 0 & 0 \\ 0 & 0 \\ 0 & \frac{1}{m_s} \\ -1 & 0 \\ 0 & 0 \end{bmatrix} \quad (4.13)$$

Since the control performance are addressed under road unevenness scenario, the RMS metrics of the filtered acceleration and road holding index are evaluated, whereas the peak value is used for the suspension stroke. The model parameters reported in Sec. 4.3.2 are used in the remainder of this investigation.

Skyhook

The skyhook logic is dedicated to the comfort improvement [116]. It aims at damping the sprung mass dynamics to minimize its vibration. To this end, a damping action c_{SH} is introduced between the sprung body and an inertial reference frame, as schematized in Fig. 4.12. Ideally, the comfort maximization requires no damping at the secondary suspension . Nevertheless, undamped unsprung mass would significantly deteriorate the handling performance. For this reason, a damping action c is introduced.

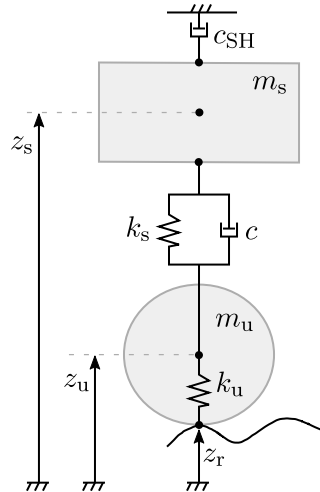


Figure 4.12: Quarter-car vehicle model with skyhook control

The following REmSA force synthesizes the skyhook control logic:

$$F_{\text{act}} = c_{\text{SH}}\dot{z}_s + c(\dot{z}_s - \dot{z}_u) \quad (4.14)$$

It can be rewritten in the form of an equivalent damping coefficient at the level of the secondary suspension:

$$c_{\text{eq,SH}} = c_{\text{SH}} \frac{\dot{z}_s}{\dot{z}_s - \dot{z}_u} + c \quad (4.15)$$

The equivalent damping depends on the vehicle states, i.e. sprung and unsprung mass velocities. It can assume positive and negative values, which correspond to passive and active operation, respectively. The latter cannot be implemented through semi-active solutions as they must observe the passivity constraint.

Two control parameters allow to set the control strategy. To address the vehicle performance at the diverse control tuning, several (c_{SH}, c) combinations are simulated to obtain the meaningful metrics. Specifically, Eq. 4.14 is implemented into the quarter-car model, which experiences the ISO B road profile at 70 km/h. Then, the performance indexes are extracted and plotted in Figs. 4.13. The tuning coefficients are varied as a logarithm distribution: c in the range 10 to 10 000 Ns/m, whereas c_{SH} between 10 and 20 000 Ns/m. Overall, 2500 combinations are simulated.

Figs. 4.13a and 4.13b show the iso- c curves in the handling-comfort and stroke-comfort planes, respectively. Specifically, each iso- c curve is obtained by varying the parameter c_{SH} while fixing c . The red dots indicate the condition $c_{\text{SH}} = 10$ Ns/m, helping to figure out the performance evolution with the parameter c_{SH} . Figs. 4.13c and 4.13d draw the iso- c_{SH} curves in the handling-comfort and stroke-comfort planes, respectively. The red dots indicate the condition $c = 10$ Ns/m.

Fig. 4.13a shows how very large damping c deteriorates the comfort performance, while improving the vehicle handling. Above a certain value, also the handling is worsened since the secondary suspension starts acting as a rigid element. At the same time, increasing c_{SH} significantly improves the comfort when approximately $\log_{10} c < 3$, as can be noted from the same figure by moving away from the red dots. This is clear also from Fig. 4.13c, which highlights how the best comfort is obtained at very high c_{SH} and small c . Fig. 4.13b shows that the secondary suspension locking (very large c) significantly reduces the maximum stroke. On the other hand, $\log_{10} c_{\text{SH}}$ values in the range 2.5 to 3 optimizes the stroke.

Overall, the best comfort is given by the combination $c = 168$ Ns/m and $c_{\text{SH}} = 20\,000$ Ns/m, which corresponds to the minimum RMS value of the sprung mass filtered acceleration (approximately $2 \cdot 10^{-2}$ g). The best handling follows from the combination $c = 1842$ Ns/m and $c_{\text{SH}} = 1431$ Ns/m, which gives a RMS value of the road holding index of 0.055.

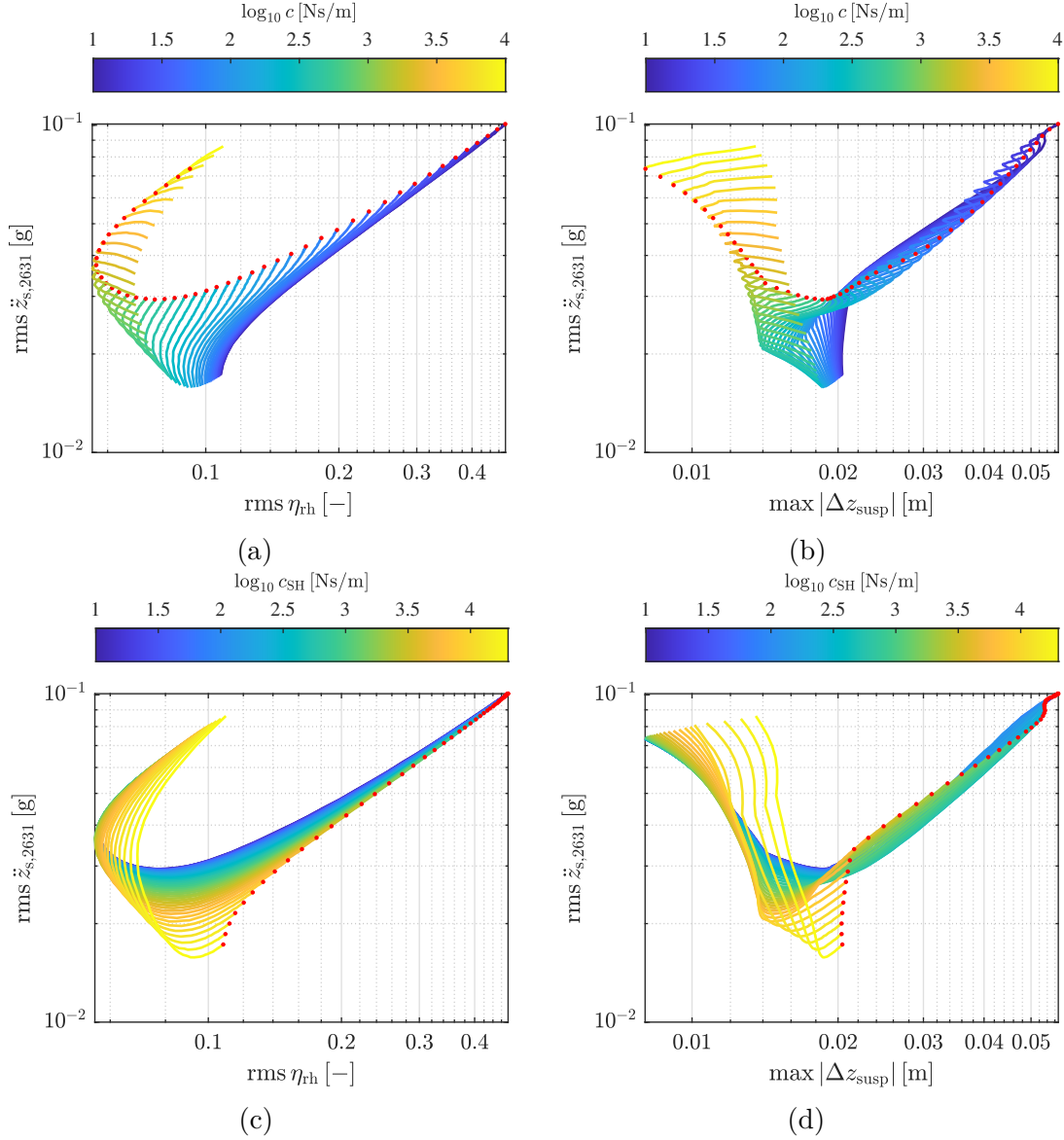


Figure 4.13: Carpet plot using the skyhook control logic into the linear quarter-car model. Iso- c curves in the handling-comfort (a) and stroke-comfort (b) planes, where the red dots indicate the condition $c_{SH} = 10$ Ns/m. Iso- c_{SH} curves in the handling-comfort (c) and stroke-comfort (d) planes, where the red dots indicate the condition $c = 10$ Ns/m.

Groundhook

The groundhook logic is dedicated to the handling performance of the vehicle [116]. Hence, it aims at minimizing the tire deflection under dynamic operation, as it corresponds to a variation of the tire-ground contact force. To this end, a

damping action c_{GH} is ideally introduced at the contact point between the ground and the unsprung mass, as shown in Fig. 4.14. This leads to the same advantages of increasing the damping of the tire. On the other hand, the latter would be not convenient as it raises the rolling resistance with a strong heating of the tire. Similarly to the skyhook strategy, no damping of the secondary suspension maximizes the performance, in this case the handling one. Nevertheless, undamped sprung mass would significantly deteriorate the comfort. For this reason, a damping action c must be introduced.

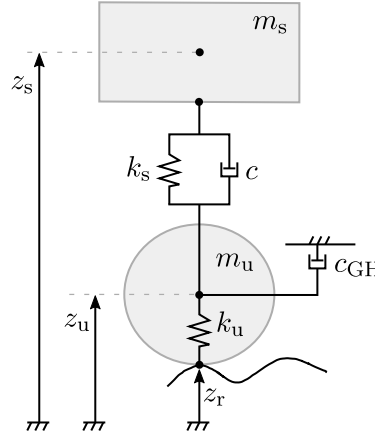


Figure 4.14: Quarter-car vehicle model with groundhook control

The following REmSA force synthesizes the groundhook control logic:

$$F_{\text{act}} = -c_{GH}\dot{z}_u + c(\dot{z}_s - \dot{z}_u) \quad (4.16)$$

It can be rewritten in the form of an equivalent damping coefficient at the level of the secondary suspension:

$$c_{\text{eq,GH}} = -c_{GH} \frac{\dot{z}_u}{\dot{z}_s - \dot{z}_u} + c \quad (4.17)$$

As for the skyhook case, it can assume positive and negative values, which corresponds to passive and active operations, respectively. The latter cannot be implemented through semi-active solutions as they must observe the passivity constraint.

Two control parameters allow to set the control strategy. To address the vehicle performance at the diverse control tuning, several (c_{GH}, c) combinations are simulated to obtain the meaningful metrics. Specifically, Eq. 4.16 is implemented into the quarter-car model, which undergoes the ISO B road profile at 70 km/h. Then, the performance indexes are extracted and plotted in Figs. 4.15. The tuning parameters are varied as a logarithm distribution: c in the range 10 to 10 000 Ns/m, whereas c_{GH} between 10 and 1000 Ns/m. Overall, 1470 combinations are simulated.

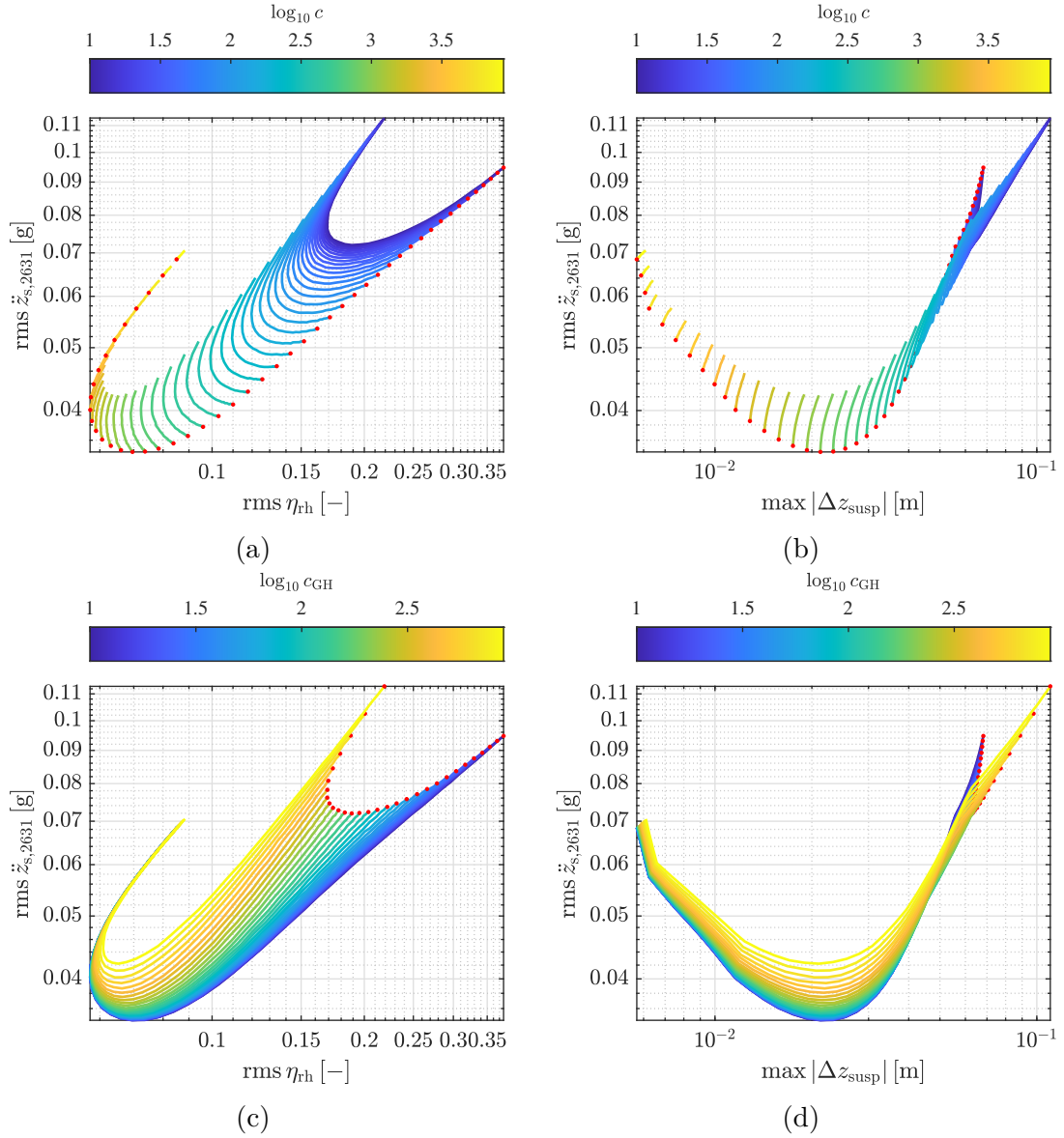


Figure 4.15: Carpet plot using the groundhook control logic into the linear quarter-car model. Iso- c curves in the handling-comfort (a) and stroke-comfort (b) planes, where the red dots indicate the condition $c_{\text{GH}} = 10 \text{ Ns/m}$. Iso- c_{GH} curves in the handling-comfort (c) and stroke-comfort (d) planes, where the red dots indicate the condition $c = 10 \text{ Ns/m}$.

Figs. 4.15a and 4.15b show the iso- c curves in the handling-comfort and stroke-comfort planes, respectively. Specifically, each iso- c curve is obtained by varying the parameter c_{GH} while fixing c . The red dots indicate the condition $c_{\text{GH}} = 10 \text{ Ns/m}$, helping to figure out the performance evolution with the parameter c_{GH} . Figs.

4.15c and 4.15d draw the iso- c_{GH} curves in the handling-comfort and stroke-comfort planes, respectively. The red dots indicate the condition $c = 10$ Ns/m.

The best comfort is obtained at low c_{GH} values, corresponding to the combination $c = 910$ Ns/m and $c_{GH} = 10$ Ns/m. This can be seen also in Figs. 4.15c and 4.15d: the suspension stroke is minimized by low c_{GH} values. As for the skyhook logic, the larger the damping c , the smaller the suspension stroke. Overall, parameter c_{GH} improves the handling performance only. The best handling is obtained from the combination $c = 2121$ Ns/m and $c_{GH} = 40$ Ns/m, which gives a RMS value of the road holding index of 0.057. In conclusion, the groundhook logic improves the handling of the vehicle. Nevertheless, the best handling setting gives comparable performance as its skyhook counterpart tuned for the handling optimization.

Spring negation

The spring negation strategy aims at isolating the sprung mass from the external disturbance coming from the terrain. Therefore, the logic is dedicated to the comfort improvement. To this end, the actuator introduces a negative stiffness contribution k_{SN} to counteract the dynamic variation of the elastic force of the secondary suspension. If the latter is fully compensated ($k_{SN} = k_s$) and no damping action is introduced, the sprung and unsprung masses are completely decoupled. In this way, the road disturbance cannot be transmitted to the sprung mass and, consequently, the comfort is maximized. On the other hand, very poor handling is obtained because of the completely undamped unsprung mass. For this reason, a damping action c must be introduced.

The following REmSA force synthesizes the spring negation control logic:

$$F_{act} = -k_{SN}(z_s - z_u) + c(\dot{z}_s - \dot{z}_u) \quad (4.18)$$

Two control parameters allow to set the control strategy. To address the vehicle performance at the diverse control tuning, several (k_{SN}, c) combinations are simulated to obtain the meaningful metrics. Specifically, Eq. 4.18 is implemented into the quarter-car model, which undergoes the ISO B road profile at 70 km/h. Then, the performance indexes are extracted and plotted in Figs. 4.16. The tuning parameters are varied as a logarithm distribution: c in the range 10 to 10 000 Ns/m, whereas k_{SN} between 1 and k_s (23 kN/m). Overall, 10 000 combinations are simulated.

Figs. 4.16a and 4.16b show the iso- c curves in the handling-comfort and stroke-comfort planes, respectively. Specifically, each iso- c curve is obtained by varying the parameter k_{SN} while fixing c . The red dots indicate the condition $k_{SN} = 1$ N/m, helping to figure out the performance evolution with the parameter k_{SN} . Figs. 4.16c and 4.16d show the iso- k_{SN} curves in the handling-comfort and stroke-comfort planes, respectively. The red dots indicate the condition $c = 10$ N/m.

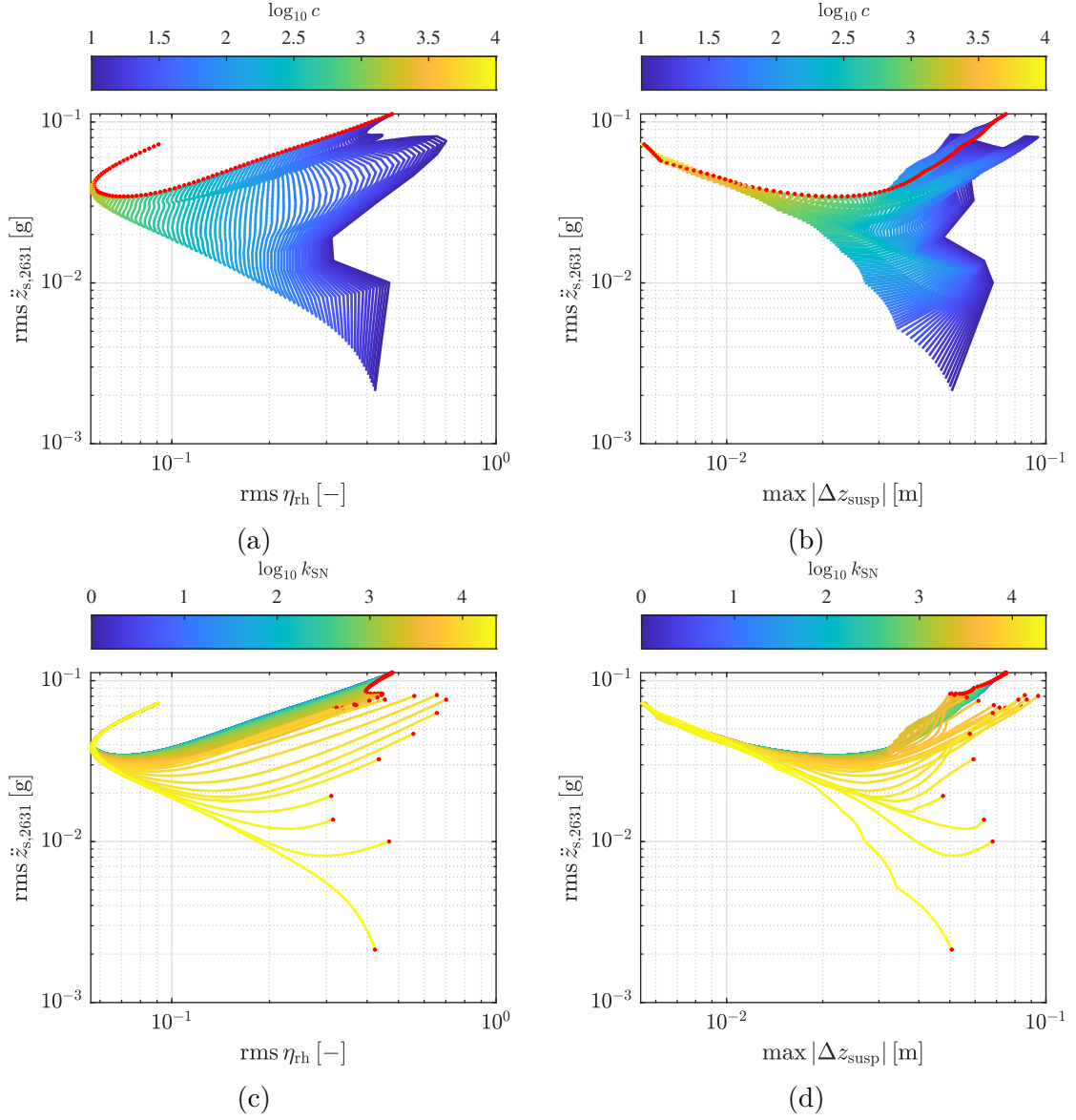


Figure 4.16: Carpet plot using the spring negation control logic into the linear quarter-car model. Iso- c curves in the handling-comfort (a) and stroke-comfort (b) planes, where the red dots indicate the condition $k_{SN} = 1 \text{ N/m}$. Iso- k_{SN} curves in the handling-comfort (c) and stroke-comfort (d) planes, where the red dots indicate the condition $c = 10 \text{ Ns/m}$.

The best comfort (0.002 g of comfort index) is obtained at the minimum value of c and $k_{SN} = k_s$. In fact, this condition allows to isolate the sprung mass from the road disturbance. Nevertheless, poor handling and suspension stroke performance

are obtained. The increase of damping c improves the handling, whose best performance is obtained from the combination $c = 2154 \text{ Ns/m}$ and $k_{\text{SN}} = 9230 \text{ N/m}$ and gives a road holding index of 0.056. Overall, the spring negation logic leads to the best comfort performance among the above-reported control strategies, even if it implies too poor handling and stroke results.

Linear-Quadratic Regulator

The LQR for active suspension control was introduced by Hrovat [94], who highlighted the performance improvement of a vehicle model equipped with ideal force actuators controlled through the LQR approach. This strategy minimizes a quadratic cost function that includes the performance indexes related to ride comfort and handling. Few weighting coefficients are sufficient to tune the control. Thanks to its simple implementation and high computational efficiency, the LQR approach is regarded as a very advantageous solution for the active suspension control. By converse, full state feedback is required, thus implying additional sensors or state observers for its implementation on real applications.

The LQR approach relies on the state-space description of the system (Eq. 4.8). The states of the system are rewritten in terms of the performance indexes that must be optimized. To this end, the state vector is transformed by means of the full-rank matrix \mathbf{T} :

$$\begin{aligned} \mathbf{x} &= [z_s - z_u \quad z_u \quad \dot{z}_s \quad \dot{z}_u]^\top = \mathbf{T}\mathbf{z} \\ \mathbf{T} &= \begin{bmatrix} 1 & -1 & 0 & 0 \\ 0 & 1 & 0 & 0 \\ 0 & 0 & 1 & 0 \\ 0 & 0 & 0 & 1 \end{bmatrix} \end{aligned} \quad (4.19)$$

The redefined state vector includes the secondary suspension stroke and the tire deflection. The latter neglects the effect of the road profile z_r , which is considered as a perturbation. By combining Eqs. 4.8 and 4.19, the state space formulation is written as:

$$\dot{\mathbf{x}} = \mathbf{A}_x \mathbf{x} + \mathbf{B}_x u_x \quad (4.20)$$

where the input is $u_x = F_s$, and the matrices are:

$$\mathbf{A}_x = \mathbf{T}\mathbf{A}\mathbf{T}^{-1} \quad \mathbf{B}_x = \mathbf{T} \begin{bmatrix} 0 \\ 0 \\ \frac{1}{m_s} \\ -\frac{1}{m_u} \end{bmatrix} \quad (4.21)$$

The LQR is a state-feedback controller: it finds the control law u_x that minimizes the quadratic cost function

$$J(u_x) = \int_0^\infty (\mathbf{x}^\top \mathbf{Q} \mathbf{x} + R u_x^2) dt \quad (4.22)$$

where

$$u_x = F_s = -\mathbf{K}\mathbf{x} = -\mathbf{K}\mathbf{T}\mathbf{z} \quad (4.23)$$

\mathbf{K} being the optimal gain matrix found by solving the Riccati equation associated to the problem [117]. The weights in the cost function are:

$$\mathbf{Q} = \begin{bmatrix} r_s & 0 & 0 & 0 \\ 0 & r_h & 0 & 0 \\ 0 & 0 & 0 & 0 \\ 0 & 0 & 0 & 0 \end{bmatrix} \quad R = \frac{1}{m_s} \quad (4.24)$$

where r_s and r_h weight the suspension stroke and tire deflection, respectively. The scalar R determines the sprung mass acceleration from the secondary suspension force $u_x = F_s$. Therefore, the control strategy can be tuned toward the optimization of handling or comfort by means of the two weights r_s and r_h . Specifically, low value of the tuning parameters gives more importance to the comfort, as the sprung mass acceleration dominates the cost function.

To address the vehicle performance at the diverse control tuning, several (r_s, r_h) combinations are simulated to obtain the meaningful metrics. Specifically, Eq. 4.23 is implemented into the quarter-car model, which undergoes the ISO B road profile at 70 km/h. Note that the REmSA force is obtained by substituting the LQR command $u_x = F_s$ into Eq. 4.6. The performance indexes are extracted and plotted in Figs. 4.17. The tuning parameters r_h and r_s are varied as a logarithm distribution in the range 1 to 10^8 . Overall, 2500 combinations are simulated. It must be remarked that the quarter-car model used for the analysis is linear: it does not include saturation of the actuator and the tire-ground detachment condition.

Figs. 4.17a and 4.17b show the iso- r_h curves in the handling-comfort and stroke-comfort planes, respectively. Specifically, each iso- r_h curve is obtained by varying the parameter r_s while fixing r_h . The red dots indicate the condition $r_s = 1$, helping to figure out the performance evolution with the parameter r_s . Figs. 4.17c and 4.17d draw the iso- r_s curves in the handling-comfort and stroke-comfort planes, respectively. The red dots indicate the condition $r_h = 1$. Results in the comfort-stroke plane point out that combining low r_s and high r_h gives unfeasible performance, as too large stroke makes the suspension hit the stops. The weight r_h improves the handling of the vehicle at the cost of the comfort performance.

The best handling performance, which features road holding index of 0.038, is given by the combination $r_h = 22.29 \cdot 10^6$ and $r_s = 3.39 \cdot 10^6$. Once the gain matrix \mathbf{K} is computed, the secondary suspension force is obtained from Eq. 4.23. Then, the REmSA force is computed through Eq. 4.6. By substituting and gathering the coefficients that multiply the states, the REmSA force resulting from the best handling setup can be written as:

$$F_{\text{act}} \approx -a_1(z_s - z_u) - a_2 z_u + a_3(\dot{z}_s - \dot{z}_u) - a_4 \dot{z}_u. \quad (4.25)$$

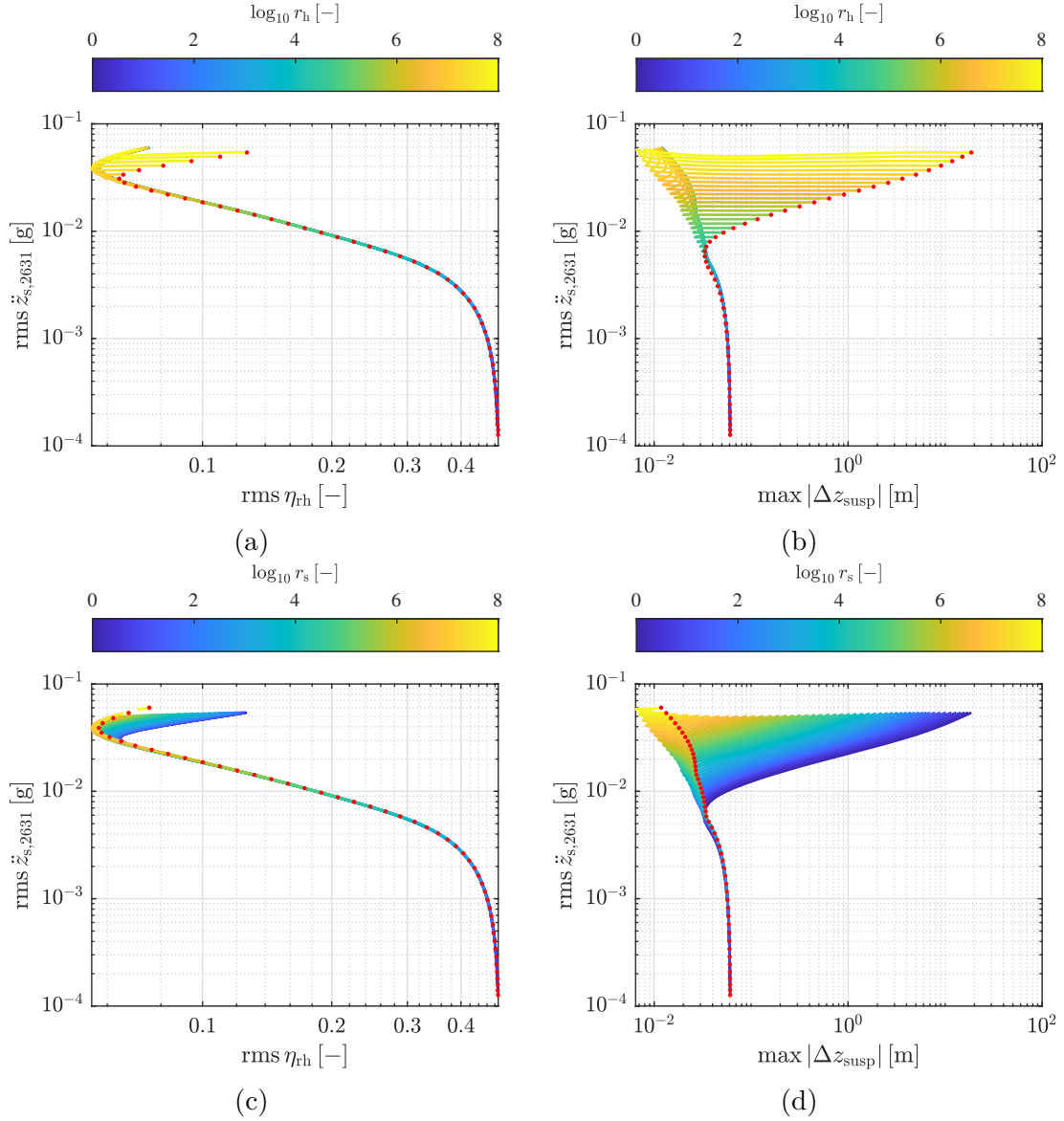


Figure 4.17: Carpet plot using the LQR control strategy into the linear quarter-car model. Iso- r_h curves in the handling-comfort (a) and stroke-comfort (b) planes, where the red dots indicate the condition $r_s = 1$. Iso- r_s curves in the handling-comfort (c) and stroke-comfort (d) planes, where the red dots indicate the condition $r_h = 1$.

where $a_1 = -1.46 \cdot 10^4 \text{ N/m}$, $a_2 = 1.62 \cdot 10^4 \text{ N/m}$, $a_3 = 1.57 \cdot 10^3 \text{ Ns/m}$, and $a_4 = 4.38 \cdot 10^3 \text{ Ns/m}$. By comparing the obtained relationship with Eqs. 4.14, 4.16 and 4.18, it is clear that the LQR gives a combination of the above-discussed control strategies: $-a_1(z_s - z_u)$ represents the spring negation contribution, where the

negative coefficient a_1 means that the secondary suspension stiffness is increased by the control logic, $a_3(\dot{z}_s - \dot{z}_u) - a_4\dot{z}_u$ is the groundhook. The term $-a_2z_u$ physically represents a spring connecting the unsprung mass to the inertial reference frame.

By following the same reasoning, the best comfort performance—comfort index of $1 \cdot 10^{-4}$ g obtained from from the combination $r_h = 1$ and $r_s = 1$ —gives a REmSA force that can be written as:

$$F_{\text{act}} \approx -a_1(z_s - z_u) + a_3(\dot{z}_s - \dot{z}_u) + a_5\dot{z}_s. \quad (4.26)$$

where $a_1 = 2.3 \cdot 10^4$ N/m, $a_3 = 13 \cdot 10^5$ Ns/m, and $a_5 = 0.5$ Ns/m. Also in this case, the LQR gives a combination of the above-discussed control strategies: $-a_1(z_s - z_u)$ represents the spring negation contribution, $a_3(\dot{z}_s - \dot{z}_u) + a_5\dot{z}_s$ is the skyhook. The latter term is very small, as the spring negation contribution dominates the present tuning.

However, the comfort tuning results in very poor handling performance. For this reason, a combination that gives a trade off between comfort and handling is found: $r_h = 3556$ and $r_s = 43$. It features road holding and comfort indexes of 0.13 and $14 \cdot 10^{-3}$ g, respectively. For this setting, the REmSA force can be written as:

$$F_{\text{act}} \approx -a_1(z_s - z_u) + a_3(\dot{z}_s - \dot{z}_u) + a_5\dot{z}_s. \quad (4.27)$$

where $a_1 = 2.25 \cdot 10^4$ N/m, $a_3 = 217$ Ns/m, and $a_5 = 118$ Ns/m. It is a combination of spring negation and skyhook. The latter term has a tuning more oriented to the handling than the comfort-oriented setting (Eq. 4.26).

The system performance with the three above-reported LQR settings is further investigated in the frequency domain. Figs. 4.18 show the FRF of the weighted sprung mass acceleration (a) and tire deflection (b) when the input is the road displacement. The comfort setting (blue) completely filters the road disturbance to the sprung mass, as can be noted by the very smooth behavior at frequency values close to 1 Hz, i.e. the sprung mass natural frequency. On the other hand, the unsprung mass is poorly damped. For this reason, the tire deflection features a very large resonance in correspondence of the unsprung mass natural frequency, thus resulting in poor handling performance. Conversely, the handling tuning (yellow) well damps the sprung and unsprung mass resonances, at the cost of increased sprung mass acceleration along the whole frequency range under investigation. This causes deteriorated comfort performance. The comfort-handling trade-off (orange) stays between these two settings.

Final considerations

Overall, the LQR logic gives a combination of the skyhook, spring negation and groundhook strategies. From the designer viewpoint, it is very advantageous as all these control strategies are achieved by tuning two parameters. For this reason,

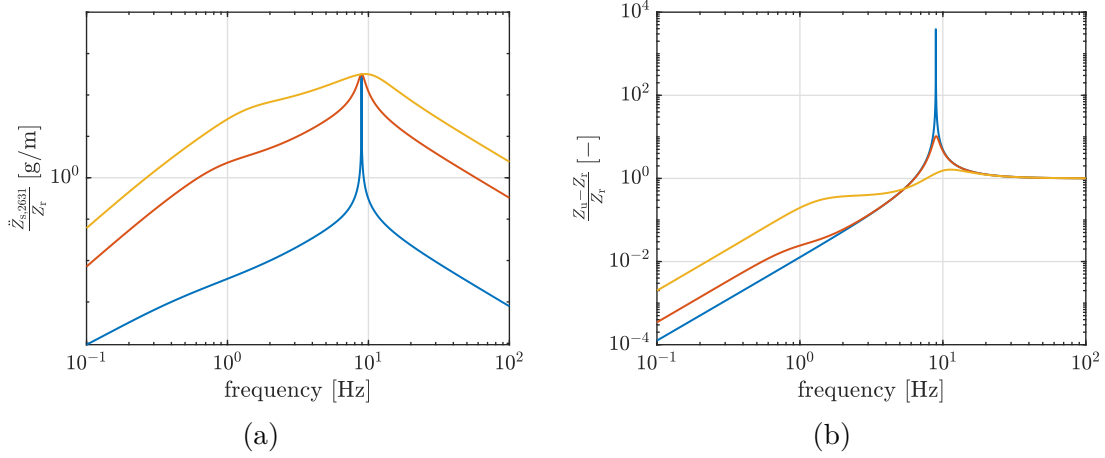


Figure 4.18: FRFs of the quarter-car with LQR suspension control when the input is the road displacement. Sprung mass filtered acceleration (a) and tire deflection (b) FRFs of the comfort-oriented (blue), comfort-handling trade-off (orange) and handling-oriented (yellow) LQR settings.

the LQR control is used in the remainder of the present chapter. Specifically, the three identified settings—which are reported in Table 4.1—are further investigated. These configurations optimize the vehicle performance in the considered road scenario (ISO B-class at 70 km/h). Although the LQR was tuned on a linear model, rougher road unevenness could lead to excessive suspension stroke thus making the identified settings unfeasible.

Table 4.1: Results of the quarter-car with LQR suspension control when the vehicle experiences the ISO B-class road at 70 km/h.

Feature	Value		
	Setting		
	Comfort-oriented	Trade-off	Handling-oriented
Weight r_h	1	$3.56 \cdot 10^5$	$22.23 \cdot 10^6$
Weight r_s	1	42.9	$3.39 \cdot 10^6$
Comfort performance index	$1 \cdot 10^{-4}$ g	$1.4 \cdot 10^{-2}$ g	$3.8 \cdot 10^{-2}$ g
Road holding index	0.49	0.13	0.05
Max. suspension stroke	61 mm	71 mm	18 mm

In conclusion, the above-discussed control strategies are suitable for random road unevenness scenarios. Especially the LQR approach, as it is appropriate for

the optimization of RMS metrics. When lumped obstacles or vehicle maneuvers are considered, the RMS metrics are not indicative anymore. Therefore, the LQR control is limited and more suitable strategies must be explored to achieve better vehicle performance.

A clear example is the collocation-type trajectory optimization control proposed by Čorić [15], which specifically addresses the bump and pothole road scenario of a vehicle equipped with active suspensions. The optimization finds a control trajectory that minimizes a cost function. It includes the sprung mass acceleration, the tire deflection, the suspension stroke and the first time-derivative of the actuation force. The latter is needed to avoid oscillations in the system response. In some cases, the objective function is completed with the energy consumption of the actuator, and a variable indicating the wheel damage. Some user-defined weights tune the control strategy. The hard-constraints of the optimization are the maximum actuator force and the tire-ground contact force. The latter avoids the tire-ground detachment: it is one of the main advantages of the proposed strategy with respect to LQ-based controls. In fact, they cannot avoid the detachment as they minimize RMS metrics. The comparison with the passive suspension performance highlights the potential of the proposed strategy, especially when large road disturbance is considered. According to the control settings, the lumped road disturbance could be completely filtered so that the sprung mass does not experience very little acceleration.

The collocation-type trajectory optimization control requires the knowledge of the road profile. Therefore, its implementation on autonomous vehicles is straightforward, as sensors for the environment perception are already present on-board. The idea could be to use LQ-based control strategies in random road unevenness conditions, then switch to the collocation-type trajectory optimization control (or similar strategy) as a lumped obstacle is perceived.

4.3 Results

Numerical investigation is carried out to assess REmSA impact on the vehicle performance, as well as the effect of the low and high level controls. The latter considers the three LQR settings reported in Table 4.1. In addition, a control strategy that reproduces the conventional passive damper operation is also implemented. Due to the project timeline, the investigation is based on the prototype developed for the automotive application (Appx. A).

4.3.1 REmSA model identification

The REmSA model presented in Sec. 4.1.1 is composed of the electric machine and the mechanical subsystem. The former is populated with the loss map extracted from FluxMotor simulation (Fig. 4.5), the latter requires the tuning of

their parameters. To this end, an identification process is carried out by using the experimental data obtained by means of a dedicated test bench (see Sec. 5.3.1). Specifically, the lever mounted on the input shaft of the prototype was driven with sinusoidal displacement profiles through a hydraulic linear actuator. At the same time, the electric machine was connected to a controlled power module to reproduce a damping action. Specifically, the high level control multiplies the linear velocity of the hydraulic actuator by a damping coefficient to compute the REmSA force request. Then, the torque request—which is sent to the controlled power module—is computed by means of the overall transmission ratio τ_t . No low level control was used: the mechanical dynamics of the prototype is not compensated on purpose so that it emerges from the experimental measurements.

By referring to Fig. 4.2, the suspension velocity and the electric machine torque are the inputs of the mechanical subsystem. The former coincides with the hydraulic actuator velocity, which is obtained as the first time-derivative of the measured position. The latter is computed from the q-axis current reference commanding the controlled power module. Specifically, the electric machine torque constant K_t relates the current command and the electric machine torque. The main assumption is that the torque control of the electric machine does not introduce any effect in the frequency range of interest. The torque constant is left as a free parameter to be identified. Its initial value is estimated from electromagnetic finite element simulation. The REmSA force is the output of the model. In the real system, it is measured by means of a load cell that is mounted on the hydraulic actuator head.

The identification is performed through the nonlinear least-squares algorithm, which is available in Matlab[®]. It solves nonlinear least-squares curve fitting problems by minimizing the sum of squared residuals:

$$\min_x \|f(x)\|_2^2 = \min_x (f_1(x)^2 + f_2(x)^2 + \dots + f_n(x)^2) \quad (4.28)$$

x being the set of design variables and f_i the tracking error computed at sampling time instants, i.e. the difference between the experimental measured force and the model output. Sampling frequency equal to 4 kHz was used.

Overall, the algorithm searches for the design variable set that minimizes the least-square tracking error. The design variable array is composed of eight elements, whose lower and upper bounds are defined to speed the convergence up and avoid non-physical values. Specifically, each element x_i is defined as a gain that multiplies the nominal value of the i th parameter. Therefore, the i th tuned parameter p_i is written as:

$$p_i = x_i p_{\text{nom}} \quad (4.29)$$

p_{nom} being the i th nominal parameter. The nominal values and the identified design variables are reported in Table 4.2. Nominal values of the compliant mount, i.e. stiffness and damping, equivalent mass, and mechanical loss damping are taken from the experimental fitting reported in Sec. 5.3.1. The backlash-related parameters, i.e. bounds, transition region and mount damping are completely unknown.

Therefore, their initial guess was found by means of a trial-and-error process. Note that the torque constant is not included into the REmSA model: it is used for identification purposes only, as it converts the experimental reference current into electric machine torque.

Table 4.2: Nominal parameters and identified design variables of the REmSA mechanical subsystem (Sec. 4.1.1).

Model block	Feature	Value	
		Nominal parameter	Identified design variable
Equivalent mass	Mass	5.6 kg	1.100
	Bound	$2 \cdot 10^{-4}$ m	0.046
Backlash and compliant mount	Contact stiffness	$5 \cdot 10^5$ N/m	1.352
	Contact damping	100 Ns/m	5.452
	Transition region	$1.5 \cdot 10^{-3}$ m	2.558
Mech. loss	Damping	70 Ns/m	1.519
Mount damping	Damping	500 Ns/m	0.590
-	Torque constant	$49.3 \cdot 10^{-3}$ Nm/A	0.866

The identified model is compared to the experimental data at diverse test settings, i.e. frequency of the imposed displacement and damping coefficient of REmSA high level control. Figs. 4.19 and 4.20 compares the REmSA force—simulated (blue) and experimental (orange)—in the force-displacement and force-time planes. Specifically, Figs. 4.19 show the results at 15 Hz input displacement frequency when the control damping is set at 0 Hz (a and b) and 4 kNs/m (c and d). Figs. 4.20 refers to the test condition with 5 Hz input displacement frequency and 4 kNs/m control damping.

The maximum force mismatch in absolute value and the energy percentage error are reported in Table 4.3. The latter—which refers to the error on the energy dissipated by the REmSA—is obtained from the area of the displacement-force loop. Although the force error is not negligible, the identified model is able to reproduce the dynamic behavior of the real system at diverse input frequencies and force levels, as shown in the above-reported figures. Furthermore, the small energy error confirms that the identified model accurately reproduces the dissipative behavior of the prototype.

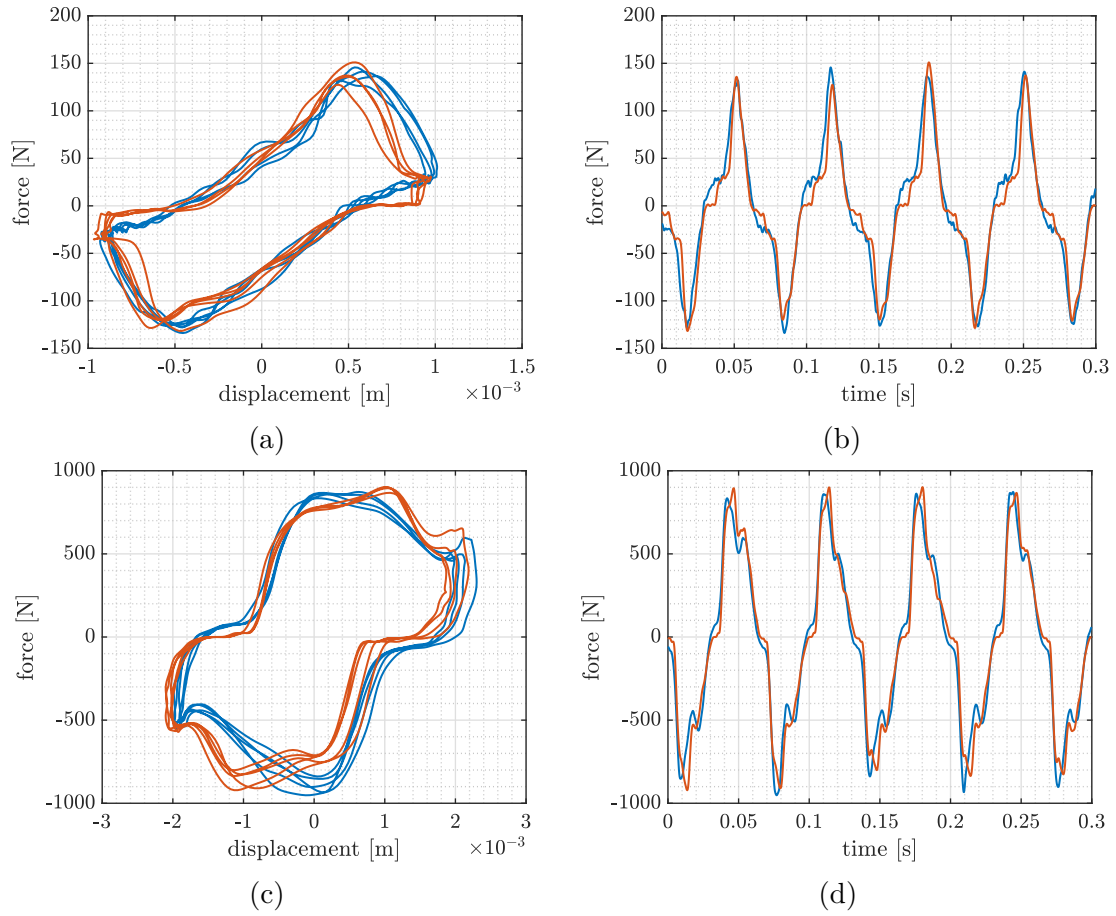


Figure 4.19: Comparison of the REmSA force—simulated (blue) and experimental (orange)—in the force-displacement (a and c) and force-time (b and d) planes. Test at 15 Hz input displacement frequency with the high level control damping set at 0 kNs/m (a and b) and 4 kNs/m (c and d).

Table 4.3: Results of the REmSA mechanical subsystem model identification

Description	Units	Value		
Input frequency	Hz	15	15	5
Control damping	kNs/m	0	4	4
Maximum force mismatch	N	63	307	128
Energy error	%	1.75	1.79	-0.27

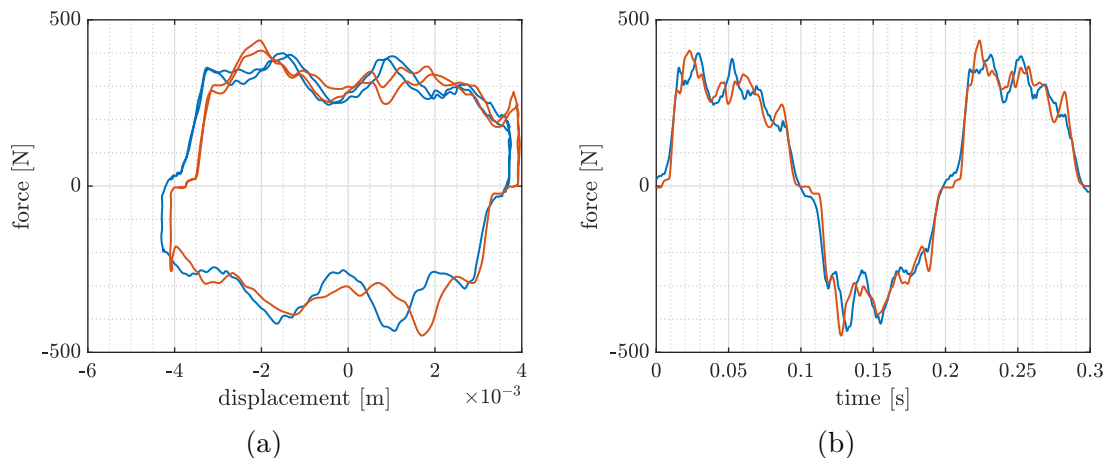


Figure 4.20: Comparison of the REmSA force—simulated (blue) and experimental (orange)—in the force-displacement (a) and force-time (b) planes. Test at 5 Hz input displacement frequency with the high level control damping set at 4 kNs/m.

4.3.2 Vehicle dynamics simulations

The complete model (discussed in Sec. 4.1) is simulated to assess the performance in terms of vehicle dynamics and energetic features of the active suspension. It includes the REmSA and the quarter-car model, whose parameters are reported in Table 4.4. The REmSA is composed of the mechanical subsystem—whose identified parameters are reported in Table 4.2—and the electric machine, whose power loss map and maximum torque curve are shown in Fig. 4.5.

Table 4.4: Parameters of the quarter-car vehicle model

Description	Symbol	Value
Sprung mass	m_s	417 kg
Unsprung mass	m_u	40 kg
Secondary suspension stiffness	k_s	23 kN/m
Tire stiffness	k_u	126 kN/m

The low level control—i.e. the force control of the REmSA—is a PID with filtered derivative, which is implemented in the parallel structure:

$$LL = P + \frac{I}{s} + \frac{Ds}{s/N + 1} \quad (4.30)$$

s being the Laplace variable. The controller is designed to achieve an actuation bandwidth of 60 Hz: the tuned control gains are reported in Table 4.5.

Table 4.5: Low level control gains tuned for 60 Hz bandwidth

Description	Symbol	Value
Proportional	P	7.4
Integral	I	1000 N/s
Derivative	D	$5.9 \cdot 10^{-3}$ Ns
Filter coefficient	N	6283 rad/s

As discussed in Sec. 4.2.2, the high level control implements the LQR strategy. Specifically, the three settings reported in Table 4.1 are tested: comfort-oriented, comfort-handling trade-off, and handling-oriented. Additionally, a damping control strategy is also implemented to make a comparison with the LQR logic. Specifically, it makes the REmSA reproduce the conventional damper operation, as described in Sec. 3.3.1. Maximum and minimum damping settings are implemented, whose characteristics are reported in Fig. 4.21. The damping corresponding to the steepest part of the characteristic is 10 kNs/m and 2.6 kNs/m for the maximum and minimum damping curves, respectively.

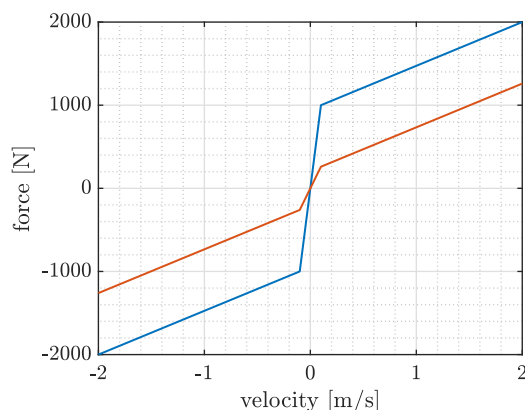


Figure 4.21: Maximum (blue) and minimum (orange) damping characteristics implemented in the high level damping control strategy. The damping corresponding to the steepest part of the characteristic is 10 kNs/m and 2.6 kNs/m for the maximum and minimum damping curves, respectively.

The simulations are performed when the vehicle experiences an ISO B-class road at 70 km/h. The resulting road profile (z_r) is shown in Fig. 4.22. Simulation time of 15 s is chosen to reproduce dynamic behaviors more than one decade below the slowest dynamics of the system, i.e. the sprung mass one.

The quarter-car with quasi-ideal and realistic REmSA are compared. The former features realistic electric machine and ideal mechanical subsystem (only the

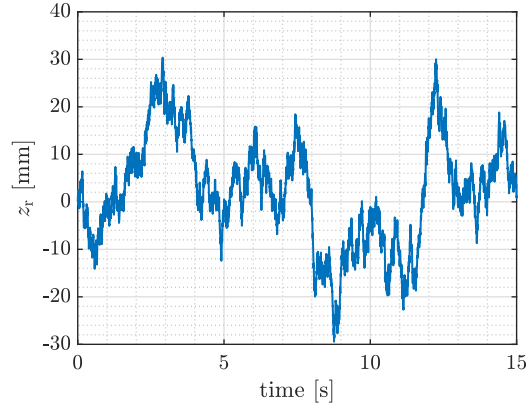


Figure 4.22: Time history of the ISO B-class road at 70 km/h

electric machine power loss is present), the latter includes also the realistic model of the REmSA (it accounts for the mechanical dynamics and the power dissipation of the mechanical subsystem). At the end, the vehicle with realistic REmSA is simulated with no low level control to understand how it impacts the energetic performance of the active suspension and the and vehicle dynamics.

The energetic performance are expressed in terms of average power, which is computed by dividing the energy in the simulated time-frame by the simulation time. In technical terms, it is the active component of the apparent power (see Para. 4.3.2). Additionally, the duty cycle of the REmSA is assessed: it is the fraction of total simulation time in which the system operates in the active or passive quadrants. In the same way, the duty cycle of the electric machine is computed. Part of the electric machine operation in the passive quadrants regenerates energy ($P_{el} > 0$). Therefore, the duty cycle of the regenerative operation is also assessed. The power convention was discussed in Sec. 4.1.1.

All the results obtained from the quasi-ideal and realistic models are compared at the end of this section.

Active, reactive and apparent power The instantaneous power signals are described by their apparent power, which is a well-known concept in the electrical domain where it is adopted in the case of AC systems. The same considerations can be extended to the mechanical domain [118], where the force and velocity quantities are equivalent to voltage and current, respectively. The apparent power features an active component, which corresponds to a net transfer of energy between two systems, and a reactive one. The latter represents energy that bounces back and forth between the two systems, which are:

- The suspension and the mechanical subsystem (for the mechanical power at the REmSA shaft).

- The mechanical subsystem and the electric machine (for the mechanical power at the electric machine shaft).
- The electric machine and the battery (for the electrical power).

However, the apparent power is commonly adopted for sinusoidal signals, which is not the present case. It is quantified by means of the procedure described by Mizoguchi *et al.*, where non-sinusoidal force and velocity are interpreted as *distorted* waves, i.e. a combination of the sinusoidal contributions composing the signals [118]. Then, the apparent power is computed as the product between the RMS value of the force and velocity distorted waves. The latter are calculated as:

$$S_{\text{rms,d}} = \sqrt{\sum_{k=1}^K S_{k,\text{rms}}^2} \quad (4.31)$$

where S is the signal (force or velocity), and $S_{k,\text{rms}} = S_k/\sqrt{2}$ the RMS value of the k th harmonics. S_k is the amplitude of the k th harmonic, which is extracted from the Fourier decomposition of the signal. The active power is the time-integral average of the instantaneous power.

After the active and apparent power terms are computed, the power factor is computed as the ratio between the active and apparent powers. It indicates the amount of power which corresponds to a net energy transfer: when the reactive power is null, unitary power factor indicates that all the power performs real work.

The reactive power do not directly impact the efficiency of the system. However, it quantifies the energy amount that bounces back and forth between two systems. The latter features intrinsic dissipation: when the energy moves, a certain amount is wasted. Overall, large reactive power indicates the bouncing of a large amount of energy, thus leading to higher energy loss.

Both the quasi-ideal and realistic models could feature non-unitary power factor. Specifically, this happens when the high level control strategy implements some elastic contribution, for instance the spring negation logic. In such case, the REmSA is seen by the suspension as a reactive system. However, the apparent power is analyzed for the realistic model, whereas the active component only is reported for the quasi-ideal case.

Quasi-ideal REmSA

The quarter-car is equipped with the REmSA model that feature realistic electric machine and ideal mechanical subsystem. Specifically, the REmSA includes the electric machine power loss and the limited actuation capability imposed by the maximum torque curve. Conversely, the mechanical dynamics and friction are not considered: the mechanical subsystem described in Sec. 4.1.1 is replaced by a

rigid connection between the electric machine and the REmSA shaft. In the following, the vehicle model is simulated when it experiences an ISO B-class road profile at 70 km/h with diverse high level control strategies.

Maximum damping control The results are extracted from the quasi-ideal model with the high level control reproducing the maximum damping characteristic reported in Fig. 4.21.

The time response of the REmSA force is shown in Fig. 4.23a. It coincides with the force requested by the high level control, as no torque saturation of the electric machine occurs and the mechanical subsystem is ideal. The latter makes the mechanical power entering the REmSA ($P_{\text{mech,REmSA}}$) coincide with the power flowing to the electric machine.

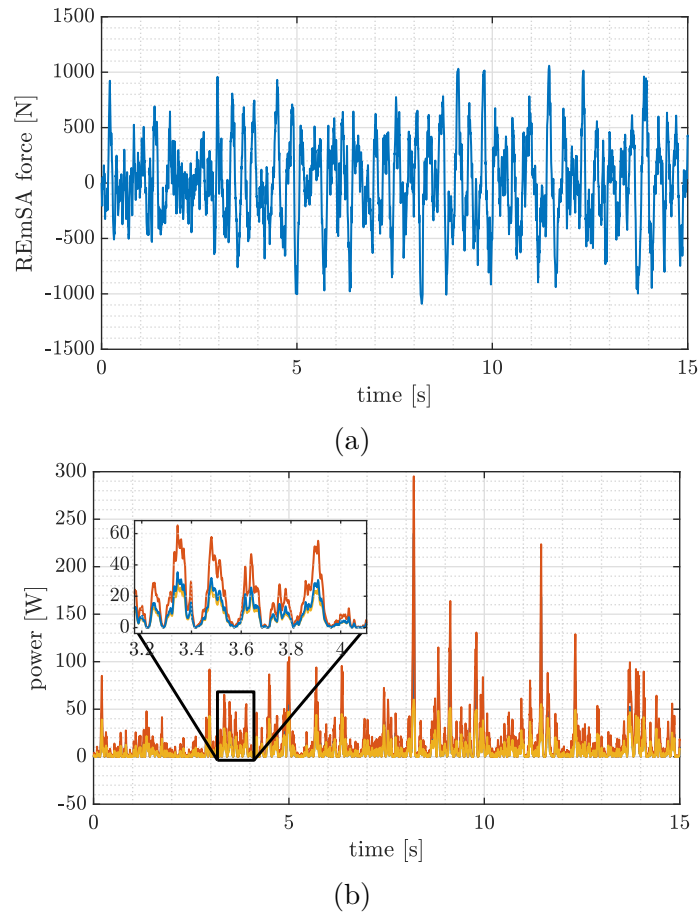


Figure 4.23: Quasi-ideal model with the high level control reproducing the maximum damping characteristic. REmSA force (a) and instantaneous power (b): electrical (blue), mechanical (orange) and loss (yellow).

Fig. 4.23b shows the involved instantaneous power, i.e. the electrical power

(blue), mechanical power (orange) and power loss (yellow). The power loss is related to the dissipation in the electric machine. These power terms are always positive: the actuator always works as a damper, i.e. mechanical energy is absorbed from the suspension and regenerated in the form of electricity. Such operation follows from the high level control, which aims at reproducing the damper operation.

In terms of vehicle dynamics, the time response of the tire-ground contact force and filtered sprung mass acceleration are shown in Figs. 4.24. No tire-ground detachment occurs. Furthermore, the force dynamic variation is small, which results in a road holding index of 0.096. The filtered acceleration of the sprung mass gives stable response, which results in a comfort performance index of 0.077 g. According to the standard [92], such level is categorized as fairly uncomfortable. It must be highlighted that maximum damping setting penalizes the comfort to the advantage of the handling performance.

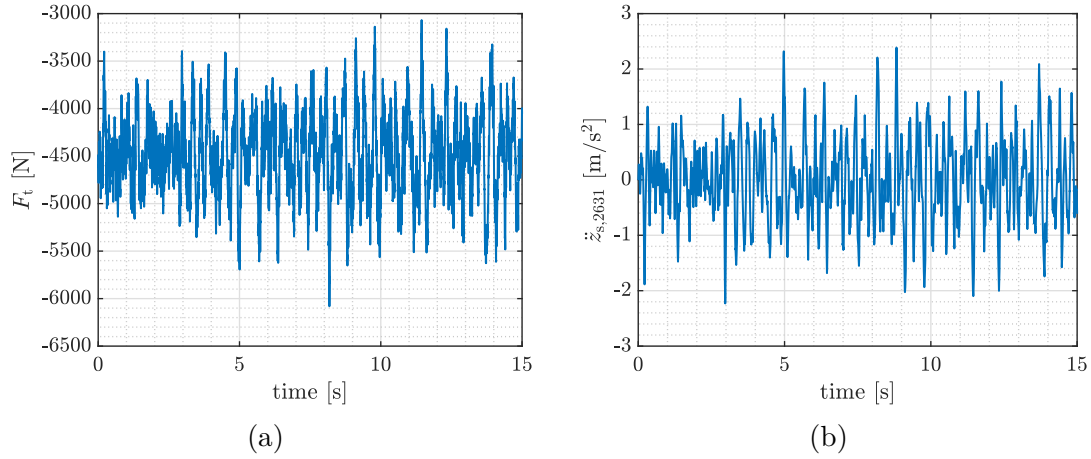


Figure 4.24: Quasi-ideal model with the high level control reproducing the maximum damping characteristic. Tire-ground contact force (a) and filtered sprung mass acceleration (b).

Figs. 4.25a and 4.25b show the force-speed operation of the REmSA at the suspension and electric machine levels, respectively. These coincide (minus the overall transmission ratio) as the ideal mechanical subsystem rigidly connects the electric machine to the suspension with no mechanical loss. The system well reproduces the maximum damping characteristic: it works always in the passive quadrants, where 92% of the time is covered by regenerative operation.

The energetic and vehicle dynamics performance are reported in Table 4.6. The average mechanical power is $P_{\text{mech,REmSA}} = 15.4 \text{ W}$, which flows from the suspension to the electric machine. The latter wastes $P_{\text{loss,EM}} = 6.9 \text{ W}$, and regenerates $P_{\text{el}} = 8.6 \text{ W}$. The peak electric power is 253.1 W. Overall, the REmSA conversion efficiency is $\eta_{\text{REmSA}} = 56 \%$, which is due to the electric machine.

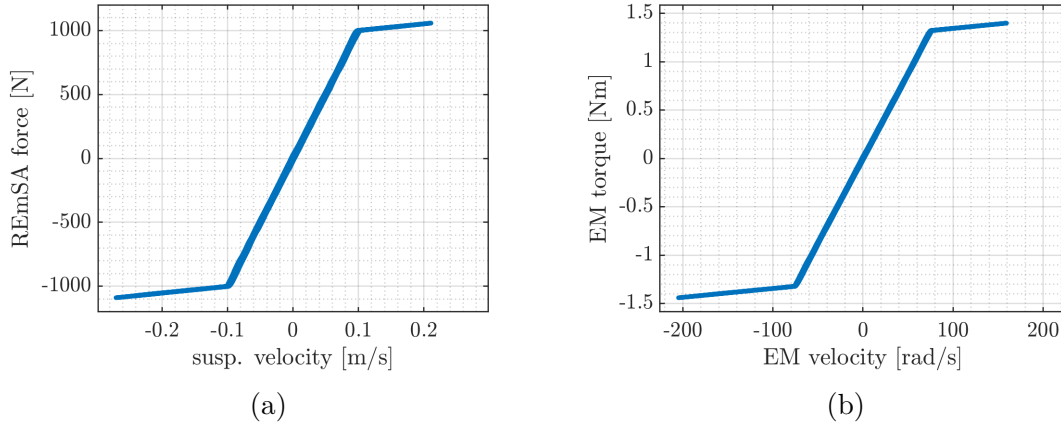


Figure 4.25: Quasi-ideal model with the high level control reproducing the maximum damping characteristic. Force-speed operation of the REmSA at the suspension (a) and electric machine (b) levels.

Table 4.6: Energetic and vehicle dynamics performance of the quasi-ideal model with the high level control reproducing the maximum damping characteristic.

Feature	Value
Electrical power	8.6 W
Mechanical power	15.4 W
Power loss	6.9 W
Conversion efficiency	56%
Active duty	0%
Passive duty	100%
Regeneration duty	92%
Comfort performance index	0.077 g
Road holding index	0.096

Minimum damping control The results are extracted from the quasi-ideal model with the high level control reproducing the minimum damping characteristic reported in Fig. 4.21.

The time response of the REmSA force is shown in Fig. 4.26a. It coincides with the force requested by the high level control, as no torque saturation of the electric machine occurs and the mechanical subsystem is ideal. The latter makes the mechanical power entering the REmSA ($P_{\text{mech,REmSA}}$) coincide with the power flowing to the electric machine.

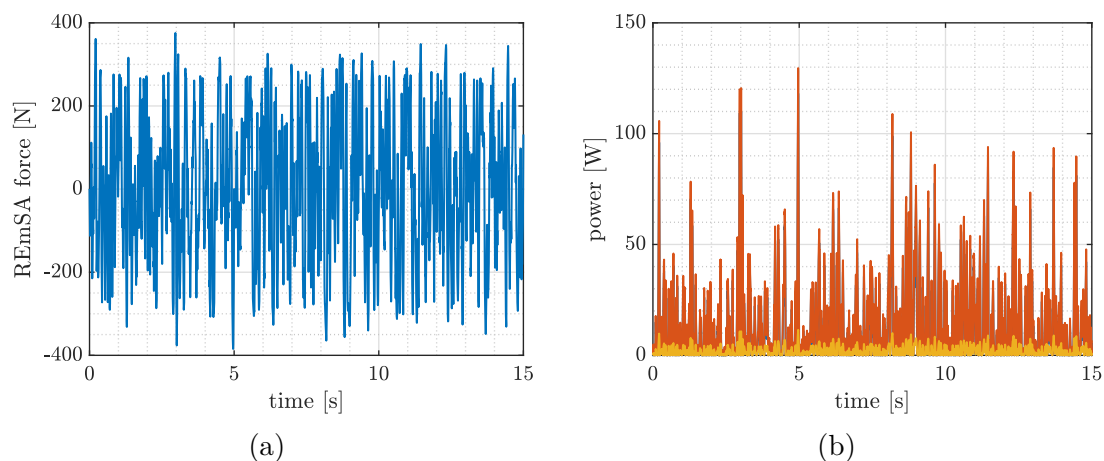


Figure 4.26: Quasi-ideal model with the high level control reproducing the minimum damping characteristic. REmSA force (a) and instantaneous power (b): electrical (blue), mechanical (orange) and loss (yellow).

Fig. 4.26b shows the involved instantaneous power, i.e. the electrical power (blue), mechanical power (orange) and power loss (yellow). The power loss is related to the dissipation in the electric machine. These power terms are always positive: the actuator always works as a damper, i.e. mechanical energy is absorbed from the suspension and regenerated in the form of electricity. Such operation follows from the high level control, which aims at reproducing the damper operation.

In terms of vehicle dynamics, the time response of the tire-ground contact force and filtered sprung mass acceleration are shown in Figs. 4.27. No tire-ground detachment occurs. Furthermore, the force dynamic variation is small, which results in a road holding index of 0.061. The filtered acceleration of the sprung mass gives stable response, which results in a comfort performance index of 0.042 g. According to the standard [92], such level is categorized as little uncomfortable.

The energetic and vehicle dynamics performance are reported in Table 4.7. The average power terms are positive: the energy flow goes from the suspension to the battery, which regenerates electrical energy. Overall, the REmSA conversion efficiency is $\eta_{\text{REmSA}} = 86\%$. The system always operates in the passive quadrants, and 94% of the total time regenerates energy. This control strategy results in higher efficiency than the maximum damping case: the electric machine operates in regions of the torque-velocity plane that feature better efficiency.

Comfort-oriented LQR The results are extracted from the quasi-ideal model with the high level control implementing the LQR with comfort-oriented setting (Table 4.1). The time response of the sprung mass filtered acceleration, tire-ground contact force and REmSA force are shown in Figs. 4.28. Tire-ground detachment occurs starting from 10 s, condition represented by the null contact force in 4.28b.

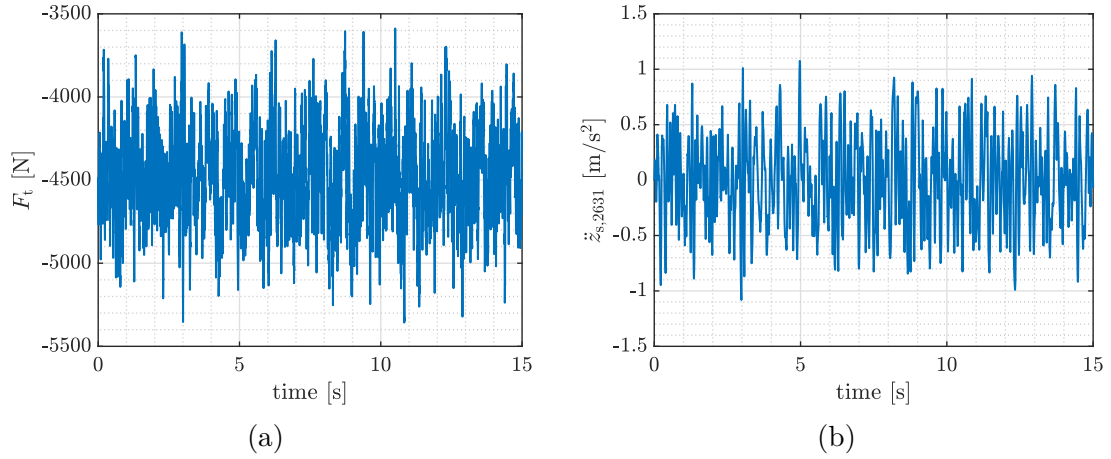


Figure 4.27: Quasi-ideal model with the high level control reproducing the minimum damping characteristic. Tire-ground contact force (a) and filtered sprung mass acceleration (b).

Table 4.7: Energetic and vehicle dynamics performance of the quasi-ideal model with the high level control reproducing the minimum damping characteristic.

Feature	Value
Electrical power	12.8 W
Mechanical power	14.9 W
Power loss	2.1 W
Conversion efficiency	86%
Active duty	0%
Passive duty	100%
Regeneration duty	94%
Comfort performance index	0.042 g
Road holding index	0.061

Repeated actuator saturation is evident from Fig. 4.28c.

Overall, the vehicle performance highlights a kind of unstable behavior, which was not present in the results reported in Sec. 4.2.2 for the same LQR setting. In this case, the non-linear description of the quarter-car model—i.e. torque saturation of the actuator and tire-ground detachment condition—significantly impacts the system response. Specifically, the LQR does not account for the system non-linear behavior, whereas the comfort-oriented tuning was derived from a linearized version. For these reasons, the non-linear model features deteriorated stability. The

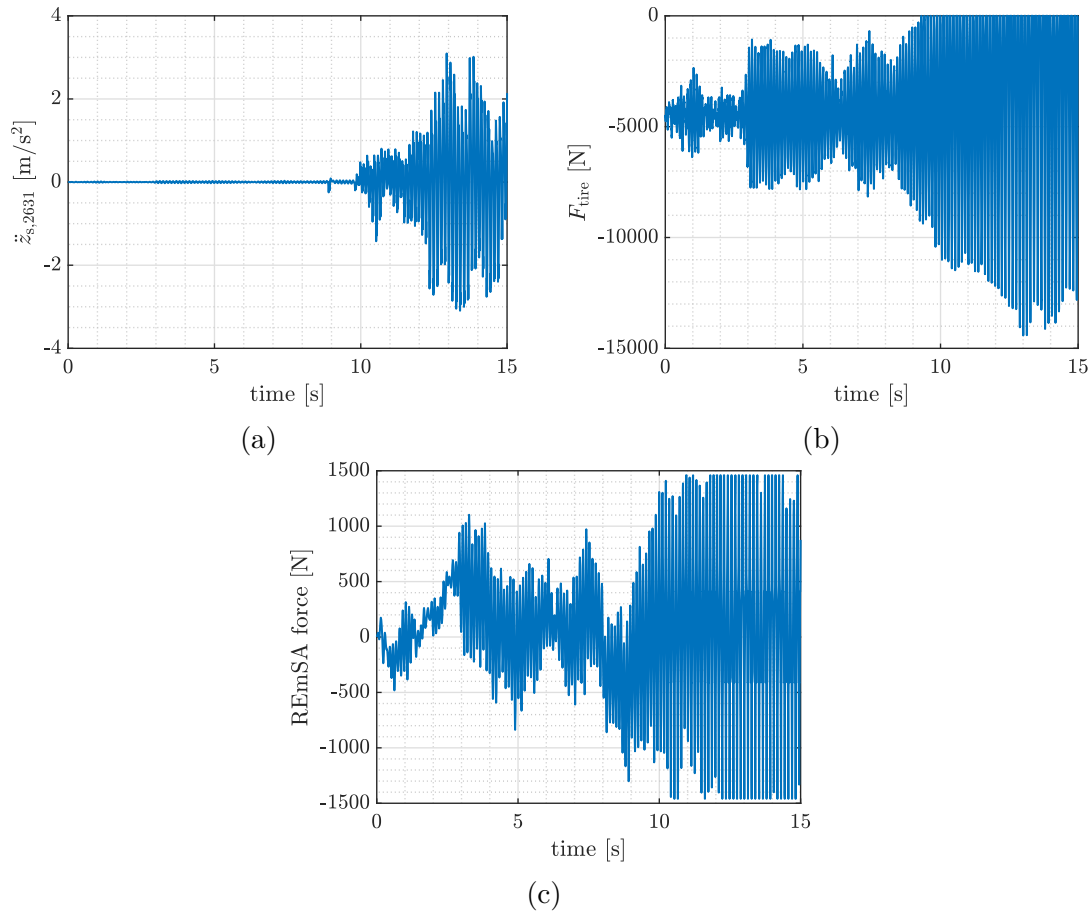


Figure 4.28: Quasi-ideal model with the high level control implementing the LQR with comfort-oriented setting (Table 4.1). Filtered sprung mass acceleration (a), tire-ground contact force (b), and REmSA force (c). The system response exhibits unstable behavior.

best solution would be to tune the LQR strategy by means of the non-linear description of the quarter-car vehicle: it would penalize the unstable LQR settings thus resulting optimum tuning with stable performance. Nevertheless, this procedure raises the computational effort.

In conclusion, the results obtained from the comfort-oriented LQR are not considered in the present investigation because it compromises the system stability.

Comfort-handling trade-off LQR The results are extracted from the quasi-ideal model with the high level control implementing the LQR with comfort-handling trade-off setting (Table 4.1).

The time response of the REmSA force is shown in Fig. 4.29a. It coincides with the force requested by the high level control, as no torque saturation of the

electric machine occurs and the mechanical subsystem is ideal. The latter makes the mechanical power entering the REmSA ($P_{\text{mech,REmSA}}$) coincide with the power flowing to the electric machine.

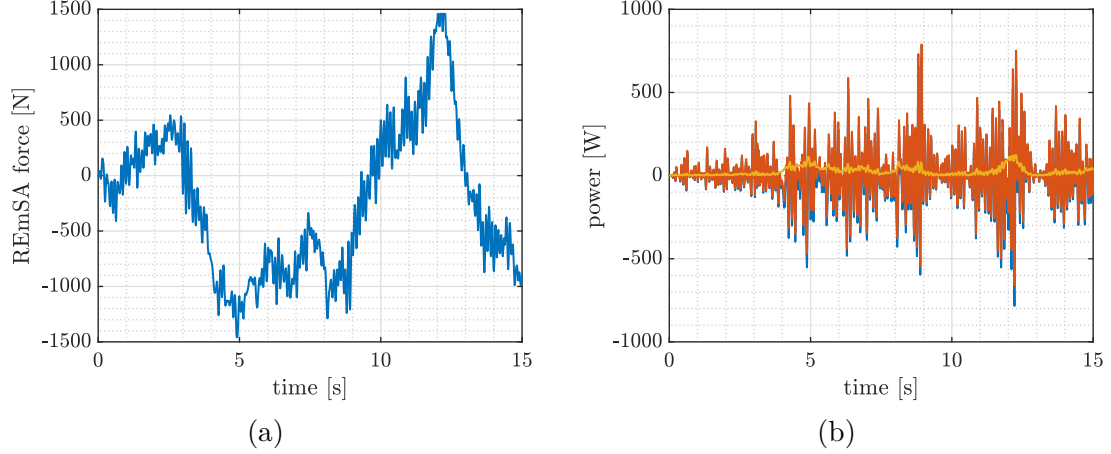


Figure 4.29: Quasi-ideal model with the high level control implementing the LQR with comfort-handling trade-off setting. REmSA force (a) and instantaneous power (b): electrical (blue), mechanical (orange) and loss (yellow).

Fig. 4.29b shows the involved instantaneous power, i.e. the electrical power (blue), mechanical power (orange) and power loss (yellow). The power loss is related to the dissipation in the electric machine. Differently from the damping control strategy shown in the previous paragraphs, the present case gives positive and negative mechanical and electrical power terms. Indeed, the actuator involves passive but also active operation. The latter features negative electrical and mechanical power values.

In terms of vehicle dynamics, the time response of the tire-ground contact force and filtered sprung mass acceleration are shown in Figs. 4.30. No tire-ground detachment occurs. Furthermore, the force dynamic variation is small, which results in a road holding index of 0.123. The filtered acceleration of the sprung mass gives stable response, which results in a comfort performance index of 0.014 g. According to the standard [92], such level is categorized as not uncomfortable.

The results obtained in this case match the performance obtained from the linear model with the same LQR setting (Table 4.1). Therefore, the non-ideal electric machine does not impact the vehicle dynamics. Additionally, the system non-linearity is marginally involved, as no tire-ground detachment occurs and localized actuator saturation is present.

Figs. 4.31a and 4.31b show the force-speed operation of the REmSA at the suspension and electric machine levels, respectively. These coincides (minus the overall transmission ratio) because the ideal mechanical subsystem rigidly connects the electric machine to the suspension with no mechanical loss. Differently from the

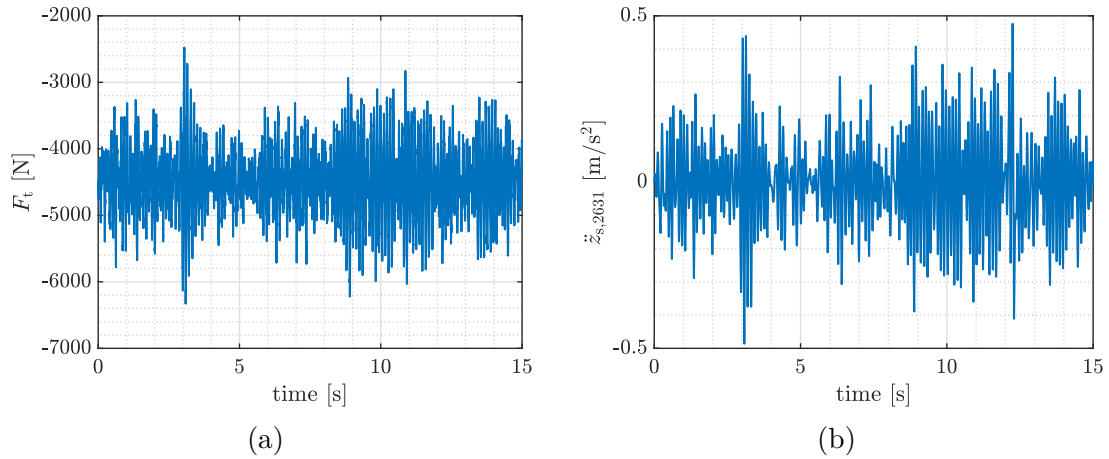


Figure 4.30: Quasi-ideal model with the high level control implementing the LQR with comfort-handling trade-off setting. Tire-ground contact force (a) and filtered sprung mass acceleration (b).

high-level damping control case, the system works both in the passive and active quadrants. Although localized actuator force saturation occurs, the overall vehicle performance are slightly affected.

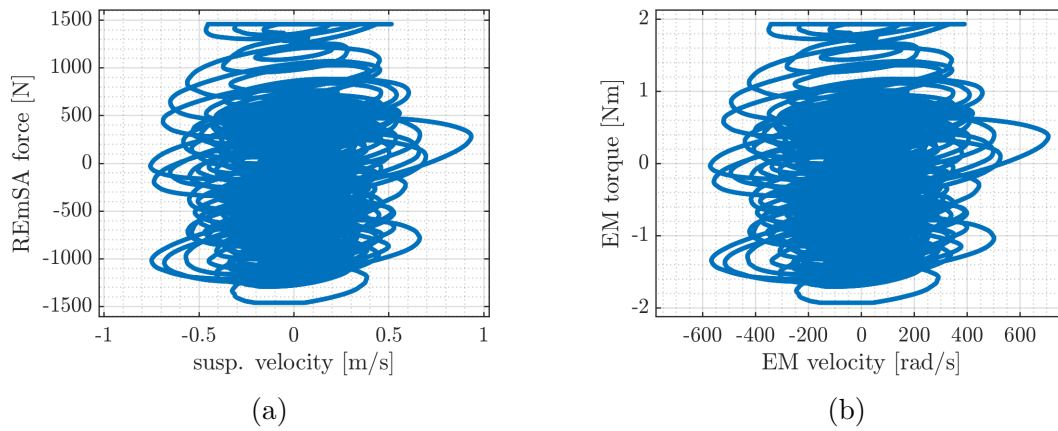


Figure 4.31: Quasi-ideal model with the high level control implementing the LQR with comfort-handling trade-off setting. Force-speed operation of the REmSA at the suspension (a) and electric machine (b) levels.

The energetic and vehicle dynamics performance are reported in Table 4.8. The average mechanical power is positive, meaning that the energy is absorbed from the suspension. Nevertheless, the power loss of the electric machine overcomes the mechanical power coming from the suspension. As consequence, the average electric power is negative, which corresponds to energy consumption. Overall, the REmSA

conversion efficiency is negative, which means that both electrical and mechanical power terms flow into the system and are completely dissipated.

Table 4.8: Energetic and vehicle dynamics performance of the quasi-ideal model with the high level control implementing the LQR with comfort-handling trade-off setting.

Feature	Value
Electrical power	−13.7 W
Mechanical power	12.2 W
Power loss	25.8 W
Conversion efficiency	< 0
Active duty	49%
Passive duty	51%
Regeneration duty	45%
Comfort performance index	0.014 g
Road holding index	0.123

Active and passive operations are almost balanced, as can be noted from the duty cycles close to 50%. The REmSA works in regenerative mode 47% of the total simulation time.

Handling-oriented LQR The results are extracted from the quasi-ideal model with the high-level control implementing the LQR with handling-oriented setting (Table 4.1).

The time response of the REmSA force is shown in Fig. 4.32a. It coincides with the force requested by the high level control, as no torque saturation of the electric machine occurs and the mechanical subsystem is ideal. The latter makes the mechanical power entering the REmSA ($P_{\text{mech,REmSA}}$) coincide with the power flowing to the electric machine.

Fig. 4.32b shows the involved instantaneous power, i.e. the electrical power (blue), mechanical power (orange) and power loss (yellow). The power loss is related to the dissipation in the electric machine. Differently from the damping control strategy shown in the previous paragraphs, the present case gives positive and negative mechanical and electrical power terms. Indeed, the actuator involves passive but also active operation.

In terms of vehicle dynamics, the time response of the tire-ground contact force and filtered sprung mass acceleration are shown in Figs. 4.33. No tire-ground detachment occurs. Furthermore, the force dynamic variation is small, which results

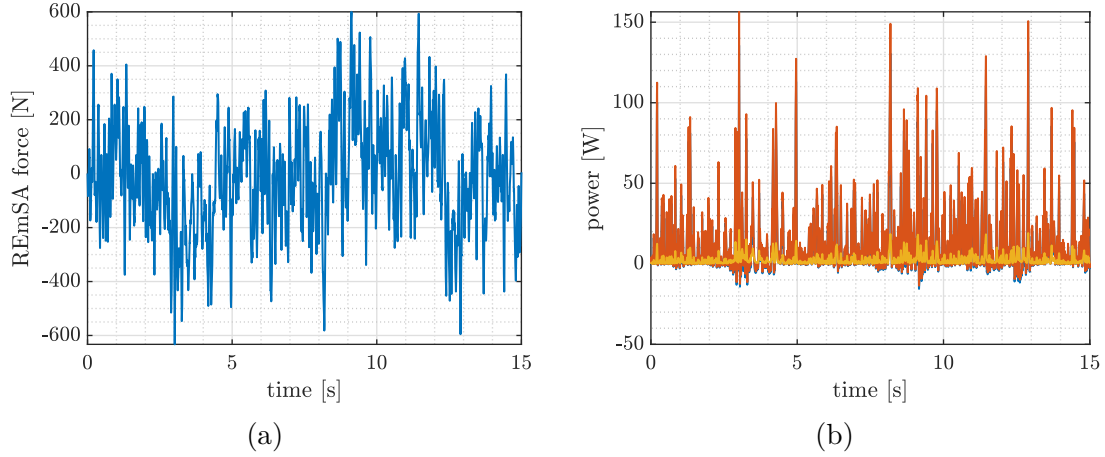


Figure 4.32: Quasi-ideal model with the high level control implementing the LQR with handling-oriented setting. REmSA force (a) and instantaneous power (b): electrical (blue), mechanical (orange) and loss (yellow).

in a road holding index of 0.057. The filtered acceleration of the sprung mass gives stable response, which results in a comfort performance index of 0.040 g. According to the standard [92], such level is categorized as little uncomfortable. All in all, the handling-oriented strategy achieves very good handling performance, while keeping acceptable comfort level.

The results obtained in this case match the performance obtained from the linear model with the same LQR setting (Table 4.1). Therefore, the non-ideal electric machine does not impact the vehicle dynamics. Additionally, the system non-linearity is marginally involved, as no tire-ground detachment occurs and localized actuator saturation is present.

Figs. 4.34a and 4.34b show the force-speed operation of the REmSA at the suspension and electric machine levels, respectively. These coincides (minus the overall transmission ratio) because the ideal mechanical subsystem rigidly connects the electric machine to the suspension with no mechanical loss. No actuator force saturation occurs. Although the system works both in the passive and active quadrants, the REmSA operation in the force-speed plane resembles a conventional damper: the handling-oriented LQR setting tends to reproduce a damping behavior at the suspension.

The energetic and vehicle dynamics performance are reported in Table 4.9. The average power terms are positive: the energy flow goes from the suspension to the battery, which regenerates electric energy. Overall, the REmSA conversion efficiency is $\eta_{\text{REmSA}} = 83\%$. The system works most of the time in the passive quadrants (81% duty), whereas the remaining 19% is covered by active operation. Most of the passive operation features regenerative mode (77% of the total simulation time).

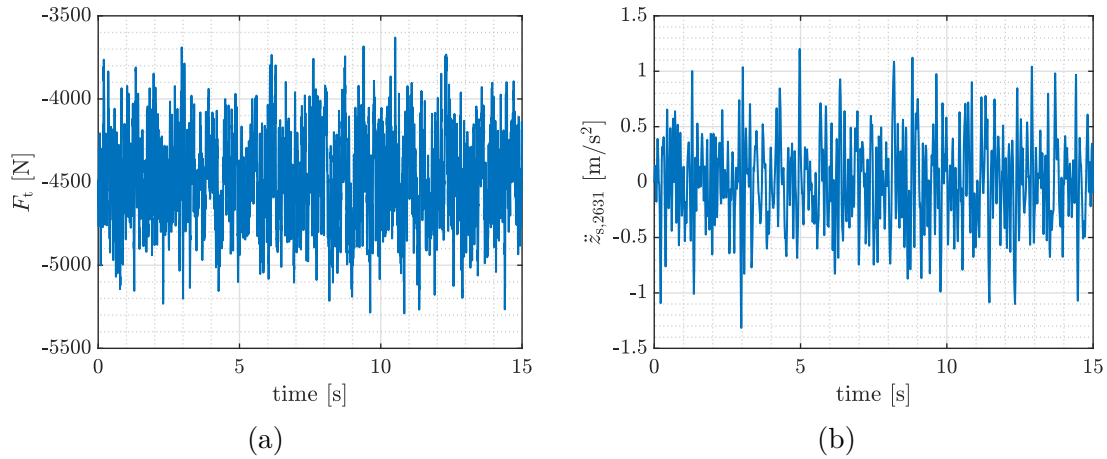


Figure 4.33: Quasi-ideal model with the high level control implementing the LQR with handling-oriented setting. Tire-ground contact force (a) and filtered sprung mass acceleration (b).

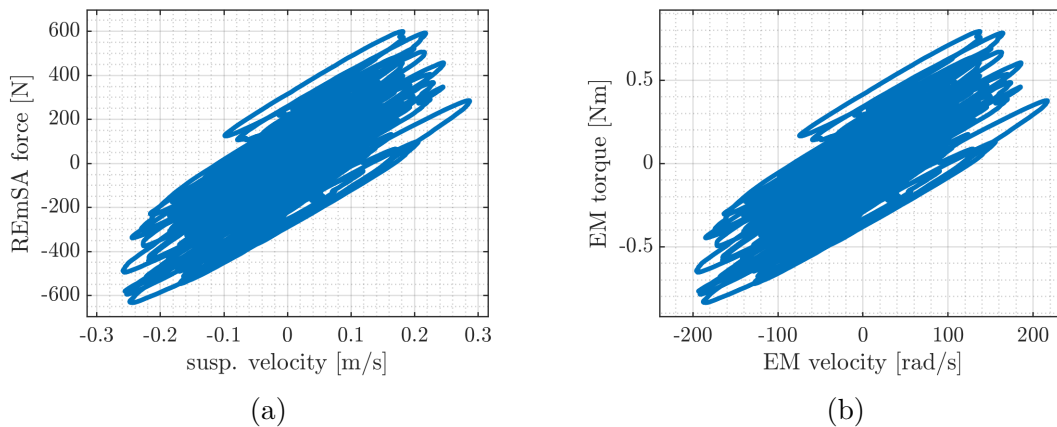


Figure 4.34: Quasi-ideal model with the high level control implementing the LQR with handling-oriented setting. Force-speed operation of the REmSA at the suspension (a) and electric machine (b) levels.

Realistic REmSA

The quarter-car is equipped with the realistic REmSA model, which accounts for the realistic behavior of both the electric machine and the mechanical subsystem. Specifically, the REmSA includes the electric machine power loss and the limited actuation capability imposed by the maximum torque curve. Additionally, the mechanical subsystem models the mechanical dynamics and friction, as described in Sec. 4.1.1.

In the following, some preliminary simulations are carried out to check the model

Table 4.9: Energetic and vehicle dynamics performance of the quasi-ideal model with the high level control implementing the LQR with handling-oriented setting.

Feature	Value
Electrical power	12.1 W
Mechanical power	14.7 W
Power loss	2.6 W
Conversion efficiency	83%
Active duty	19%
Passive duty	81%
Regeneration duty	77%
Comfort performance index	0.040 g
Road holding index	0.057

validity and understand its basic behavior. For this case, the analysis considers the high level control reproducing the maximum damping characteristic. Then, the vehicle model with diverse high level control strategies is simulated when it experiences an ISO B-class road profile at 70 km/h.

The mechanical subsystem model requires an implicit solver. To this end, ode15s variable-step variable-order solver was used, which is recommended for stiff differential problems. One of the simulation output is the energetic performance of the REmSA, which involves energy computation. The latter is an integral quantity that suffers drift issues related to numerical errors. Consequently, the energy error introduced by the solver must be minimized. To this end, the maximum step size was set to $5 \cdot 10^{-6}$ s, which corresponds to 200 kHz sampling frequency.

Realistic model analysis The model with the high level control reproducing the maximum damping characteristic is simulated to assess the model validity and clarify its basic behavior. The analysis considers a harmonic external force acting on the sprung mass (1 Hz frequency and 500 N amplitude).

Fig. 4.35a shows the actual (solid blue) and requested (dashed orange) REmSA force. Although the mechanical subsystem dynamics decouples the electric machine from the REmSA shaft, good force tracking is obtained thanks to the low level controller. However, this scenario slightly involves the mechanical dynamics of the REmSA because of the low frequency of the actuation.

Fig. 4.35b shows the time domain response of the instantaneous powers: electric (P_{el}), mechanical at the REmSA shaft ($P_{mech,REmSA}$), and total loss. The latter includes the dissipation of both the electric machine and the mechanical subsystem.

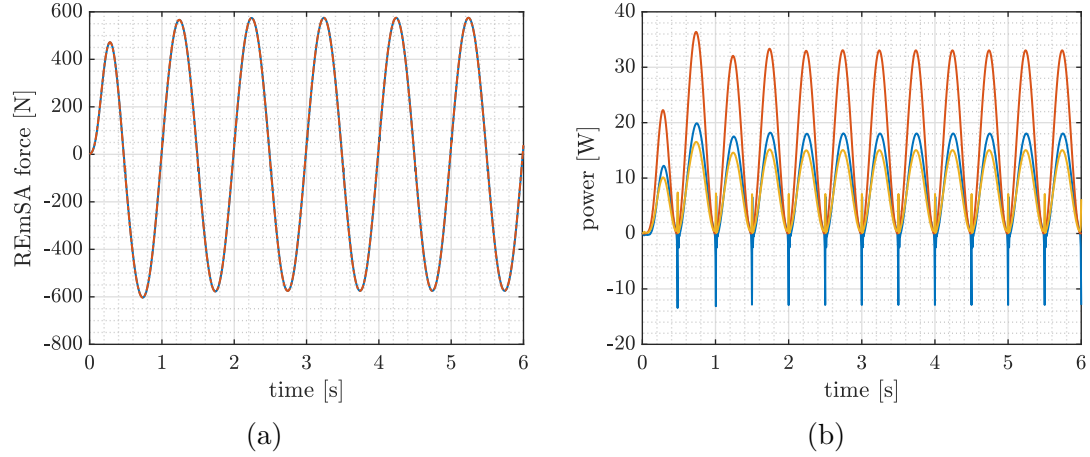


Figure 4.35: Analysis of the realistic model: (a) REmSA force—actual (solid blue) and requested (dashed orange)—and (b) instantaneous power—electrical (blue), mechanical at the REmSA shaft (orange), total loss (yellow).

The mechanical power (orange in Fig. 4.35b) is always positive: the REmSA works as a damper and absorbs energy from the suspension. The electrical power is mainly positive, i.e. regenerated. It is given by the mechanical power at the REmSA shaft decreased by the total loss. Note that the instantaneous power is harmonic with 2 Hz frequency, which is double the external disturbance frequency (1 Hz): the mechanical power approaches zero when the suspension velocity is null, which occurs twice per cycle.

Figs. 4.36 show the force-speed operation of the REmSA at the suspension (a) and electric machine (b) levels. Active operation of the electric machine does not always translate into active operation of the REmSA at the suspension level, as the mechanical subsystem dynamics decouples the electric machine from the REmSA shaft. Thanks to the low level force control, the REmSA reproduces at the suspension the damping characteristic of the high level control. It works the 100% of the total simulation time in the passive quadrants, whereas the electric machine the 96%. The remaining 4% covered by active operation occurs to compensate for the effects of the inertia and the compliant mount—which are extremely limited in this scenario because of the low frequency disturbance—but mostly the friction of the mechanical subsystem.

The same scenario is simulated for a modified version of the realistic model: the friction of the REmSA is increased by amplifying the mechanical loss term (Table 4.2) by a factor 100. Fig. 4.37 shows the time domain response of the instantaneous powers: electric (P_{el}), mechanical at the REmSA shaft ($P_{mech,REmSA}$), and total loss. The mechanical power (orange in Fig. 4.37a) is always positive: the REmSA works as a damper and absorbs energy from the suspension. In this case, the electrical power is always negative, i.e. consumed. This is due to the very large intrinsic

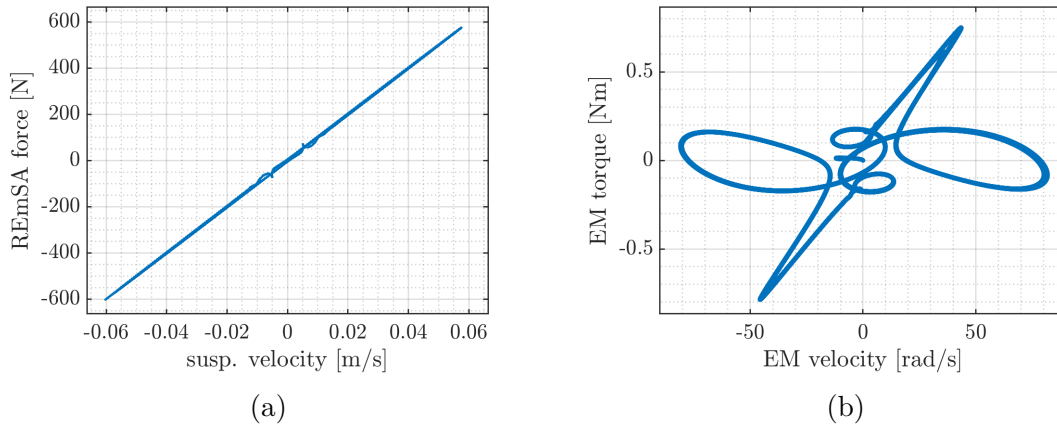


Figure 4.36: Analysis of the realistic model: force-speed operation of the REmSA at the suspension (a) and electric machine (b) levels.

dissipation of the REmSA, which is due to the mechanical subsystem because of the amplified mechanical loss term.

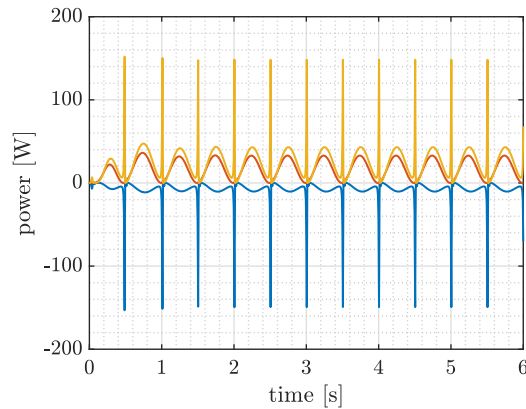


Figure 4.37: Analysis of the realistic model when the mechanical subsystem friction is amplified by a factor 100. Instantaneous power: electrical (blue), mechanical at the REmSA shaft (orange), total loss (yellow).

Figs. 4.38 show the force-speed operation of the REmSA at the suspension (a) and electric machine (b) levels. The REmSA works the 99% of the total simulation time in the passive quadrants, whereas the electric machine only 7%. Its remaining active operation compensates for the friction of the mechanical subsystem, which has been amplified in the present scenario.

Overall, the REmSA works as a damper in both the simulated cases: the average mechanical power entering the REmSA is positive (16 W), meaning that energy is absorbed from the suspension. The case with the amplified friction gives a negative

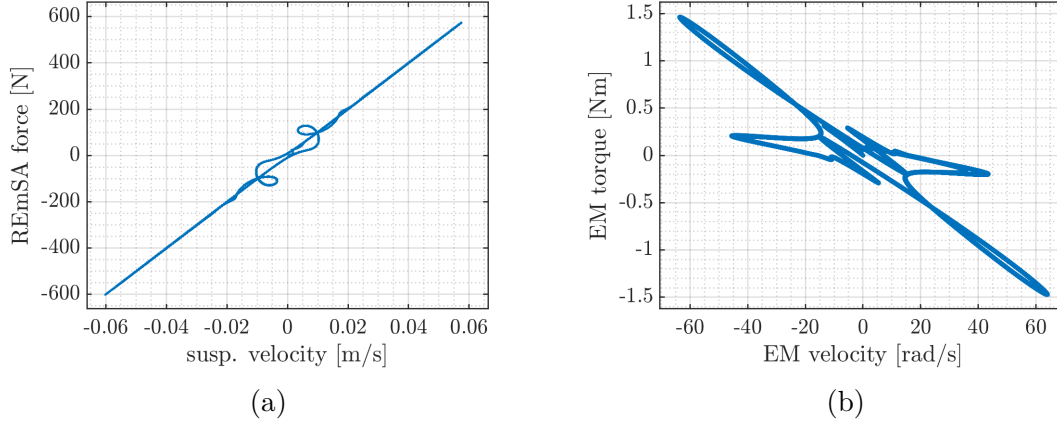


Figure 4.38: Analysis of the realistic model when the mechanical subsystem friction is amplified by a factor 100. Force-speed operation of the REmSA at the suspension (a) and electric machine (b) levels.

average electrical power (-9 W). Therefore, the system needs active power from the electric machine to counteract the internal mechanical loss, that otherwise would give a damping action at the suspension larger than what is requested by the high level control (i.e. the maximum damping characteristic). Conversely, the model with non-amplified friction is able to regenerate energy, resulting in 9 W average electrical power.

Active and reactive power The mechanical power that enters and exits the mechanical subsystem do not coincide. Its difference is due to the internal loss and the power terms associated to the inertia of the equivalent mass and the elastic force of the compliant mount. The instantaneous power of the two latter contributions is shown in Fig. 4.39: blue for the elastic term, orange for the inertia one. Physically speaking, the spring and the mass are storage elements, which are equivalent to the capacitor and the inductor, respectively, in the electrical domain. They accumulate energy in form of potential (elastic) and kinetic energy. Consequently, their power terms indicate the change in time of the energy stored into the system.

These power signals are related to inertia and stiffness elements. Therefore, they feature null mean value (null active power), thus contributing to the reactive power only. For this reason, these components do not directly impact the efficiency of the system. However, the potential and kinetic energies are continuously converted from one form to the other, bouncing back and forth between the electric machine and the suspension. When these energy terms moves, a certain amount is wasted because of the dissipative components of the mechanical subsystem (friction). Overall, large reactive power indicates the movement of a large amount of potential and kinetic energy, which leads to higher energy loss.

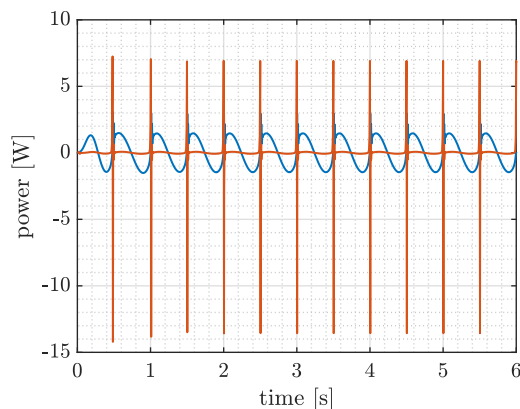


Figure 4.39: Analysis of the realistic model: instantaneous power associated to the inertia force of the equivalent mass (orange) and to the elastic force of the compliant mount (blue).

In the simulated scenario, the active, reactive and power factor are computed for the mechanical power at the REmSA and electric machine shafts. The former features unitary power factor: it is seen by the suspension as a dissipative device, i.e. a conventional damper. This is due to the high level control strategy that reproduces a damping behavior. The power factor at the electric machine shaft is slightly lower (0.96): the electric machine must compensate for the mount compliance and the inertia effect, even if their contribution is minimum because of the low actuation frequency.

Maximum damping control The results are extracted from the realistic model with the high level control reproducing the maximum damping characteristic reported in Fig. 4.21. The vehicle experiences an ISO B-class road profile at 70 km/h.

Figs. 4.40a and 4.40b show the time response of the REmSA force and its zoom-in, respectively. Good tracking is achieved thanks to the low level control. Specifically, the REmSA applies to the suspension the exact force requested by the high level control.

Fig. 4.40c shows the instantaneous powers, i.e. the electrical (blue), mechanical at the REmSA shaft (orange) and power loss (yellow). The latter includes both the electric machine and the mechanical subsystem contributions. The active powers are reported in Table 4.10: the mechanical power at the REmSA shaft is $P_{\text{mech,REmSA}} = 15.4 \text{ W}$, which flows from the suspension to the mechanical subsystem. The latter dissipates 3.8 W, 1.0 W in the mechanical loss element (see Sec. 4.1.1) and 2.8 W in the compliant mount. The mechanical power entering the electric machine is 11.6 W, where 8.6 W are dissipated and the remaining 3.1 W are regenerated in form of electricity.

Fig. 4.40d shows the instantaneous power related to the inertia of the equivalent

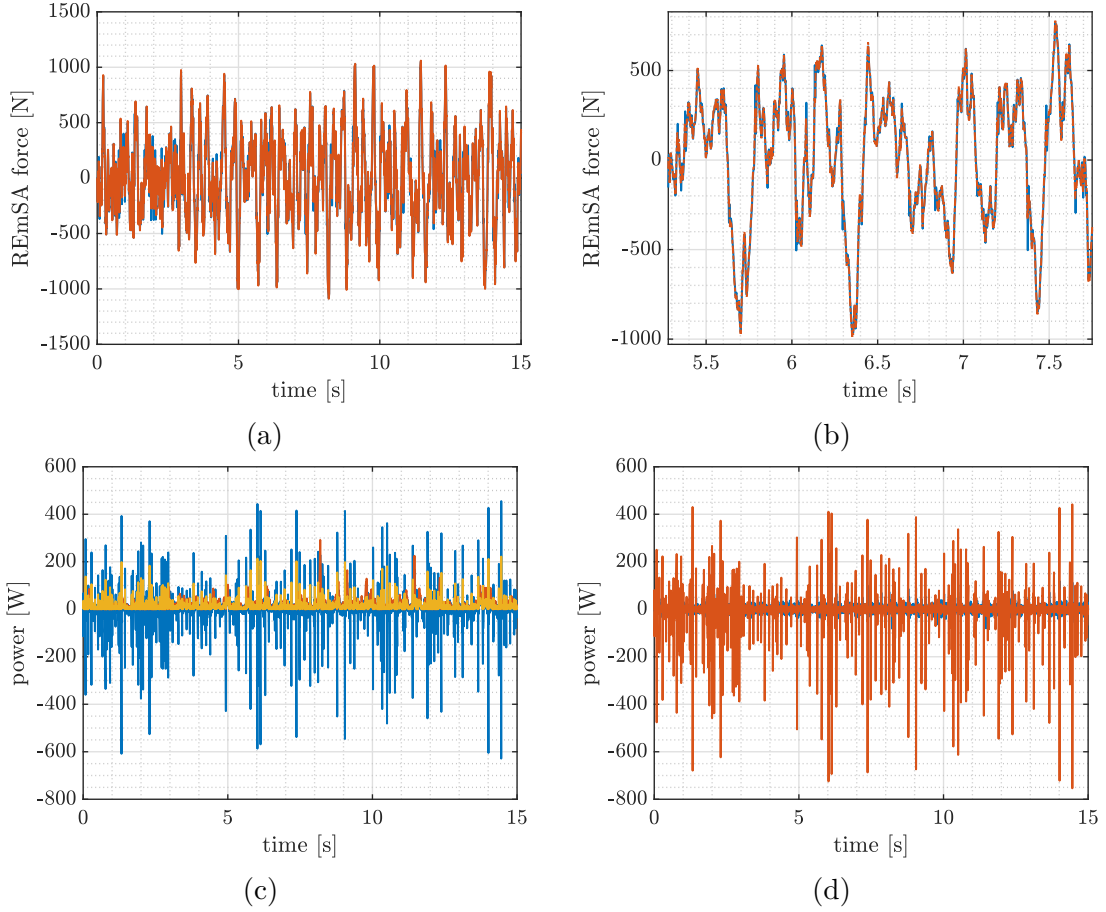


Figure 4.40: Realistic model with the high level control reproducing the maximum damping characteristic. (a) REmSA force and (b) zoom-in: actual (solid blue) and requested (dotted orange). (c) Instantaneous power: electrical (blue), mechanical at the REmSA shaft (orange) and power loss (yellow). (d) Instantaneous power associated to the inertia force of the equivalent mass (orange) and to the elastic force of the compliant mount (blue).

mass (orange) and to the stiffness of the compliant mount (blue). Their apparent power—which is completely reactive—is computed by following the procedure reported in Para. 4.3.2: 31.0 W and 20.6 W for the elastic and the inertia elements, respectively.

The REmSA shaft features unitary power factor: the device is seen by the suspension as a dissipative device. This is due to the high level control strategy that imposes a damping behavior. Conversely, the power factor at the electric machine shaft is much lower (0.32): the electric machine must compensate for the mount compliance and the inertia effect of the mechanical subsystem.

In terms of vehicle dynamics, the time response of the tire-ground contact force

Table 4.10: Energetic and vehicle dynamics performance of the realistic model with the high level control reproducing the maximum damping characteristic.

System	Feature	Value
REmSA	Electrical power	3.1 W
	Peak instantaneous el. power	-628.7 W
	Apparent power @ EM shaft	36.6 W
	Active power	11.6 W
	Power factor	0.32
	Apparent power @ REmSA shaft	15.4 W
	Active power	15.4 W
	Power factor	1.00
	Power loss	12.4 W
	Conversion efficiency	20%
Electric machine	Power loss	8.6 W
	Conversion efficiency	27%
	Active duty	26%
	Passive duty	74%
	Regeneration duty	67%
Mechanical subsystem	Power loss	3.8 W
	Compliant mount	2.8 W
	Mech. loss element	1.0 W
	Conversion efficiency	76%
	Active duty	2%
	Passive duty	98%
	Compliant mount reactive power	31.0 W
Eq. mass reactive power	20.6 W	
Vehicle	Comfort performance index	0.076 g
	Road holding index	0.096

and filtered sprung mass acceleration are shown in Figs. 4.41. No tire-ground detachment occurs. Furthermore, the force dynamic variation is small, which results in a road holding index of 0.096. The filtered acceleration of the sprung mass gives stable response, which results in a comfort performance index of 0.076 g. These performance coincide with the values obtained from the quasi-ideal model,

thus indicating that the low-level control successfully compensates for the non-ideal behavior of the mechanical subsystem.

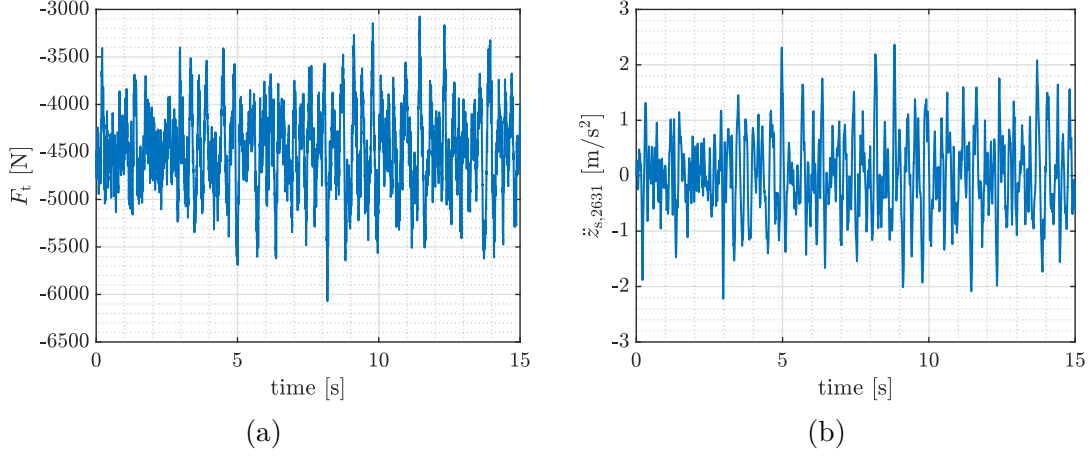


Figure 4.41: Realistic model with the high level control reproducing the maximum damping characteristic. Tire-ground contact force (a) and filtered sprung mass acceleration (b).

Figs. 4.42a and 4.42b show the force-speed operation of the REmSA at the suspension and electric machine levels, respectively. Localized saturation of the electric machine torque occurs, which are the points close to the 2 Nm limit. The mechanical subsystem dynamics decouples the electric machine from the REmSA shaft: active operation of the electric machine does not always translate into active operation of the REmSA at the suspension level. This aspect is accentuated by the reactive elements of the mechanical subsystem. Overall, the REmSA reproduces, at the suspension, the damping characteristic of the high level control. In fact, it works the 98% of the total simulation time in the passive quadrants. On the other hand, the electric machine works 74% passively: its 24% active operation aims at compensating for the inertia and compliance mount effects. 67% of the duty is regenerative operation.

Overall, the REmSA features a efficiency of 20% and regenerates electrical energy. It is dominated by the 27% conversion efficiency of the electric machine, which is lowered by the active duty. The mechanical subsystem features a conversion efficiency of 76%. The very important result is that the system works as a conventional damper in terms of vehicle dynamics, but it regenerates energy.

Minimum damping control The results are extracted from the realistic model with the high level control reproducing the minimum damping characteristic reported in Fig. 4.21. The vehicle experiences an ISO B-class road profile at 70 km/h.

Figs. 4.43a shows the time response of the REmSA force, which achieves good tracking thanks to the low-level control. Specifically, the REmSA applies to the

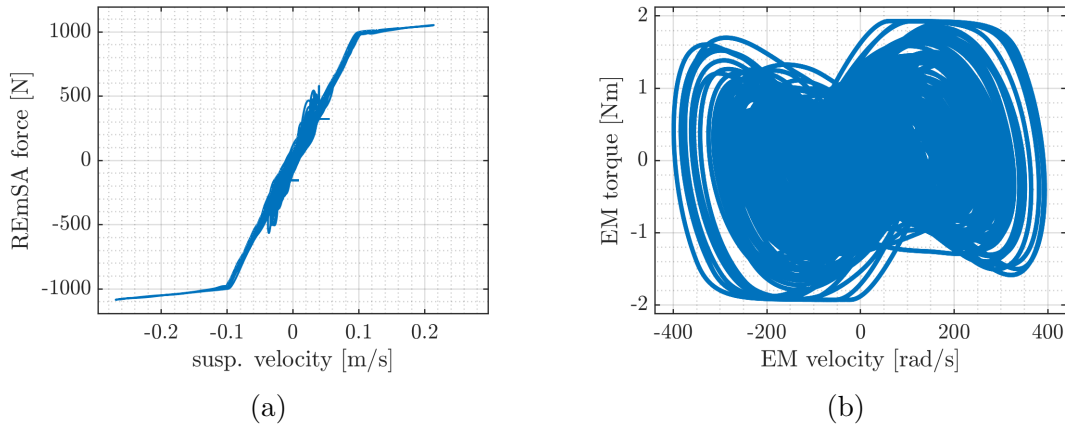


Figure 4.42: Realistic model with the high level control reproducing the maximum damping characteristic. Force-speed operation of the REmSA at the suspension (a) and electric machine (b) levels.

suspension the exact force requested by the high-level control.

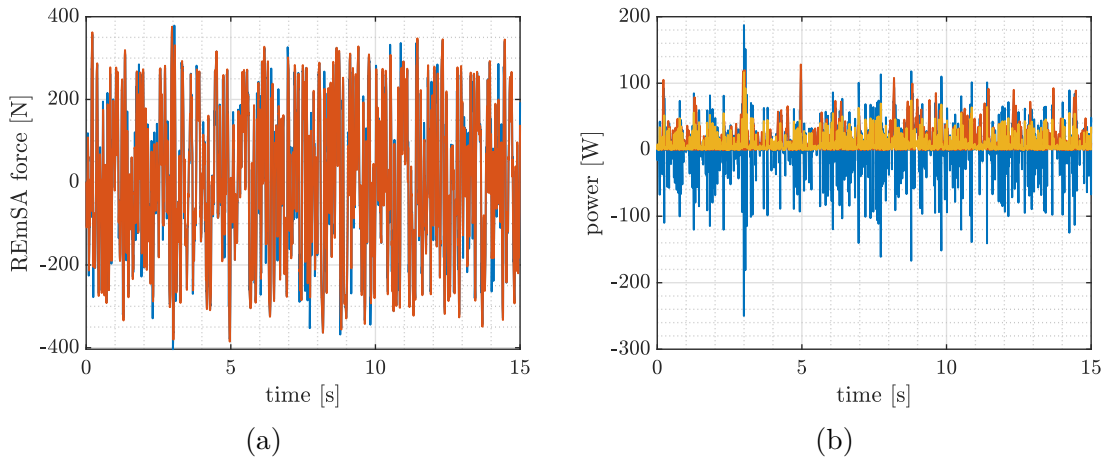


Figure 4.43: Realistic model with the high level control reproducing the minimum damping characteristic. (a) REmSA force: actual (solid blue) and requested (dotted orange). (b) Instantaneous power: electrical (blue), mechanical at the REmSA shaft (orange) and power loss (yellow).

Fig. 4.43b shows the instantaneous powers, i.e. the electrical (blue), mechanical at the REmSA shaft (orange) and power loss (yellow). The latter includes both the electric machine and the mechanical subsystem contributions. The active powers are reported in Table 4.11: the mechanical power at the REmSA shaft is $P_{\text{mech,REmSA}} = 14.9 \text{ W}$, which flows from the suspension to the mechanical subsystem. The latter dissipates 3.1 W: 1.3 W in the mechanical loss element (see Sec.

Table 4.11: Energetic and vehicle dynamics performance of the realistic model with the high level control reproducing the minimum damping characteristic.

System	Feature	Value
REmSA	Electrical power	9.2 W
	Peak instantaneous el. power	−249.9 W
	Apparent power @ EM shaft	19.5 W
	Active power	11.8 W
	Power factor	0.61
	Apparent power @ REmSA shaft	15.1 W
	Active power	14.9 W
	Power factor	0.99
	Power loss	5.7 W
	Conversion efficiency	62%
Electric machine	Power loss	2.6 W
	Conversion efficiency	78%
	Active duty	20%
	Passive duty	80%
	Regeneration duty	77%
Mechanical subsystem	Power loss	3.1 W
	Compliant mount	1.8 W
	Mech. loss element	1.3 W
	Conversion efficiency	79%
	Active duty	2%
	Passive duty	98%
	Compliant mount reactive power	11.5 W
Eq. mass reactive power	14.0 W	
Vehicle	Comfort performance index	0.042 g
	Road holding index	0.061

4.1.1), 1.8 W in the compliant mount. The mechanical power entering the electric machine is 11.8 W, where 2.6 W are dissipated and the remaining 9.2 W are regenerated in the form of electrical energy.

The apparent power related to the inertia and stiffness of the compliant mount is completely reactive. It is computed by following the procedure reported in Para.

4.3.2: 11.5 W and 14.0 W for the elastic and inertia elements, respectively. The REmSA shaft features unitary power factor: it is seen by the suspension as a pure dissipative device. This is due to the high level control strategy that imposes a damping behavior. Conversely, the power factor at the electric machine shaft is 0.61: the electric machine must compensate for the effects of the compliant mount and equivalent mass of the mechanical subsystem.

In terms of vehicle dynamics, the time response of the tire-ground contact force and filtered sprung mass acceleration are shown in Figs. 4.44. No tire-ground detachment occurs. Furthermore, the force dynamic variation is small, which results in a road holding index of 0.061. The filtered acceleration of the sprung mass gives stable response, which results in a comfort performance index of 0.041 g. These performance coincide with the values obtained from the quasi-ideal model, thus indicating that the low-level control successfully compensates for the non-ideal behavior of the mechanical subsystem.

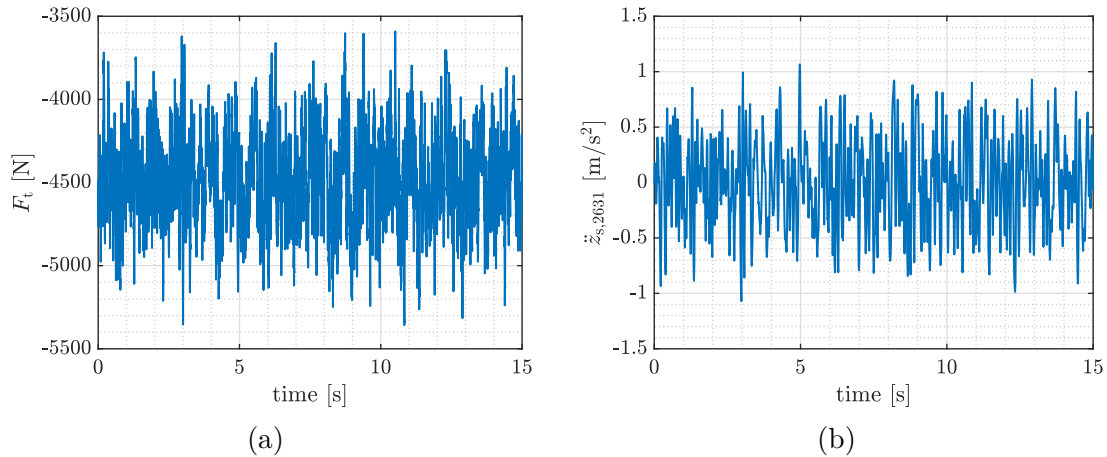


Figure 4.44: Realistic model with the high level control reproducing the minimum damping characteristic. Tire-ground contact force (a) and filtered sprung mass acceleration (b).

Figs. 4.45a and 4.45b show the force-speed operation of the REmSA at the suspension and electric machine levels, respectively. Differently from the maximum damping case, no torque saturation of the electric machine occurs. Overall, the REmSA reproduces, at the suspension, the damping characteristic of the high level control. In fact, it works the 98% of the total simulation time in the passive quadrants. On the other hand, the electric machine works 80% passively: its 20% active operation occurs to compensate for the inertia and compliance mount contributions. The 77% duty is regenerative operation, more than the maximum damping case.

Overall, the REmSA results in 62% conversion efficiency with regeneration of electrical energy. The electric machine and the mechanical subsystem feature 78%

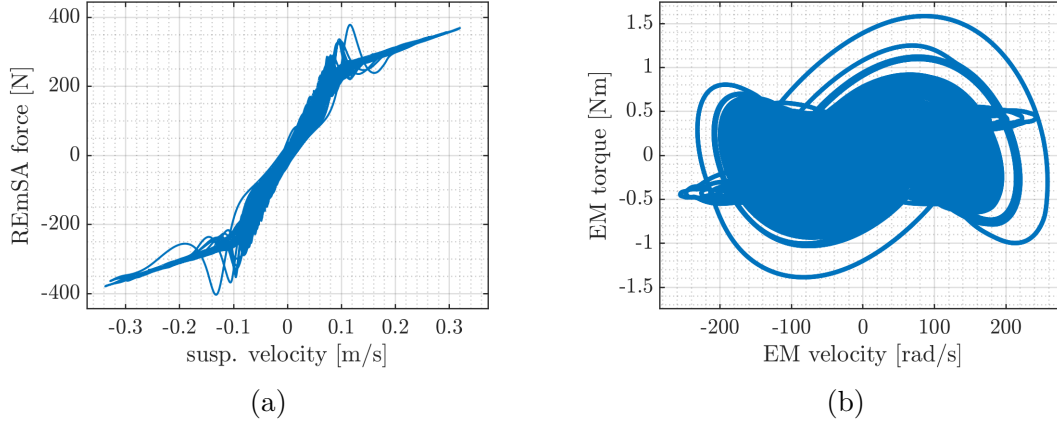


Figure 4.45: Realistic model with the high level control reproducing the minimum damping characteristic. Force-speed operation of the REmSA at the suspension (a) and electric machine (b) levels.

and 79% conversion efficiency, respectively. Also in this case, the system works as a conventional damper in terms of vehicle dynamics, but with energy regeneration.

Comfort-handling trade-off LQR The results are extracted from the realistic model with the high level control implementing the LQR with comfort-handling trade-off setting (Table 4.1). The ISO B-class road profile at 70 km/h is simulated.

Figs. 4.46a shows the time response of the REmSA force, which achieves good tracking thanks to the low-level control. Specifically, the REmSA applies to the suspension the exact force requested by the high-level control.

Fig. 4.46b shows the instantaneous powers, i.e. the electrical (blue), mechanical at the REmSA shaft (orange) and power loss (yellow). The latter includes both the electric machine and the mechanical subsystem contributions. The active power values are reported in Table 4.12: the mechanical power at the REmSA shaft is $P_{\text{mech,REmSA}} = 13.3 \text{ W}$, which flows from the suspension to the mechanical subsystem. The latter dissipates 9.1 W: 8.8 W in the mechanical loss element (see Sec. 4.1.1), 0.3 W in the compliant mount. The remaining amount of energy (4.1 W) goes to the electric machine that wastes 23.7 W. The loss is larger than the power absorbed from the mechanical subsystem: the electric machine consumes electrical energy. In fact, the electric power active component is negative (-19.5 W).

The apparent power related to the inertia and stiffness of the compliant mount is completely reactive. It is computed by following the procedure reported in Para. 4.3.2: 17.7 W and 29.8 W for the elastic and inertia elements, respectively. The REmSA shaft features very low power factor (0.08): it is seen by the suspension as a reactive device. This follows from the high level control strategy: the implemented LQR setting includes a significant contribution of spring negation (Eq.

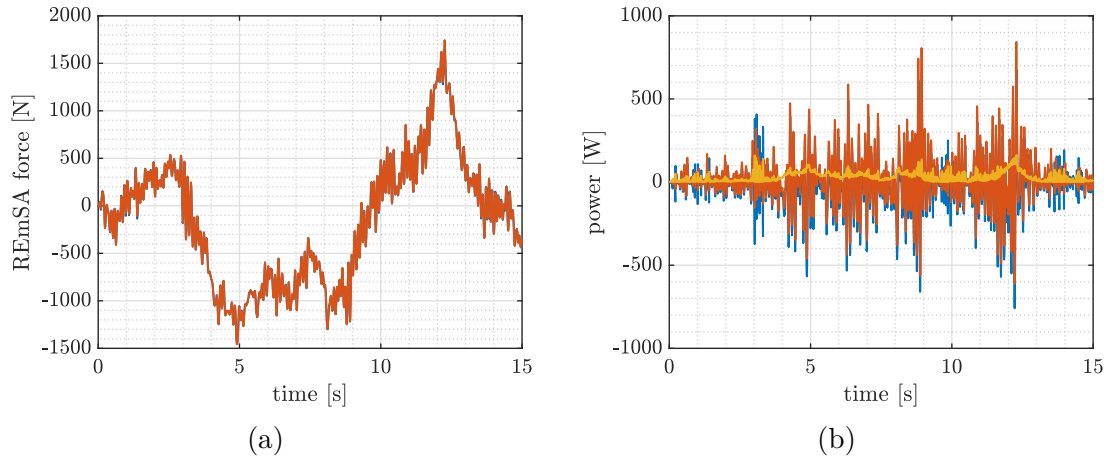


Figure 4.46: Realistic model with the high-level control reproducing the LQR with comfort-handling trade-off setting. (a) REmSA force: actual (solid blue) and requested (dotted orange). (b) Instantaneous power: electrical (blue), mechanical at the REmSA shaft (orange) and power loss (yellow).

4.27). The power factor at the electric machine shaft is even lower (0.02), as it must compensate for the effects of the compliant mount and equivalent mass of the mechanical subsystem.

In terms of vehicle dynamics, the time response of the tire-ground contact force and filtered sprung mass acceleration are shown in Figs. 4.47. No tire-ground detachment occurs. Furthermore, the force dynamic variation is small, which results in a road holding index of 0.124. The filtered acceleration of the sprung mass gives stable response, which results in a comfort performance index of 0.014 g. These performance coincide with the values obtained from the quasi-ideal model, thus indicating that the low-level control successfully compensates for the non-ideal behavior of the mechanical subsystem.

Figs. 4.48a and 4.48b show the force-speed operation of the REmSA at the suspension and electric machine levels, respectively. The latter highlights localized torque saturation of the electric machine, which occurs at approximately 2 Nm. At the suspension level, the REmSA works 53% of the total simulation time in the passive quadrants, whereas the 47% in the active ones. This yields from the LQR tuning: it requires extensive active work on the suspension because of the spring negation contribution. The electric machine works 51% of the time in the passive quadrants, and the remaining part in the active ones. Regenerative operation covers 45% of the duty

Overall, the REmSA results in negative conversion efficiency as it absorbs power both from the battery and the suspension. This is due to the electric machine, which dissipates a large amount of power. The mechanical subsystem features 31% conversion efficiency.

Table 4.12: Energetic and vehicle dynamics performance of the realistic model with the high level control implementing the LQR with comfor-handling trade-off setting.

System	Feature	Value
REmSA	Electrical power	−19.5 W
	Peak instantaneous el. power	−759.2 W
	Apparent power @ EM shaft	169.7 W
	Active power	4.1 W
	Power factor	0.02
	Apparent power @ REmSA shaft	163.0 W
	Active power	13.3 W
	Power factor	0.08
	Power loss	32.8 W
	Conversion efficiency	< 0%
Electric machine	Power loss	23.7 W
	Conversion efficiency	< 0%
	Active duty	49%
	Passive duty	51%
	Regeneration duty	45%
Mechanical subsystem	Power loss	9.1 W
	Compliant mount	0.3 W
	Mech. loss element	8.8 W
	Conversion efficiency	31%
	Active duty	47%
	Passive duty	53%
	Compliant mount reactive power	17.7 W
Eq. mass reactive power	29.8 W	
Vehicle	Comfort performance index	0.014 g
	Road holding index	0.124

Handling-oriented LQR The results are extracted from the realistic model with the high level control implementing the LQR with handling-oriented setting (Table 4.1). An ISO B-class road profile at 70 km/h is simulated.

Figs. 4.49a shows the time response of the REmSA force, which achieves good

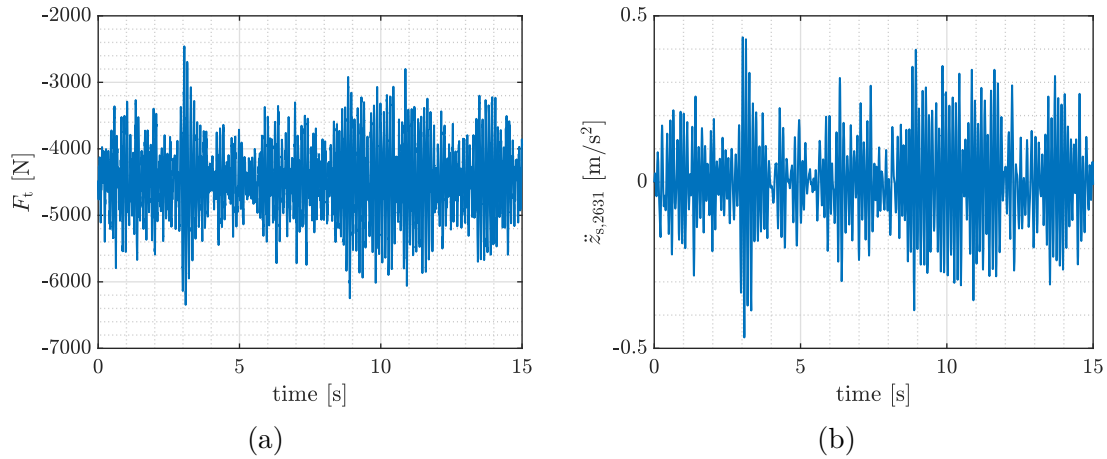


Figure 4.47: Realistic model with the high level control reproducing the LQR with comfort-handling trade-off setting. Tire-ground contact force (a) and filtered sprung mass acceleration (b).

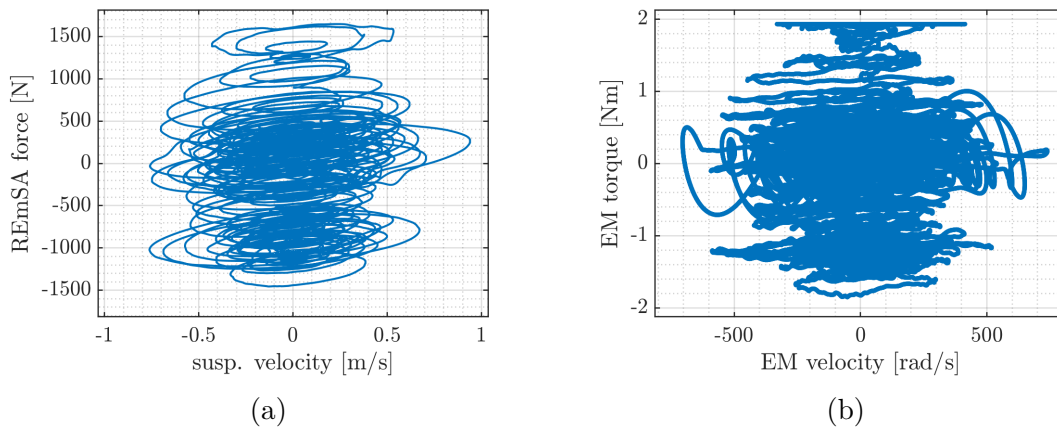


Figure 4.48: Realistic model with the high level control implementing the LQR with comfort-handling trade-off setting. Force-speed operation of the REmSA at the suspension (a) and electric machine (b) levels.

tracking thanks to the low-level control. Specifically, the REmSA applies to the suspension the exact force requested by the high-level control.

Fig. 4.49b shows the instantaneous powers, i.e. the electrical (blue), mechanical at the REmSA shaft (orange) and power loss (yellow). The latter includes both the electric machine and the mechanical subsystem contributions. The active power values are reported in Table 4.13: the mechanical power at the REmSA shaft is $P_{\text{mech,REmSA}} = 14.6 \text{ W}$, which flows from the suspension to the mechanical subsystem. The latter dissipates 2.2 W : 1.1 W in the mechanical loss element (see Sec. 4.1.1), 1.1 W in the compliant mount. The remaining amount of energy goes

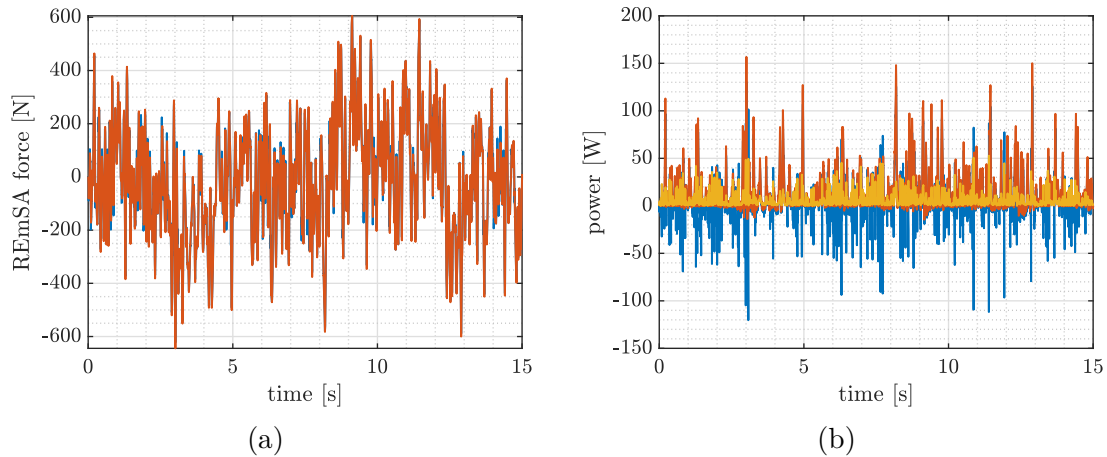


Figure 4.49: Realistic model with the high-level control reproducing the LQR with handling-oriented setting. (a) REmSA force: actual (solid blue) and requested (dotted orange). (b) Instantaneous power: electrical (blue), mechanical at the REmSA shaft (orange) and power loss (yellow).

to the electric machine (12.5 W of active power at the electric machine shaft), which wastes 2.7 W. Overall, electrical energy is regenerated (9.8 W active power).

The apparent power related to the inertia and stiffness of the compliant mount is completely reactive. It is computed by following the procedure reported in Para. 4.3.2: 10.5 W and 9.1 W for the elastic and inertia elements, respectively. The REmSA shaft features 0.83 power factor: it is seen by the suspension as a reactive device with both elastic and damping contributions. This follows from the high level control strategy: the implemented LQR setting includes both spring negation and groundhook contributions (Eq. 4.25). The power factor at the electric machine shaft is 0.66, as it must compensate for the effects of the compliant mount and equivalent mass of the mechanical subsystem.

In terms of vehicle dynamics, the time response of the tire-ground contact force and filtered sprung mass acceleration are shown in Figs. 4.50. No tire-ground detachment occurs. Furthermore, the force dynamic variation is small, which results in a road holding index of 0.057. The filtered acceleration of the sprung mass gives stable response, which results in a comfort performance index of 0.040 g. These performance coincide with the values obtained from the quasi-ideal model, thus indicating that the low-level control successfully compensates for the non-ideal behavior of the mechanical subsystem.

Figs. 4.51a and 4.51b show the force-speed operation of the REmSA at the suspension and electric machine levels, respectively. The 81% of the total simulation time is spent in the passive quadrants, whereas only the 19% in the active ones. Differently, the electric machine works only the 73% passively. The 69% duty covers regenerative operation.

Table 4.13: Energetic and vehicle dynamics performance of the realistic model with the high level control implementing the LQR with handling-oriented setting.

System	Feature	Value
REmSA	Electrical power	9.8 W
	Peak instantaneous el. power	130.6 W
	Apparent power @ EM shaft	18.9 W
	Active power	12.4 W
	Power factor	0.66
	Apparent power @ REmSA shaft	17.6 W
	Active power	14.7 W
	Power factor	0.83
	Power loss	4.9 W
	Conversion efficiency	67%
Electric machine	Power loss	2.7 W
	Conversion efficiency	79%
	Active duty	27%
	Passive duty	73%
	Regeneration duty	69%
Mechanical subsystem	Power loss	2.2 W
	Compliant mount	1.1 W
	Mech. loss element	1.1 W
	Conversion efficiency	85%
	Active duty	19%
	Passive duty	81%
	Compliant mount reactive power	10.5 W
Eq. mass reactive power	9.1 W	
Vehicle	Comfort performance index	0.040 g
	Road holding index	0.057

Overall, the REmSA features 67% conversion efficiency with regeneration of electrical energy. The electric machine and the mechanical subsystem feature 79% and 85% conversion efficiency, respectively. Also in this case, the system guarantees satisfactory vehicle dynamics while regenerating energy.

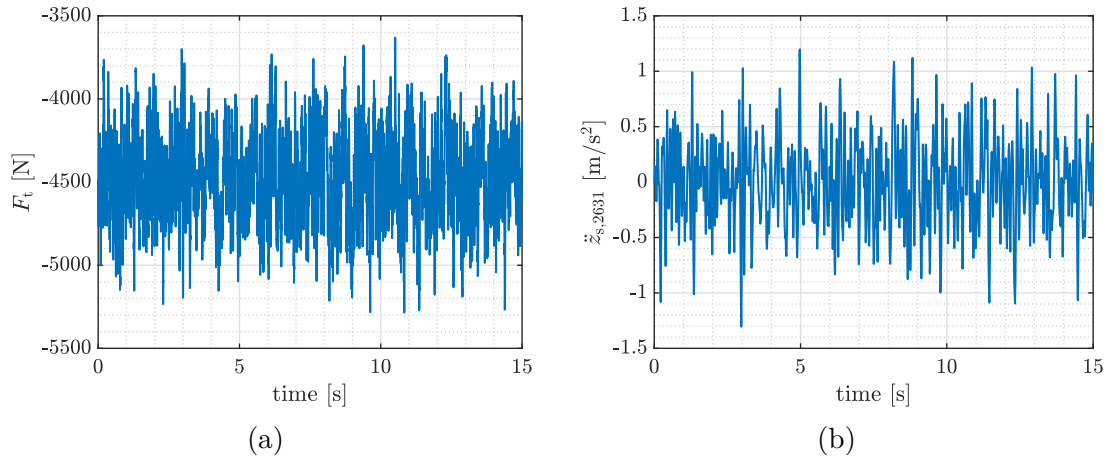


Figure 4.50: Realistic model with the high level control reproducing the LQR with handling-oriented setting. Tire-ground contact force (a) and filtered sprung mass acceleration (b).

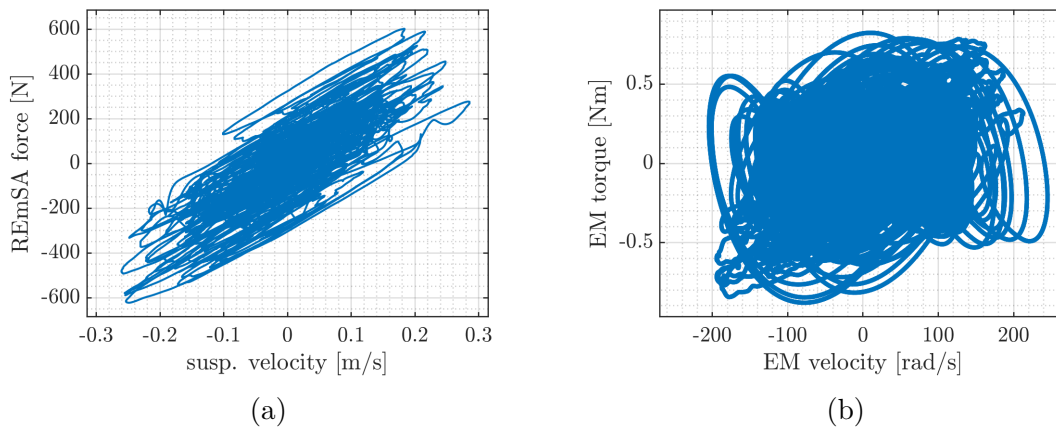


Figure 4.51: Realistic model with the high level control implementing the LQR with handling-oriented setting. Force-speed operation of the REmSA at the suspension (a) and electric machine (b) levels.

Realistic REmSA with no low level control

The low level control is disabled to understand how it impacts the realistic system operation. Simulations are performed for the ISO B-class road profile at 70 km/h. The high level control reproducing the minimum damping characteristic (Fig. 4.21) is used for the comparison.

The time response of the REmSA force is shown in Fig. 4.52. The absence of the low level control leads to poor force tracking.

The comparison between the simulation with the low level controller enabled

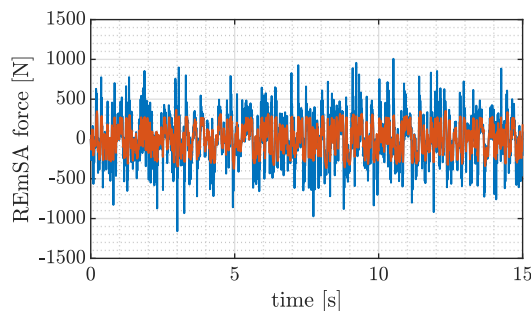


Figure 4.52: Realistic model with disabled low level control. The high level control reproduces the minimum damping characteristic. Actual (solid blue) and requested (dotted orange) REmSA force.

and disabled is reported in Table 4.14. The active component of the power at the REmSA shaft is $P_{\text{mech,REmSA}} = 15.2 \text{ W}$, which flows from the suspension to the mechanical subsystem. The latter dissipates 5.4 W : 1.5 W in the mechanical loss element (see Sec. 4.1.1), 3.9 W in the compliant mount. The mechanical power entering the electric machine is 9.8 W , where 2.3 W are dissipated and the remaining 7.5 W are regenerated in the form of electrical energy. Although the enabled and disabled low level control cases feature similar amount of power absorbed from the suspension, the latter yields to larger loss. Consequently, lower energy is regenerated. Especially the power lost in the mechanical subsystem has increased. The cause relies on the larger amount of energy stored into the elastic component of the compliant mount and the inertia of the equivalent mass, which is indicated by the larger reactive power (20.4 W and 13.6 W , respectively). As discussed in Para. 4.3.2, this leads to larger energy dissipation

Differently from the case with enabled low level control, the REmSA shaft does not feature unitary power factor. In this case, the power factor is 0.83 , thus indicating that the REmSA is not seen by the suspension as a conventional damper. This is an unwanted result: the high level control tries to impose a damping behavior but it cannot succeed because of the mechanical dynamics that decouples the electric machine and REmSA shafts. The power factor at the electric machine shaft is 0.53 .

The REmSA features a conversion efficiency of 49% with regeneration of electrical power. It is lower than the case with enabled low level control. The electric machine and the mechanical subsystem feature conversion efficiency of 77% and 64% , respectively.

Figs. 4.53a and 4.53b show the force-speed operation of the REmSA at the suspension and electric machine levels, respectively. In this case, the poor force tracking impedes the REmSA from reproducing, at the suspension, the damping characteristic of the high level control: working points in the force-speed plane do not resemble a damping characteristic. The REmSA works only the 90% of the

Table 4.14: Energetic and vehicle dynamics performance of the realistic model with the high level control reproducing the minimum damping characteristic. Comparison between the enabled and disabled low level control cases.

System	Feature	Value	
		Low level control enabled	disabled
REmSA	Electrical power	9.2 W	7.5 W
	Peak instantaneous el. power	-249.9 W	118.0 W
	Apparent power @ EM shaft	19.5 W	18.5 W
	Active power	11.8 W	9.8 W
	Power factor	0.61	0.53
	Apparent power @ REmSA shaft	15.1 W	18.3 W
	Active power	14.9 W	15.2 W
	Power factor	0.99	0.83
	Power loss	5.7 W	7.7 W
	Conversion efficiency	62%	49%
Electric machine	Power loss	2.6 W	2.3 W
	Conversion efficiency	78%	77%
	Active duty	20%	35%
	Passive duty	80%	65%
	Regeneration duty	77%	61%
Mechanical subsystem	Power loss	3.1 W	5.4 W
	Compliant mount	3.9 W	9.2 W
	Mech. loss element	1.5 W	9.2 W
	Conversion efficiency	79%	64%
	Active duty	2%	10%
	Passive duty	98%	90%
	Compliant mount reactive power	11.5 W	20.4 W
Eq. mass reactive power	14.0 W	13.6 W	
Vehicle	Comfort performance index	0.042 g	0.062 g
	Road holding index	0.061	0.045

total simulation time in the passive quadrants. The electric machine works 65% passively, whereas 61% of the duty covers regenerative operation.

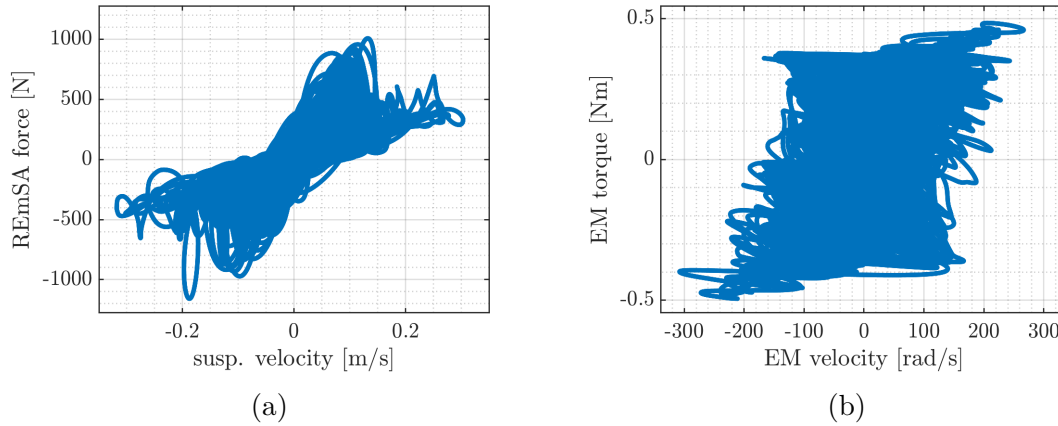


Figure 4.53: Realistic model with disabled low level control. The high level control reproduces the minimum damping characteristic. Force-speed operation of the REmSA at the suspension (a) and electric machine (b) levels.

In terms of vehicle dynamics, no tire-ground detachment occurs. The resulting road holding index and comfort performance are 0.062 and 0.045 g, respectively. The absence of the low level controller slightly deteriorates these performance.

In conclusion, the present scenario considered the minimum damping characteristic in the high level control. The absence of the low level control significantly impacts the energetic performance of the REmSA, with an important decrease of the conversion efficiency. The performance in terms of vehicle dynamics are slightly affected. However, different result occurs when the high level control implements more demanding strategies, for instance the maximum damping characteristic or the investigated LQR settings. In such cases, the vehicle model tends to be unstable: the high level force request at mid-high frequencies is applied to the suspension with phase-delay and amplitude attenuation. In fact, the equivalent inertia and compliance mount effects dominate the response of the REmSA in such frequency range.

Quasi-ideal and realistic REmSA comparison

Finally, the results obtained from the quasi-ideal and realistic models with the implemented high-level control strategies are compared. The vehicle experiences the ISO B-class road profile at 70 km/h.

Figs. 4.54 compare the quasi-ideal (blue) and realistic (orange) models in terms of vehicle dynamics performance. The two models give identical results: the mechanical dynamics of the REmSA does not impact the vehicle performance. This

outcome follows from the low level control, which is able to compensate for the equivalent inertia and compliance of the prototype, as well as its internal friction. Furthermore, the LQR performance matches the results obtained from the linear ideal model (Table 4.1).

For what concerns the high level control strategy, the best comfort is achieved by the LQR with the comfort-handling trade-off setting (Fig. 4.54a). The obtained result (0.014 g) is well below the *not uncomfortable* limit indicated by the standard, i.e. 0.032 g. Therefore, the passengers of the vehicle would experience an ISO B-class profile—which is considerably rough—without any uncomfortable feeling. By converse, this setting yields the worse road holding among the tested control strategies (Fig. 4.54b). The best handling performance is achieved by the LQR with handling-oriented tuning. All in all, the LQR control strategy outdoes the damping one both in the comfort and handling performance. In terms of vehicle dynamics, the REmSA with the damping control strategy can be considered equivalent to a passive conventional damper: the results demonstrate that the vehicle performance can be significantly improved by means of an active suspension—i.e. the REmSA with the LQR control—especially for what regards the comfort.

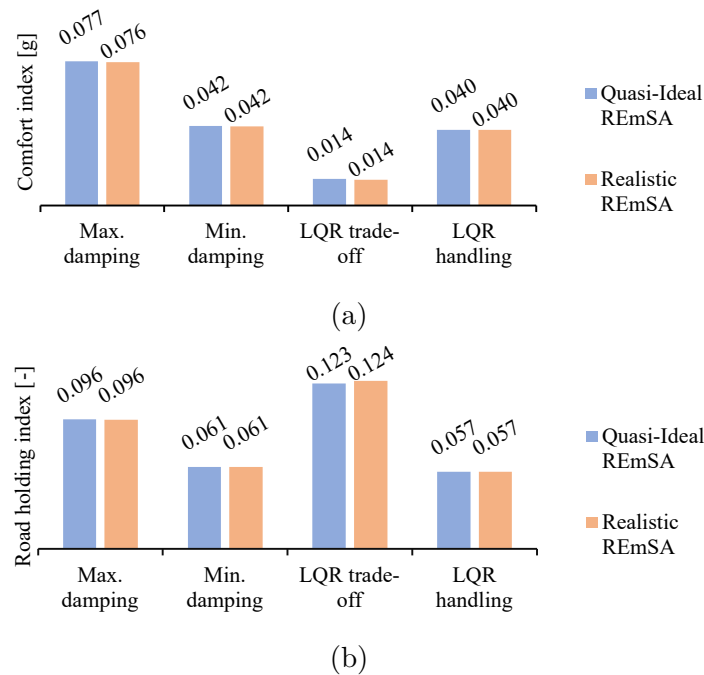


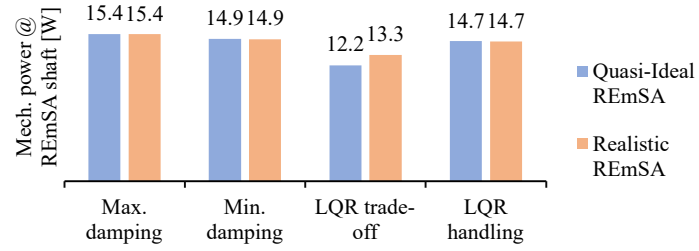
Figure 4.54: Comparison between the quasi-ideal (blue) and realistic (orange) models at the diverse high level control strategies. Vehicle dynamics performance: comfort index (a) and road holding index (b).

The quasi-ideal (blue) and realistic (orange) models are compared in Figs. 4.55 in terms of energetic performance. The power results refers to the active component

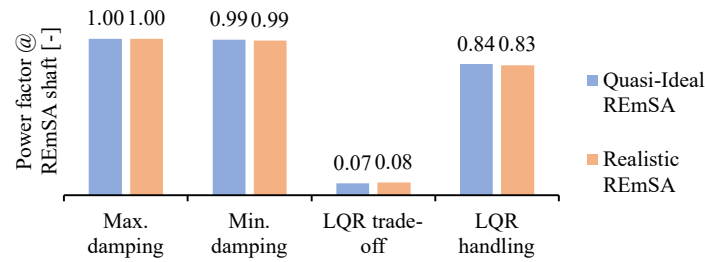
of the apparent power. Figs. 4.55a and 4.55b show the mechanical power and the power factor at the shaft of the REmSA. The quasi-ideal and realistic models give almost identical result, hence the vehicle performance does not change in the two cases. This is in perfect agreement with the results in terms of vehicle dynamics: the mechanical non-ideality of the REmSA is completely compensated through the low level control and consequently the vehicle performance is not affected. The power factor of the damping control cases is unitary, which means that the REmSA is seen by the suspension as a dissipative component, i.e. a passive damper. By converse, the LQR strategies make the REmSA behave as a reactive element, as the control logic includes some spring negation contributions (Eqs. 4.27 and 4.25).

Fig. 4.55c reports the electric power that goes to the battery. Specifically, the damping control cases and the handling-oriented LQR give positive power value (i.e. regenerated), whereas the LQR with comfort-handling trade-off setting features electrical power consumption. Here, the effect of the mechanical non-ideality of the REmSA is clear: the compensation of the mechanical dynamics and the friction loss impact the energetic performance of the REmSA. In fact, the realistic model features lower regenerated power and, for the LQR trade-off case, larger electrical consumption. This is evident also from the conversion efficiency results (Fig. 4.55d): the realistic REmSA exhibits decreased efficiency. The LQR trade-off case features negative efficiency as the REmSA absorbs power both from the battery and the suspension.

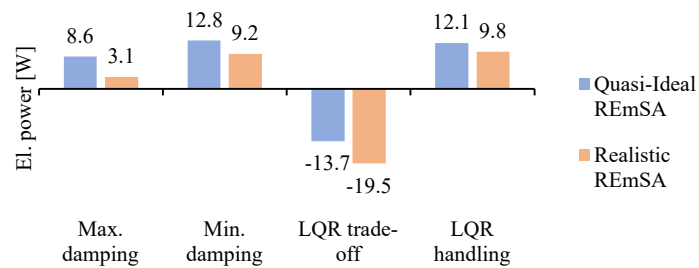
Overall, the proposed investigation demonstrates how the REmSA is able to improve the vehicle performance when compared to conventional passive dampers. Furthermore, its realistic behavior requires proper control to compensate for its mechanical non-idealities, i.e. inertia, compliance and friction. In fact, no difference between the vehicle dynamics performance of the quasi-ideal and realistic model is appreciated when the low level control is implemented. However, such non-idealities impact the energy performance of the REmSA because the mechanical dynamics compensation and the internal friction requires additional energy. The most important result is that the REmSA can reproduce the operation of a conventional damper, with the significant advantage of electrical energy regeneration. Therefore, such system can improve the energy management of the vehicle by keeping unchanged the comfort and handling performance. Additionally, it can implement more complex control strategies, i.e. the LQR, to improve the comfort and the handling. According to the adopted high level control logic, the energetic performance of the REmSA changes, moving from the regeneration (typically for handling-oriented strategies) to the consumption (typically for comfort-oriented strategies). All in all, vehicle performance and energetic aspects strictly depends on the adopted high-level control strategy.



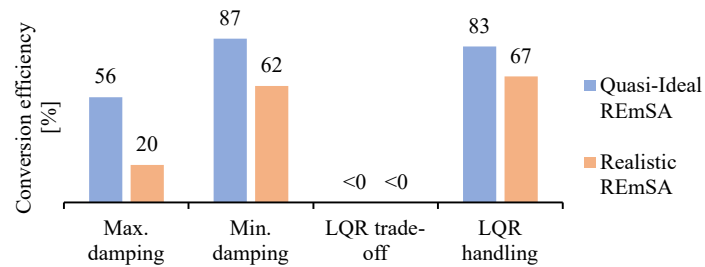
(a)



(b)



(c)



(d)

Figure 4.55: Comparison between the quasi-ideal (blue) and realistic (orange) models at the diverse high level control strategies. Energetic performance: mechanical power (a) and power factor (b) at the REmSA shaft, electrical power (c), and REmSA conversion efficiency (d).

Chapter 5

Experimental investigation

This chapter presents the experimentation aimed at characterizing the developed REmSA prototype. Due to the project timeline, only the campaign related to the automotive system presented in Appx. A is discussed.

At first, the experimental equipment is presented. Dedicated test-beds were developed on purpose for the experimentation of REmSA devices. Then, the static characterization is discussed. The prototype was tested with the electric machine shunted by an external resistance, then it was driven through a controlled power module. First-quadrant and four-quadrants operations were addressed. Subsequently, the dynamic characterization is proposed. It was aimed at the assessment of the frequency response of the prototype. The passive quadrant operation was characterized in terms of mechanical impedance. Then, the active mode was addressed. Finally, acoustic tests were carried out in an anechoic room to assess the noise level of the characterized prototype. At the end, a Hardware-In-the-Loop approach is proposed to assess the performance of a vehicle equipped with REmSA devices. Preliminary tests are presented.

5.1 Experimental equipment

The REmSA was tested in two configurations. The first one interfaces the prototype to a three-phase diode rectifier with a discretely-adjusted shunt resistance (R_{shunt}). The literature commonly uses such approach to test regenerative dampers. According to Eq. 3.73, the variation of the resistive load sets diverse damping coefficients on the electric machine of the REmSA.

The second configuration interfaces the electric machine of the REmSA to a three-phase controlled power module connected to a 48 V battery. The REmSA is current-controlled: the power module receives a q-axis current request, then the FOC strategy drives the electronics. The rotor angular position is required. To this end, the module receives the signals from hall sensors mounted in the prototype,

then it computes the angular position by means of a numerical routine.

The controlled power module was developed by Laboratorio di Meccatronica (Politecnico di Torino). It includes a TMS320F28335 Digital Signal Controller provided by Texas Instrument[®], which features a high-performance 32-bit CPU and clock frequency up to 150 MHz. The three-phase bridge is composed of three N-Channel Power MOSFETs (FMM150-0075X2F) featuring phase leg topology. The switches are characterized by 5.8 mΩ drain-source resistance and 75 V drain-source breakdown voltage. Each gate is driven through an Infineon[®] IR2010S, which is an isolated single channel high-voltage IGBT gate driver designed for motor drives above 5 kW. Overall, the MOSFETs withstand impulsive currents up to 120 A and DC bus voltage up to 75 V, thus providing some margin with respect to the 48 V battery. The module features a plate fin heat sink designed to guarantee continuous operation of 40 Arms.

The remainder of the section presents the test-beds developed for the experimentation of REmSA prototypes.

Belt-driven test-bed The test rig shown in Fig. 5.1 was devised to drive the REmSA with constant-velocity profiles. It is composed of a driving motor (Kollmorgen DBL51700 brushless PM motor) featuring 68 Nm peak impulsive torque that is interfaced to the REmSA by means of a belt transmission with 2 : 1 ratio. A synchronous belt (HTD-8M) was selected and properly preloaded to guarantee a maximum input torque of 160 Nm at the prototype shaft.

The driving motor was connected to a dedicated inverter unit (Kollmorgen Servostar S748). It is controlled through a PC connected via serial communication (RS232). The inverter unit outputs the q-axis current and angular velocity of the driving motor as analog signals. These are acquired by means of a LMS SCADAS data acquisition unit featuring 24-bit analog channels opportunely scaled and sampled. The same hardware is used to acquire the electrical signals at the REmSA side. When the prototype is connected to the diode rectifier, oscilloscope voltage probes are used to sense the voltage drop across the shunt resistance. When the controlled power module is used, voltage and current quantities at the DC bus are sensed through dedicated probes.

Hydraulic test-bed The test rig shown in Fig. 5.2 was devised to drive the REmSA with alternate (or more complex) position profiles. To this end, the shaft of the prototype is connected to a hydraulic actuator through a lever ($\tau_{tb} = 125 \text{ mm/rad}$). The actuator consists of a hydraulic piston controlled through a motor-pump unit. The former—which was manufactured by a local workshop—is a double-acting piston with through rod featuring an area of 640 mm². The latter is composed of a positive displacement gerotor pump—Parker MGG20030 with displacement of 11.47 cc/rev—and a driving motor—Kollmorgen DBL51700 brushless PM motor—that are connected through a bellows expansion joint. The driving

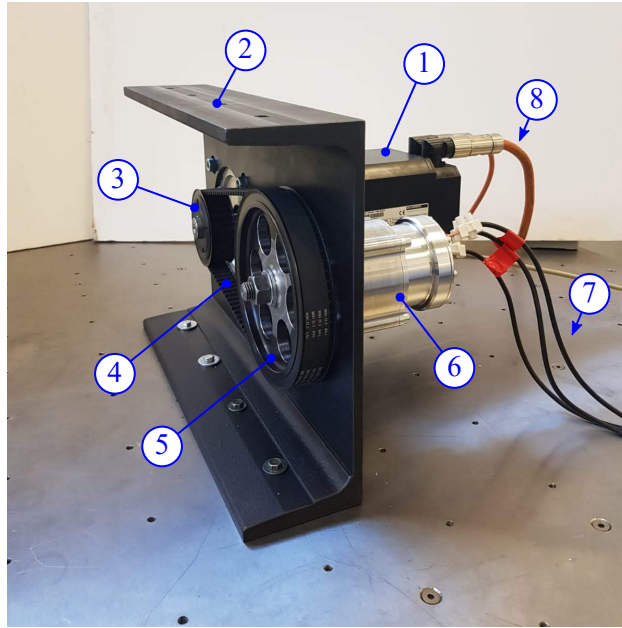


Figure 5.1: Belt-driven test-bed: driving motor (1), test rig flange (2), driving pulley (3), toothed belt (4), driven pulley (5), REmSA prototype (6), prototype phases (7), driving motor phases and feedback (8).

motor is controlled by a dedicated inverter unit (Kollmorgen Servostar S748). Both the motor and the inverter are the same used in the belt-driven test-bed.

The hydraulic piston is equipped with a magnetostrictive position transducer (Gefran RK2) to measure its stroke. Two pressure sensors (Gefran TK) are mounted at the ports of the pump unit. A load cell (Gefran TU K5C, 500 kg range) is mounted on the piston head to measure the force exerted by the REmSA. The load cell signal is conditioned through a MGCplus Data Acquisition system and given as analog output. All these signals are acquired through the analog channels of a dSpace MicroLabBox.

The electronic control units of the test bench are interfaced through CAN communication. The network includes the inverter unit of the driving motor, the controlled power module of the REmSA, the BMS of the battery and the dSpace MicroLabBox. The latter is the master node that manages the test bench. It performs diverse safety checks needed to avoid dangerous operation and damages. Additionally, it implements the position control of the piston. To this end, a PID control is used, where the feedback is closed through the measurement of magnetostrictive position transducer. The dSpace is connected to a PC (via ethernet), where a host is used to manage the test bench, check and log the diverse signals.

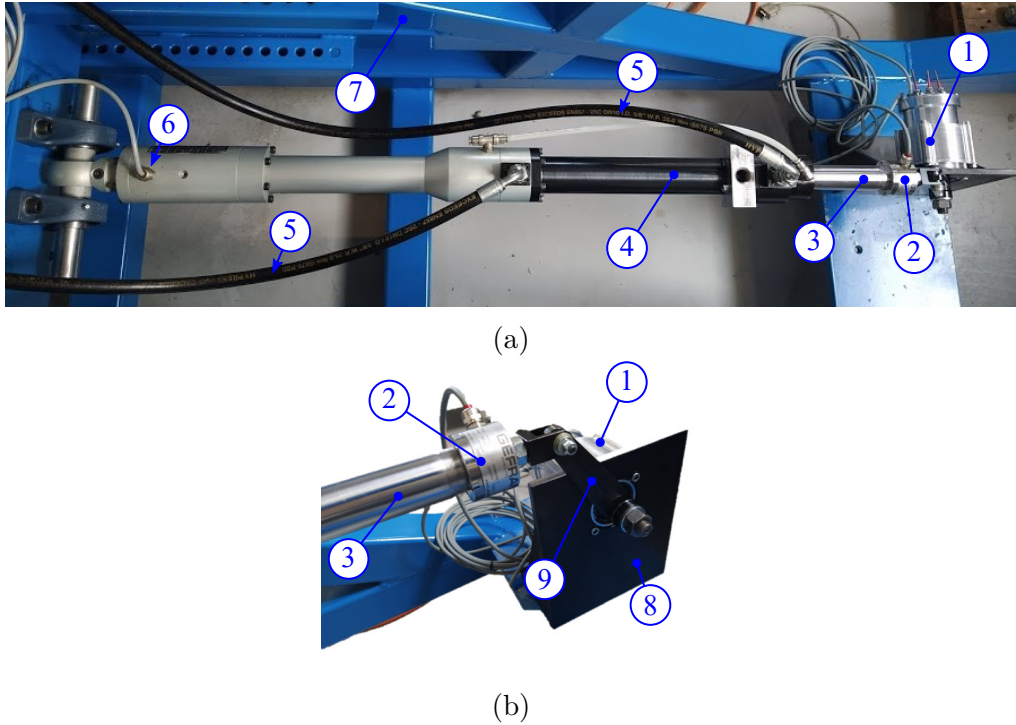


Figure 5.2: Hydraulic test-bed (a) and zoom-in of the piston head-REmSA connection (b). REmSA prototype (1), load cell (2), hydraulic piston (3), hydraulic cylinder (4), pipelines to the motor-pump unit (5), position sensor cable (6), frame (7), REmSA mount (8), REmSA lever (9).

5.2 Static characterization

This section presents the static characterization of the REmSA prototype. For this purpose, steady-state operation—which does not involve any inertia and compliance contribution—were reproduced.

5.2.1 First quadrant operation

The REmSA operation in the first quadrant (passive) was investigated through the belt-driven test bench (Fig. 5.1).

Shunted electric machine At first, the prototype was interfaced to the three-phase diode rectifier with discretely-adjusted shunt resistance (R_{shunt}). Although the power at the resistive load is dissipated, its measurement is useful to evaluate the conversion efficiency, i.e. the ratio between output electrical power and input mechanical power on the REmSA. In fact, such power could be potentially harvested when an active power stage is used. The conversion efficiency was computed

as:

$$\eta = \frac{V_{\text{shunt}}^2}{R_{\text{shunt}} T \omega} \cdot 100\% \quad (5.1)$$

V_{shunt} being the measured voltage drop across the shunt resistance, T_{REmSA} and ω_{REmSA} the torque and angular velocity at the REmsA shaft. The latter were computed from the estimated torque and the measured angular velocity of the driving motor. This procedure is valid since the static conditions avoid any inertia and compliance contributions from the belt transmission. The driving motor torque was estimated as the product between the measured current and the motor torque constant (0.92 Nm/A).

The test was performed as follows: the shunt resistance was fixed. Then, the driving motor was set to run at constant speed. Afterwards, measurement data were extracted. These steps were repeated at diverse driving motor speeds. Five shunt resistance conditions were tested: open circuit ($R_{\text{shunt}} \rightarrow \infty$), 465 m Ω , 135 m Ω , 55 m Ω and short circuit ($R_{\text{shunt}} \rightarrow 0$). Measured torque and angular velocity were converted to the linear domain by means of the retained transmission ratio $\tau_1 = 0.115$ m/rad (Table A.1).

At first, preliminary tests assessed the diverse dissipative contributions of the prototype. The obtained force-velocity curves are reported in Fig. 5.3. The prototype with only the gearbox—the electric machine stator and rotor were disassembled—gives the blue curve, whose damping contribution (101 Ns/m in the low-speed region) is due to the mechanical loss of the gearbox. The prototype with the gearbox and the electric machine rotor—only the stator was removed—gives the orange curve. Differently from the previous configuration, the sun ring of the second stage—which is machined on the rotor of the electric machine—is engaged and the rotor bearings are present. The resulting damping (249 Ns/m in the low-speed region) is significantly increased as the friction at the rotor level contributes with the gearbox transmission ratio squared, as described by Eq. 3.5. Finally, the complete prototype was tested in open circuit. The resulting curve (yellow) represents the minimum damping achievable without investing active power (351 Ns/m in the low-speed region).

Then, the prototype was tested at diverse shunt resistances [83]. The damping points are shown in Fig. 5.4a as well as their interpolation through first-degree polynomials. As described by Eq. 3.73, the behavior is predominantly viscous-dissipative and inversely proportional to the shunt resistance. Slight attenuation of the damping characteristic appears at high speeds. The fitted damping values are reported in Table 5.1. Overall, the prototype achieves a damping-to-mass ratio of 3.23 kNs/m kg, whereas maximum values of 2.44 kNs/m kg can be found in the literature [102].

Some considerations are extracted from the presented results. The torque was estimated from the driving motor current. For this reason, it contains not only the electromagnetic damping component, but also the mechanical losses associated to

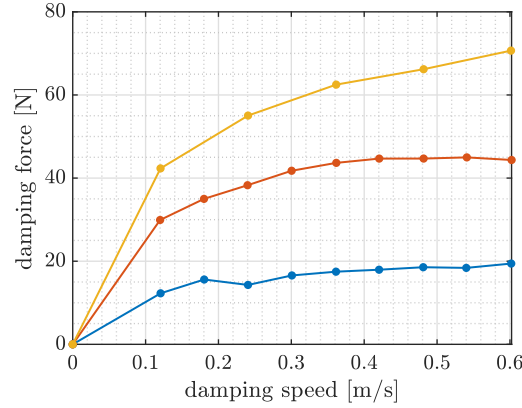


Figure 5.3: Static characterization of the diverse dissipative contributions of the prototype. Gearbox without the sun gear of the second stage (blue), complete gearbox and bearings of the electric machine (orange), complete prototype in open circuit (yellow).

the gearbox and bearings of the driving motor as well as the contribution of the two pulleys. Secondly, the diodes in the bridge rectifier introduce a bias voltage drop (quantified to 0.4 V) and a Joule loss that increases exponentially with the current. The former introduces a dead-band effect on the damping characteristic: the curves tend to intersect the ordinate axis at negative force values. The latter dominates the high-speed region, thus causing the slight attenuation of the damping behavior. Table 5.1 reports the damping values extracted from the first-order polynomial interpolation and the maximum electrical power measured at the shunt resistance.

Fig. 5.4b shows the resulting conversion efficiency computed by means of Eq. 5.1. Short- and open-circuit conditions lead to null conversion, as they correspond to null voltage and infinite shunt resistance, respectively. The obtained efficiency curves are convex, whose maximum is reported in Table 5.1. The 465 m Ω shunt resistance gives the maximum conversion efficiency of 59.9%. Note that the results are conservative: the input mechanical power, i.e. the denominator of Eq. 5.1, is overestimated as it includes the driving motor and belt transmission losses. Furthermore, the force-speed plane is only partially explored because of the application of discrete shunt loads. Therefore, regions with larger conversion efficiency could be present. Nevertheless, the REmSA prototype exhibits high conversion efficiency that are promising when compared to other technologies. For instance, efficiency values of electro-hydrostatic dampers rarely overcome 40% [39].

Controlled electric machine The REmSA prototype was driven through the three-phase controlled power module, whose DC bus was connected to four lead acid car batteries (12 V) in series. The voltage and current at the DC bus were measured to extract the electrical power. Then, the conversion efficiency was obtained as the

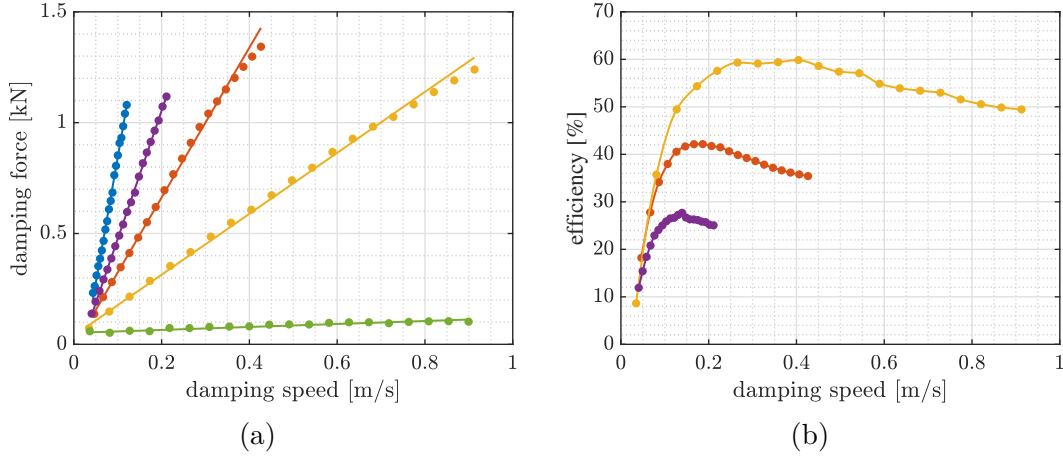


Figure 5.4: Static characterization with the electric machine shunted by an external resistance: damping force (a) and conversion efficiency (b). Open circuit (green), 465 mΩ (yellow), 135 mΩ (orange), 55 mΩ (purple) and short circuit (blue). Experimental points (dots) and interpolated damping force by using a first-degree polynomial (solid in Fig. a).

Table 5.1: Results of the static characterization with the electric machine shunted by an external resistance.

Shunt resistance	Damping [kNs/m]	Max. efficiency [%]	Max. recoverable power [W]
$R_s \rightarrow \infty$	0.07	—	—
$R_s = 465 \text{ m}\Omega$	1.37	59.9	146.8
$R_s = 135 \text{ m}\Omega$	3.38	42.2	48.7
$R_s = 55 \text{ m}\Omega$	5.78	27.7	26.4
$R_s \rightarrow 0$	19.57	—	—

ratio between the electrical and the mechanical power. Also in this case, the latter was estimated by means of the driving motor current.

The test was performed as follows: constant driving motor speed was set. Then, a braking current ramp with slope 1 A/s was applied to the REmSA through the controlled power module. The test was stopped when the driving motor or the controlled power module reached current saturation. Note that the current ramp was set slow enough to avoid any dynamic effect. Therefore, the test reproduced static conditions.

Speed and current of the driving motor as well as the electrical quantities at the DC bus of the power module were acquired. For demonstration purposes, Figs. 5.5 show the signals acquired during the test corresponding to 0.3 m/s suspension

speed (orange in 5.5a). The damping current reference follows a ramp profile (blue in 5.5a). Fig. 5.5b shows the electrical quantities at the DC bus. The regenerated current (blue) escalates with the speed. At the same time, the voltage (orange) increases since the used lead acid batteries were not able to maintain stable voltage level while charging.

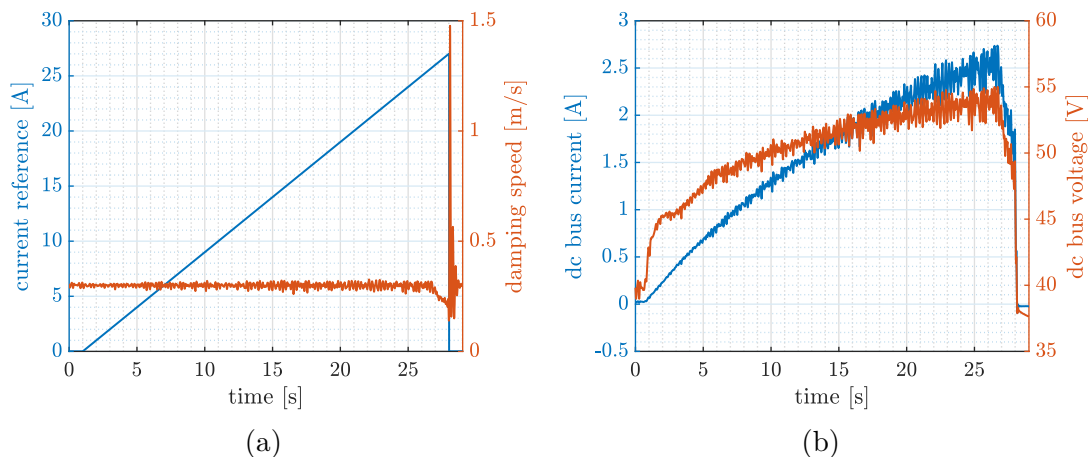


Figure 5.5: Static characterization with the electric machine driven through the three-phase controlled power module. Measurements from the test corresponding to 0.3 m/s suspension speed. (a): current reference (blue) and damping speed (orange). DC bus quantities (b): current (blue) and voltage (orange).

By repeating the test procedure at diverse driving motor speeds, constant-speed efficiency curves were extracted and then interpolated along the velocity coordinate to obtain the efficiency maps shown in Figs. 5.6. Two separate campaigns were needed to explore the low- and high- speed regions, which are reported in Fig. 5.6a and 5.6b, respectively. The points corresponding to electrical energy consumption are removed, which occur in the low-speed high-force region and in the low-force one (see Sec. 2.2.1). Such regions are delimited by the maximum and minimum damping curves shown in the test with the shunted electric machine.

Overall, the obtained results are promising: a maximum conversion efficiency spot at 82% was found (Fig. 5.6b). Furthermore, values larger than 70% were obtained in a broad region. Also in this case, the obtained results contain additional loss contribution out of the studied prototype, i.e. the driving motor and inverter efficiency, as well as the belt transmission. The maximum regenerated power is 499 W occurring at the largest tested velocity and force (0.9 m/s and 876 N).

5.2.2 Four-quadrant operation

The hydraulic test-bed shown in Fig. 5.2 was used to investigate the REmSA operation in the four force-velocity quadrants. The prototype was driven through

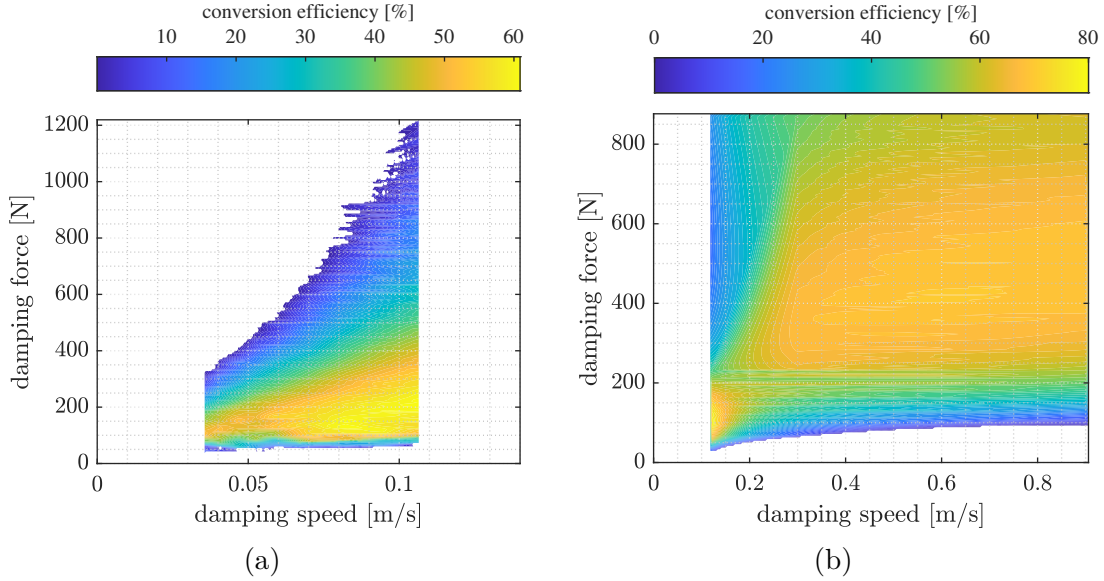


Figure 5.6: Static characterization with the electric machine driven through the three-phase controlled power module. Conversion efficiency maps in the force-speed plane: low-speed (a) and high-speed (b) regions.

the three-phase controlled power module, whose DC bus was connected to a 48 V lithium-ion battery pack.

The test was performed as follows: constant current reference was set to the controlled power module. This corresponds to constant force provided by the REmSA. Then, saw-tooth position profiles—which corresponds to positive-negative piecewise constant speed—were imposed through the hydraulic actuator. Diverse amplitude and frequency combinations were set to reproduce diverse speed values.

The load cell force, the hydraulic actuator position and the electrical quantities at the DC bus of the power module were acquired. Note that the REmSA lever of the test-bed features transmission ratio 0.125 m/rad, which is different from the designed value ($\tau_1 = 0.115$ m/rad in Table A.1). Therefore, the measured force (position) was multiplied (divided) by a factor 0.125/0.115. Then, the velocity was obtained as the first time-derivative of the measured position.

For demonstration purposes, Figs. 5.7 show the signals acquired during the test that corresponds to suspension speed of 0.2 m/s. The suspension stroke (blue) and velocity (orange) are reported in Fig. 5.7a, whereas Fig. 5.7b shows the stroke (blue) and the force (orange). The saw-tooth profile corresponds to piecewise constant velocity. The constant current reference translates into almost constant force (right-axis in Fig. 5.7b). Force peaks occurring at the motion inversion are due to the inertial effects. The latter are evident in the stroke-force curve reported in Fig. 5.7c. Fig. 5.7d shows the mechanical (blue) and electrical (orange) instantaneous power. As discussed in Chap. 4, positive power indicates energy

flow from the suspension to the battery: the test procedure makes the REmSA alternate active and passive (regenerative in this case) operation. In active mode, the mechanical power is smaller than the electrical one because of the prototype conversion efficiency. The opposite occurs in regenerative operation.

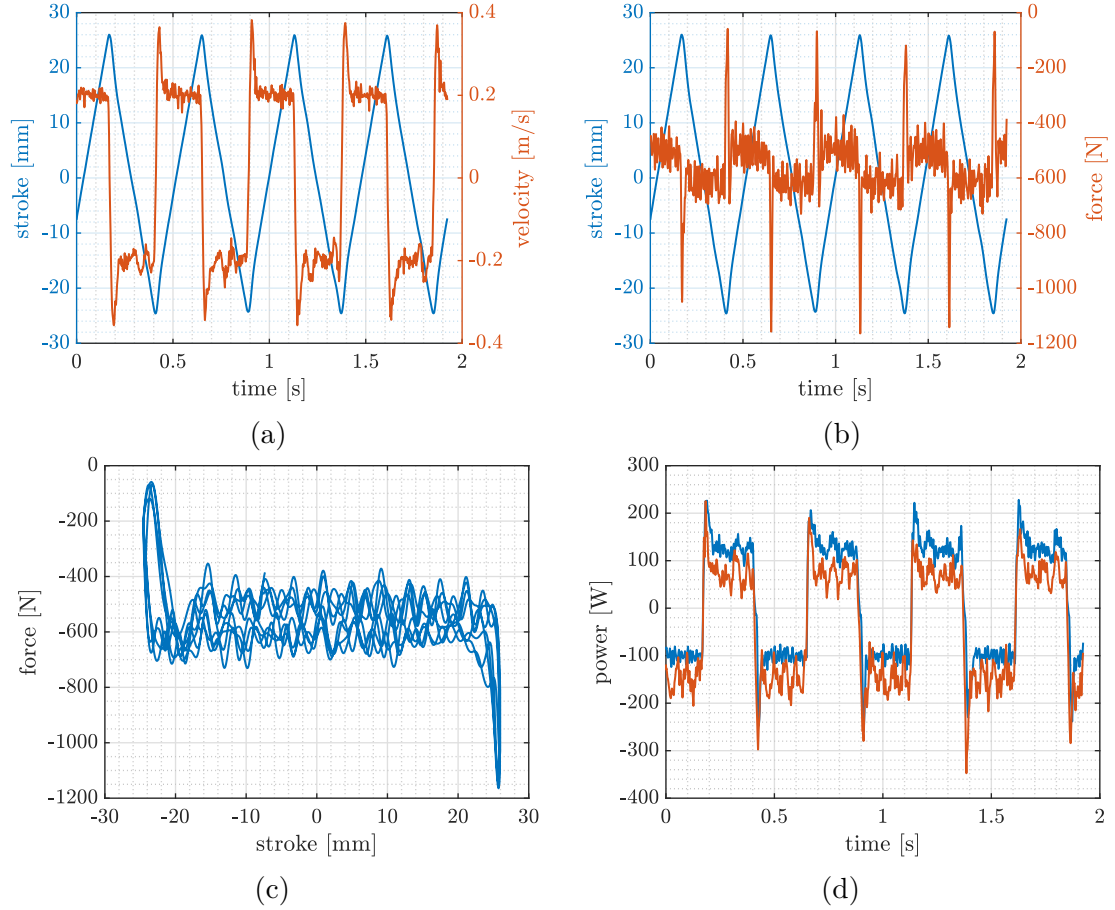


Figure 5.7: Static characterization in the four force-speed quadrants. Measurements from the test corresponding to 0.2 m/s suspension speed. (a): suspension stroke (blue) and velocity (orange). (b): suspension stroke (blue) and REmSA force (orange). (c): REmSA force vs suspension stroke. (d): Mechanical (blue) and electrical (orange) power.

The above-reported signals were processed to extract the average value over the window centered on the null stroke point. In this way, the transient occurring at the motion reversal is finished and the results still consider static conditions. Several points in the force-speed plane were explored by spanning diverse amplitude-frequency combinations and reference current values. The active component of the mechanical and electrical power signals were extracted at each test-point. Then,

the conversion efficiency was computed. Finally, the obtained values were interpolated to get the electrical power and conversion efficiency maps reported in Figs. 5.8a and 5.8b, respectively. Velocity values lower than 0.04 m/s were not explored because of stick slip issues of the hydraulic actuator, which dominates the response at very low speed.

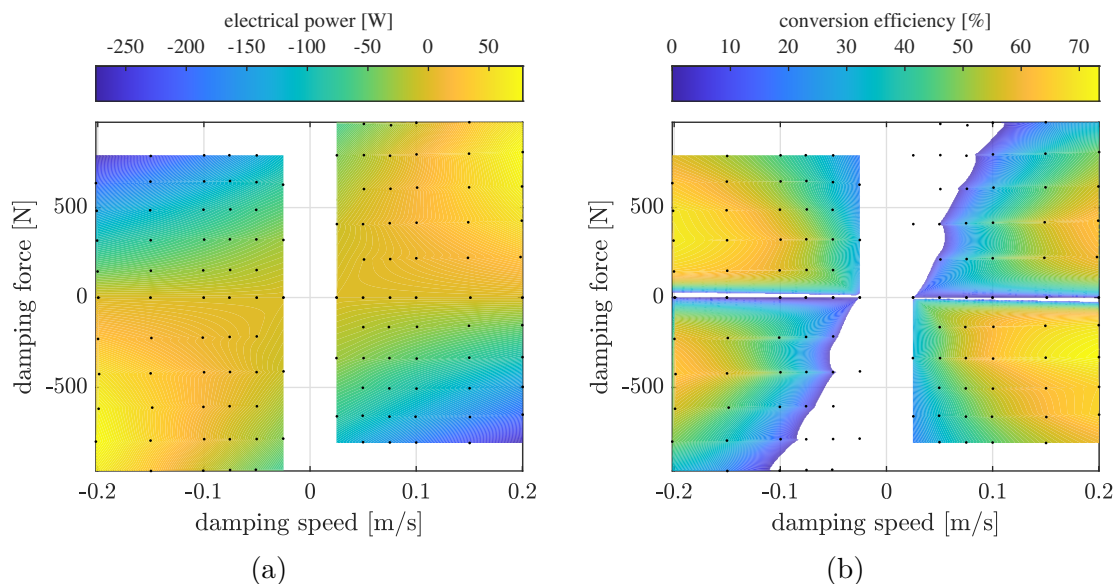


Figure 5.8: Static characterization in the four force-speed quadrants: electrical power (a) and regenerative conversion efficiency (b). Test-points (dots) and interpolated data (color map).

Similarly to Fig. 5.6, the efficiency map in the passive quadrants (I and III) reports only the regenerative operation, whose maximum is 64%. In active mode, the maximum conversion efficiency is 74%.

5.3 Dynamic characterization

The REmSA prototype was characterized under dynamic operation both in passive and active modes.

5.3.1 Mechanical impedance

The mechanical impedance is discussed in Appx. B. It was experimentally characterized through the hydraulic test-bed (Fig. 5.2) by imposing harmonic position profiles. Shunted and controlled electric machine tests were performed.

Shunted electric machine

The prototype was interfaced to the three-phase diode rectifier with discretely-adjusted shunt resistance (R_{shunt}) to reproduce a damping behavior, as described by Eq. 3.73. The test was performed as follows: the shunt resistance was fixed. Then, a harmonic position profile with given frequency was imposed. Finally, the measurements were acquired. The procedure was repeated at diverse shunt resistances and position profile frequencies.

The measured signals were the load cell force and the hydraulic actuator position. The REmSA lever of the test-bed features transmission ratio 0.125 m/rad, which is different from the designed value ($\tau_1 = 0.115$ m/rad in Table A.1). Therefore, the measured force (position) was multiplied (divided) by a factor 0.125/0.115.

For each combination of shunt resistance and imposed position frequency, the logged time signals were processed. Specifically, the fourier transforms of the measured force and position were computed. Then, the fundamental component was extracted. The position transform was multiplied by the fundamental harmonic frequency to obtain the velocity. Finally, the mechanical impedance magnitude at the given frequency was computed according to Eq. B.1.

Fig. 5.9 shows the obtained mechanical impedance, where the x-markers represent the tested points. The impedance computed through the the fitted lumped parameter model (see Appx. B) is shown in dashed and solid line. The model achieves a good match with the experimental results. The tuned parameters are reported in the Appendix.

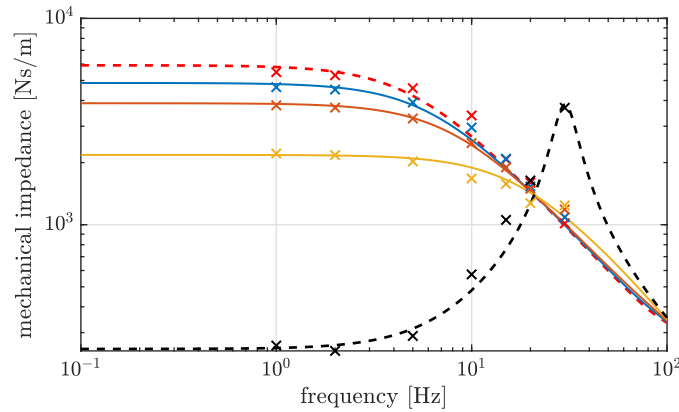


Figure 5.9: Mechanical impedance magnitude obtained by shunting the electric machine through an external resistance. Open circuit (black), 465 m Ω (yellow), 135 m Ω (orange), 55 m Ω (blue), short circuit (red). Experimental (x-marker) and lumped parameter response (dashed and solid lines).

As discussed in Appx. B, the open circuit response exhibits a strong inerter behavior. Conversely, the other damping values move such behavior to the high

frequency range, where the compliant mount dominates the response, i.e. after the mechanical resonance that is evident for the open circuit curve. The electromagnetic pole attenuates the response of the high damping curves. However, such effect can be compensated by means of a controlled power module.

Controlled electric machine

The prototype was driven through the three-phase controlled power module, whose DC bus was connected to a 48 V lithium-ion battery pack. No low level control was implemented to have the REmSA behavior not compensated. The high level control with damping logic was implemented: the hydraulic actuator velocity was multiplied by a damping coefficient to obtain the force reference of the prototype. The latter was converted into a current reference that was given to the controlled power module.

The test was performed as follows: the damping of the high level control was fixed. Then, a harmonic position profile with given frequency was imposed. Finally, the measurements were acquired. These steps were repeated at diverse damping values and frequencies of the position profile .

The measured signals were the load cell force and the hydraulic actuator position. The REmSA lever of test-bed features transmission ratio 0.125 m/rad, which is different from the designed one ($\tau_1 = 0.115$ m/rad in Table A.1). Therefore, the measured force (position) was multiplied (divided) by a factor 0.125/0.115. The data acquired in this test were used to identify the REmSA non-linear numerical model (see Sec. 4.3.1).

For each combination of damping value and imposed position frequency, the logged time signals were processed. Specifically, the fourier transforms of the measured force and position were computed. Then, the fundamental component was extracted. The position transform was multiplied by the fundamental harmonic frequency to obtain the velocity. Finally, the mechanical impedance magnitude at the given frequency was computed according to Eq. B.1.

Fig. 5.10 shows the obtained mechanical impedance, where the x-markers represent the tested points. Differently from the shunted electric machine case (Fig. 5.9), the electromagnetic pole does not attenuate the response: the controlled power module compensates for the electrical dynamics without spending active power. Overall, the inerter contribution influences the response at all the damping settings, especially the null-damping one (blue in Fig. 5.9). As discussed in Appx. B, the position of the zero related to the inerter effect is proportional to the damping. However, such effect can be mitigated through the force control implemented in the low level control, as discussed in Chap. 4.

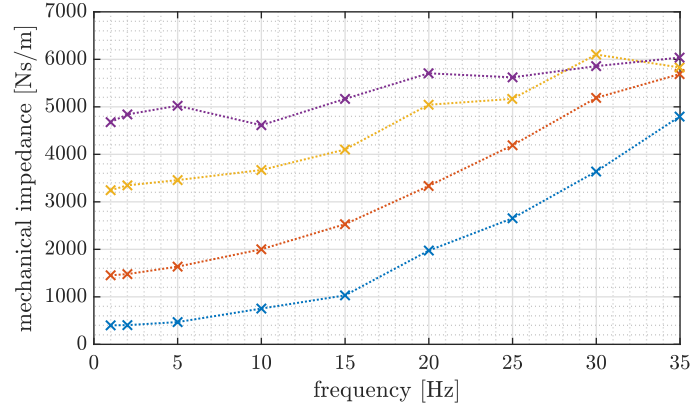


Figure 5.10: Mechanical impedance magnitude obtained through the controlled electric machine at diverse damping values of the high level control.

5.3.2 Active-mode FRF

The REmSA operation in active mode was investigated through the setup shown in Fig. 5.11. The REmSA (1) was mounted on the flange (2). The lever end (3) was connected to the load cell (4) that was clamped on the frame. The electric machine of the prototype was connected to the three-phase controlled power module, which was provided with a sinusoidal current reference. A chirp signal was used to explore the frequency range of interest. Non-null bias value was needed to preload the kinematic chain between the electric machine and the load cell. In this way, backlash and mount clearance effects were avoided.

The current reference profile, the angular position of the electric machine rotor and the load cell force were acquired. The latter was corrected through a geometric factor accounting for the angle between the lever and load cell axis (27 deg). Furthermore, the lever features transmission ratio 0.125 m/rad, which is different from the designed value ($\tau_1 = 0.115$ m/rad in Table A.1). Therefore, the measured force was multiplied by a factor 0.125/0.115.

The test was performed at 12 A bias and 2 A current amplitude. The measured signals are shown in Figs. 5.12. The frequency is logarithmic with the time. Both the force and angle responses exhibit a mechanical resonance occurring at about 85 s.

The measured data were processed to extract the force-current (Fig. 5.13a) and force-angle (Fig. 5.13b) FRFs. The former features a mechanical resonance in the range 60 to 70 Hz. The latter is the compliance of the transmission that goes from the electric machine rotor to the load cell. It is almost constant over the investigated frequency range.

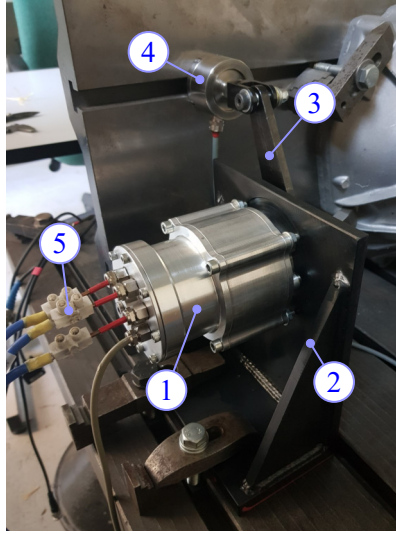


Figure 5.11: Experimental test-bed used for dynamic characterization in active mode. REmSA prototype (1), mounting flange (2), lever (3), load cell (4), electric machine phase cables (5).

5.4 Acoustic characterization

Noise and vibration harshness (NVH) are critical aspects to consider in the automotive field. For this reason, the REmSA prototype was tested inside an anechoic chamber to evaluate the produced noise levels without the influence of sound reflections [83]. The experimental setup is shown in Fig. 5.14. The prototype was placed over a foam layer (5). Two microphones (AVM MI 17 1/4", free-field) were placed at one meter of distance from its front (6) and side (4). Their signals were sampled at 12.8 kHz through the 24-bit analog channels of a LMS SCADAS data acquisition hardware.

The measured time histories were filtered using the A-weighting continuous-time function to account for human sensitivity to noise levels [119]:

$$H_A(s) = \frac{7.4 \cdot 10^9 \cdot s^4}{(s + 12.4)^2(s + 7.7 \cdot 10^4)^2(s + 4.6 \cdot 10^3)(s + 676.7)} \quad (5.2)$$

The filtered signals were then expressed as sound pressure levels (*SPL*) in dBA referenced to $p_0 = 20 \mu\text{Pa}$:

$$SPL = 20 \log_{10} \left(\frac{p_A}{p_0} \right) \quad (5.3)$$

p_A being the A-filtered front/side acoustic pressure signal. Finally, the RMS value was computed.

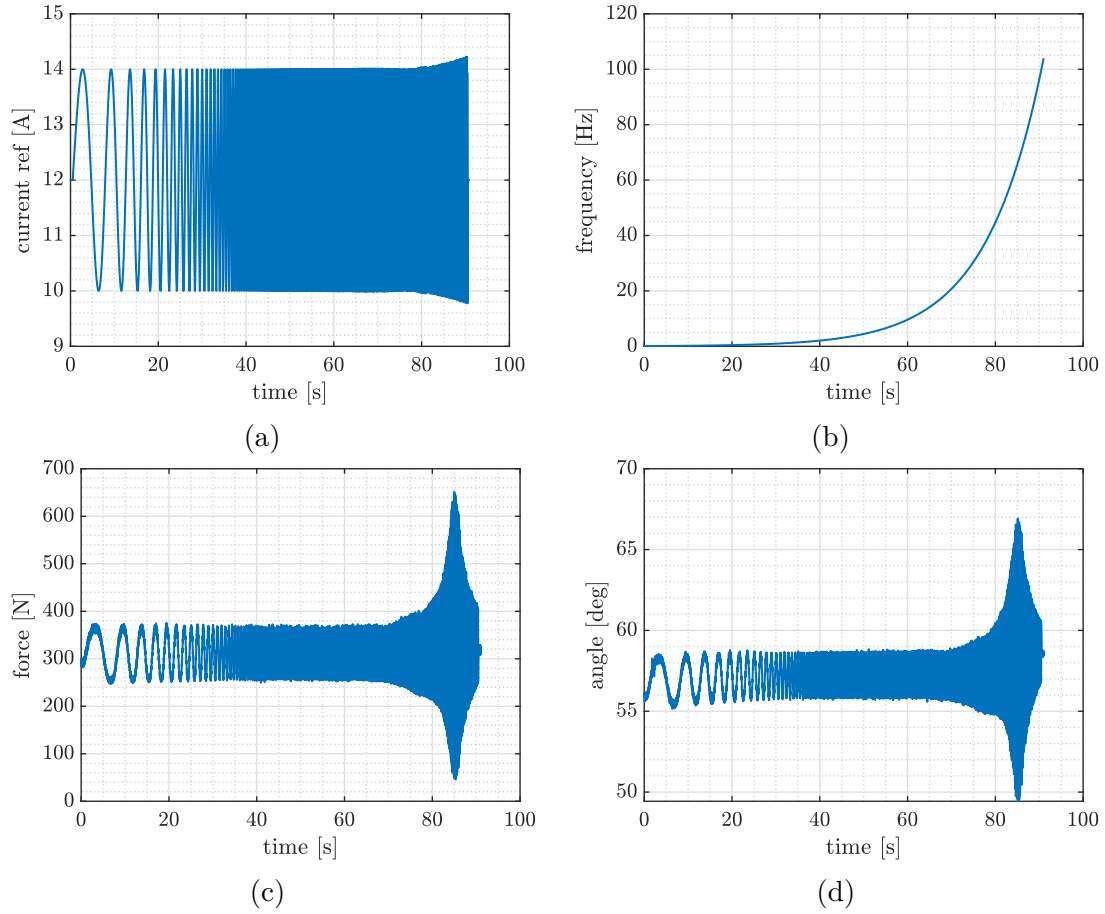


Figure 5.12: Active-mode dynamic test measurements. Harmonic reference current (a) and frequency (b), measured force (c), rotor angle (d).

The REmSA electric machine was driven as a motor through the controlled power module. Constant and sinusoidal speed references were provided. The results of the acoustic test are reported in Table 5.2, where the velocity is expressed in the linear domain by means of the lever transmission ratio $\tau_1 = 0.115 \text{ m/rad}$ (see Table A.1).

Overall, side measurements are slightly larger than the front ones. The worst scenario occurs at constant speed of 341 m/s, which gave noise level of 49.63 dBA. As a reference, a 24-hour exposure limit of 55 dBA is established by the United States Environmental Protection Agency [120]. However, the performed acoustic test is not indicative of the noise level of the prototype when mounted on the vehicle. In such case, the mechanical interface between the device and the chassis significantly impacts the transmission of vibrations, as well as the media used to isolate the cabin from the chassis components.

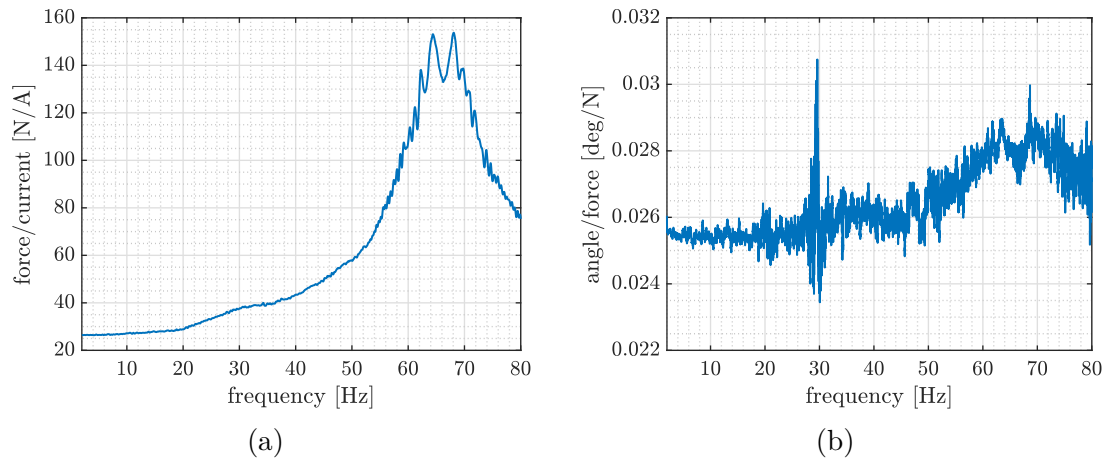


Figure 5.13: Active-mode frequency response function: force-current (a) and compliance (b).

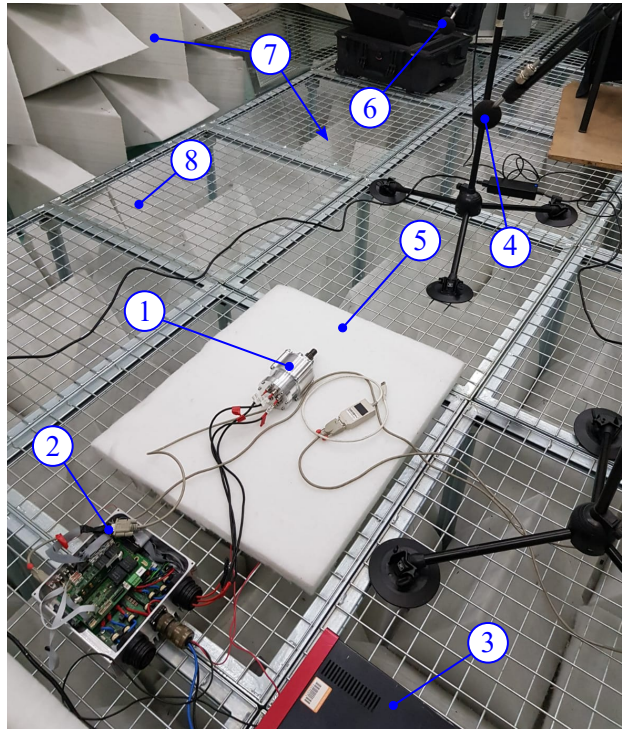


Figure 5.14: Experimental setup for acoustic characterization. REMSA prototype (1), controlled power module (2), power supply (3), side microphone (4), foam pad (5), front microphone (6), wall and floor foam blocks (7), supporting structure (8).

Table 5.2: Measured sound pressure levels with constant and sinusoidal input velocities.

Input type	Velocity input		RMS <i>SPL</i> [dBA]	
	amplitude [mm/s]	frequency [Hz]	front	side
Constant	96	–	36.03	36.92
	178	–	42.3	44.08
	341	–	47.89	49.63
Sinusoidal	41	2	37.07	35.23
	62	1.5	37.01	37.36
	328	1	46.97	48.69

5.5 Preliminary Hardware-In-the-Loop test

A Hardware-In-the-Loop (HIL) approach was devised to assess the performance of a vehicle equipped with REmSA devices. The prototype mounted in the hydraulic test-bed was interfaced with the vehicle model running in real time on a simulation platform. This approach is the transition between the numerical investigation proposed in Chap. 4—where the vehicle was equipped with the REmSA model identified through experimental data—and the future implementation of the REmSA on real vehicle.

The proposed HIL architecture is shown in Fig. 5.15. The real-world components—i.e. the REmSA with its controlled power module and the hydraulic actuator—are highlighted through the green frame. Conversely, the quarter-car vehicle model and the controllers run in real-time on the dSpace MicroLabBox (orange frame). The quarter-car model (see Sec. 4.1.2) receives the road profile and the REmSA force that is measured from the experimental test-bed. The latter is driven through the hydraulic actuator to reproduce the suspension stroke of the quarter-car model. Therefore, the REmSA undergoes the displacement and velocity profile it would experience if mounted on the suspension. At the same time, it exerts a force that is measured through the load cell and given as feedback to the quarter-car model. Therefore, the REmSA prototype acts on the simulated vehicle dynamics.

The control of the hydraulic actuator drives the motor-pump unit to make the hydraulic piston track the stroke of the quarter-car suspension. To this end, a position PID control is implemented: it outputs the current request that is sent to the inverter unit of the driving motor. The REmSA control was discussed in Sec. 4.2. It includes the high- and low-level controls. The latter outputs the torque request that is sent to the controlled power module to drive the REmSA.

The HIL test is performed by setting the road profile—i.e. unevenness or lumped obstacle as well as the vehicle speed—and the REmSA high-level control strategy,

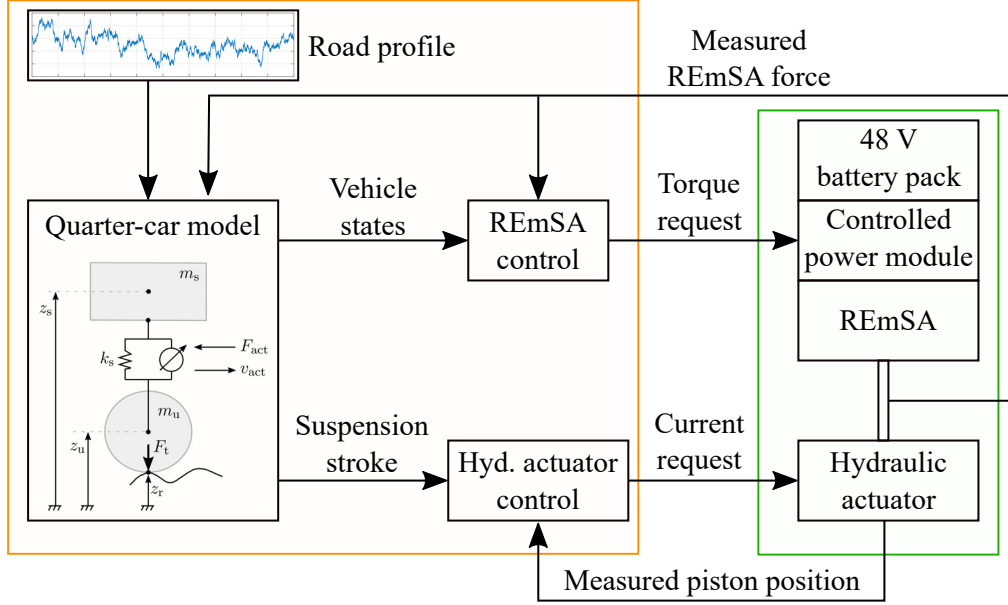


Figure 5.15: Hardware-In-the-Loop scheme. Test-bench (green frame) and models running in real time on a dSpace MicroLabBox (orange frame).

for instance damping control or LQR. Then, the quarter-car response is monitored to assess the vehicle dynamics performance. At the same time, the electrical power at the battery and the mechanical power at the REmSA shaft are measured from the test-bed to address the energetic performance. Overall, the same investigations performed in Chap. 4 can be reproduced, with the difference that the identified REmSA model is now replaced by the real prototype.

The architecture was preliminary tested with no low-level control. An ISO B-class at 70 km/h was considered as road scenario, whose profile is shown in Fig. 5.16a. The high level REmSA control was set to reproduce a 1000 Ns/m damping behavior. Fig. 5.16b reports the angular position of the REmSA shaft: the orange dashed line is the measured signal, the blue solid curve is the reference that is computed from the stroke of the quarter-car suspension by applying the lever transmission ratio. Fig. 5.16c shows the quarter-car sprung (blue) and unsprung (orange) mass responses. Note that the sprung mass is poorly damped. Fig. 5.16d reports the REmSA force measured through the load cell and provided as feedback to the quarter-car. The force response highlights a localized unstable behavior. This could be due to the absence of the low-level control, which results in limited REmSA bandwidth. In fact, the prototype should behave as a damper because of the implemented high level control strategy. However, the force it exerts on the suspension force features significant phase lag at mid-high frequency. In such frequency range, the REmSA introduces a force that is delayed with respect to a damping action, thus impacting the HIL stability.

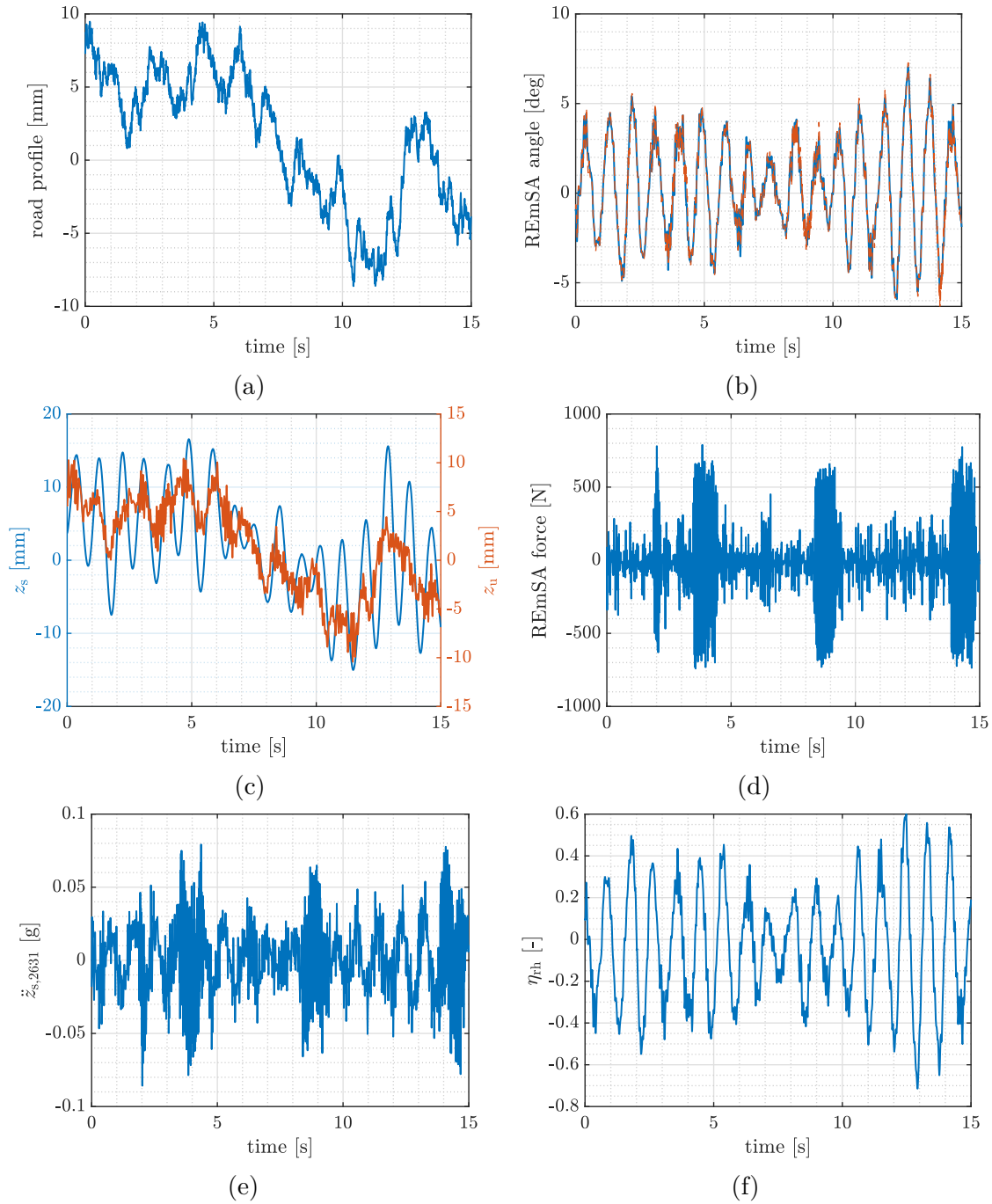


Figure 5.16: Hardware-In-the-Loop test with an ISO B-class road at 70 km/h and the high level REmSA control set to reproduce a 1000 Ns/m damping behavior. Road profile (a). REmSA shaft angular position (b): reference (solid blue) and measured (dashed orange). Quarter-car response (c): sprung (blue) and unsprung (orange) mass vertical motions. REmSA measured force (d). Quarter-car performance indexes: comfort (e) and road holding (f).

Figs. 5.16e and 5.16f report the filtered sprung mass acceleration and road holding index of the quarter-car vehicle model. The RMS indicators can be extracted to assess the vehicle dynamics performance. However, the present test is not indicative as it features poor stability.

Fig. 5.17a shows the electrical measurements at the DC bus of the controlled power module, i.e. current (blue) and voltage (orange), whereas the electrical power (blue) and the mechanical power at the REmSA shaft (orange) are reported in Fig. 5.17b. The sign convention considers positive power when the energy flow goes from the suspension to the battery, i.e. regenerated power. Also in these results, the poor stability emerges. The average power values can be computed and then used to assess the conversion efficiency of the REmSA.

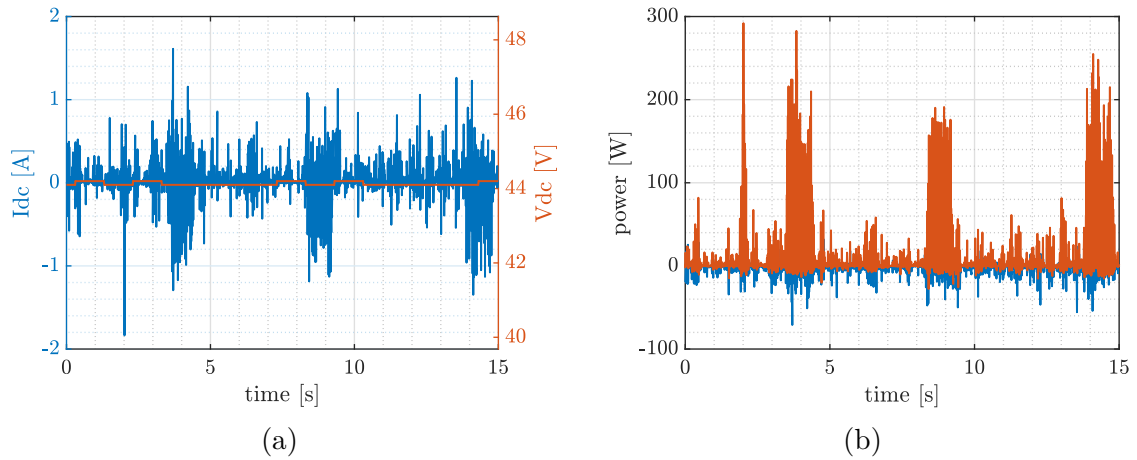


Figure 5.17: Hardware-In-the-Loop test with an ISO B-class road at 70 km/h and the high level REmSA control set to reproduce a 1000 Ns/m damping behavior. Electrical measurements at the DC bus (a): current (blue) and voltage (orange). Measured power (b): electrical (blue) and mechanical at the REmSA shaft (orange).

Overall, additional effort must be dedicated to the HIL experimentation: it is a powerful approach to assess the REmSA performance in the perspective of its implementation on real vehicle. However, the present dissertation aimed at presenting the strategy. Although extensive work has been done [121], further experimentation is left for future research.

5.6 Final remarks

Overall, the REmSA prototype presented in Appx. A was characterized through dedicated experiments. At first, static characterization in regenerative mode highlighted advantageous efficiency performance, especially when compared to other electromagnetic damper technologies. Then, the prototype was statically tested

in the four quadrants: both the passive and active operations gave promising efficiency results. Dynamic tests in the passive quadrant addressed the mechanical impedance. At first, the prototype with shunted electric machine was investigated. A lumped parameter model was identified and then used to address the basic behavior of the REmSA. Inerter and compliant mount contributions were highlighted, as well as the attenuation due to the electric machine dynamics. The latter is mitigated by means of a controlled power module, as confirmed by dedicated experiments that were performed without any low level control. Additional dynamic tests were aimed at the REmSA response in active mode: the compliance and force-current FRFs were assessed. The latter shown the mechanical resonance due to the mount compliance. Finally, the acoustic characterization highlighted non-negligible noise generation. Nevertheless, the level was below the limits indicated by the standard.

Further experimentation should focus on the REmSA with the low-level controller to assess the energetic and force-tracking capability. The proposed HIL experimental approach must be completed with the low-level control to improve the system stability. Moreover, the prototype presented in Chap. 3 should be experimentally characterized and then implemented on the retained motorcycle. All these activities are the starting point of future work.

Chapter 6

Conclusions

Active electromagnetic suspensions attracted many research efforts in the context of the emission reduction and driving automation trends that most of the carmakers are chasing. The significant number of scientific outcomes and patents published in the last decades testifies the momentum involving such devices. Nevertheless, few efforts were dedicated to rotary linkage-based and full-active systems. Furthermore, the scientific literature lacks a design methodology that gives compact linkage-based layouts starting from vehicle performance and packaging requirements. These aspects cover a relevant role when the research goal is the implementation of such technology at an industry level. Finally, the literature review highlighted a significant gap between the industry and the scientific research: the industry is interested more in the active feature than the regenerative one, which is considered as a secondary aspect to limit the energy consumption related to the active operation. Conversely, the academic research focuses on the regenerative aspect and usually disregards the active feature: most of the research effort addresses regenerative suspensions that are not capable of active operation. In this context, the present dissertation focused on linkage-based rotary electromagnetic suspensions for automotive and motorcycle applications.

Chapter 3 proposed a dedicated system-level design methodology for REmSAs. It establishes specific steps that allow the designer to develop and integrate a REmSA prototype into the retained vehicle suspension. The methodology was applied to a case study to detail the diverse steps and present considerations as well as analytic and numerical modeling approaches. Once the design constraints and the requirements were assessed by means of packaging and vehicle dynamics considerations, the electric machine and linkage were optimized. Subsequently, gearbox and electric machine were matched to minimize the inertia features of the prototype. The detailed design of the diverse components concluded the methodology. Overall, a very compact prototype for motorcycle application was obtained and then manufactured. The present research also led to the development and manufacture of a prototype for an automotive application that was designed with a previous

version of the proposed methodology. The motorcycle device featured larger force capability while having very similar outer envelope to the automotive one. This result was achieved thanks to the upgraded design methodology and better utilization of the prototype volume. Furthermore, the optimization of the diverse components resulted in a lower equivalent inertia, which is a crucial aspect when dealing with electromechanical suspensions. The developed methodology intends to be a guideline for both academy and industry moving towards the development of REmSAs.

Chapter 4 addressed the modeling and control of REmSAs. A model able to reproduce the real behavior of REmSA systems was developed to account for the dissipative effects of both the electric machine and gearbox, the backlash, and the mechanical dynamics. The model was identified through experimental data. Due to the project timeline, the prototype developed for the automotive application was used. Then, the developed model was integrated into the quarter-car model of the vehicle. The control of REmSAs was discussed. Two different control layers are required: the low level controls the force that the REmSA applies to the suspension, the high level aims at controlling the vehicle dynamics to optimize comfort and handling. The main strategies—i.e. skyhook and groundhook, spring negation, and LQR—were compared by using a vehicle model that includes an ideal REmSA. It was demonstrated that the LQR gives a combination of skyhook, groundhook and spring negation. For this reason, the subsequent results focused on the LQR strategy with diverse settings aimed at the comfort, handling or trading off these two performance. Specifically, the quarter-car vehicle including the developed REmSA model was simulated to assess the performance of the diverse LQR high-level control strategies. The impact of the REmSA realistic behavior was investigated, along with the effect of the low-level compensator. The apparent powers, i.e. active and power factor, at the REmSA and electric machine shafts were analyzed. Overall, the proposed investigation demonstrated how the REmSA is capable of improving the vehicle performance when compared to conventional passive dampers. However, its realistic behavior requires proper control. In fact, no difference between the vehicle dynamics performance of the quasi-ideal and realistic model was appreciated when the low-level control was implemented to compensate for the prototype mechanical non-idealities, i.e. inertia, compliance and friction. However, such non-idealities impact the energy performance of the REmSA because the mechanical dynamics compensation and the internal friction requires additional energy. However, the most important result is that the REmSA can reproduce the operation of a conventional damper, with the significant advantage of electrical energy regeneration. Therefore, such system can improve the energy management of the vehicle by keeping unchanged the comfort and handling performance. Additionally, it can implement more complex control strategies, i.e. the LQR, to improve the comfort and the handling. According to the adopted high level control logic, the energetic performance of the REmSA changes, moving from the regeneration (typically

for handling-oriented strategies) to the consumption (typically for comfort-oriented strategies).

Chapter 5 presented the Experimental characterization of the automotive REmSA prototype. To this end, dedicated test-beds were developed. At first, static characterization both in active regenerative mode highlighted advantageous efficiency performance, especially when compared to other electromagnetic damper technologies. Dynamic tests in the passive quadrant addressed the mechanical impedance with both the shunted and controlled electric machine. The latter allows to compensate for the electric machine dynamics. Additional dynamic tests were aimed at the REmSA response in active mode. The compliance and force-current FRFs were assessed, which highlighted a mechanical resonance due to the mount compliance. Subsequently, acoustic characterization highlighted non-negligible noise generation. Nevertheless, the level was below the limits indicated by the standard. Finally, a HIL approach was devised to assess the performance of a vehicle equipped with REmSA devices. The prototype mounted in the hydraulic test-bed was interfaced with the vehicle model running in real time on a simulation platform. Preliminary testing highlighted localized unstable behavior. This could be due to the absence of the low-level control, which resulted in limited REmSA bandwidth.

6.1 Future work

The present work focused on the integrated design of REmSA by considering the retained vehicle architecture and performance requirements. However, the implementation at an industry level imposes REmSAs to meet Automotive Safety Integrity Level (ASIL) requirements. The latter establish safety requirements for automotive components to be compliant with the ISO 26262, ranging from grade A (lowest) to D (highest hazard). REmSAs would be classified in D-grade—as for power steering and semi-active suspension systems—because of the risks associated with its failure. In this perspective, the design of the prototype and its power electronics must account for such aspects.

From the experimental perspective, the present dissertation left several open aspects that are the starting point of future research. The motorcycle REmSA prototype must be characterized on the developed test-beds and then mounted on the retained vehicle. The latter activity involves extensive experimentation on road and allows the assessment of NVH aspects. Then, the HIL approach must be further investigated to address its stability issues. Specifically, the low-level control must be implemented to improve the REmSA bandwidth.

In the control area, the present dissertation focused on the low-level and high-level controls. The former implemented a force control to compensate for the REmSA dynamics. However, the control requires the measurement of the REmSA

force, which is feasible only during laboratory testing but not in vehicle implementation. In this context, a force observer must be designed to estimate the force that the REmSA exerts on the suspension. For what regards the high-level control, well-known strategies aimed at the vehicle dynamics under road unevenness scenario were implemented. Future research must investigate strategies aimed at lumped obstacle scenarios. These could be integrated with perception systems already present on autonomous vehicles that sense the road profile.

Appendix A

Design of the automotive prototype

The present research led to the development and manufacture of a REmSA prototype for a B-class vehicle. It was designed with a previous but incomplete version of the methodology proposed in Chap. 3, which is reported in reference [83]. For the sake of brevity, a recap of the design is presented and the main differences with the methodology of Chap. 3 are highlighted. More details can be found in [83].

The design methodology counts four steps, which are schematized in Fig. A.1.

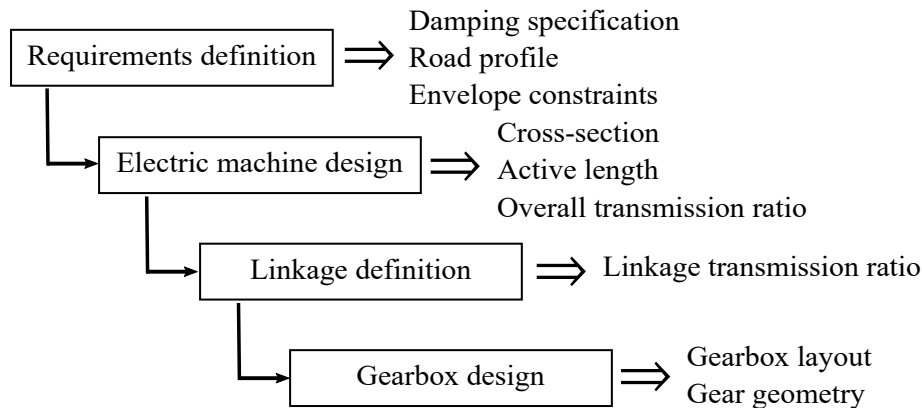


Figure A.1: Previous version of the proposed REmSA design methodology [83]

At first, the preliminary packaging in the retained suspension is investigated to identify the envelope constraints of the prototype. Then, the performance specifications are addressed. Specifically, the REmSA is considered as a shock absorber with regenerative features. To this end, it must reproduce the damping characteristic of the retained suspension. Furthermore, the road profile that the suspension experiences during operation is defined. Differently from the methodology of Chap. 3,

only the road unevenness profile is considered whereas no lumped obstacle scenario is accounted for.

The electric machine design is divided into two passages. At first, the electric machine cross-section is optimized in a similar way to what is proposed in Sec. 3.3.2. However, the optimization is performed for one single value of stator outer diameter. In fact, the methodology fixes the outer envelope of the prototype. This is a significantly penalizing aspect: several solutions that could achieve way better performance are not considered.

Then, the electric machine and gearbox are matched to define the overall transmission ratio and the electric machine active length. As no lumped obstacle or maneuver are considered, the peak force is not a requirement. Hence, only the maximum regenerative damping capability and the RMS force are the constraints. Differently from the methodology of Chap. 3, the unique solution is given by the intersection between the force line and the damping parabola requirements. Therefore, unique transmission ratio and active length are found, and no cost function is minimized. Consequently, the gearbox and electric machine match is not optimum.

Fig. A.2 resumes the match process, which results in electric machine active length of 22 mm and overall transmission ratio of 1.35 mm/rad. By making a comparison with the method followed in Sec. 3.3.2 (Fig. 3.25), the optimum solution is not given by the intersection between the force and damping requirements. In fact, solutions that does not lie on the intersection minimize the cost function, even if they would be oversized for some of the constraints. This aspect is discussed in Sec. 3.3.2. Furthermore, the methodology fixes the outer envelope of the prototype, which is an important design variable in the REmSA optimization.

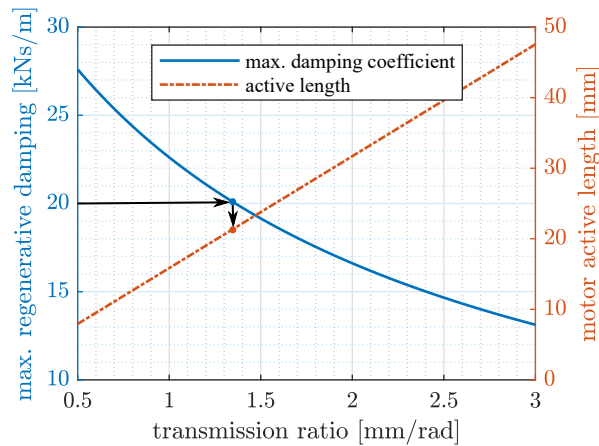


Figure A.2: Selection of the overall transmission ratio as a function of the maximum regenerative damping capability. The selection of the transmission ratio defines the electric machine active length [83].

The linkage definition follows packaging constraints in the retained vehicle suspension. However, trial-and-error process is used to achieve the minimum transmission ratio while observing the constraints on the transmission quality. Conversely, the methodology proposed in the present dissertation addresses the linkage definition through an optimization process. Fig. A.3 shows the selected layout. It uses two links, where the longest one is hinged on the damper tube. The prototype is placed close to the pivot of the lower arm. As result, the linkage transmission is 115 mm/rad, which results in the gearbox ratio of 1/87.

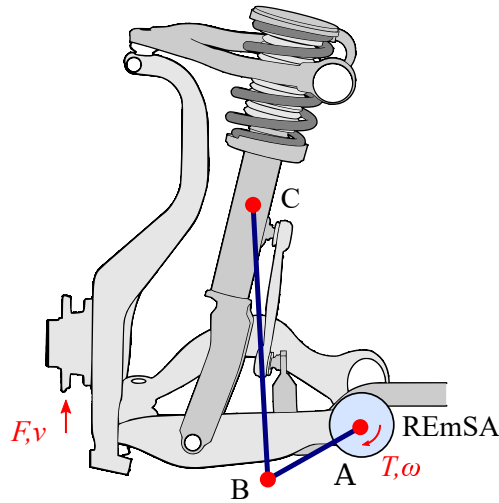


Figure A.3: Proposed linkage solution (thick solid lines) for the REmSA integration into a double wishbone suspension [83].

The gearbox design follows the same procedure presented in Chap. 3. The designed REmSA is shown in Fig. A.4. The overall layout is similar to the prototype designed for the motorcycle application. The main difference regards the support scheme of the input shaft. In fact, the automotive prototype features a double-row angular contact ball bearing, as the shaft has one support only and the bearing is subject to bending load. The latter is caused by the axial misalignment between the linkage input force and the support itself.

For control purposes, a set of permanent magnets is mounted on the rotor end. Then, the angular position is estimated by measuring their magnetic field with an array of Allegro A1326 analog Hall sensors, which are installed on the electric machine cover.

The achieved prototype weighs 3.2 kg, divided approximately into 1.5 kg of the gearbox and 1.7 kg of the electric machine. The moment of inertia of the rotating components reported at the wheel level is 15.9 kg. After some modifications, the rotor was slightly modified to reduce the equivalent inertia. Value of approximately 6.7 kg was achieved. In terms of performance ratings, the electric machine peak

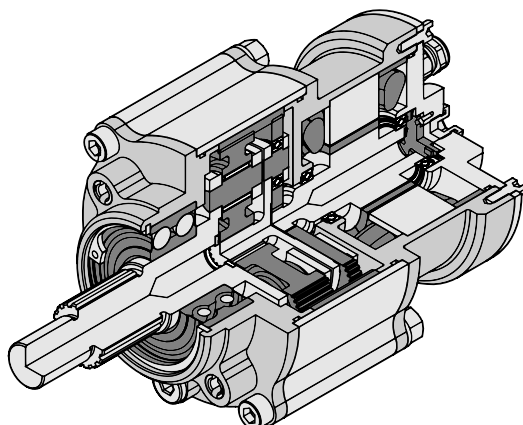


Figure A.4: Isometric cut view of the REmSA designed for the automotive application [83]

Table A.1: Comparison between the automotive prototype [83] and the motorcycle one designed in Chap. 3.

Feature	Value	
	Proto	
	Motorcycle	Automotive
Peak force at wheel	2700 N	1727 N
Peak torque at REmSA shaft	459.0 Nm	204 Nm
Peak torque at el. machine shaft	6.0 Nm	2.3 Nm
Equivalent inertia	4.9 kg	6.7 kg
Gearbox transmission ratio	1/76.9	1/87.3
Linkage transmission ratio (nominal)	170 mm/rad	115 mm/rad
Mass	4.5 kg	3.2 kg
Diameter envelope	110 mm	110 mm
Axial envelope	197 mm	194 mm

torque is 2.3 Nm, which gives a torque at the REmSA input shaft of 204 Nm. The latter results in 1727 N at the wheel.

The comparison with the motorcycle prototype designed in Chap. 3 is reported in Table A.1. Then, they are shown in Fig. A.5.

Although the motorcycle one has larger force capability, the two prototypes feature similar outer envelope (Fig. A.5). This is achieved thanks to the upgraded design methodology and better utilization of the prototype volume. Furthermore,

the optimization of the diverse components results in a lower equivalent inertia, which is a crucial aspect when dealing with electromechanical suspensions.

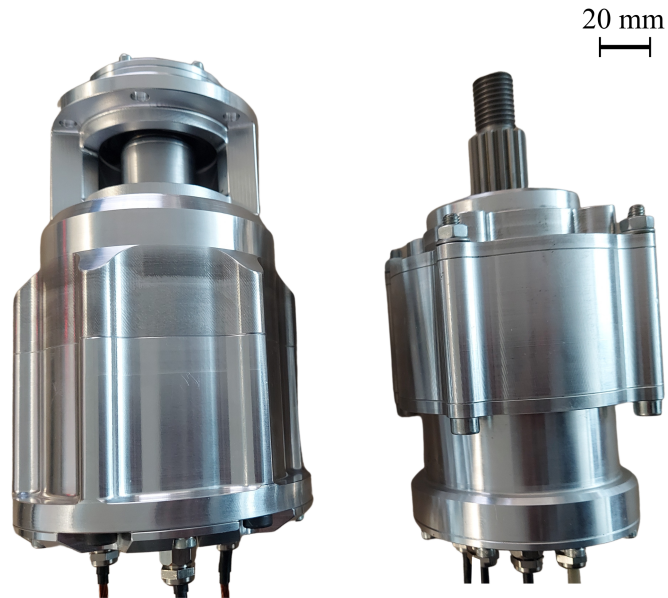


Figure A.5: REmSA prototypes designed and manufactured during the present research: prototype for the motorcycle (left) and the automotive (right) application. The scale is shown at the top-right corner.

Appendix B

Mechanical impedance and REmSA lumped parameter model

The mechanical impedance $Z(\omega)$ is the frequency-dependent relationship between force and motion:

$$Z(j\omega) = \frac{F(j\omega)}{v(j\omega)} \quad (\text{B.1})$$

ω being the angular frequency. It can be thought as a damping characteristic in the frequency domain, which is characterized by amplitude and phase. When the latter is null, the system behaves as a damper. Differently, elastic and inerter behaviors are indicated by 90 deg phase lag and lead, respectively. The former case means that the force anticipates by 90 deg the velocity, i.e. it is in phase with the acceleration, whereas 90 deg phase lag means that the force is in phase with the displacement.

As proposed by Tonoli *et al.* [38], the shunted REmSA can be modeled through a lumped parameter approach in the linear domain, i.e. suspension force and translation. The model is shown in Fig. B.1, where only spring-mass-damper elements are used. The term c_{eq} models the mechanical loss of the system. The compliant mount is modeled as a spring-damper parallel. The electric-related quantities are expressed through their mechanical equivalence. Specifically, the electric machine is modeled as a spring-damper series, whose coefficients are:

$$c_e = \frac{K_t K_e}{\tau_t^2 (R_{\text{ph}} + R_{\text{shunt}})} \quad (\text{B.2})$$

$$k_e = \frac{K_t K_e}{\tau_t^2 L_{\text{ph}}} \quad (\text{B.3})$$

K_t and $K_e = 2/3 \cdot K_t$ being the machine torque and back EMF constants, respectively, R_{ph} the phase resistance and L_{ph} the phase inductance. The transmission ratio τ_t reports the quantities from the electric machine shaft to the suspension level.

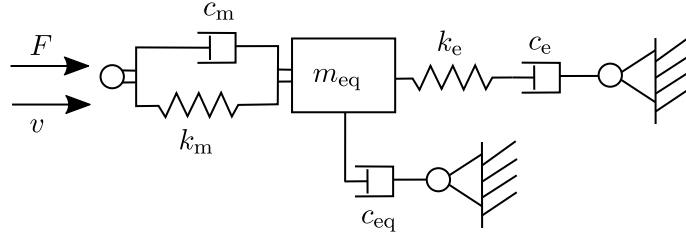


Figure B.1: REmSA lumped parameter model

From the lumped parameter model, the transfer function of the mechanical impedance can be written as:

$$Z(s) = \frac{F(s)}{v(s)} = \frac{s + \frac{1}{m_{\text{eq}}} \left[c_{\text{eq}} + \frac{c_e}{\frac{s}{\omega_e} + 1} \right]}{s^2 + \frac{s}{m_{\text{eq}}} \left[c_{\text{eq}} + c_m + \frac{c_e}{\frac{s}{\omega_e} + 1} \right] + \omega_m^2} \cdot (s c_m + k_m) \quad (\text{B.4})$$

s being the Laplace variable, ω_e the electromagnetic pole and ω_m the mechanical natural frequency. The latter are given by:

$$\omega_e = \frac{k_e}{c_e} = \frac{R_{\text{ph}} + R_{\text{shunt}}}{L_{\text{ph}}} \quad (\text{B.5})$$

$$\omega_m = \sqrt{\frac{k_m}{m_{\text{eq}}}} \quad (\text{B.6})$$

The mechanical impedance can be written in the fourier domain ($s = j\omega$). Fig. B.2 shows the frequency response function when the model is populated with the parameters reported in Table B.1. Specifically, the resistance and inductance of the electric machine were measured through an impedance-meter, the remaining coefficients were identified by means of the experimental results discussed in Sec. 5.3.1, which are related to the REmSA prototype presented in Sec. A. The response was computed at diverse shunt resistance values, ranging from open circuit to short circuit. An additional term of 70 m Ω was added to the shunt resistance to account for the diode rectifier resistance.

The compliant mount introduces a mechanical resonance at frequency ω_m that attenuates the impedance in the range $\omega > \omega_m$. At frequency well below the mechanical pole ($\omega \ll \omega_m$), the compliant mount can be considered rigid ($k_m \rightarrow \infty$). Hence, the mechanical impedance is simplified into:

$$Z(j\omega) = j\omega m_{\text{eq}} + c_{\text{eq}} + \frac{c_e}{j\frac{\omega}{\omega_e} + 1} \quad (\text{B.7})$$

The first term represents the inerter contribution, which is proportional to the excitation frequency. When $\omega \ll \omega_e$, no electromagnetic attenuation occurs and

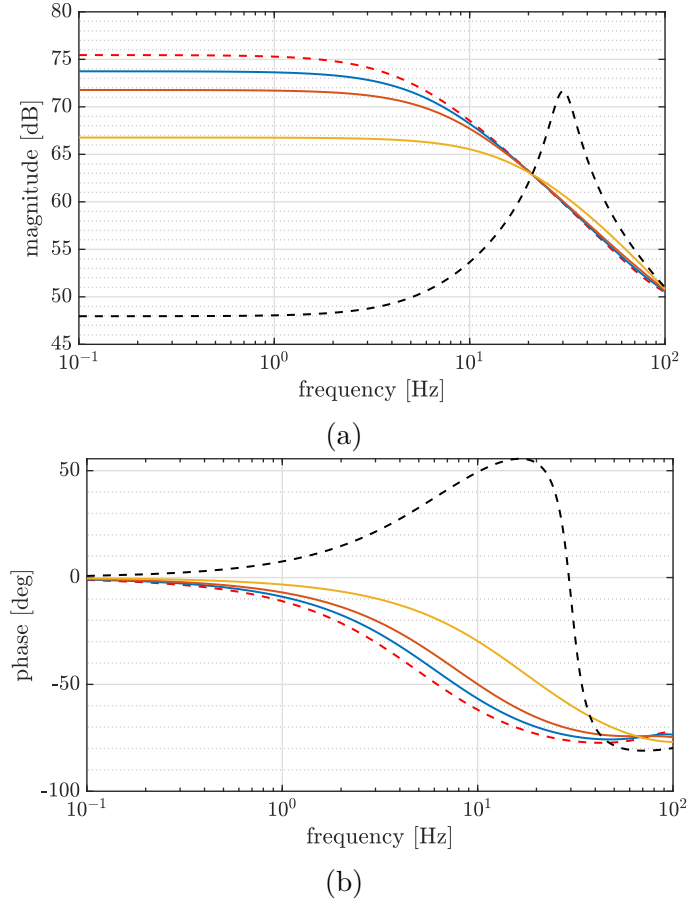


Figure B.2: Mechanical impedance magnitude (a) and phase (b) of the REmSA lumped parameter model computed at diverse shunt resistances: open circuit (black), 465 m Ω (yellow), 135 m Ω (orange), 55 m Ω (blue), short circuit (red).

the mechanical impedance is further simplified into:

$$Z(j\omega) = j\omega m_{\text{eq}} + c_{\text{eq}} + c_e \quad (\text{B.8})$$

which features a zero at $\omega_{z,i} = \frac{c_{\text{eq}} + c_e}{m_{\text{eq}}}$. The inerter effect dominates the response when the zero remains at low frequency, i.e. the electromagnetic damping is small (open circuit). In such case, the mechanical impedance is inertia-dominated in the region between $\omega_{z,i}$ and ω_e . The second term of Eq. B.4 is the friction contribution, which is constant with the excitation frequency. When the electromagnetic damping is small (open circuit), such term dominates the response at very low frequency, i.e. close to the static condition ($\omega \rightarrow 0$). The last term of Eq. B.4 is the electromagnetic component, which attenuates the impedance response at frequency values $\omega > \omega_e$. It dominates the response when the electromagnetic pole remains at low frequency, i.e. large electromagnetic damping (short circuit).

Table B.1: Measured and identified coefficients of the REmSA lumped parameter model

Description	Symbol	Value
Equivalent mass	m_{eq}	5.6 kg
Equivalent loss	c_{eq}	250 Ns/m
Mount stiffness	k_{m}	$2 \cdot 10^5$ N/m
Mount damping	c_{m}	50 Ns/m
Phase inductance	L_{ph}	348.7 μH
Phase resistance	R_{ph}	68.3 m Ω
Torque constant	K_{t}	49.3 mNm/A

By looking at the phase response (Fig. B.2b), the REmSA behaves as a damper at low frequency. When the inerter effect begins, the phase goes positive (open circuit curve). This means that the force tends to be in phase with the inertia: the REmSA behaves as an inerter, hence its action is not a damping one. Finally, the phase goes negative at high frequency: the force is in phase with the displacement. Therefore, the REmSA provides an elastic force that is significantly attenuated. This behavior is explained as follows: the equivalent mass is standstill at high frequency because of the inertia effect. Therefore, the force output is due to the compliant mount deformation, which is a pure elastic contribution.

Bibliography

- [1] C. S. F. Kuhnert, A. Koster, [Five trends transforming the automotive industry](#) (2018. Accessed online: Nov 04, 2021.).
URL <https://www.pwc.com/gx/en/industries/automotive/assets/pwc-five-trends-transforming-the-automotive-industry.pdf>
- [2] S. Chu, A. Majumdar, Opportunities and challenges for a sustainable energy future, *Nature* 488 (7411) (2012) 294–303. doi:10.1038/nature11475.
- [3] G. Fontaras, N.-G. Zacharof, B. Ciuffo, Fuel consumption and CO₂ emissions from passenger cars in Europe – Laboratory versus real-world emissions, *Progress in Energy and Combustion Science* 60 (2017) 97–131. doi:10.1016/j.pecs.2016.12.004.
- [4] [Car manufacturer outlook is fines as eu emissions regulations start to bite](#) (2021. Accessed online: Nov 04, 2021.).
URL <https://www.am-online.com/dealer-management/manufacture-nsight/car-manufacturer-outlook-is-fines-as-eu-emissions-regulations-start-to-bite>
- [5] S. F. Tie, C. W. Tan, A review of energy sources and energy management system in electric vehicles, *Renewable and Sustainable Energy Reviews* 20 (2013) 82–102. doi:10.1016/j.rser.2012.11.077.
- [6] [Advanced driver assistance systems](#) (Accessed online: Nov 04, 2021.).
URL <https://injuryfacts.nsc.org/motor-vehicle/occupant-protection/advanced-driver-assistance-systems/data-details/>
- [7] H. Bellem, B. Thiel, M. Schrauf, J. F. Krems, Comfort in automated driving: An analysis of preferences for different automated driving styles and their dependence on personality traits, *Transportation Research Part F: Traffic Psychology and Behaviour* 55 (2018) 90–100. doi:10.1016/j.trf.2018.02.036.
- [8] D. Karnopp, Active and Semi-Active Vibration Isolation, *Journal of Vibration and Acoustics* 117 (B) (1995) 177–185. doi:10.1115/1.2838660.
- [9] L. Li, Y. Zhang, C. Yang, B. Yan, C. Marina Martinez, Model predictive control-based efficient energy recovery control strategy for regenerative braking system of hybrid electric bus, *Energy Conversion and Management* 111 (2016) 299–314. doi:10.1016/j.enconman.2015.12.077.

-
- [10] D. Shi, P. Pisu, L. Chen, S. Wang, R. Wang, Control design and fuel economy investigation of power split HEV with energy regeneration of suspension, *Applied Energy* 182 (2016) 576–589. doi:[10.1016/j.apenergy.2016.08.034](https://doi.org/10.1016/j.apenergy.2016.08.034).
- [11] M. A. Abdelkareem, L. Xu, M. K. A. Ali, A. Elagouz, J. Mi, S. Guo, Y. Liu, L. Zuo, Vibration energy harvesting in automotive suspension system: A detailed review, *Applied Energy* 229 (2018) 672–699. doi:[10.1016/j.apenergy.2018.08.030](https://doi.org/10.1016/j.apenergy.2018.08.030).
- [12] J. C. Dixon, *The shock absorber handbook*, John Wiley & Sons, 2008.
- [13] G. Q. B. Tran, T.-P. Pham, O. Sename, E. Costa, P. Gaspar, Integrated Comfort-Adaptive Cruise and Semi-Active Suspension Control for an Autonomous Vehicle: An LPV Approach, *Electronics* 10 (7) (2021) 813. doi:[10.3390/electronics10070813](https://doi.org/10.3390/electronics10070813).
- [14] M. Ataei, E. Asadi, A. Goodarzi, A. Khajepour, M. B. Khamesee, Multi-objective optimization of a hybrid electromagnetic suspension system for ride comfort, road holding and regenerated power, *Journal of Vibration and Control* 23 (5) (2017) 782–793. doi:[10.1177/1077546315585219](https://doi.org/10.1177/1077546315585219).
- [15] M. Čorić, J. Deur, L. Xu, H. E. Tseng, D. Hrovat, Optimisation of active suspension control inputs for improved vehicle ride performance, *Vehicle System Dynamics* 54 (7) (2016) 1004–1030. doi:[10.1080/00423114.2016.1177655](https://doi.org/10.1080/00423114.2016.1177655).
- [16] R. Zhang, X. Wang, S. John, A Comprehensive Review of the Techniques on Regenerative Shock Absorber Systems, *Energies* 11 (5) (2018) 1167. doi:[10.3390/en11051167](https://doi.org/10.3390/en11051167).
- [17] T. Pham, J. Jacob, S. Wilkins, C. Lauwerys, M. Dhaens, Integrated model for battery Electric Vehicles with energy harvesting active suspension system, in: 2017 Twelfth International Conference on Ecological Vehicles and Renewable Energies (EVER), IEEE, 2017, pp. 1–10.
- [18] B. Hu, C. Chen, Z. Zhan, X. Su, T. Hu, G. Zheng, Z. Yang, Progress and recent trends in 48 V hybridisation and e-boosting technology on passenger vehicles – a review, *Proceedings of the Institution of Mechanical Engineers, Part D: Journal of Automobile Engineering* 232 (11) (2018) 1543–1561. doi:[10.1177/0954407017729950](https://doi.org/10.1177/0954407017729950).
- [19] W. Sun, H. Gao, P. Shi, *Advanced Control for Vehicle Active Suspension Systems*, Vol. 204 of *Studies in Systems, Decision and Control*, Springer International Publishing, Cham, 2020. doi:[10.1007/978-3-030-15785-2](https://doi.org/10.1007/978-3-030-15785-2).
- [20] P. Li, L. Zuo, Influences of the electromagnetic regenerative dampers on the vehicle suspension performance, *Proceedings of the Institution of Mechanical Engineers, Part D: Journal of Automobile Engineering* 231 (3) (2017) 383–394. doi:[10.1177/0954407016639503](https://doi.org/10.1177/0954407016639503).
- [21] X. D. Xue, K. W. E. Cheng, Z. Zhang, J. K. Lin, D. H. Wang, Y. J. Bao, M. K. Wong, N. Cheung, Study of art of automotive active suspensions, in: 2011 4th International Conference on Power Electronics Systems and Applications,

- IEEE, Hong Kong, China, 2011, pp. 1–7. doi:10.1109/PESA.2011.5982958.
- [22] Audi is working on a suspension that gets power from bumpy roads (Accessed online: Jan 13, 2022.).
URL <https://www.autoblog.com/2016/08/10/audi-erot-electric-suspension-48-volt/>
- [23] Multifaceted personality: predictive active suspension in the a8 flagship model (Accessed online: Jan 13, 2022.).
URL <https://www.audi-mediacycenter.com/en/press-releases/multifaceted-personality-predictive-active-suspension-in-the-a8-flagship-model-11905>
- [24] Why bose’s electromagnetic car suspension system never made it to market (Accessed online: Jan 13, 2022.).
URL <https://incompliancemag.com/bose-electromagnetic-car-suspension-system/>
- [25] L. Yu, S. Huo, W. Xuan, L. Zuo, Assessment of Ride Comfort and Braking Performance Using Energy-Harvesting Shock Absorber, SAE International Journal of Passenger Cars - Mechanical Systems 8 (2) (2015) 482–491. doi:10.4271/2015-01-0649.
- [26] Z. Zhang, X. Zhang, W. Chen, Y. Rasim, W. Salman, H. Pan, Y. Yuan, C. Wang, A high-efficiency energy regenerative shock absorber using supercapacitors for renewable energy applications in range extended electric vehicle, Applied Energy 178 (2016) 177–188. doi:10.1016/j.apenergy.2016.06.054.
- [27] S. Cytrynski, U. Neerpasch, R. Bellmann, B. Danner, The Active Suspension of the New Mercedes-Benz GLE, ATZ worldwide 120 (12) (2018) 42–45. doi:10.1007/s38311-018-0172-y.
- [28] W. Sun, H. Gao, P. Shi, Advanced Control for Vehicle Active Suspension Systems, Vol. 204 of Studies in Systems, Decision and Control, Springer International Publishing, Cham, 2020. doi:10.1007/978-3-030-15785-2.
- [29] P. Gáspár, Z. Szabó, G. Szederkényi, J. Bokor, Design of a two-level controller for an active suspension system, Asian Journal of Control 14 (3) (2012) 664–678. doi:10.1002/asjc.386.
- [30] H. Du, N. Zhang, control of active vehicle suspensions with actuator time delay, Journal of Sound and Vibration 301 (1-2) (2007) 236–252. doi:10.1016/j.jsv.2006.09.022.
- [31] A. Alleyne, R. Liu, A simplified approach to force control for electro-hydraulic systems, Control Engineering Practice (2000) 10.
- [32] A. Alleyne, J. Hedrick, Nonlinear adaptive control of active suspensions, IEEE Transactions on Control Systems Technology 3 (1) (1995) 94–101. doi:10.1109/87.370714.
- [33] D. Fischer, R. Isermann, Mechatronic semi-active and active vehicle suspensions, Control Engineering Practice 12 (11) (2004) 1353–1367. doi:

- [10.1016/j.conengprac.2003.08.003](https://doi.org/10.1016/j.conengprac.2003.08.003).
- [34] J. Lee, K. Oh, K. Yi, A novel approach to design and control of an active suspension using linear pump control-based hydraulic system, *Proceedings of the Institution of Mechanical Engineers, Part D: Journal of Automobile Engineering* 234 (5) (2020) 1224–1248. [doi:10.1177/0954407019882223](https://doi.org/10.1177/0954407019882223).
- [35] M. Strassberger, J. Guldner, BMW's dynamic drive: an active stabilizer bar system, *IEEE Control Systems* 24 (4) (2004) 28–29. [doi:10.1109/MCS.2004.1316650](https://doi.org/10.1109/MCS.2004.1316650).
- [36] G. Koch, O. Fritsch, B. Lohmann, Potential of low bandwidth active suspension control with continuously variable damper, *Control Engineering Practice* 18 (11) (2010) 1251–1262. [doi:10.1016/j.conengprac.2010.03.007](https://doi.org/10.1016/j.conengprac.2010.03.007).
- [37] M. Jonasson, F. Roos, Design and evaluation of an active electromechanical wheel suspension system, *Mechatronics* 18 (4) (2008) 218–230. [doi:10.1016/j.mechatronics.2007.11.003](https://doi.org/10.1016/j.mechatronics.2007.11.003).
- [38] A. Tonoli, N. Amati, J. G. Detoni, R. Galluzzi, E. Gasparin, Modelling and validation of electromechanical shock absorbers, *Vehicle System Dynamics* 51 (8) (2013) 1186–1199. [doi:10.1080/00423114.2013.789538](https://doi.org/10.1080/00423114.2013.789538).
- [39] R. Galluzzi, Y. Xu, N. Amati, A. Tonoli, Optimized design and characterization of motor-pump unit for energy-regenerative shock absorbers, *Applied Energy* 210 (2018) 16–27. [doi:10.1016/j.apenergy.2017.10.100](https://doi.org/10.1016/j.apenergy.2017.10.100).
- [40] Yongchao Zhang, Kun Huang, Fan Yu, Yonghui Gu, Daofei Li, Experimental verification of energy-regenerative feasibility for an automotive electrical suspension system, in: *2007 IEEE International Conference on Vehicular Electronics and Safety*, IEEE, Beijing, China, 2007, pp. 1–5. [doi:10.1109/ICVES.2007.4456407](https://doi.org/10.1109/ICVES.2007.4456407).
- [41] L. Zuo, X. Tang, Large-scale vibration energy harvesting, *Journal of Intelligent Material Systems and Structures* 24 (11) (2013) 1405–1430. [doi:10.1177/1045389X13486707](https://doi.org/10.1177/1045389X13486707).
- [42] P. Múčka, Energy-harvesting potential of automobile suspension, *Vehicle System Dynamics* 54 (12) (2016) 1651–1670, publisher: Taylor & Francis.
- [43] Y. Zhang, K. Guo, D. Wang, C. Chen, X. Li, Energy conversion mechanism and regenerative potential of vehicle suspensions, *Energy* 119 (2017) 961–970. [doi:10.1016/j.energy.2016.11.045](https://doi.org/10.1016/j.energy.2016.11.045).
- [44] X. Lv, Y. Ji, H. Zhao, J. Zhang, G. Zhang, L. Zhang, Research Review of a Vehicle Energy-Regenerative Suspension System, *Energies* 13 (2) (2020) 441. [doi:10.3390/en13020441](https://doi.org/10.3390/en13020441).
- [45] D. Chandler, More power from bumps in the road, *MIT Tech Talk* 53 (15) (2009) 4.
- [46] Y. Suda, S. Nakadai, K. Nakano, Hybrid Suspension System with Skyhook Control and Energy Regeneration (Development of Self-Powered Active Suspension), *Vehicle System Dynamics* 29 (sup1) (1998) 619–634. [doi:10.1080/00423119808969590](https://doi.org/10.1080/00423119808969590).

- [47] J. Paulides, L. Encica, E. Lomonova, A. Vandenput, Design considerations for a semi-active electromagnetic suspension system, *IEEE Transactions on Magnetics* 42 (10) (2006) 3446–3448. doi:10.1109/TMAG.2006.879963.
- [48] B. Gysen, J. Paulides, J. Janssen, E. Lomonova, Active Electromagnetic Suspension System for Improved Vehicle Dynamics, *IEEE Transactions on Vehicular Technology* 59 (3) (2010) 1156–1163. doi:10.1109/TVT.2009.2038706.
- [49] B. L. J. Gysen, T. P. J. van der Sande, J. J. H. Paulides, E. A. Lomonova, Efficiency of a Regenerative Direct-Drive Electromagnetic Active Suspension, *IEEE Transactions on Vehicular Technology* 60 (4) (2011) 1384–1393. doi:10.1109/TVT.2011.2131160.
- [50] L. Zuo, B. Scully, J. Shestani, Y. Zhou, Design and characterization of an electromagnetic energy harvester for vehicle suspensions, *Smart Materials and Structures* 19 (4) (2010) 045003. doi:10.1088/0964-1726/19/4/045003.
- [51] R. Zhang, X. Wang, Z. Liu, A novel regenerative shock absorber with a speed doubling mechanism and its Monte Carlo simulation, *Journal of Sound and Vibration* 417 (2018) 260–276. doi:10.1016/j.jsv.2017.12.017.
- [52] A. Gupta, J. A. Jendrzeczyk, T. M. Mulcahy, J. R. Hull, Design of electromagnetic shock absorbers, *International Journal of Mechanics and Materials in Design* 3 (3) (2006) 285–291. doi:10.1007/s10999-007-9031-5.
- [53] D. Karnopp, Permanent Magnet Linear Motors Used as Variable Mechanical Dampers for Vehicle Suspensions, *Vehicle System Dynamics* 18 (4) (1989) 187–200. doi:10.1080/00423118908968918.
- [54] K. E. Graves, P. G. Iovenitti, D. Toncich, Electromagnetic regenerative damping in vehicle suspension systems, *International Journal of Vehicle Design* 24 (2/3) (2000) 182. doi:10.1504/IJVD.2000.005181.
- [55] P. Li, L. Zuo, J. Lu, L. Xu, Electromagnetic regenerative suspension system for ground vehicles, in: 2014 IEEE International Conference on Systems, Man, and Cybernetics (SMC), IEEE, San Diego, CA, USA, 2014, pp. 2513–2518. doi:10.1109/SMC.2014.6974304.
- [56] R. J. Tyler, Deval Patrick to deliver graduation address, *MIT Tech Talk* 53 (15) (2009) 8.
- [57] Clearmotion, a ground-breaking active suspension system to transform the driving experience (Accessed online: Feb 03, 2022.). URL <https://www.speedgoat.com/success-stories/speedgoat-user-stories/clearmotion>
- [58] Clear motion, inc. (Accessed online: Feb 03, 2022.). URL <https://www.clearmotion.com/>
- [59] C. Li, P. W. Tse, Fabrication and testing of an energy-harvesting hydraulic damper, *Smart Materials and Structures* 22 (6) (2013) 065024. doi:10.1088/0964-1726/22/6/065024.
- [60] Z. Li, L. Zuo, J. Kuang, G. Luhrs, Energy-harvesting shock absorber with a mechanical motion rectifier, *Smart Materials and Structures* 22 (2) (2013)

025008. doi:10.1088/0964-1726/22/2/025008.
- [61] C. Chen, Y. S. Chan, L. Zou, W.-H. Liao, Self-powered magnetorheological dampers for motorcycle suspensions, *Proceedings of the Institution of Mechanical Engineers, Part D: Journal of Automobile Engineering* 232 (7) (2018) 921–935. doi:10.1177/0954407017723761.
- [62] D. A. Weeks, D. A. Bresie, J. H. Beno, A. M. Guenin, *The Design of an Electromagnetic Linear Actuator for an Active Suspension*, 1999, pp. 1999–01–0730. doi:10.4271/1999-01-0730.
- [63] D. A. Weeks, J. H. Beno, A. M. Guenin, D. A. Bresie, *Electromechanical Active Suspension Demonstration for Off-Road Vehicles*, 2000, pp. 2000–01–0102. doi:10.4271/2000-01-0102.
- [64] S. Guo, Y. Liu, L. Xu, X. Guo, L. Zuo, Performance evaluation and parameter sensitivity of energy-harvesting shock absorbers on different vehicles, *Vehicle System Dynamics* 54 (7) (2016) 918–942. doi:10.1080/00423114.2016.1174276.
- [65] M. Montazeri-Gh, O. Kavianipour, Investigation of the passive electromagnetic damper, *Acta Mechanica* 223 (12) (2012) 2633–2646. doi:10.1007/s00707-012-0735-8.
- [66] Y. Liu, L. Xu, L. Zuo, Design, Modeling, Lab, and Field Tests of a Mechanical-Motion-Rectifier-Based Energy Harvester Using a Ball-Screw Mechanism, *IEEE/ASME Transactions on Mechatronics* 22 (5) (2017) 1933–1943. doi:10.1109/TMECH.2017.2700485.
- [67] P. Li, L. Zuo, Assessment of Vehicle Performances with Energy-Harvesting Shock Absorbers, *SAE International Journal of Passenger Cars - Mechanical Systems* 6 (1) (2013) 18–27. doi:10.4271/2013-01-0170.
- [68] M. Yu, C. Arana, S. A. Evangelou, D. Dini, G. D. Cleaver, Parallel Active Link Suspension: A Quarter-Car Experimental Study, *IEEE/ASME Transactions on Mechatronics* 23 (5) (2018) 2066–2077. doi:10.1109/TMECH.2018.2864785.
- [69] M. Yu, C. Arana, S. A. Evangelou, D. Dini, Quarter-Car Experimental Study for Series Active Variable Geometry Suspension, *IEEE Transactions on Control Systems Technology* 27 (2) (2019) 743–759. doi:10.1109/TCST.2017.2772912.
- [70] S. Evangelou, D. Dini, G. Cleaver, C. A. Ramirez, Vehicle Suspension System, Patent EP3600924 B1 (2020).
- [71] P. E. Todmal, S. Melzi, Crank-Lever Electromagnetic Damper (CLEMD) Design for Automobile Suspension System, *SAE International Journal of Passenger Cars - Mechanical Systems* 13 (1) (2020) 06–13–01–0002. doi:10.4271/06-13-01-0002.
- [72] W. Harrison, Electric shock absorber, Patent US 1752844 A (1930).
- [73] C. Voy, G. Sammet, W. Freund, V. Besnault, J. Schulze, Actuator for Active Regulation Chassis, Patent EP1184214 A2 (2002).

- [74] M. Willems, Electric Damper, Patent US 9136743 B2 (2015).
- [75] M. Willems, Wheel Suspension with Rotation Damper, Patent US 9120361 B2 (2015).
- [76] M. Willems, Rotation Damper, Patent US 10288145 B2 (2019).
- [77] D. Mohrlock, R. Goldberg, A. Schindler, Wheel Suspension for a Motor Vehicle, Patent US 9469174 B2 (2016).
- [78] M. Groen, J. Schmitt, P. Leibl, Actively Adjustable Wheel Suspension for the Wheels of an Axle of a Motor Vehicle, Patent US 10166833 B2 (2019).
- [79] S. H. Yoo, S. B. Jang, B. G. Kang, U. K. Lee, Energy Regeneration Device of Suspension System for Vehicle, Patent US 2014182955 A1 (2014).
- [80] N. I. Berg, R. K. Holm, P. O. Rasmussen, A novel magnetic lead screw active suspension system for vehicles, in: 2014 IEEE Energy Conversion Congress and Exposition (ECCE), IEEE, Pittsburgh, PA, USA, 2014, pp. 3139–3146. doi:10.1109/ECCE.2014.6953827.
- [81] A. Ali, L. Qi, T. Zhang, H. Li, A. Azam, Z. Zhang, Design of novel energy-harvesting regenerative shock absorber using barrel cam follower mechanism to power the auxiliaries of a driverless electric bus, Sustainable Energy Technologies and Assessments 48 (2021) 101565. doi:10.1016/j.seta.2021.101565.
- [82] A. Gonzalez, J. L. Olazagoitia, J. Vinolas, I. Ulacia, M. Izquierdo, An Innovative Energy Harvesting Shock Absorber System for Motorbikes, IEEE/ASME Transactions on Mechatronics (2021) 1–11doi:10.1109/TMECH.2021.3109383.
- [83] R. Galluzzi, S. Circosta, N. Amati, A. Tonoli, Rotary regenerative shock absorbers for automotive suspensions, Mechatronics 77 (2021) 102580.
- [84] T. J. E. Miller, Brushless permanent-magnet and reluctance motor drives, no. 21 in Monographs in electrical and electronic engineering, Clarendon Press ; Oxford University Press, Oxford : New York, 1989.
- [85] P. Sekerak, V. Hrabovcova, J. Pyrhonen, L. Kalamen, P. Rafajdus, M. Onufer, Comparison of Synchronous Motors With Different Permanent Magnet and Winding Types, IEEE Transactions on Magnetics 49 (3) (2013) 1256–1263. doi:10.1109/TMAG.2012.2230334.
- [86] P. L. García, S. Crispel, E. Saerens, T. Verstraten, D. Lefeber, Compact Gearboxes for Modern Robotics: A Review, Frontiers in Robotics and AI 7 (2020) 103. doi:10.3389/frobt.2020.00103.
- [87] D. G. Dorrell, M.-F. Hsieh, M. Popescu, L. Evans, D. A. Staton, V. Grout, A Review of the Design Issues and Techniques for Radial-Flux Brushless Surface and Internal Rare-Earth Permanent-Magnet Motors, IEEE Transactions on Industrial Electronics 58 (9) (2011) 3741–3757. doi:10.1109/TIE.2010.2089940.
- [88] 752s (Accessed online: Feb 12, 2022.).
URL <https://italy.benelli.com/product/752s>

- [89] V. Cossalter, *Motorcycle dynamics*, Lulu. com, 2006.
- [90] British Standards Institution, Organisation internationale de normalisation, ISO 8608:2016. Mechanical vibration — Road surface profiles — Reporting of measured data, 2016.
- [91] L. Zuo, P.-S. Zhang, Energy Harvesting, Ride Comfort, and Road Handling of Regenerative Vehicle Suspensions, *Journal of Vibration and Acoustics* 135 (1) (2013) 011002. doi:[10.1115/1.4007562](https://doi.org/10.1115/1.4007562).
- [92] British Standards Institution, Organisation internationale de normalisation, Mechanical vibration and shock: evaluation of human exposure to whole-body vibration. Part 1, 1997, oCLC: 848057325.
- [93] L. Zuo, S. Nayfeh, Low order continuous-time filters for approximation of the ISO 2631-1 human vibration sensitivity weightings, *Journal of Sound and Vibration* 265 (2) (2003) 459–465. doi:[10.1016/S0022-460X\(02\)01567-5](https://doi.org/10.1016/S0022-460X(02)01567-5).
- [94] D. Hrovat, Survey of Advanced Suspension Developments and Related Optimal Control Applications, *Automatica* 33 (10) (1997) 1781–1817. doi:[https://doi.org/10.1016/S0005-1098\(97\)00101-5](https://doi.org/10.1016/S0005-1098(97)00101-5).
- [95] H. ALT, Der ubertragungswinkel und seine bedeutung fur das konstruieren periodischer getriebe, *Werkstattstechnik* 26 (4) (1932) 61.
- [96] S. S. Balli, S. Chand, Transmission angle in mechanisms (triangle in mech), *Mechanism and Machine Theory* 37 (2) (2002) 175–195. doi:[https://doi.org/10.1016/S0094-114X\(01\)00067-2](https://doi.org/10.1016/S0094-114X(01)00067-2).
- [97] H. Afshari, W. Hare, S. Tesfamariam, Constrained multi-objective optimization algorithms: Review and comparison with application in reinforced concrete structures, *Applied Soft Computing* 83 (2019) 105631. doi:[10.1016/j.asoc.2019.105631](https://doi.org/10.1016/j.asoc.2019.105631).
- [98] G. Liu, X. Han, C. Jiang, A novel multi-objective optimization method based on an approximation model management technique, *Computer Methods in Applied Mechanics and Engineering* 197 (33-40) (2008) 2719–2731. doi:[10.1016/j.cma.2007.12.014](https://doi.org/10.1016/j.cma.2007.12.014).
- [99] D. C. Hanselman, *Brushless permanent-magnet motor design*, McGraw-Hill, New York, 1994.
- [100] D. C. Hanselman, *Brushless Permanent Magnet Motor Design*, Magna Physics Publishing, Lebanon, OH, USA, 2006.
- [101] COMSOL AB, *COMSOL Multiphysics v.5.5 User’s Guide* (2019).
- [102] N. Amati, A. Festini, A. Tonoli, Design of electromagnetic shock absorbers for automotive suspensions, *Vehicle System Dynamics* 49 (12) (2011) 1913–1928. doi:[10.1080/00423114.2011.554560](https://doi.org/10.1080/00423114.2011.554560).
- [103] R. Krishnan, *Permanent Magnet Synchronous and Brushless DC Motor Drives*, CRC Press, Boca Raton, FL, USA, 2010.
- [104] E. Saerens, S. Crispel, P. L. García, T. Verstraten, V. Ducastel, B. Vanderborght, D. Lefeber, Scaling laws for robotic transmissions, *Mechanism and Machine Theory* 140 (2019) 601–621. doi:[10.1016/j.mechmachtheory.2019.05.014](https://doi.org/10.1016/j.mechmachtheory.2019.05.014).

9.06.027.

- [105] J. E. Shigley, Shigley's mechanical engineering design, Tata McGraw-Hill Education, NY, USA, 2011.
- [106] KISSSoft AG, KISSSoft Release 03/2017 User Manual (2017).
- [107] ISO 6336-1:2006. Calculation of load capacity of spur and helical gears – Part 1: Basic principles, introduction and general influence factors.
- [108] ISO 6336-1:2006. Calculation of load capacity of spur and helical gears – Part 2: Calculation of surface durability (pitting).
- [109] ISO 6336-1:2006. Calculation of load capacity of spur and helical gears – Part 3: Calculation of tooth bending strength.
- [110] ISO 6336-1:2006. Calculation of load capacity of spur and helical gears – Part 6: Calculation of service life under variable load.
- [111] *Elife international* (Accessed online: Feb 26, 2022.).
URL [https://https://www.elifelifeinternational.com/](https://www.elifelifeinternational.com/)
- [112] B. Lave, Field-oriented current control for a permanent-magnet brushless motor used in regenerative shock absorbers, Master's thesis, Politecnico di Torino (2021).
- [113] S.-H. Kim, Electric motor control: DC, AC and BLDC motors, Elsevier, Cambridge, Massachusetts, 2017, oCLC: ocn965339831.
- [114] W. Soong, T. Miller, Theoretical limitations to the field-weakening performance of the five classes of brushless synchronous ac motor drive, in: 1993 Sixth International Conference on Electrical Machines and Drives (Conf. Publ. No. 376), IET, 1993, pp. 127–132.
- [115] J. Simanek, J. Novak, O. Cerny, R. Dolecek, FOC and flux weakening for traction drive with permanent magnet synchronous motor, in: 2008 IEEE International Symposium on Industrial Electronics, IEEE, Cambridge, UK, 2008, pp. 753–758. doi:10.1109/ISIE.2008.4677099.
- [116] G. Genta, L. Morello, The Automotive Chassis. Vol. 2: System design, 1st Edition, Mechanical Engineering Series, Springer, Berlin, 2009, oCLC: 836855039.
- [117] S. Skogestad, I. Postlewait, Multivariable Feedback Control, John Wiley & Sons, 2005.
- [118] T. Mizoguchi, T. Nozaki, K. Ohnishi, The power factor in mechanical system, in: 2013 IEEE International Conference on Mechatronics (ICM), 2013, pp. 576–581. doi:10.1109/ICMECH.2013.6519106.
- [119] DIN EN 61672-1: 2014-07. Electroacoustics – Sound level meters – Part 1: Specifications.
- [120] M. S. Hammer, T. K. Swinburn, R. L. Neitzel, Environmental noise pollution in the united states: developing an effective public health response, Environmental health perspectives 122 (2) (2013) 115–119.
- [121] M. Tornabene, Rotary regenerative shock absorber for automotive applications: Control strategies and hardware-in-the-loop implementation, Master's

thesis, Politecnico di Torino (Luglio 2021).

This Ph.D. thesis has been typeset by means of the T_EX-system facilities. The typesetting engine was pdfL^AT_EX. The document class was `toptesi`, by Claudio Beccari, with option `tipotesi=scudo`. This class is available in every up-to-date and complete T_EX-system installation.